

UNIVERSITY OF OKLAHOMA

GRADUATE COLLEGE

VIBRATIONAL SPECTROSCOPY OF PHOSPHATE-BASED  
ELECTRODES FOR LITHIUM RECHARGEABLE BATTERIES

A Dissertation

SUBMITTED TO THE GRADUATE FACULTY

in partial fulfillment of the requirements for the

degree of

Doctor of Philosophy

by

Christopher M. Burba

Norman, Oklahoma

2006

UMI Number: 3205285



---

UMI Microform 3205285

Copyright 2006 by ProQuest Information and Learning Company.  
All rights reserved. This microform edition is protected against  
unauthorized copying under Title 17, United States Code.

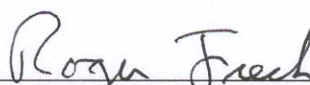
---

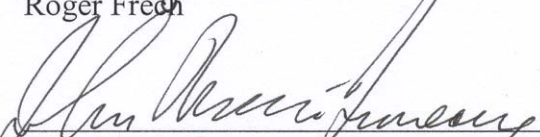
ProQuest Information and Learning Company  
300 North Zeeb Road  
P.O. Box 1346  
Ann Arbor, MI 48106-1346


VIBRATIONAL SPECTROSCOPY OF PHOSPHATE-BASED  
ELECTRODES FOR LITHIUM RECHARGEABLE BATTERIES


A DISSERTATION APPROVED FOR THE  
DEPARTMENT OF CHEMISTRY AND BIOCHEMISTRY

BY

  
\_\_\_\_\_  
Roger Frech

  
\_\_\_\_\_  
John Moore-Furneaux

  
\_\_\_\_\_  
George Richter-Addo

  
\_\_\_\_\_  
Wai Tak Yip

© Copyright by Christopher M. Burba 2006

All Rights Reserved.

## Acknowledgements

---

I have been working towards a Ph.D. in chemistry for the past ten years. The road has been long and often hard; there were even a few times that I came close to abandoning my goal. When I look back over these years, I see a multitude of people who helped me along my journey. First and foremost I want to thank my wife, **Elizabeth Burba**. Without you, I would not have achieved this dream. You were always there to encourage, support, and love me, even when the road got rough. I love you very much and I am deeply indebted to you.

**Roger Frech**, thank you for your patience and advice over the past six years. You were always willing to let me work on my side-projects. I cherish the opportunities I had working with you and hope for more in the future. I pray for the very best for you and your family in the years to come. I am also grateful to my committee members: **John Moore-Furneau**, **George Richter-Addo**, **Rudolf Wehmschulte**, **Ralph Wheeler**, and **Ivan Yip**. I appreciate each of you for your enthusiasm for science, and I feel that I have greatly benefited from having you as mentors. **Josh Thomas** and **Anton Nytén**, I greatly enjoyed the interesting collaborations.

**Xulong Zhang** and **Chris Rhodes**, thank you for taking me under your wing when I was a SURF student in 1998 and 1999. When I look back, I see those summers as a pivotal point in my academic career. An intense desire for research was born in my heart during those summer months. **Chris Rhodes**, you have been an especially wonderful friend and role model. I also wish to express my gratitude to past and current members of Roger Frech's research group: **Shawna York**, **Barry Klassen**, **Aishui Yu**, **Varuni Seneviratne**, **Fred McKenna**, **Rebecca Sanders**, **Matt Petrowsky**, **Nathalie**

**Rocher, Gwen Giffin, Rachel Mason, Allison McCoy, and Dilhani Jayathilaka.** You have all been wonderful colleagues. I thank you for your friendship and wish the best for each of you. **Mike Erickson,** thank you for carpooling with me to Kerr-McGee. The polymer battery research was fun, even during the frustrating times. **Charles Kelley,** thank you for keeping the X-ray diffractometer in good working order, and **George Morgan,** thank you for your help with the electron microprobe measurements. **Jean Keil,** I really appreciate all you have done for me. Without you, the paperwork would have buried me. **Patrick Bell, Jeff Moore, and Susan Meeker,** you inspired me to enter the field of science during my high school years.

I am very grateful to the **Department of Chemistry and Biochemistry** at the **University of Oklahoma** and the **Army Research Office** for financial assistance. I also thank **Rick Howard** and **Steve Sheargold** for the opportunity to work at **Kerr-McGee Chemical, LLC.** I treasure the time I had working there.

To my parents **Tim and Cindy Reed** and **Rick and Janet Burba** as well as my **extended family** and **in-laws,** thank you for supporting me over the past 10 years. This dream has been difficult to pursue, and I appreciate your advice and love during this time. I am deeply indebted to my church family at **Trinity Baptist Church.** You have all impacted my life in more ways than you know. I especially want to thank **Jason** and **Mandy Martin, Scott and Kim Martinson, Alan and Aubrey Maricle,** and **Steve and Holly Shaull.** Your friendship has sustained me through many storms during graduate school. I would also like to thank **Jason Martin, Larry Toothaker, Justin Devero** and **Jerry Brotzge** for the weekly lunches at Wendy's and the interesting conversations. **Billy Wolfe,** I greatly appreciate the advice you gave during my last year of graduate

school. **Ronnie Rogers**, thank you for the thought provoking sermons and making a place for me at the Round Table. It is wonderful to get away from the science once in a while and think about the really important things in life. Above all, I want to thank my savior and lord, **Jesus Christ** for sustaining me, hearing my prayers, and making such a wonderful world to study.

## Table of Contents

|   |              |
|---|--------------|
| <b>Acknowledgements</b>   | <b>iv</b>    |
| <b>List of Tables</b>   | <b>x</b>     |
| <b>List of Figures</b>  | <b>xi</b>    |
| <b>List of Schematics</b>   | <b>xv</b>    |
| <b>Abstract</b>   | <b>xvi</b>   |
| <b>Prolegomenon</b>   | <b>xviii</b> |
| <b>Chapter 1 LITHIUM RECHARGEABLE BATTERIES</b>   | <b>1</b>     |
| 1.1 Introduction to Basic Battery Principles  | 1            |
| 1.2 Materials Overview for Lithium Rechargeable Batteries   | 10           |
| 1.2.1 Anode Materials   | 10           |
| 1.2.2 Cathode Materials   | 14           |
| 1.2.3 Electrolyte Systems   | 16           |
| 1.3 Parameters that Control Energy Density, Cell Power, and Cyclability   | 20           |
| 1.4 Safety Concerns   | 23           |
| 1.5 References  | 24           |
| <b>Chapter 2 PHOSPHO-OLIVINE <math>\text{LiMPO}_4</math> (M = Mn, Fe, Co Ni) CATHODES</b>   | <b>36</b>    |
| 2.1 Introduction  | 36           |
| 2.2 Experimental Methods  | 40           |
| 2.3 Results and Discussion  | 42           |
| 2.3.1 $\text{LiMPO}_4$ (M = Fe, Mn, Co, Ni)   | 42           |
| 2.3.2 $\text{LiFePO}_4$ and $\text{NaFePO}_4$   | 50           |
| 2.3.3 $\text{Li}_x\text{FePO}_4$ ( $0 \leq x \leq 1$ ) Cathodes   | 59           |
| 2.3.4 $\text{Li}_x(\text{Mn}_y\text{Fe}_{1-y})\text{PO}_4$ ( $0 \leq x, y \leq 1$ ) Cathodes                                      | 72           |
| 2.4 Conclusions   | 82           |
| 2.5 References  | 86           |
| <b>Chapter 3 LISICON <math>\text{Li}_3\text{V}_2(\text{PO}_4)_3</math> and <math>\text{LiTi}_2(\text{PO}_4)_3</math> CATHODES</b> | <b>92</b>    |
| 3.1 Introduction  | 92           |
| 3.2 Experimental Methods  | 96           |
| 3.3 Results   | 98           |
| 3.3.1 Powder X-Ray Diffraction  | 98           |



|                  |   |            |
|------------------|---|------------|
| 3.3.2            | Electron Microprobe Analysis  | 98         |
| 3.3.3            | Symmetry-based Analysis of the Vibrational Modes  | 101        |
| 3.3.4            | Raman Spectroscopy  | 102        |
| 3.3.4.1          | Pure Materials  | 102        |
| 3.3.4.2          | $\text{Li}_x\text{Ti}_2(\text{PO}_4)_3$   | 107        |
| 3.3.5            | Infrared Spectroscopy   | 109        |
| 3.3.5.1          | Pure Materials  | 109        |
| 3.3.5.2          | Monoclinic $\text{Li}_x\text{V}_2(\text{PO}_4)_3$   | 112        |
| 3.3.5.3          | Rhombohedral $\text{Li}_x\text{V}_2(\text{PO}_4)_3$   | 115        |
| 3.3.5.4          | $\text{Li}_x\text{Ti}_2(\text{PO}_4)_3$   | 117        |
| 3.4              | Discussion  | 119        |
| 3.4.1            | Monoclinic $\text{Li}_x\text{V}_2(\text{PO}_4)_3$   | 119        |
| 3.4.2            | Rhombohedral $\text{Li}_x\text{V}_2(\text{PO}_4)_3$ and $\text{Li}_x\text{Ti}_2(\text{PO}_4)_3$ | 123        |
| 3.5              | Conclusions   | 127        |
| 3.6              | References  | 130        |
| <b>Chapter 4</b> | <b>TIN PHOSPHATE ANODES</b>   | <b>135</b> |
| 4.1              | Introduction  | 135        |
| 4.2              | Experimental Methods  | 137        |
| 4.3              | Results   | 138        |
| 4.3.1            | Particle Size and Surface Area Measurements   | 138        |
| 4.3.2            | Electrochemical Data  | 139        |
| 4.3.3            | Powder X-Ray Diffraction Data   | 141        |
| 4.3.4            | Symmetry-Based Analysis of the Vibrational Modes  | 142        |
| 4.3.5            | Infrared Spectra during $\text{Li}^+$ Ion Insertion   | 146        |
| 4.3.6            | Differential Scanning Calorimetry   | 150        |
| 4.4              | Discussion  | 151        |
| 4.4.1            | Impedance and X-Ray Diffraction Data  | 151        |
| 4.4.2            | Vibrational Spectroscopy  | 154        |
| 4.4.3            | Thermal Data  | 158        |
| 4.5              | Conclusions   | 160        |
| 4.6              | References  | 162        |
| <b>Chapter 5</b> | <b><i>IN SITU</i> VIBRATIONAL SPECTROSCOPIC STUDIES</b>   | <b>164</b> |
| 5.1              | Introduction  | 164        |
| 5.2              | <i>In Situ</i> Raman Spectroelectrochemistry  | 167        |
| 5.2.1            | <i>In Situ</i> Raman Spectroelectrochemical Cell  | 167        |
| 5.2.1.1          | Cathode Preparation   | 167        |
| 5.2.1.2          | Spectroelectrochemical Cell Design  | 167        |
| 5.2.1.3          | Electrochemical and Spectroscopic Experiments   | 168        |
| 5.2.2            | Lithium Insertion into $\text{V}_2\text{O}_5$ Cathodes  | 168        |
| 5.2.2.1          | Electrochemistry  | 168        |
| 5.2.2.2          | Raman Spectroscopy  | 172        |
| 5.2.3            | Lithium Insertion into Phosphate-Based Cathodes   | 174        |

|                   |   |            |
|-------------------|---|------------|
| 5.3               | <i>In Situ</i> Transmission FTIR Spectroelectrochemistry                | 174        |
| 5.3.1             | <i>In Situ</i> Transmission FTIR Spectroelectrochemical Cell            | 174        |
| 5.3.1.1           | Cathode Preparation   | 174        |
| 5.3.1.2           | Spectroelectrochemical Cell Design                                      | 175        |
| 5.3.1.3           | Electrochemical and Spectroscopic Experiments                           | 177        |
| 5.3.2             | Lithium Insertion into Orthorhombic FePO <sub>4</sub>                   | 177        |
| 5.4               | Conclusions   | 182        |
| 5.5               | References  | 184        |
| <b>Chapter 6</b>  | <b>IONIC ASSOCIATION OF LiPF<sub>6</sub> IN NONAQUEOUS ELECTROLYTES</b> | <b>187</b> |
| 6.1               | Introduction  | 187        |
| 6.2               | Experimental Method   | 188        |
| 6.3               | Results and Discussion  | 189        |
| 6.3.1             | Ion-Ion Interactions  | 189        |
| 6.3.2             | Ion-Solvent Interactions  | 192        |
| 6.4               | Conclusions   | 196        |
| 6.5               | References  | 196        |
| <b>Chapter 7</b>  | <b>CONCLUDING REMARKS</b>   | <b>200</b> |
| <b>Appendix A</b> | <b>EXPERIMENTAL METHODS</b>   | <b>203</b> |
| A.1               | Powder X-Ray Diffraction  | 203        |
| A.2               | Elemental Analysis  | 203        |
| A.3               | Particle Size and Surface Area Measurements                             | 203        |
| A.4               | Impedance Spectroscopy  | 204        |
| A.5               | Infrared Spectroscopy   | 204        |
| A.6               | Raman Spectroscopy  | 204        |
| A.7               | Differential Scanning Calorimetry                                       | 205        |
| A.8               | Reference   | 205        |

## List of Tables

---

|              |   |     |
|--------------|---|-----|
| Table II-I   | Lattice parameters for $\text{LiMPO}_4$ compounds.  | 43  |
| Table II-II  | Factor group correlation of the internal and external vibrations for $\text{LiFePO}_4$ .  | 45  |
| Table II-III | Factor group correlation of the internal and external vibrations for $\text{NaFePO}_4$ .  | 54  |
| Table II-IV  | The calculated Fe/P ratios for $\text{Li}_x\text{FePO}_4$ materials.  | 61  |
| Table III-I  | Lattice parameters for A- and B- $\text{Li}_3\text{V}_2(\text{PO}_4)_3$ , $\text{Na}_3\text{V}_2(\text{PO}_4)_3$ , and $\text{LiTi}_2(\text{PO}_4)_3$ .   | 99  |
| Table III-II | A factor group correlation of the $\text{PO}_4^{3-}$ internal modes for monoclinic $\text{Li}_x\text{V}_2(\text{PO}_4)_3$ and rhombohedral $\text{Li}_x\text{M}_2(\text{PO}_4)_3$ ( $x = 1, 3$ and $\text{M} = \text{Ti, V}$ ). | 102 |
| Table IV-I   | Factor group correlation of the intramolecular $\text{PO}_4^{3-}$ modes in $\text{LiSn}_2(\text{PO}_4)_3$ and $\text{Sn}_3(\text{PO}_4)_2$ .  | 143 |

## List of Figures

---

|            |   |    |
|------------|---|----|
| Figure 1-1 | Comparison of gravimetric and volumetric energy densities for several rechargeable battery technologies.  | 2  |
| Figure 1-2 | Changes in gravimetric and volumetric energy densities for lithium rechargeable batteries between 1991 and 2004.  | 3  |
| Figure 1-3 | Breakdown of the total rechargeable battery market according to type of technology for the year 2000.   | 3  |
| Figure 1-4 | Cost (in U.S. dollars) of lithium rechargeable batteries between 1991 and 2004.   | 4  |
| Figure 1-5 | A schematic diagram of a lithium rechargeable battery.  | 5  |
| Figure 1-6 | A typical cycle for a lithium rechargeable battery.   | 7  |
| Figure 1-7 | Free energy and voltage curves for a first-order transition between compositions $x_1$ to $x_2$ .   | 9  |
| Figure 1-8 | Electrochemical voltages for some intercalation anodes and cathodes used in lithium rechargeable batteries.   | 11 |
| Figure 1-9 | A Ragone plot comparing several rechargeable battery technologies.  | 20 |
| Figure 2-1 | Powder XRD diffractograms of $\text{LiMPO}_4$ compounds.  | 43 |
| Figure 2-2 | Representation of the phospho-olivine $\text{LiMPO}_4$ unit cell.   | 43 |
| Figure 2-3 | Infrared absorption spectra of $\text{LiMPO}_4$ .   | 45 |
| Figure 2-4 | Infrared absorption spectra of $\nu_4$ for $\text{LiMPO}_4$ .   | 47 |
| Figure 2-5 | Linear correlation between the factor group splitting of $\nu_4$ and the second ionization energy of the divalent transition metal ion in $\text{LiMPO}_4$ ( $r = 0.9921$ , $p = 0.0079$ ). | 48 |
| Figure 2-6 | Raman scattering spectra of $\text{LiMPO}_4$ .  | 49 |
| Figure 2-7 | Raman scattering spectra of ${}^6\text{LiFePO}_4$ and ${}^7\text{LiFePO}_4$ .   | 50 |
| Figure 2-8 | Infrared absorption spectra of ${}^6\text{LiFePO}_4$ and ${}^7\text{LiFePO}_4$ .  | 51 |

|             |  |    |
|-------------|--|----|
| Figure 2-9  | GITT data of the electrochemical insertion of Na <sup>+</sup> ions into FePO <sub>4</sub> .  | 53 |
| Figure 2-10 | Infrared absorption spectra of ν <sub>1</sub> and ν <sub>3</sub> for LiFePO <sub>4</sub> and NaFePO <sub>4</sub> .   | 54 |
| Figure 2-11 | Raman scattering spectra of ν <sub>1</sub> and ν <sub>3</sub> for LiFePO <sub>4</sub> and NaFePO <sub>4</sub> .  | 56 |
| Figure 2-12 | Infrared absorption spectra of ν <sub>4</sub> and the Li <sup>+</sup> ion cage modes for LiFePO <sub>4</sub> and NaFePO <sub>4</sub> .   | 56 |
| Figure 2-13 | Electron microprobe images of LiFePO <sub>4</sub> and FePO <sub>4</sub> at 200x magnification.   | 60 |
| Figure 2-14 | Powder XRD diffractograms of Li <sub>x</sub> FePO <sub>4</sub> .   | 62 |
| Figure 2-15 | Infrared absorption spectra of ν <sub>1</sub> and ν <sub>3</sub> for Li <sub>x</sub> FePO <sub>4</sub> .   | 64 |
| Figure 2-16 | Raman scattering spectra of ν <sub>1</sub> and ν <sub>3</sub> for Li <sub>x</sub> FePO <sub>4</sub> .  | 64 |
| Figure 2-17 | Infrared absorption spectra of ν <sub>4</sub> , ν <sub>2</sub> , and the external modes for Li <sub>x</sub> FePO <sub>4</sub> .  | 66 |
| Figure 2-18 | Raman scattering spectra of ν <sub>4</sub> , ν <sub>2</sub> , and the external modes for Li <sub>x</sub> FePO <sub>4</sub> .   | 68 |
| Figure 2-19 | Infrared absorption spectra of ν <sub>4</sub> and the Li <sup>+</sup> ion cage modes for LiFePO <sub>4</sub> , NaFePO <sub>4</sub> , and FePO <sub>4</sub> .   | 70 |
| Figure 2-20 | Raman scattering spectrum of carbon-coated Li(Mn <sub>0.5</sub> Fe <sub>0.5</sub> )PO <sub>4</sub> .   | 73 |
| Figure 2-21 | Infrared absorption spectra of ν <sub>1</sub> and ν <sub>3</sub> for Li(Mn <sub>y</sub> Fe <sub>1-y</sub> )PO <sub>4</sub> (y = 0, 0.5, 1).  | 75 |
| Figure 2-22 | Infrared absorption spectra of ν <sub>4</sub> and the Li <sup>+</sup> ion cage modes for Li(Mn <sub>y</sub> Fe <sub>1-y</sub> )PO <sub>4</sub> (y = 0, 0.5, 1).  | 77 |
| Figure 2-23 | Cyclic voltammogram of Li(Mn <sub>0.5</sub> Fe <sub>0.5</sub> )PO <sub>4</sub> between 2.85 and 4.6 V (0.5 mV/sec).  | 78 |
| Figure 2-24 | Infrared absorption spectra of ν <sub>1</sub> and ν <sub>3</sub> for Li <sub>x</sub> (Mn <sub>0.5</sub> Fe <sub>0.5</sub> )PO <sub>4</sub> at various states of charge and FePO <sub>4</sub> .         | 79 |
| Figure 2-25 | Infrared absorption spectra of ν <sub>4</sub> and the lithium cage modes for Li <sub>x</sub> (Mn <sub>0.5</sub> Fe <sub>0.5</sub> )PO <sub>4</sub> at various states of charge and FePO <sub>4</sub> . | 80 |

|             |  |     |
|-------------|--|-----|
| Figure 3-1  | Powder XRD patterns for A- and B- $\text{Li}_3\text{V}_2(\text{PO}_4)_3$ , $\text{Na}_3\text{V}_2(\text{PO}_4)_3$ , and $\text{LiTi}_2(\text{PO}_4)_3$ .                           | 99  |
| Figure 3-2  | Electron microprobe images of A- and B- $\text{Li}_3\text{V}_2(\text{PO}_4)_3$ at a magnification of 250x (inset: 1000x).  | 100 |
| Figure 3-3  | Raman scattering spectrum of $\nu_1$ and $\nu_3$ for $\text{LiTi}_2(\text{PO}_4)_3$ .  | 103 |
| Figure 3-4  | Raman scattering spectrum of $\text{LiTi}_2(\text{PO}_4)_3$ .  | 104 |
| Figure 3-5  | Raman scattering spectra of A- and B- $\text{Li}_3\text{V}_2(\text{PO}_4)_3$ .   | 106 |
| Figure 3-6  | GITT data for the electrochemical insertion of $\text{Li}^+$ into $\text{LiTi}_2(\text{PO}_4)_3$ .   | 107 |
| Figure 3-7  | Raman scattering spectra of $\text{Li}_x\text{Ti}_2(\text{PO}_4)_3$ .  | 108 |
| Figure 3-8  | Infrared absorption spectra of A- and B- $\text{Li}_3\text{V}_2(\text{PO}_4)_3$ , $\text{Na}_3\text{V}_2(\text{PO}_4)_3$ , and $\text{LiTi}_2(\text{PO}_4)_3$ .                    | 109 |
| Figure 3-9  | Electrochemical cycling of A- $\text{Li}_3\text{V}_2(\text{PO}_4)_3$ .   | 113 |
| Figure 3-10 | Infrared absorption spectra of A- $\text{Li}_x\text{V}_2(\text{PO}_4)_3$ recorded at different points along the first cycle.   | 114 |
| Figure 3-11 | Electrochemical cycling of B- $\text{Li}_3\text{V}_2(\text{PO}_4)_3$ .   | 115 |
| Figure 3-12 | Infrared absorption spectra of B- $\text{Li}_x\text{V}_2(\text{PO}_4)_3$ recorded at different points along the first cycle.   | 116 |
| Figure 3-13 | Infrared absorption spectra of $\text{Li}_x\text{Ti}_2(\text{PO}_4)_3$ .   | 118 |
| Figure 3-14 | Infrared absorption spectra of A- $\text{V}_2(\text{PO}_4)_3$ and a $\text{V}_2\text{O}_5\text{-P}_2\text{O}_5$ glass with a nominal composition of 2:3.                           | 121 |
| Figure 3-15 | Infrared absorption spectra comparing $\text{Li}_x\text{Ti}_2(\text{PO}_4)_3$ and B- $\text{Li}_x\text{V}_2(\text{PO}_4)_3$ where $x = 1$ and 3.                                   | 123 |
| Figure 4-1  | Particle size analyses of the as-synthesized $\text{LiSn}_2(\text{PO}_4)_3$ and $\text{Sn}_3(\text{PO}_4)_2$ powders.  | 138 |
| Figure 4-2  | The first electrochemical discharge of $\text{LiSn}_2(\text{PO}_4)_3$ and $\text{Sn}_3(\text{PO}_4)_2$ electrodes.   | 140 |
| Figure 4-3  | X-ray diffractograms ( $10\text{-}50^\circ$ , $0.50^\circ/\text{min}$ ) of $\text{LiSn}_2(\text{PO}_4)_3$ and $\text{Sn}_3(\text{PO}_4)_2$ before and after discharging to 0.01 V. | 141 |

|             |  |     |
|-------------|--|-----|
| Figure 4-4  | Infrared absorption spectra of $\text{LiSn}_2(\text{PO}_4)_3$ and $\text{Sn}_3(\text{PO}_4)_2$ .   | 144 |
| Figure 4-5  | Raman scattering spectra of $\text{LiSn}_2(\text{PO}_4)_3$ and $\text{Sn}_3(\text{PO}_4)_2$ .  | 144 |
| Figure 4-6  | Mid-IR spectra of $\text{LiSn}_2(\text{PO}_4)_3$ at various states of discharge.   | 146 |
| Figure 4-7  | Far-IR spectra of $\text{LiSn}_2(\text{PO}_4)_3$ at various states of discharge.   | 148 |
| Figure 4-8  | Mid-IR spectra of $\text{Sn}_3(\text{PO}_4)_2$ at various states of discharge.   | 149 |
| Figure 4-9  | Far-IR spectra of $\text{Sn}_3(\text{PO}_4)_2$ at various states of discharge.   | 149 |
| Figure 4-10 | First and second DSC heating curves for $\text{LiSn}_2(\text{PO}_4)_3$ and $\text{Sn}_3(\text{PO}_4)_2$ as a function of voltage.                  | 151 |
| Figure 4-11 | Differential capacity plots for $\text{LiSn}_2(\text{PO}_4)_3$ and $\text{Sn}_3(\text{PO}_4)_2$ between 0.60 and 1.00 V.                           | 156 |
| Figure 5-1  | Electrochemical (a) discharging and (b) charging curves for <i>in situ</i> Raman spectroelectrochemical and normal cells.                          | 170 |
| Figure 5-2  | Effect of cell type on discharge capacity.   | 171 |
| Figure 5-3  | <i>In situ</i> Raman scattering spectra recorded during the first cycle of a $\text{Li}/\text{V}_2\text{O}_5$ cell.                                | 172 |
| Figure 5-4  | First discharge of $\text{FePO}_4$ in the <i>in situ</i> transmission FTIR spectroelectrochemical cell.  | 178 |
| Figure 5-5  | Electrochemical cycling of $\text{FePO}_4$ inside a coin cell.   | 179 |
| Figure 5-6  | <i>In situ</i> transmission FTIR spectra recorded during the first discharge of $\text{FePO}_4$ .  | 180 |
| Figure 5-7  | Infrared transmission spectra of $\text{FePO}_4$ and $\text{LiFePO}_4$ .   | 181 |
| Figure 6-1  | Possible coordination environments of the $\text{Li}^+\cdots\text{PF}_6^-$ ion pairs.  | 190 |
| Figure 6-2  | Infrared absorption spectra of $\text{LiPF}_6$ dissolved in a series of aprotic solvents (20:1 composition).                                       | 191 |
| Figure 6-3  | Raman scattering and infrared absorption spectra of diglyme: $\text{LiPF}_6$ and ethyl acetate: $\text{LiPF}_6$ solutions.                         | 193 |
| Figure 6-4  | Infrared absorption spectra comparing diglyme: $\text{LiPF}_6$ solutions to ethyl acetate: $\text{LiPF}_6$ and acetone: $\text{LiPF}_6$ solutions. | 195 |

## List of Schematics

---

|            |  |     |
|------------|--|-----|
| Scheme 5-1 | A diagram of the modified <i>in situ</i> Raman spectroelectrochemical cell (not drawn to scale).                       | 168 |
| Scheme 5-2 | A diagram of the <i>in situ</i> transmission FTIR spectroelectrochemical cell (not drawn to scale).                    | 176 |
| Scheme 5-3 | A drawing of the KBr windows in the <i>in situ</i> transmission FTIR spectroelectrochemical cell (not drawn to scale). | 176 |



## Abstract

---

The favorable energy densities and cycling performances attainable from lithium rechargeable batteries has prompted aggressive research in this field for over 30 years. In particular, phosphate-based electrodes receive much attention due to their competitive redox potentials, capacities, and enhanced safety compared to currently commercialized systems. In developing these materials, it is critical to have a good understanding of the fundamental reactions that occur during cycling. Vibrational spectroscopy is particularly useful in this regard because it is sensitive to the local structure of the electrodes. However, few researchers use vibrational spectroscopy to study lithium intercalation in phosphate-based electrodes. The intramolecular vibrations of the phosphate anions yield intense bands in the Raman and infrared spectrum that are sensitive to the immediate local environment of the phosphate anions; thus they are natural candidates for the technique. Measuring the infrared or Raman spectrum of these materials at various states of charge can provide a wealth of information about local structural changes and charge compensation reactions occurring within an electrode from the perspective of the phosphate anions.

The first objective of this dissertation is to examine lithium intercalation with vibrational spectroscopy for three families of phosphate-based electrodes: phospho-olivine  $\text{LiMPO}_4$  ( $M = \text{Fe}, \text{Mn}$ ) cathodes, LISICON  $\text{Li}_3\text{M}_2(\text{PO}_4)_3$  ( $M = \text{V}, \text{Ti}$ ) cathodes, and  $\text{LiSn}_2(\text{PO}_4)_3$  and  $\text{Sn}_3(\text{PO}_4)_2$  anodes. Symmetry-based analyses are used to interpret the vibrational modes of each compound. Vibrational spectra recorded at various states of charge demonstrate the sensitivity of the phosphate anions to the presence of lithium ions and provide insight into the lithium intercalation reactions that occur within these

materials. The second objective of this dissertation is to describe new *in situ* electrochemical cells for Raman and infrared spectroscopy. For example, a relatively cheap *in situ* Raman cell based on modified coin cells is tested with  $V_2O_5$  cathodes. The field of *in situ* infrared spectroscopy is extended to include transmission experiments. The performance of a new *in situ* transmission FT-IR spectroelectrochemical cell is tested with  $FePO_4$  cathodes, and the results agree very well with *ex situ* experiments. Both techniques provide new ways to study lithium intercalation for a range of advanced electrode materials.

## Prolegomenon

---

This dissertation is a compilation of material that has been published in or submitted to several peer-reviewed journals. The appropriate references for each chapter are listed below:

- Chapter 1** The first chapter serves as a general introduction to the field of lithium rechargeable batteries. A brief overview of various anode, cathode, and electrolyte systems as well as parameters that influence energy density, power, and cyclability is provided.
- Chapter 2** Christopher M. Burba and Roger Frech, “Raman and FTIR Spectroscopic Study of  $\text{Li}_x\text{FePO}_4$  ( $0 \leq x \leq 1$ )” *J. Electrochem. Soc.*, **151**(7) A1032-A1038 (2004)
- Christopher M. Burba and Roger Frech, “Vibrational Spectroscopic Investigation of Structurally-Related  $\text{LiFePO}_4$ ,  $\text{NaFePO}_4$ , and  $\text{FePO}_4$  Compounds” *Spectrochim. Acta A*, **in press** (2005)
- Christopher M. Burba, Roger Frech, Anton Nyttén, and J. O. Thomas, “Local Structures in Carbon-Coated  $\text{Li}_x(\text{Mn}_y\text{Fe}_{1-y})\text{PO}_4$  Cathodes” *J. Power Sources*, **to be submitted** (2005)
- Chapter 3** Christopher M. Burba and Roger Frech, “Vibrational Spectroscopic Studies of Monoclinic and Rhombohedral  $\text{Li}_3\text{V}_2(\text{PO}_4)_3$ ” *Solid State Ionics*, **submitted** (2005)
- Christopher M. Burba and Roger Frech, “Vibrational Spectroscopic Study of Lithium Intercalation into  $\text{LiTi}_2(\text{PO}_4)_3$ ” *Solid State Ionics*, **submitted** (2005)

- Chapter 4** Christopher M. Burba and Roger Frech, “Electrochemical, Spectroscopic, and Thermal Investigations of  $\text{LiSn}_2(\text{PO}_4)_3$  and  $\text{Sn}_3(\text{PO}_4)_2$  Anodes during the First Discharge” *J. Electrochem. Soc.*, **152**(6) A1233-A1240 (2005)
- Chapter 5** Christopher M. Burba and Roger Frech, “Modified Coin Cells for *In Situ* Raman Spectroelectrochemical Measurements of Lithium Batteries” *Appl. Spectrosc.*, **submitted** (2005)
- Christopher M. Burba and Roger Frech, “*In Situ* Transmission FTIR Spectroelectrochemistry: A New Technique for Studying Lithium Batteries” *Electrochim. Acta*, **submitted** (2005)
- Chapter 6** Christopher M. Burba and Roger Frech, “Spectroscopic Measurements of Ionic Association in Solutions of  $\text{LiPF}_6$ ” *J. Phys. Chem. B*, **109**(31) 15161-15164 (2005)
- Chapter 7** This final chapter summarizes the principle results of the dissertation.

## Chapter 1: LITHIUM RECHARGEABLE BATTERIES

---

### 1.1 Introduction to Basic Battery Principles

A considerable amount of fundamental and applied research is invested in producing lightweight, portable power sources. Potential applications (e.g., industrial, military, or commercial), economics, and environmental concerns all affect the development of this field. As a result, a variety of technologies have been explored to meet these needs (e.g., batteries, fuel cells, electrochemical capacitors, photovoltaics, and others). Two major applications for high-energy devices are hybrid electric vehicles (HEVs) and portable electronics such as laptop computers, personal digital assistants, or cellular telephones. The first is especially interesting because alternative energy sources for vehicles could decrease automotive emissions as well as lower the United States' dependence on foreign petroleum. Fuel cells have been aggressively investigated for this market niche; however, other technologies are also being implemented. For example, the 2005 model of the HEV Toyota Prius employs a nickel metal hydride rechargeable battery [1].

In the most simplistic sense, a battery is a device that converts chemical energy into electrical energy. Strictly speaking, a single electrochemical power system is termed a "cell" and a series or parallel connection of cells is called a "battery." However, these definitions are used loosely throughout the literature. All batteries may be divided into two broad categories: primary and secondary cells. A primary battery may be used one time and is discarded after it is completely exhausted. In contrast, a secondary battery

may be charged and discharged multiple times. Secondary batteries comprise several different technologies including lithium ion, lead acid, nickel metal hydride (NiMH), and nickel-cadmium (Ni-Cd). Lithium ion batteries are particularly attractive, because of their high gravimetric and volumetric energy densities compared to the other systems (Fig. 1-1) [2-4]. These characteristics may lead to smaller and lighter cells that are ideal for portable electronics or HEVs. As shown in Fig. 1-2, lithium rechargeable batteries have gradually improved in terms of gravimetric and volumetric energy density over the past fifteen years [5]. For example, in 1991 cells typically delivered about 200 Wh/L, whereas in 2004 the reported value exceeded 500 Wh/L. It is estimated that secondary batteries constitute about 8% of the total portable battery market [6], with NiMH and Ni-Cd technologies dominating the secondary battery market (Fig. 1-3) [6]. In 2000, one market analyst assigned lithium ion batteries to 18% of the total rechargeable battery market, while together NiMH and Ni-Cd constituted over 73%.

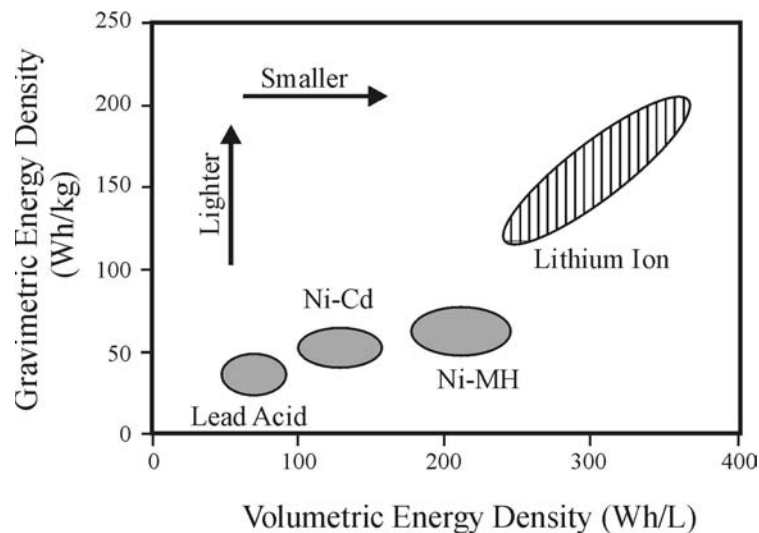


**Figure 1-1:** Comparison of gravimetric and volumetric energy densities for several rechargeable battery technologies [3].

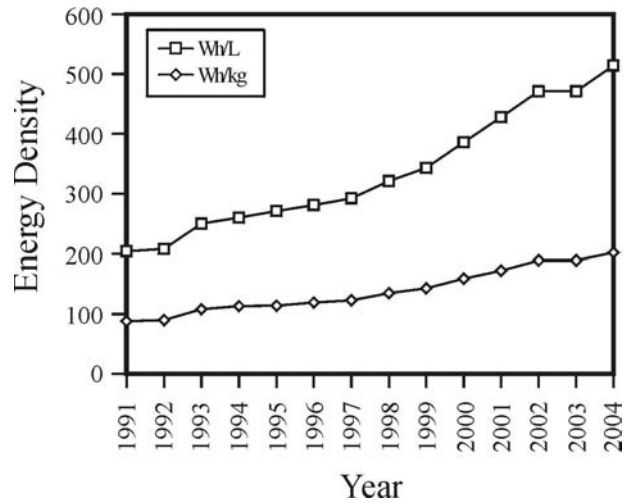


**Figure 1-2:** Changes in gravimetric ( $\diamond$ ) and volumetric ( $\square$ ) energy densities for lithium rechargeable batteries between 1991 and 2004 [5].

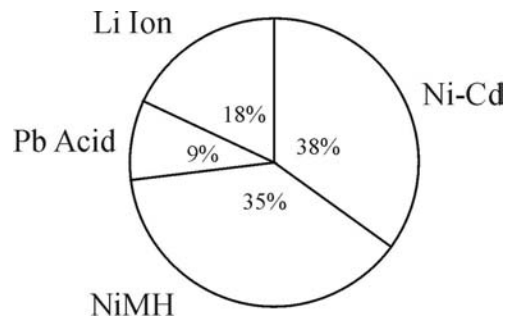


**Figure 1-3:** Breakdown of the total rechargeable battery market according to technology for the year 2000 [6].

As a whole, batteries encompass a multibillion-dollar industry. According to Saxman [7], the value of the battery market reached over \$13 billion in 2004 (lithium rechargeable batteries amounted to \$1.7 billion). In many ways, the total cost of storing energy is a more important metric than the gravimetric or volumetric energy densities, for this directly affects competition between rival technologies. Fig. 1-4 illustrates the relative cost of lithium rechargeable batteries between 1991 and 2004. In the early

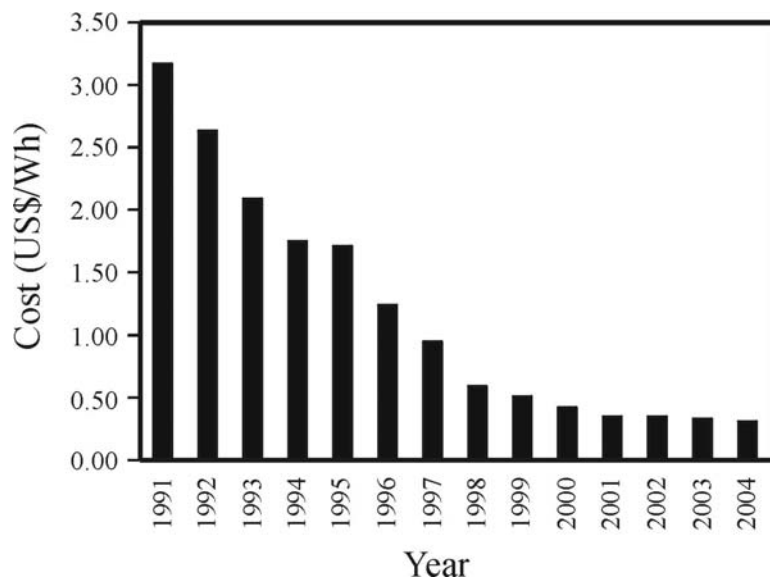


**Figure 1-4:** Cost (in U.S. dollars) of lithium rechargeable batteries between 1991 and 2004.

1990s, the cost to store energy with lithium rechargeable batteries was quite expensive (>\$3.00/Wh); however, the cost has steadily declined and by 1997 was below \$1.00/Wh [5].

An electrochemical cell consists of two electrodes, an electrolyte, and external circuitry. A pictorial representation of a typical lithium ion battery ( $\text{Li}_x\text{C}$  anode and  $\text{Li}_x\text{FePO}_4$  cathode) is presented in Fig. 1-5. The electrolyte and separator are not drawn to simplify the cartoon. The electrode with the higher redox potential with respect to lithium metal is called the cathode and the lower redox potential electrode is the anode. Reductive chemical reactions occur at the cathode, while oxidative chemical reactions are associated with the anode. When the circuit is closed, electrons and lithium ions flow from the anode to the cathode. The electrons travel through the external circuitry to reach the cathode, whereas the lithium ions migrate through the electrolyte. In a secondary



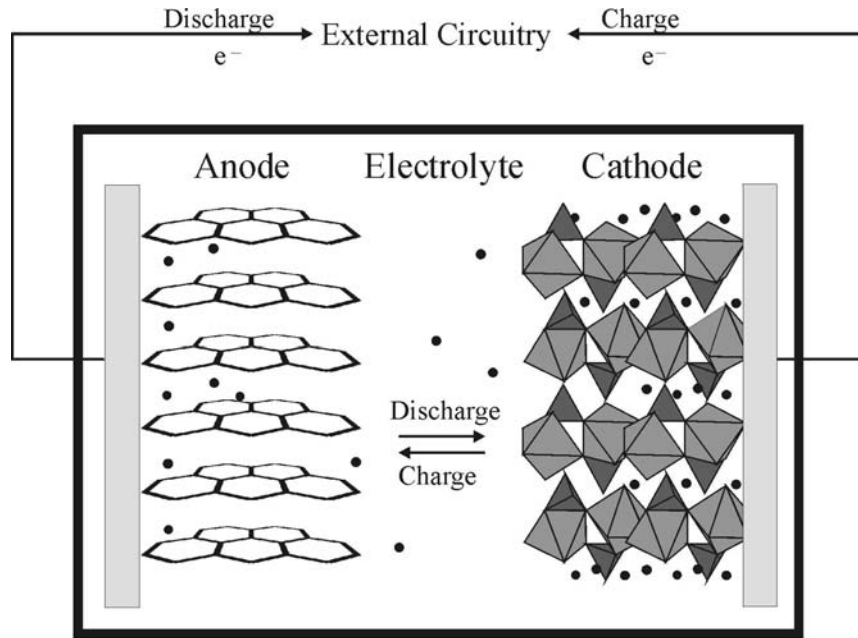


**Figure 1-5:** A schematic diagram of a lithium rechargeable battery. Lithiated graphite and  $\text{LiFePO}_4$  represent the anode and cathode, respectively. The electrolyte molecules are not drawn to simplify the cartoon.

lithium battery, these electrochemical reactions may be reversed by the addition of energy (recharging the cell). Strictly speaking, the labels “cathode” and “anode” should be switched during the charging process because the oxidative reactions would proceed at the positive terminal and the negative electrode would experience reduction. However, most researchers do not make this distinction, and the positive terminal is always referred to as the cathode even when the cell is being charged.

The open circuit voltage ( $E_{OC}$ ) of a lithium battery is determined by the difference in the lithium chemical potential in the cathode ( $\mu_{\text{Li}(c)}$ ) and anode ( $\mu_{\text{Li}(a)}$ ):

$$E_{OC} = \frac{\mu_{\text{Li}(c)} - \mu_{\text{Li}(a)}}{z\mathcal{F}} \quad \text{[Equation 1-1]}$$

where  $z$  is the charge of the charge carriers ( $z = +1$  for  $\text{Li}^+$  ions) and  $\mathcal{F}$  is Faraday’s constant [8]. Reactions that have a large difference in the lithium chemical potential will

have a large cell potential. Various thermodynamic quantities may also be obtained for the cell reaction [9]. For example, the net amount of useful energy that may be used to perform electrical work is equal to the change in Gibb's free energy for the reaction ( $\Delta G$ ). The relationship between Gibb's free energy and cell potential is clearly seen if Eq. 1-1 is written in a more familiar form:

$$\Delta G = -n \mathcal{F} E \quad \text{[Equation 1-2]}$$

where  $n$  is the number of electrons transferred per mole of reactants and  $E$  is the electromotive force. Furthermore, the change in entropy ( $\Delta S$ ) may be evaluated from temperature-dependant measurements of the cell's potential at constant pressure:

$$\Delta S = -n \mathcal{F} \left( \frac{\partial E}{\partial T} \right)_P \quad \text{[Equation 1-3]}$$

where  $T$  is the absolute temperature. The change in enthalpy ( $\Delta H$ ) is then determined by the following relationship:

$$\Delta G = \Delta H - T\Delta S \quad \text{[Equation 1-4]}$$

Systems that have a positive  $dE/dT$  at constant pressure will heat when charged and cool when discharged. The opposite is true for systems with a negative  $dE/dT$ , and lead acid batteries are an example of a cell that cools during charge and heats during discharge [10].

The number of lithium ions and electrons involved in the electrochemical reactions determines the capacity of a cell. It is desirable for electrode materials to have a very high specific capacity in order to maximize the energy density of a manufactured cell. Eq. 1-5 may be used to calculate the gravimetric specific capacity (denoted as  $C_{grav}$ ) for an electrode material of molecular weight  $MW$ .

$$C_{grav} = \frac{n\mathcal{F}}{MW} \quad [\text{Equation 1-5}]$$

The volumetric specific capacity is calculated by multiplying  $C_{grav}$  with the density of the material. Gravimetric and volumetric specific capacities are usually reported with units of mAh/g and mAh/ml, respectively. Of course, the practical capacity of an electrode is rarely equal to the theoretical capacity, and limitations on cell capacity are discussed in Section 1.3.

The shape of a cycling curve is largely determined by the kinetics of the electrochemical reaction and the phase behavior of the electrodes during cycling [10]. A typical cycle for a lithium rechargeable battery is presented in Fig. 1-6. The cycle typically consists of three distinct steps: charge, rest, and discharge. Both the charging and discharging portions may be divided into four general regions. Initially, a cell experiences a small  $IR$  drop when the circuit is first closed. Afterwards, the cell undergoes activation polarization due to kinetic hindrances of charge-transfer at the

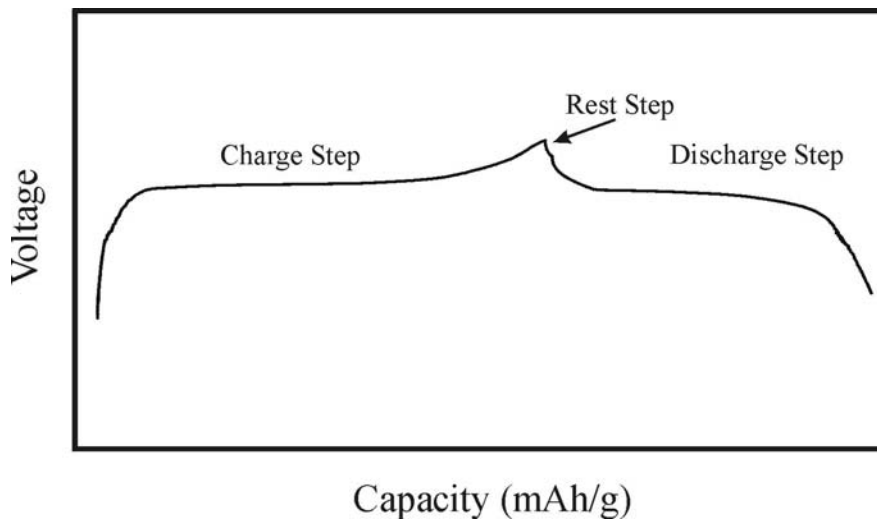


**Figure 1-6:** A typical cycle for a lithium rechargeable battery.

electrode-electrolyte interface. Transition state theory describes cell kinetics in this region of the discharge curve, and the Tafel equation (Eq. 1-6) is often used to characterize cell polarization,  $\eta$  [10,11]:

$$\eta = a \pm b \log|i| \quad \text{[Equation 1-6]}$$

Here,  $i$  corresponds to the current density and  $a$  and  $b$  are characteristic constants of the reaction. In this equation, cell polarization is defined as the departure of the closed circuit cell potential ( $E_{cc}$ ) from its equilibrium value ( $E_{oc}$ ). That is,  $\eta = E_{oc} - E_{cc}$ . The positive term in Eq. 1-6 is used for cathodic over potentials and the negative sign for anodic over potentials.

With further discharging or charging, the kinetics becomes dominated by ohmic polarization losses [10]. This is due to accumulated resistances of the electrolyte, the composite cathodes, contact between the electrodes and the current collectors, cell connections, etc. Ohm's Law holds for these processes, therefore in this region of the curve, cell polarization is directly proportional to the applied current:

$$\eta = IR \quad \text{[Equation 1-7]}$$

At the end of the discharge or charge step, the chemical reagents become depleted and mass transport limitations within the battery result in greater cell polarization. Typical cycling protocols include a rest step after each discharge or charge. During a rest step the cell potential approaches an equilibrium value characteristic of the electrodes composition. This phenomenon can be seen in Fig. 1-5.

The composition-dependant phase diagram of an electrode material also influences the shape of the cycling curves. Quasi-equilibrium measurements of  $E_{oc}$  as a

function of composition must be measured to discriminate the kinetic and phase equilibria effects. Gibb's phase rule may be used to determine the number of intensive variables (degrees of freedom,  $\Phi$ ) that must be fixed in order to completely define the state of a system [12]. For a system with  $C$  components and  $P$  phases, it is given as:

$$\Phi = C - P + 2 \quad \text{[Equation 1-8]}$$

According to this rule, the open-circuit voltage will depend on the composition of the electrode for a single-phase transition, but for a two-phase transition, the open-circuit potential will be independent of composition. Figure 1-7 further illustrates why the cell potential does not depend on electrode composition during a two-phase transition [13]. A phase change occurs whenever there is a discontinuity in the first derivative of a thermodynamic potential function (such as the chemical potential), and cell potential is proportional to the difference in the chemical potential of lithium ions in the cathode and the anode (cf., Eq. 1-1). Throughout a two-phase transition (the domain  $x_1$  to  $x_2$  on Fig.

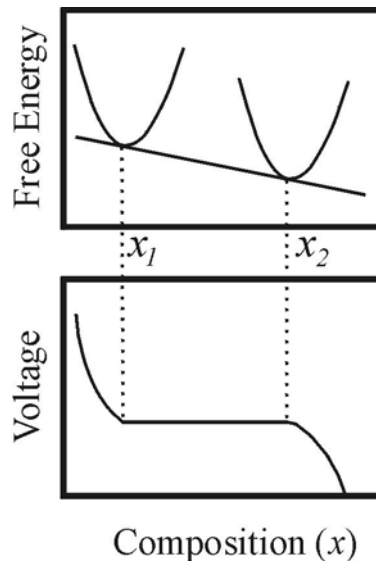


**Figure 1-7:** Free energy and voltage curves for a first-order transition between compositions  $x_1$  to  $x_2$  [13].

1-7), the first derivative of Gibb's free energy with respect to the electrode composition is constant. Consequently, the measured cell potential is independent of composition over this range. Experimentally, this appears as a divergence in a plot of  $\partial E/\partial x$  vs.  $x$ . In contrast, there are no discontinuities in the first derivative of Gibb's free energy for a single-phase transition; hence, the cell potential changes as a function of the electrode composition.

## **1.2 Materials Overview for Lithium Rechargeable Batteries**

The discovery of intercalation electrodes in the late 1970s is primarily responsible for the success of lithium rechargeable batteries [14]. Intercalation is defined as the insertion of a guest species (lithium ions in this application) into a host structure [15]. Several different intercalation compounds have been explored as cathode and anode materials for lithium batteries and the redox potentials for some of these materials are briefly summarized in Fig. 1-8. In general, anode materials must have a very low redox potential ( $<2$  V vs.  $\text{Li}^+/\text{Li}$ ), whereas the redox potential of the cathode should be as large as possible without exceeding the electrochemical stability window of the supporting electrolyte system. Some of the more prominent electrodes materials are elaborated upon in Sections 1.2.1 and 1.2.2 and various electrolyte systems are commented on in Section 1.2.3.

### *1.2.1 Anode Materials*

Lithium metal is a natural choice as an anode for lithium rechargeable batteries

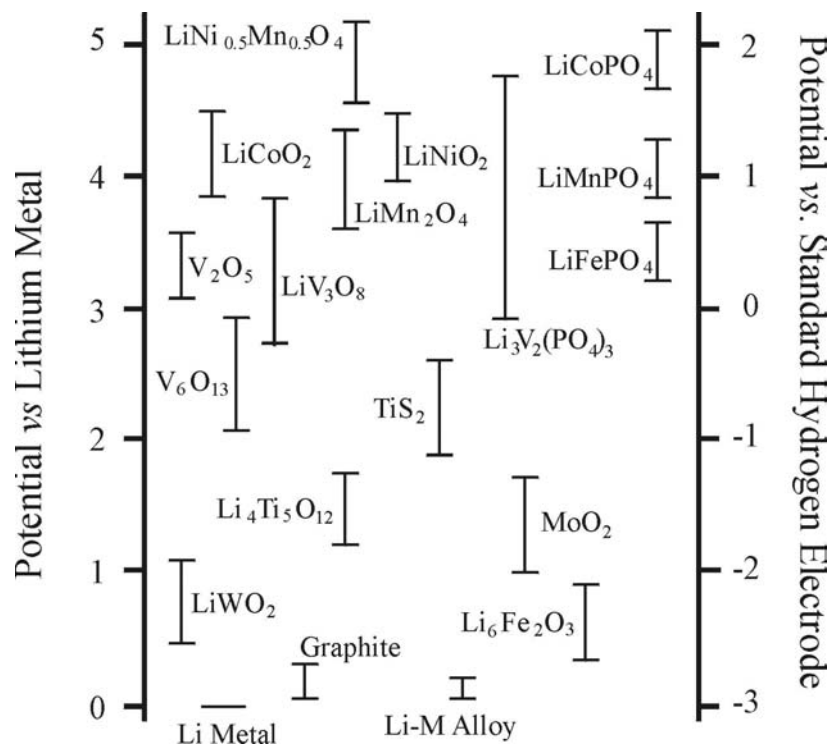


**Figure 1-8:** Electrochemical voltages for some intercalation anodes and cathodes used in lithium rechargeable batteries [16-18].

due to its very large theoretical gravimetric and volumetric specific capacities (3.86 Ah/g and 2.06 Ah/ml, respectively). Additionally, lithium metal electrodes have the lowest reduction potential versus the standard hydrogen electrode of any available anode material. Therefore, cells using a lithium anode have a higher voltage and, consequently, higher energy densities. Unfortunately, rechargeable batteries employing metallic lithium are susceptible to a number of safety issues. During the charging process, lithium deposition on the surface of the anode is not uniform, and repeated cycling causes the growth of lithium dendrites on the anode surface [19-25]. Dendrites can internally short the cell by breaking off the bulk electrode or puncturing the separator. Furthermore, repeatedly stripping and depositing lithium metal on the anode produces a mossy surface

that is less dense than the original, bulk material [23,24]. This reduces the volumetric energy density and affects the overall performance of the cell. For these reasons, metallic lithium is largely limited to primary cells in commercial applications. Lithium ion batteries (or “rocking chair” batteries) were developed as a solution to the safety issues posed by metallic lithium anodes. In these systems, intercalation materials replace metallic lithium; thus, lithium ions are never reduced to metallic lithium.

The earliest lithium ion cells employed a low-potential intercalation compound such as  $\text{Li}_x\text{WO}_2$  [26]. Later work identified lithiated carbonaceous materials as potential anodes [27-31]. Carbonaceous compounds are very attractive because lithium ions may be intercalated up to a maximum composition of  $\text{LiC}_6$  at potentials  $<0.5 \text{ V vs. Li}^+/\text{Li}$  [32]. Cycling performance is depends on the nature and source of the carbon. In general, carbonaceous materials may be divided into graphitic and non-graphitic carbons based on the degree of crystallinity present in the sample [33-37]. Graphitic compounds have some degree of crystallographic order and range from highly oriented pyrolytic graphite to graphitic carbons that possess some number of structural defects and/or turbostratic disorder. Non-graphitic (disordered) carbons maintain a basic unit of planar aromatic structures (typically 5-10 rings) but do not possess long-range crystallographic order [33]. The latter may be further sub-divided into soft and hard carbons depending on the mechanical properties of the materials. The electrochemistry of carbonaceous materials is quite complex and a detailed review of the subject is not within the scope of this dissertation.

Although carbonaceous anodes have several attractive qualities, they suffer from poor low temperature performance [38,39], incompatibility with some electrolytes [40],



and relatively low theoretical capacities compared to lithium metal. Some materials that have been proposed to address these undesirable attributes include low voltage oxides (e.g., spinel  $\text{Li}_4\text{Ti}_5\text{O}_{12}$  [41]), nitrides and phosphides (e.g.,  $\text{Ge}_3\text{N}_4$ ,  $\text{Zn}_3\text{N}_2$ , or  $\text{MnP}_4$ ) [42], and various metals that alloy with lithium. Lithium-metal alloys offer much higher capacities compared to carbonaceous anodes and lithium insertion occurs at sufficiently low potentials to be competitive. The number of binary and tertiary lithium-metal alloys that have been explored constitutes a very large family of potential anode materials. For instance, Li-Al, Li-Bi, Li-Cd, Li-Ga, Li-In, Li-Pb, Li-Sb, and Li-Sn are examples of the binary systems, while Li-Cd-Sn is an example of a tertiary system [43].

Unfortunately, metallic anodes often suffer from very large volume fluctuations during lithium insertion and extraction. For example, the unit cell volume of metallic tin increases about 250% when  $\text{Li}_{22}\text{Sn}_5$  is formed [44,45]. This causes significant particle cracking and fragmentation. Ultimately the structural integrity of the anode is degraded when these anodes cycled, causing poor long-term performance [45-48]. Composite materials (such as  $\text{Sn}_{1.0}\text{B}_{0.56}\text{P}_{0.40}\text{Al}_{0.42}\text{O}_{3.6}$  [49]) have been suggested as one way to overcome the poor long-term performance of tin anodes. Here, lithium first reacts with the anode irreversibly to form domains of metallic tin embedded in an inorganic matrix; second, lithium reversibly alloys with the tin domains [50]. The inorganic matrix functions as a “glue” to preserve the structural integrity of the composite anode during the extreme volume fluctuations that accompany the alloying process [45,51-53]. This strategy will be further elaborated upon in Chapter 4.

### 1.2.2 Cathode Materials

The first intercalation cathode identified for lithium rechargeable batteries was titanium disulfide [54,55]. This compound has a layered structure in which one lithium ion per formula unit may be reversibly intercalated between the  $\text{TiS}_2$  sheets at  $\sim 2.5$  V vs.  $\text{Li}^+/\text{Li}$  with good reversibility [56]. The discovery of this compound sparked a worldwide emphasis on identifying other intercalation materials that possess superior electrochemical performance. In the 1980s, Goodenough *et al.* [57] suggested oxide-based cathodes (such as  $\text{LiCoO}_2$  [57,58]) for lithium rechargeable batteries. These compounds offer higher energy densities than their sulfide-based counterparts. Since that time, a wide variety of oxide-based materials have been proposed [14,17], including layered  $\text{LiMO}_2$  ( $M = \text{Co}, \text{Ni}, \text{Mn}, \text{V}$ ), spinel  $\text{LiMn}_2\text{O}_4$ , lithiated vanadium oxides (*viz.*,  $\text{LiV}_3\text{O}_8$ ,  $\text{V}_2\text{O}_5$ , and  $\text{V}_6\text{O}_{13}$ ), and other transition metal oxides. The research and development of oxide-based cathode materials culminated in the commercialization of the first lithium ion battery in 1991 by Sony Energytec, Inc. The cell consisted of a  $\text{LiCoO}_2$  cathode, a graphitic anode, and a nonaqueous electrolyte [58]. Most of today's research efforts focus on replacing the relatively expensive and toxic  $\text{LiCoO}_2$  cathodes.

Layered  $\text{LiNiO}_2$  [59-61] and solid solutions of  $\text{LiNiO}_2$  and  $\text{LiCoO}_2$  (e.g.,  $\text{LiNi}_x\text{Co}_{1-x}\text{O}_2$  [62-65] and  $\text{LiNi}_x\text{M}_{1-x}\text{O}_2$  [ $M \neq \text{Co}$ ] or  $\text{LiCo}_x\text{M}_{1-x}\text{O}_2$  [ $M \neq \text{Ni}$ ] [62, 66-79]) have a two-dimensional framework structure similar to  $\text{LiTiS}_2$  and exhibit comparable cycling performance and higher redox potentials than  $\text{LiCoO}_2$ . Spinel  $\text{LiMn}_2\text{O}_4$  has also been extensively investigated as an alternative to the cobalt-based cathodes, primarily due to its high redox potentials, low cost, and environmentally benign constituents (e.g., see Refs. [80-89]). Lithium ions are extracted from this compound to form  $\lambda$ - $\text{MnO}_2$  along a

4.1 V plateau. Subsequently, two lithium ions per formula unit may be reinserted to form  $\text{Li}_2\text{Mn}_2\text{O}_4$ . Unfortunately, there is a sharp drop in cell voltage near the composition  $\text{LiMn}_2\text{O}_4$  associated with a cubic to tetragonal phase change within the cathode. Repeated cycling over this phase transition causes catastrophic structural fatigue in the cathode and results in poor electrochemical performance.

In recent years, polyatomic-based cathode materials have generated substantial interest as cathode materials [18,90]. This is primarily due to their competitive redox potentials (see Fig. 1-8) and capacities as well as the possibility of preparing cheaper and safer alternatives to the oxide-based compounds. Although the redox potential of a cathode is strongly affected by the choice of transition metal ion, the electric crystal field about the transition metal ion also affects the measured voltage. The polarization of electrons towards the X atoms of the polyatomic units (X = P, S, W, As, Mo, or V) reduces the covalent character of the M–O bonds, thus decreasing the energy level of a transition metal ion's redox couple compared to the Fermi level of lithium metal [91-96]. For example, the  $\text{Fe}^{3+}/\text{Fe}^{2+}$  redox couple lies at 3.0, 3.0, 3.6, and 2.8 V against  $\text{Li}^+/\text{Li}$  for  $\text{Li}_x\text{Fe}_2(\text{XO}_4)_3$  where X = Mo [97], W [97], S [98], or P [94], respectively. Furthermore, the structure of the compound influences the placement of the redox potential [93], for the  $\text{Fe}^{3+}/\text{Fe}^{2+}$  couple decreases as the structure changes:  $\text{LiFePO}_4$  (3.5 V) >  $\text{Fe}_4(\text{P}_2\text{O}_7)_3$  (3.1 V) >  $\text{LiFeP}_2\text{O}_7$  (2.9 V) >  $\text{Li}_3\text{Fe}_2(\text{PO}_4)_3$  (2.8 V) [93]. The changes in the  $\text{Fe}^{2+}/\text{Fe}^{3+}$  redox potential is attributed to differences in the P–O bond lengths as well as changes in the crystalline electric field at the iron sites. The ability to tune the redox potential of a cathode by a judicious choice of structure and anion type provides a useful means to address key scientific issues in developing electrodes for lithium batteries.

### 1.2.3 Electrolyte Systems

Lithium batteries require a supporting electrolyte system to facilitate lithium ion transport between the two electrodes. Three general classes of electrolytes have been proposed for lithium rechargeable batteries: nonaqueous liquids, polymers, and fast ion solid state conductors. A number of hybrid systems (such as gel polymer electrolytes) have also been proposed, but these systems will not be reviewed here.

The general criteria for any electrolyte system are high lithium ion conductivity, excellent thermal properties, and a wide electrochemical window [99]. In addition, it is critical that the electrolyte exhibit good chemical stability towards the electrodes. Most electrolytes react with the electrode materials, in particular the anode [100-102], during the first cycle to form a solid electrolyte interphase (SEI) on the surface of the electrode particles [103-107]. As an aside, an SEI layer is viewed as a distinct *phase* that forms at the electrode-electrolyte *interface*. The SEI is believed to be selectively permeable towards lithium ions, yet it is impermeable towards other electrolyte components [103]. Furthermore, the SEI should have good lithium ion transport properties and not retard charge transfer from the electrolyte to the electrode. Most researchers agree that an SEI layer consists of a complex mixture of lithium salts, fully oxidized inorganic species, and decomposed solvent molecules that passivate the electrodes toward further electrolyte decomposition [108-120]. Other electrolyte decomposition products may be liquid, in which case they will accumulate in the electrolyte solution, or even gaseous [113,115,117,118]. The exact composition and electrochemical properties of the SEI heavily depend on the nature of the electrolyte solution; therefore, tailoring the

electrolyte solutions to optimize the SEI is a major aspect of research and development in this field.

Nonaqueous liquid and polymeric electrolytes for lithium rechargeable batteries consist of dissolved lithium salts in a suitable solvent system. Lithium salts must have good chemical stability towards reduction and oxidation at the anode and cathode, respectively. Furthermore, the salts must have low lattice energies to minimize ion-ion interactions in solution and enhance conductivity [121]. Based on these criteria, a number of lithium salts have been proposed:  $\text{LiXF}_6$  ( $X = \text{P, As, Sb}$ ),  $\text{LiClO}_4$ ,  $\text{LiBF}_4$ ,  $\text{LiCF}_3\text{SO}_3$ ,  $\text{Li}(\text{CF}_3\text{SO}_2)_2$ ,  $\text{LiSCN}$ ,  $\text{LiI}$ , and  $\text{LiBOB}$  ( $\text{BOB} = \text{bis(oxalatoborate)}$ ). Typical solvents for liquid electrolytes are linear and cyclic alkyl carbonates, ethers, and esters [122]. In practice, binary, tertiary, and sometimes even quaternary solvent solutions must be prepared to optimize the conductivity, thermal properties, and viscosity of the electrolyte.

Ion-solvent interactions are believed to influence electrolyte conductivity, melting points, boiling points, and viscosity; therefore, it is important to have a reliable means of characterizing these interactions. Aurbach and Weissman [123] note that typical measurements of solvent polarity (such as the dielectric constant or dipole moment) are often insufficient to fully characterize the interactions between the solute and the solvent. Instead, they propose the use of donor/acceptor numbers [123,124] or hard/soft acid base theories [125,126] to describe these interactions. Cation-anion interactions are also believed to affect electrolyte conductivity. The total ionic conductivity ( $\sigma$ ) of a dilute electrolyte is given by a Kohlrausch summation over all of the charge carriers present in solution:

$$\sigma(T, P) = \sum_i n_i q_i \mu_i \quad [\text{Equation 1-9}]$$

where  $n_i$ ,  $q_i$ , and  $\mu_i$  is the concentration, charge, and mobility for the  $i^{\text{th}}$  species, respectively [127]. A high degree of ionic association within an electrolyte solution can have a deleterious affect on the overall conductivity of a solution by producing neutral species (i.e., ion pairs) or low-mobility charged aggregates.

Liquid cells require a physical separation between the two electrodes; else the cell will internally short. Microporous poly(ethylene)–poly(propylene) blends are widely used in the lithium battery community because of their high tensile strength, good porosity/tortuosity values, and chemical inertness [128]. However, the separator adds additional weight to the cell that reduces the overall capacity of the cell. Polymer and solid-state electrolytes offer distinct advantages over liquid electrolytes in that they function as physical separators as well as lithium ion conductors. Polymer electrolytes have been aggressively pursued for almost thirty years, yet only a handful of systems have been commercialized to date [129]. The primary issue preventing widespread commercialization is their poor room-temperature conductivities ( $<10^{-5}$  S/cm compared to  $10^{-1}$  S/cm for liquid systems) [130].

A polymer electrolyte consists of a dissolved lithium salt in a host polymer. A variety of architectures have been proposed for polymer electrolytes; however, poly(ethylene oxide) or poly(ethylene oxide) derivatives have received the most attention [131,132]. In polymer electrolytes, the lithium ions are coordinated by the heteroatoms of the polymer; thus, cation-polymer interactions affect electrochemical performance. The same constraints govern the choice of lithium salt for polymer electrolytes as for liquid electrolytes; therefore, similar salts are used in both applications.

It is thought that lithium ion transport predominantly occurs in the amorphous regions of the polymer electrolyte and is strongly correlated to the segmental motion of the polymer backbone [133-136]; thus, polymers which exhibit low crystallinity and glass-transition temperatures should exhibit improved conductivity. Several empirical (e.g., Vogel-Tamman-Fulcher [137-139] or Williams-Landel-Ferry [140]) and theoretical (e.g., free volume [141], configurational entropy [142,143], and dynamic bond percolation [141,144]) models have been proposed to describe the conductivity trends of polymer electrolytes [145]. Unfortunately, a detailed, comprehensive microscopic description of ionic transport is lacking for polymer electrolytes.

Non-polymeric, solid-state electrolytes may be divided into two general classes of compounds: crystalline and glassy electrolytes. These materials are advantageous over liquid and polymer electrolytes in that the materials are generally single ion conductors, whereas ion conduction in liquid and polymer electrolytes is generally a mixture of cation and anion motion under the applied electric field. Moreover, solid-state conductors often have higher electrochemical stability windows. Superionic conductors such as  $\beta$ -alumina have very high conductivities ( $10^{-2}$  S/cm), but conductivities of ceramic and glassy electrolytes fall between  $10^{-4}$  and  $10^{-8}$  S/cm [146]. Even though solid-state electrolytes have relatively low specific conductivities compared to liquid or polymeric electrolytes, it is possible to deposit these materials as thin films ( $\sim 1$   $\mu\text{m}$ ); thus, the overall film conductance is high enough to be competitive. Some noteworthy examples of ceramic solid-state electrolytes are  $\text{La}_{0.56}\text{Li}_{0.33}\text{TiO}_3$  with the perovskite structure [147],  $\text{Li}_{3.35}\text{Ge}_{0.35}\text{P}_{0.65}\text{S}_4$  with the  $\gamma$ - $\text{Li}_3\text{PO}_4$ -type structure [148], and doped  $\text{Li}_3\text{InBr}_6$  [149]. Glassy electrolytes (such as lithium phosphorous oxynitride, “lipon,” [150,151]) offer

distinct advantages over ceramic materials because they have isotropic conductivities, may be prepared as dense films, and lack grain boundaries. Cracks and grain boundaries may provide electron pathways through the electrolyte that can result in internal shorts, which decrease battery shelf life.

### 1.3 Parameters that Control Energy Density, Cell Power, and Cyclability

Battery power and energy densities are important parameters in designing state-of-the-art rechargeable batteries. Fig. 1-9 shows the excellent specific energy and specific power densities of lithium rechargeable batteries compared to the other technologies [152]. The nature of the electrode materials and cell engineering affect a cells specific energy and power densities. Typical battery engineering concerns include weight, volume, and heat dissipation. For instance, implementing a polymeric or solid-

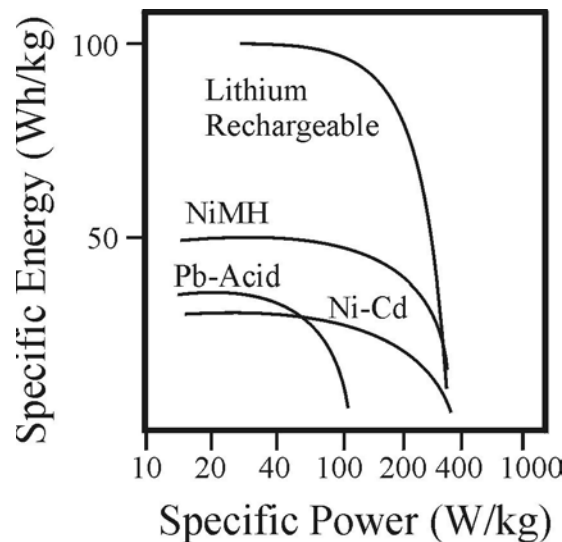


**Figure 1-9:** A Ragone plot comparing several rechargeable battery technologies [152].



state electrolyte could increase energy density because the relatively heavy metal casings, which are needed to prevent leaking of liquid electrolytes, could be discarded. In this section, only contributions from the electrode materials will be discussed.

The redox potential and capacity of an electrode material directly affects the amount of energy that may be stored in a battery. The gravimetric specific energy density ( $U_{grav}$ ) of an electrode is given as:

$$U_{grav} = \frac{EI t}{m} \text{ (units of Wh/g)} \quad [\text{Equation 1-10}]$$

where  $E$  is the cell voltage,  $I$  is the current,  $t$  is the time elapsed during the charge or discharge step, and  $m$  is the mass of the active electrode material. The volumetric specific energy density ( $U_{vol}$ ) may be calculated by multiplying  $U_{grav}$  with the density of the compound. Power density ( $P$ ) refers to the rate that energy may be retrieved from a battery and is given as:

$$P = \frac{EI}{m} \text{ (units of W/g)} \quad [\text{Equation 1-11}]$$

where  $E$ ,  $I$ , and  $m$  are defined as above. Cells that have a high power density can deliver the stored energy at high rates.

According to Eqs. 1-10 and 1-11, the energy density and power capability of a battery is controlled by cell voltage, electrode capacity, and cycling rate. Cell voltage is largely governed by the redox potentials of the transition metal ions in the electrodes, and parameters that affect redox potentials are discussed in Sections 1-1 and 1-2. The theoretical gravimetric capacity of an electrode depends on the number of electrons involved in the cell reaction and the molecular weight of the electroactive material (see

Eq. 1-5). However, the measured capacity is often less than the theoretical capacity at realistic cycling rates. Electrodes must have good intrinsic electronic and ionic conductivities as well as excellent electrical contact with the current collectors to avoid inefficient capacity utilization. Moreover, the electrolyte and electrode/electrolyte interface must have facile lithium transport kinetics. Low conductivities at any of these points can result in concentration polarization within the battery, which generates an electric field within the cell that opposes the applied field [152]. Accordingly, the measured cell voltage will decrease prematurely, causing the cycle to terminate prior to complete consumption of the active material.

Although decreasing the charging/discharging rate can increase the observed capacity of an electrode, this is not always practical. Thus, attempts to increase the delivered capacity largely center on improving the conductivity of the electrodes, electrolyte, and interfacial properties. Most cathode materials (and many anode materials) have low electronic conductivities. In fact, the polyanionic-based electrodes are described as insulators because electrons within the covalent X–O bonds (X = P, As, S, Mo, W, or V) are highly localized [153,154]. To compensate for low electronic conductivity values, cathodes are typically formulated with a small quantity (5-10 wt.%) of a conductive diluent. Most often this is a carbonaceous compound (for an example see Ref. [155]). The carbon improves the electrical contact between the electrode particles. It also enhances the conductivity between the composite electrode and the current collector (usually aluminum for cathodes and copper for anodes). A small quantity (3-5wt.%) of a polymeric binder such as poly(vinylidene fluoride) or poly(tetrafluoro-

ethylene) is also added to improve structural integrity. Of course, specific formulations must be optimized to satisfy the needs of a particular application.

It is imperative for lithium rechargeable batteries to sustain a high degree of reversibility over many cycles if they are to effectively compete with other rechargeable battery technologies. All batteries experience some degree of capacity loss when cycled, but the rate at which the capacity fades should be suppressed as much as possible. It is difficult to completely characterize capacity losses for all lithium batteries with one simple fading mechanism since capacity fade is highly dependent on the constituents, cycling protocols, and storage conditions of the cells. In addition to normal, long-term material degradation of the battery components, several mechanisms have been proposed. These include irreversible phase changes in the electrodes [156-158], dissolution of the transition metal ions into the electrolyte [159-161], structural fatigue during cycling [161], electromechanical grinding and subsequent disintegration of the electrodes [45-48], electrolyte decomposition on the electrode surfaces [100,101,161], and instability of the charged state during storage [162,163]. For example,  $\text{Li}_x\text{V}_2\text{O}_5$  ( $0 \leq x \leq 3$ ) cathodes have relatively high capacities when fully discharged ( $x \rightarrow 3$ ), but these materials undergo irreversible structural distortions when deeply discharged. This distortions promote very rapid capacity fade [157]. In contrast, several workers have pointed out the excellent long-term cycling performance of  $\text{LiFePO}_4$ -based batteries [164-169]. In fact, Huang *et al.* [166] reported low capacity fade even after 800 cycles for  $\text{LiFePO}_4$  cycled at high rates. The excellent cycling performance is attributed to the lack of significant structural changes associated with lithium intercalation and favorable interactions between the  $\text{LiFePO}_4$  cathode and the electrolyte [164].

## 1.4 Safety Concerns

Safety is of paramount importance in developing rechargeable batteries. It is estimated that over 1.6 million lithium rechargeable batteries have been recalled between 2000 and the time of this writing due to safety issues [170]. In one instance, Buchmann [171] reports a lithium battery explosion that released hot, caustic gases on a man's face. Therefore, a large aspect of designing new lithium battery cells is improving electrochemical performance, while simultaneously producing safer batteries. New batteries must tolerate a series of abuse tests (e.g., short circuit, over-charge, over-discharge, crushing, and nail penetration) before they are commercialized. Perhaps the greatest safety concern for lithium batteries is that they are prone to overheating and exploding [172]. Short-circuiting a cell often generates a large amount of heat that can increase internal reaction rates and lead to a thermal runaway [173,174]. In these circumstances, the highly flammable organic solvents in a liquid cell can react with the electrodes (particularly fully charged cathodes) and cause the cell to explode. Some strategies to reduce these safety concerns center on (1) replacing the organic solvents with less flammable polymers or room temperature ionic liquids and (2) implementing cathodes that are less reactive toward the electrolyte at high temperatures. For example, electrolytes are much less reactive (at high temperatures) towards fully charged polyanionic-based cathodes than the oxide-based compounds [175,176]. The possibility of preparing safer lithium rechargeable batteries from phosphate-based electrodes has provided a strong impetus for the development and testing of this class of compounds.

## 1.5 References

- [1] <http://www.toyota.com/prius/>
- [2] J.-M. Tarascon and M. Armand, *Nature*, **414**, (2001) 359-367.
- [3] A. Manthiram, *Lithium Batteries: Science and Technology*, G.-A. Nazri and G. Pistoia, Eds., Kluwer Academic Publishers: Boston, (2004) pp. 3-4.
- [4] H. Oman, *MRS Bulletin*, **24**, (1999) 33-39.
- [5] <http://www.batteryuniversity.com/parttwo-55.htm>
- [6] <http://www.epbaeurope.net/Recycling.html>
- [7] D. Saxman, "Lithium battery sales to reach \$2.7 billion by 2009" from *RGB-210N Lithium Batteries: Materials and Markets*, Business Communications Company, Inc.: Norwalk, CT, (2004), <http://www.bccresearch.com/editors/RGB-210N.htm>.
- [8] A. Manthiram, *Lithium Batteries: Science and Technology*, G.-A. Nazri and G. Pistoia, Eds., Kluwer Academic Publishers: Boston, (2004) pp. 5.
- [9] M. K. Kemp, *Physical Chemistry: A Step-by-Step Approach*, Marcel Dekker, Inc.: New York (1979) pp. 316-317.
- [10] M. Winter and R. J. Brodd, *Chem. Rev.*, **104**, (2004) 4245-4269.
- [11] R. D. Armstrong and M. Todd, *Solid State Electrochemistry*, P. G. Bruce, Eds., Cambridge University Press: Cambridge, (1995) pp. 277-286.
- [12] M. K. Kemp, *Physical Chemistry: A Step-by-Step Approach*, Marcel Dekker, Inc.: New York (1979) pp. 759.
- [13] W. R. McKinnon, *Solid State Electrochemistry*, P. G. Bruce, Eds., Cambridge University Press: Cambridge, (1995) pp. 177-178.
- [14] M. S. Whittingham, *Chem. Rev.*, **104**, (2004) 4271-4301.
- [15] W. R. McKinnon, *Solid State Electrochemistry*, P. G. Bruce, Eds., Cambridge University Press: Cambridge, (1995) pp. 163.
- [16] A. Manthiram, *Lithium Batteries: Science and Technology*, G.-A. Nazri and G. Pistoia, Eds., Kluwer Academic Publishers: Boston, (2004) pp. 9.
- [17] M. M. Thackeray, E. Ferg, R. J. Gummow and A. de Kock, *Mater. Res. Soc. Proc.*, **369**, (1995) 17-27.

- [18] C. Masquelier, S. Patoux, C. Wurm and M. Morcrette, *Lithium Batteries: Science and Technology*, G.-A. Nazri and G. Pistoia, Eds., Kluwer Academic Publishers: Boston, (2004) pp. 445-477.
- [19] J. O. Besenhard, J. Guertler, P. Komenda and M. Josowicz, *Primary and Secondary Ambient Temperature Lithium Batteries*, J. P. Gabano, Z. Takehara and P. Bro, Eds., Electrochemistry Society: Pennington, (1988) pp. 618-626.
- [20] D. P. Wilkinson, H. Blom, K. Brandt and D. Wainwright, *J. Power Sources*, **36**, (1991) 517-527.
- [21] I. E. Eweka, J. F. Rohan, J. R. Owen and A. G. Ritchie, *Power Sources*, **15**, (1995) 241-252.
- [22] D. Aurbach, E. Zinigrad, H. Teller and P. Dan, *J. Electrochem. Soc.*, **147**, (2000) 1274-1279.
- [23] F. Orsini, A. du Pasquier, B. Beaudoin, J. M. Tarascon, M. Trentin, N. Langenhuizen, E. de Beer and P. Notten, *J. Power Sources*, **76**, (1998) 19-29.
- [24] M. Dolle, L. Sannier, B. Beaudoin, M. Trentin and J. M. Tarascon, *Electrochem. Solid-State Lett.*, **5**, (2002) A286-A289.
- [25] W.-S. Kim and W.-Y. Yoon, *Electrochim. Acta*, **50**, (2004) 541-545.
- [26] M. Lazzari and B. Scrosati, *J. Electrochem. Soc.*, **127**, (1980) 773-774.
- [27] T. Kitamura, T. Miyazaki, S. Toyosawa, T. Nakajima, K. Suzuki and T. Kawagoe, *Secondary batteries*, Jpn. Kokai Tokkyo Koho **JP 85-214312 19850927**, (1987).
- [28] Y. Takahashi, Y. Kawai and N. Sakurai, *Anodes for secondary lithium batteries*, Jpn. Kokai Tokkyo Koho **JP 86-107759 19860513**, (1987).
- [29] Y. Takahashi, Y. Kawai and N. Sakurai, *Anode for secondary battery*, Eur. Pat. Appl. **EP 87-304091 19870507**, (1987).
- [30] R. Kanno, Y. Takeda, T. Ichikawa, K. Nakanishi and O. Yamamoto, *J. Power Sources*, **26**, (1989) 535-543.
- [31] M. Mohri, N. Yanagisawa, Y. Tajima, H. Tanaka, T. Mitate, S. Nakajima, M. Yoshida, Y. Yoshimoto, T. Suzuki and H. Wada, *J. Power Sources*, **26**, (1989) 545-551.

- [32] A. Hérold, *Chemical Physics of Intercalation*, A. P. Legrand and S. Flandrois, Eds., Plenum Press: New York, (1987) pp. 3-46.
- [33] M. Winter, K.-C. Moeller and J. O. Besenhard, *Lithium Batteries: Science and Technology*, G.-A. Nazri and G. Pistoia, Eds., Kluwer Academic Publishers: Boston, (2004) pp. 148-153.
- [34] R. E. Franklin, *Proc. Royal Soc. (London)*, **A209**, (1951) 196-218.
- [35] R. E. Franklin, *Acta Cryst.*, **4**, (1951) 253-261.
- [36] H. Azuma, H. Imoto, S. Yamada and K. Sekai, *J. Power Sources*, **81-82**, (1999) 1-7.
- [37] D. A. Stevens and J. R. Dahn, *J. Electrochem. Soc.*, **148**, (2001) A803-A811.
- [38] S. S. Zhang, K. Xu and T. R. Jow, *J. Power Sources*, **115**, (2003) 137-140.
- [39] C.-K. Huang, J. S. Sakamoto, J. Wolfenstine and S. Surampudi, *J. Electrochem. Soc.*, **147**, (2000) 2893-2896.
- [40] M. Winter, K.-C. Moeller and J. O. Besenhard, *Lithium Batteries: Science and Technology*, G.-A. Nazri and G. Pistoia, Eds., Kluwer Academic Publishers: Boston, (2004) pp. 171-174.
- [41] T. Ohzuku, A. Ueda and N. Yamamoto, *J. Electrochem. Soc.*, **142**, (1995) 1431-1435.
- [42] L. F. Nazar and O. Crosnier, *Lithium Batteries: Science and Technology*, G.-A. Nazri and G. Pistoia, Eds., Kluwer Academic Publishers: Boston, (2004) pp. 132-139.
- [43] R. A. Huggins, *Lithium Batteries: Science and Technology*, G.-A. Nazri and G. Pistoia, Eds., Kluwer Academic Publishers: Boston, (2004) pp. 270-296.
- [44] J. Sangster and C. W. Bale, *J. Phase Equilibria*, **19**, (1998) 70-75.
- [45] L. Y. Beaulieu, S. D. Beattie, T. D. Hatchard and J. R. Dahn, *J. Electrochem. Soc.*, **150**, (2003) A419-A424.
- [46] J. O. Besenhard, P. Komenda, A. Paxinos, E. Wudy and M. Josowicz, *Solid State Ionics*, **18-19**, (1986) 823-827.
- [47] A. Timmons, Z. Chen and J. R. Dahn, *206<sup>th</sup> Meeting of the Electrochemical Society and 2004 Fall Meeting of the Electrochemical Society of Japan*, **MA 2004-02**, Honolulu, HI, (October 3-8, 2004), No. 307.

- [48] J. Wolfenstine, D. Foster, J. Read, W. K. Behl and W. Luecke, *J. Power Sources*, **87**, (2000) 1-3.
- [49] Y. Idota, T. Kubota, A. Matsufuji, Y. Maekawa and T. Miyasaka, *Science*, **276**, (1997) 1395-1397.
- [50] I. A. Courtney and J. R. Dahn, *J. Electrochem. Soc.*, **144**, (1997) 2045-2052.
- [51] I. A. Courtney and J. R. Dahn, *J. Electrochem. Soc.*, **144**, (1997) 2943-2948.
- [52] I. A. Courtney, W. R. McKinnon and J. R. Dahn, *J. Electrochem. Soc.*, **146**, (1999) 59-68.
- [53] D. L. Foster, J. Wolfenstine, J. R. Read and W. K. Behl, *Electrochem. Solid-State Lett.*, **3**, (2000) 203-204.
- [54] M. S. Whittingham, *Chalcogenide battery*, U. S. Pat. Appl. **4009052 19770222**, (1977).
- [55] M. S. Whittingham, *Science*, **192**, (1976) 1126-1127.
- [56] M. S. Whittingham, *Prog. Solid State Chem.*, **12**, (1978) 41-99.
- [57] K. Mizushima, P. C. Jones, P. J. Wiseman and J. B. Goodenough, *Mater. Res. Bull.*, **15**, (1980) 783-789.
- [58] T. Nagaura and K. Tozawa, *Prog. Batt. Solar Cells*, **9**, (1990) 209-217.
- [59] J. B. Goodenough, D. G. Wickham and W. J. Croft, *Phys. Chem. Solids*, **5**, (1958) 107-116.
- [60] W. Ebner, D. Fouchard and L. Xie, *Solid State Ionics*, **69**, (1994) 238-256.
- [61] V. Bianchi, S. Bach, C. Belhomme, J. Farcy, J. P. Pereira-Ramos, D. Caurant, N. Baffier and P. Willmann, *Electrochim. Acta*, **46**, (2001) 999-1011.
- [62] C. Delmas, M. Ménétrier, L. Croguennec, I. Saadoune, A. Rougier, C. Pouillierie, G. Prado, M. Grune and L. Fournès, *Electrochim. Acta*, **45**, (1999) 243-253.
- [63] D. Carlier, M. Ménétrier and C. Delmas, *J. Mater. Chem.*, **11**, (2001) 594-603.
- [64] M. Balasubramanian, X. Sun, X. Q. Yang and J. McBreen, *J. Electrochem. Soc.*, **147**, (2000) 2903-2909.
- [65] K.-K. Lee and K.-B. Kim, *J. Electrochem. Soc.*, **147**, (2000) 1709-1717.
- [66] C. Pouillierie, F. Perton, P. Biensan, J. P. Peres, M. Broussely and C. Delmas, *J. Power Sources*, **96**, (1999) 293-302.
- [67] J. Cho, *Chem. Mater.*, **12**, (2000) 3089-3094.



- [68] C.-C. Chang, J. Y. Kim and P. N. Kumta, *J. Power Sources*, **89**, (2000) 56-63.
- [69] B. V. R. Chowdari, G. V. Subba Rao and S. Y. Chow, *Solid State Ionics*, **140**, (2001) 55-62.
- [70] S. Jouanneau, D. D. MacNeil, Z. Lu, S. D. Beattie, G. Murphy and J. R. Dahn, *J. Electrochem. Soc.*, **150**, (2003) A1299-A1304.
- [71] D. D. MacNeil, Z. Lu and J. R. Dahn, *J. Electrochem. Soc.*, **149**, (2002) A1332-A1336.
- [72] Z. Lu, D. D. MacNeil and J. R. Dahn, *Electrochem. Solid-State Lett.*, **4**, (2001) A200-A203.
- [73] M. Yoshio, H. Noguchi, J. Itoh, M. Okada and T. Mouri, *J. Power Sources*, **90**, (2000) 176-181.
- [74] H. Arai, M. Tsuda and Y. Sakurai, *J. Power Sources*, **90**, (2000) 76-81.
- [75] S. Madhavi, G. V. Subba Rao, B. V. R. Chowdari and S. F. Y. Li, *J. Power Sources*, **93**, (2001) 156-162.
- [76] J. S. Weaving, F. Coowar, D. A. Teagle, J. Cullen, V. Dass, P. Bindin, R. Green and W. J. Macklin, *J. Power Sources*, **97-98**, (2001) 733-735.
- [77] T. Ohzuku, K. Nakura and T. Aoki, *Electrochim. Acta*, **45**, (1999) 151-160.
- [78] S. H. Park, K. S. Park, Y. K. Sun, K. S. Nahm, Y. S. Lee and M. Yoshio, *Electrochim. Acta*, **8**, (2001)
- [79] J. Kim and K. Amine, *J. Power Sources*, **104**, (2002) 33-39.
- [80] Y. Xia and M. Yoshio, *Lithium Batteries: Science and Technology*, G.-A. Nazri and G. Pistoia, Eds., Kluwer Academic Publishers: Boston, (2004) pp. 361-380.
- [81] M. Pasquali, S. Passerini and G. Pistoia, *Lithium Batteries: Science and Technology*, G.-A. Nazri and G. Pistoia, Eds., Kluwer Academic Publishers: Boston, (2004) pp. 235-340.
- [82] T. Ohzuku, M. Kitagawa and T. Hirai, *J. Electrochem. Soc.*, **137**, (1990) 40-46.
- [83] T. Ohzuku, M. Kitagawa and T. Hirai, *J. Electrochem. Soc.*, **137**, (1990) 769-775.
- [84] Y. Xia and M. Yoshio, *J. Electrochem. Soc.*, **143**, (1996) 825-833.
- [85] S. Mukerjee, T. R. Thurston, N. M. Jisrawi, X. Q. Yang, J. McBreen, M. L. Daroux and X. K. Xing, *J. Electrochem. Soc.*, **145**, (1998) 466-472.

- [86] W. Liu, K. Kowal and G. C. Farrington, *J. Electrochem. Soc.*, **145**, (1998) 459-465.
- [87] T. J. Richardson, S. J. Wen, K. A. Striebel, P. N. Ross Jr. and E. J. Cairns, *Mater. Res. Bull.*, **32**, (1997) 609-618.
- [88] S. J. Wen, T. J. Richardson, L. Ma, K. A. Striebel, P. N. Ross Jr. and E. J. Cairns, *J. Electrochem. Soc.*, **143**, (1996) L136--L138.
- [89] W. Huang and R. Frech, *J. Power Sources*, **81-82**, (1999) 616-620.
- [90] M. Pasquali, S. Passerini and G. Pistoia, *Lithium Batteries: Science and Technology*, G.-A. Nazri and G. Pistoia, Eds., Kluwer Academic Publishers: Boston, (2004) pp. 347-350.
- [91] A. Manthiram and J. B. Goodenough, *J. Power Sources*, **26**, (1989) 403-408.
- [92] A. K. Padhi, V. Manivannan and J. B. Goodenough, *J. Electrochem. Soc.*, **145**, (1998) 1518-1520.
- [93] A. K. Padhi, K. S. Nanjundaswamy, C. Masquelier, S. Okada and J. B. Goodenough, *J. Electrochem. Soc.*, **144**, (1997) 1609-1613.
- [94] C. Masquelier, A. K. Padhi, K. S. Nanjundaswamy and J. B. Goodenough, *J. Solid State Chem.*, **135**, (1998) 228-234.
- [95] A. S. Andersson, B. Kalska, P. Eyob, D. Aernout, L. Häggström and J. O. Thomas, *Solid State Ionics*, **140**, (2001) 63-70.
- [96] M. Morcrette, C. Wurm and C. Masquelier, *Solid State Sciences*, **4**, (2002) 239-246.
- [97] A. Manthiram and J. B. Goodenough, *J. Solid State Chem.*, **71**, (1987) 349-360.
- [98] S. Okada, K. S. Nanjundaswamy, A. Manthiram, J. B. Goodenough, H. Ohtsuka, H. Arai and J.-I. Yamaki, *Proceedings of the 36th Power Sources Conference*, Cherry Hill, NJ, (June 1-10, 1994).
- [99] M. Nazri, *Lithium Batteries: Science and Technology*, G.-A. Nazri and G. Pistoia, Eds., Kluwer Academic Publishers: Boston, (2004) pp. 509.
- [100] R. Fong, U. von Sacken and J. R. Dahn, *J. Electrochem. Soc.*, **137**, (1990) 2009-2013.
- [101] R. Kanno, Y. Kawamoto, Y. Takeda, S. Ohashi, N. Imanishi and O. Yamamoto, *J. Electrochem. Soc.*, **139**, (1992) 3397-3404.

- [102] M. Winter and P. Novák, *J. Electrochem. Soc.*, **145**, (1998) L27-L30.
- [103] M. Winter, K.-C. Moeller and J. O. Besenhard, *Lithium Batteries: Science and Technology*, G.-A. Nazri and G. Pistoia, Eds., Kluwer Academic Publishers: Boston, (2004) pp. 158 & 167-179.
- [104] E. Peled, *J. Power Sources*, **9**, (1983) 253-266.
- [105] E. Peled, D. Golodnitsky, G. Ardel and V. Eshkenazy, *Electrochim. Acta*, **40**, (1995) 2197-2204.
- [106] E. Peled, D. Golodnitsky, G. Ardel, C. Manachem, D. Bar Tow and V. Eshkenazy, *Mater. Res. Soc. Symp. Proc.*, **393**, (1995) 209-221.
- [107] E. Peled, D. Golodnitsky, C. Menachem and D. Bar Tow, *J. Electrochem. Soc.*, **145**, (1998) 3482-3486.
- [108] D. Aurbach, *Nonaqueous Electrochemistry*, Marcel Dekker: New York (1999).
- [109] D. Aurbach, B. Markovsky, M. D. Levi, E. Levi, A. Schechter, M. Moshkovich and Y. Cohen, *J. Power Sources*, **81-82**, (1999) 95-111.
- [110] D. Aurbach, M. D. Levi, E. Levi, H. Teller, B. Markovsky, G. Salitra, U. Heider and L. Heider, *J. Electrochem. Soc.*, **145**, (1998) 3024-3034.
- [111] D. Aurbach, *J. Power Sources*, **89**, (2000) 206-218.
- [112] D. Aurbach, B. Markovsky, I. Weissman, E. Levi and Y. Ein-Eli, *Electrochim. Acta*, **45**, (1999) 67-86.
- [113] R. Imhof and P. Novák, *J. Electrochem. Soc.*, **145**, (1998) 1081-1087.
- [114] P. Novák, F. Joho, M. Lanz, B. Rykart, J.-C. Panitz, D. Alliata, R. Kötz and O. Haas, *J. Power Sources*, **97-98**, (2001) 39-46.
- [115] P. Novák, J.-C. Panitz, F. Joho, M. Lanz, R. Imhof and M. Coluccia, *J. Power Sources*, **90**, (2000) 52-58.
- [116] P. Novák, F. Joho, R. Imhof, J.-C. Pantiz and O. Haas, *J. Power Sources*, **81-82**, (1999) 212-216.
- [117] M. Lanz, E. Lehmann, R. Imhof, I. Exnar and P. Novák, *J. Power Sources*, **101**, (2001) 177-181.
- [118] H. Yoshida, T. Fukunaga, T. Hazama, M. Terasaki, M. Mizutani and M. Yamachi, *J. Power Sources*, **68**, (1997) 311-315.

- [119] E. Peled, D. Golodnitsky and G. Ardel, *J. Electrochem. Soc.*, **144**, (1997) L208-L210.
- [120] E. Peled, D. Bar Tow, A. Merson, A. Gladkich, L. Burstein and D. Golodnitsky, *J. Power Sources*, **97-98**, (2001) 52-57.
- [121] P. V. Wright, *Polymer Electrolyte Reviews*, J. R. MacCallum and C. A. Vincent, Eds., Elsevier Applied Science: New York, (1989).
- [122] D. Aurbach and I. Weissman, *Nonaqueous Electrochemistry*, D. Aurbach, Eds., Marcel Dekker: New York, (1999) pp. 3-7.
- [123] D. Aurbach and I. Weissman, *Nonaqueous Electrochemistry*, D. Aurbach, Eds., Marcel Dekker: New York, (1999) pp. 7-14.
- [124] V. Gutmann, *Coordination Chemistry in Nonaqueous Solvents*, Springer-Verlag: Vienna (1968).
- [125] R. G. Pearson, *J. Am. Chem. Soc.*, **85**, (1963) 3533-3539.
- [126] P. G. Bruce, F. Krok and C. A. Vincent, *Solid State Ionics*, **27**, (1988) 81-88.
- [127] M. K. Kemp, *Physical Chemistry: A Step-by-Step Approach*, Marcel Dekker, Inc.: New York (1979) pp. 280-282.
- [128] P. Arora and Z. Zhang, *Chem. Rev.*, **104**, (2004) 4419-4462.
- [129] D. MacArthur, *Lithium Batteries: Science and Technology*, G.-A. Nazri and G. Pistoia, Eds., Kluwer Academic Publishers: Boston, (2004) pp. 703.
- [130] T. Osaka, S. Komaba and X. Liu, *Nonaqueous Electrochemistry*, D. Aurbach, Eds., Marcel Dekker: New York, (1999) pp. 412.
- [131] J. B. Kerr, *Nonaqueous Electrochemistry*, D. Aurbach, Eds., Marcel Dekker: New York, (1999) pp. 574-622.
- [132] C. P. Rhodes, *Crystalline and Amorphous Phases in Polymer Electrolytes and Model Systems*, University of Oklahoma: Norman (2001) pp. 6-7.
- [133] C. Berthier, W. Gorecki, M. Minier, M. B. Armand, J. M. Chabagno and P. Rigaud, *Solid State Ionics*, **11**, (1983) 91-95.
- [134] M. Minier, C. Berthier and W. Gorecki, *J. Physique*, **45**, (1984) 739-744.
- [135] M. Stainer, L. C. Hardy, D. H. Whitmore and D. F. Shriver, *J. Electrochem. Soc.*, **131**, (1984) 784-790.
- [136] D. F. Shriver, R. Dupon and M. Stainer, *J. Power Sources*, **9**, (1983) 383-388.

- [137] H. Vogel, *Phys. Z.*, **22**, (1921)
- [138] G. Tamman and W. Hesse, *Z. Anorg. Allg. Chem.*, **156**, (1926) 245-257.
- [139] G. S. Fulcher, *J. Amer. Ceram. Soc.*, **8**, (1925) 339-355.
- [140] M. L. Williams, R. F. Landel and J. D. Ferry, *J. Am. Chem. Soc.*, **77**, (1955) 3701-3707.
- [141] M. A. Ratner, *Polymer Electrolyte Reviews - I*, J. R. MacCallum and C. A. Vincent, Eds., Elsevier Applied Science Publishers: London, (1987) pp. 173.
- [142] J. H. Gibbs and E. A. DiMarzio, *J. Chem. Phys.*, **28**, (1958) 373-383.
- [143] G. Adam and J. H. Gibbs, *J. Chem. Phys.*, **43**, (1965) 139-146.
- [144] M. A. Ratner and A. Nitzan, *Farad. Discuss. Chem. Soc.*, **88**, (1989) 19-42.
- [145] P. G. Bruce and F. M. Gray, *Solid State Electrochemistry*, P. G. Bruce, Eds., Cambridge University Press: Cambridge, (1995) pp. 128-143.
- [146] N. J. Dudney, *Lithium Batteries: Science and Technology*, G.-A. Nazri and G. Pistoia, Eds., Kluwer Academic Publishers: Boston, (2004) pp. 623.
- [147] Y. Inaguma, L. Chen, M. Itoh, T. Nakamura, T. Uchida, H. Ikuta and M. Wakihara, *Solid State Commun.*, **86**, (1993) 689-693.
- [148] R. Kanno and M. Murayama, *J. Electrochem. Soc.*, **148**, (2001) A742-A746.
- [149] Y. Tomita, H. Ohki, K. Yamada and T. Okuda, *Solid State Ionics*, **136-137**, (2000)
- [150] J. B. Bates, N. J. Dudney, G. R. Gruzalski, R. A. Zuhr, A. Choudhury, C. F. Luck and J. D. Robertson, *J. Power Sources*, **43**, (1993) 103-110.
- [151] X. Yu, J. B. Bates, G. E. Jellison Jr. and F. X. Hart, *J. Electrochem. Soc.*, **144**, (1997) 524-532.
- [152] J. R. Owen, *Chem. Soc. Rev.*, **26**, (1997) 259-267.
- [153] C. Delacourt, L. Laffont, R. Bouchet, C. Wurm, J.-B. Leriche, M. Morcrette, J.-M. Tarascon and C. Masquelier, *J. Electrochem. Soc.*, **152**, (2005) A913-A921.
- [154] S.-Y. Chung, J. T. Bloking and Y.-M. Chiang, *Nat. Mater.*, **1**, (2002) 123-128.
- [155] M. Y. Saïdi and J. Barker, *Solid State Ionics*, **78**, (1995) 169-173.
- [156] C. Delmas, S. Brèthes and M. Ménétrier, *J. Power Sources*, **34**, (1991) 113-118.
- [157] C. Delmas, H. Cognac-Auradou, J. M. Cocciantelli, M. Ménétrier and J. P. Doumerc, *Solid State Ionics*, **69**, (1994) 257-264.

- [158] J. M. McGraw, J. D. Perkins, J.-G. Zhang, P. Liu, P. A. Parilla, J. Turner, D. L. Schulz, C. J. Curtis and D. S. Ginley, *Solid State Ionics*, **113-115**, (1998) 407-413.
- [159] D. H. Jang, Y. J. Shin and S. M. Oh, *J. Electrochem. Soc.*, **143**, (1996) 2204-2211.
- [160] S. Patoux, C. Wurm, M. Morcrette, G. Rouse and C. Masquelier, *J. Power Sources*, **119-121**, (2003) 279-284.
- [161] Y. Xia, Y. Zhou and M. Yoshio, *J. Electrochem. Soc.*, **144**, (1997) 2593-2600.
- [162] A. du Pasquier, A. Blyr, A. Cressent, C. Lenain, G. Amatucci and J. M. Tarascon, *J. Power Sources*, **81-82**, (1999) 54-59.
- [163] E. Iwata, K.-I. Takahashi, K. Maeda and T. Mouri, *J. Power Sources*, **81-82**, (1999) 430-433.
- [164] A. S. Andersson, B. Kalska, L. Häggström and J. O. Thomas, *Solid State Ionics*, **130**, (2000) 41-52.
- [165] A. Yamada, M. Yonemura, Y. Takei, N. Sonoyama and R. Kanno, *Electrochem. Solid-State Lett.*, **8**, (2005) A55-A58.
- [166] H. Huang, S.-C. Yin and L. F. Nazar, *Electrochem. Solid-State Lett.*, **4**, (2001) A170-A172.
- [167] K. Zaghib, J. Shim, A. Guerfi, P. Charest and K. A. Striebel, *Electrochem. Solid-State Lett.*, **8**, (2005) A207-A210.
- [168] S. Franger, F. Le Cras, C. Bourbon and H. Rouault, *Electrochem. Solid-State Lett.*, **5**, (2002) A231-A233.
- [169] A. Yamada, S. C. Chung and K. Hinokuma, *J. Electrochem. Soc.*, **148**, (2001) A224-A229.
- [170] D. S. Angelo and J. Nguyen, "Safety testing imperative for lithium battery solutions" from *Battery Power Products & Technology*, Webcom Communications Corp.: Greenwood Village, (2005), <http://www.infowebcom.com>.
- [171] I. Buchmann, "Will lithium-ion batteries power the new millenium?" from *Batteries in a Portable World*, Cadex Electronics Inc.: Richmond, (2001), <http://www.buchmann.ca/Article5-Page1.asp>.

- [172] J. R. Selman, S. Al Hallaj, I. Uchida and Y. Hirano, *J. Power Sources*, **97-98**, (2001) 726-732.
- [173] S. Szpak, C. J. Gabriel and J. R. Driscoll, *Electrochim. Acta*, **32**, (1987) 239-246.
- [174] Y. Chen and J. W. Evans, *J. Electrochem. Soc.*, **143**, (1996) 2708-2712.
- [175] M. Takahashi, S.-I. Tobishima, K. Takei and Y. Sakurai, *Solid State Ionics*, **148**, (2002) 283-289.
- [176] J. R. Dahn, E. W. Fuller, M. Obrovac and U. von Sacken, *Solid State Ionics*, **69**, (1994) 265-270.

## Chapter 2: PHOSPHO-OLIVINE $\text{LiMPO}_4$ (M = Mn, Fe, Co Ni) CATHODES

---

*Christopher M. Burba and Roger Frech, J. Electrochem. Soc., 151 (7) A1032-A1038 (2004)\**

*Christopher M. Burba and Roger Frech, Spectrochim. Acta A, **accepted** (2005)<sup>†</sup>*

*Christopher M. Burba, Roger Frech, Anton Nyttén, and J. O. Thomas, J. Power Sources, **submitted** (2006)<sup>†</sup>*

### 2.1 Introduction

Orthorhombic  $\text{LiMPO}_4$  (M = Mn, Fe, Co, and Ni) phospho-olivine compounds have generated considerable interest as electrodes for the next generation of rechargeable  $\text{Li}^+$  ion batteries [1-9]. Most of the research efforts are focused on  $\text{LiFePO}_4$  because of the material's high theoretical capacity (170 mAh/g), 3.4 V operating potential against  $\text{Li}^+/\text{Li}$ , excellent coulombic efficiency, very low fade rate, and environmentally benign constituents [10]. In this compound, lithium extraction is described as a topotactic two-phase reaction, whereby  $\text{Li}^+$  ions are removed from the tryphillite-like phase of  $\text{LiFePO}_4$  (space group  $Pnma$ ) to form the heterosite-like  $\text{FePO}_4$  phase (space group  $Pnma$ ) [1,11].

A number of researchers have used a shrinking core model to explain the two-phase reaction of  $\text{Li}_x\text{FePO}_4$  cathodes [1,12,13]. This model has been confirmed with composition-dependent voltage measurements, X-ray diffraction (XRD), and Mössbauer techniques as well as mathematical simulations [1,3,11-14]. Here, the delithiation mechanism proceeds by a spinodal-like reaction scheme. In the very early stages of delithiation,  $\text{Li}_x\text{FePO}_4$  ( $1 - \beta \leq x \leq 1$ ), lithium ions diffuse from the  $\text{LiFePO}_4$  particles through a single-phase reaction pathway. When the composition reaches  $\text{Li}_{1-\beta}\text{FePO}_4$ , lithium extraction becomes two-phase and a shell of lithium-deficient  $\text{Li}_\alpha\text{FePO}_4$  is

\*© The Electrochemical Society, Inc. (2004). All rights reserved.

†© Elsevier, Inc. (2005).



produced on the surface of the particles. As the cells are further charged, the  $\text{Li}_\alpha\text{FePO}_4$  shell grows inward at the expense of the  $\text{Li}_{1-\beta}\text{FePO}_4$  core. Afterwards, the cathode material undergoes a second single-phase reaction to produce  $\text{FePO}_4$ . Powder XRD measurements of chemically prepared  $\text{Li}_x\text{FePO}_4$  suggest that  $\alpha$  and  $\beta$  are approximately 0.032 and 0.038, respectively, at room temperature [13].

Reversible  $\text{Li}^+$  intercalation has also been demonstrated for  $\text{LiMnPO}_4$  (4.1 V) [6,15-17]. Delacourt *et al.* utilized powder XRD to demonstrate that the delithiation mechanism of  $\text{LiMnPO}_4$  is a two-phase process analogous to  $\text{LiFePO}_4$  [17]. However, lithium extraction from  $\text{LiMnPO}_4$  is kinetically hindered and proceeds at much slower rates than  $\text{LiFePO}_4$  [16]. Cathodes employing  $\text{LiCoPO}_4$  (4.8 V) [8,18-21] or  $\text{LiNiPO}_4$  (5.2 V) [22,23] have also received some attention because of their high redox potentials against  $\text{Li}^+/\text{Li}$ . Unfortunately, the potential of  $\text{LiNiPO}_4$  exceeds the electrochemical stability windows for typical electrolyte systems [23,24].

Phospho-olivine solid solutions have also been targeted as potential cathode materials. Wolfenstine and Allen investigated  $\text{Li}(\text{Ni}_y\text{Co}_{1-y})\text{PO}_4$  ( $0 \leq y \leq 1$ ) [25] and a number of researchers have explored the  $\text{Li}(\text{Mn}_y\text{Fe}_{1-y})\text{PO}_4$  solid-solution series [1-3,26-30]. In the latter materials, the  $\text{Mn}^{2+}/\text{Mn}^{3+}$  redox couple can be accessed at reasonable rates. The  $\text{Li}(\text{Mn}_y\text{Fe}_{1-y})\text{PO}_4$  compounds crystallize in the *Pnma* space group with the  $\text{Mn}^{2+}$  and  $\text{Fe}^{2+}$  ions randomly distributed over the divalent transition metal sites. These materials exhibit two voltage plateaus at 3.5 and 4.1 V that correspond to the  $\text{Fe}^{2+}/\text{Fe}^{3+}$  and  $\text{Mn}^{2+}/\text{Mn}^{3+}$  redox couples, respectively [1]. The relative size of each voltage plateau depends on the manganese concentration in the cathode material.

The two-dimensional phase diagram of  $\text{Li}_x(\text{Mn}_y\text{Fe}_{1-y})\text{PO}_4$  ( $0 \leq x, y \leq 1$ ) has been

extensively investigated with XRD, X-ray absorption (XAS), and Mössbauer techniques. Yamada *et al.* reported unusual phase behavior for compounds with intermediate lithium concentrations [3]. Specifically, they noted that the presence of  $\text{Mn}^{2+}$  ions introduces a single-phase transition during the  $\text{Fe}^{2+}/\text{Fe}^{3+}$  redox couple as  $\text{Li}^+$  ions are extracted from  $\text{Li}_x(\text{Mn}_y\text{Fe}_{1-y})\text{PO}_4$  [3]. At high  $\text{Mn}^{2+}$  concentrations, the  $\text{Fe}^{2+}/\text{Fe}^{3+}$  couple proceeds entirely by the single-phase mechanism, yet the material undergoes a two-phase mechanism followed by a single-phase transition over the  $\text{Fe}^{2+}/\text{Fe}^{3+}$  couple at low  $\text{Mn}^{2+}$  concentrations. Furthermore, lithium extraction during the  $\text{Mn}^{2+}/\text{Mn}^{3+}$  redox couple is described as two-phase regardless of the manganese concentration. Bramnik *et al.* utilized high resolution synchrotron XRD to propose two-phase delithiation reactions for both the  $\text{Fe}^{2+}/\text{Fe}^{3+}$  and  $\text{Mn}^{2+}/\text{Mn}^{3+}$  redox couples of  $\text{Li}_x(\text{Mn}_{0.6}\text{Fe}_{0.4})\text{PO}_4$  [31]. However, their data could not rule out the possibility of a single-phase region for  $0.55 \leq x \leq 0.67$  in  $\text{Li}_x(\text{Mn}_{0.6}\text{Fe}_{0.4})\text{PO}_4$ .

By far, the biggest hindrance toward commercializing the  $\text{LiMPO}_4$  materials is their very poor intrinsic conductivities [17,32]. For example, the experimentally measured intrinsic conductivity of  $\text{LiFePO}_4$  is between  $10^{-9}$  and  $10^{-8}$  S/cm at room temperature [33]. In fact,  $\text{LiFePO}_4$  is a semiconductor with a  $\sim 0.3$  eV crystal field band gap and  $\text{LiMnPO}_4$  is an insulator with a  $\sim 2$  eV spin exchange band gap [30]. In comparison,  $\text{LiCoO}_2$  has a room temperature electronic conductivity of  $10^{-3}$  S/cm [34]. Several approaches have been employed to circumvent the poor electronic conductivity of the  $\text{LiMPO}_4$  materials and improve their cycling performance. Of course, performance may be improved by formulating the composite cathode material with an excessive amount of conductive carbon, but this sacrifices the volumetric energy density of the

composite electrode. Yamada *et al.* was able to extract >95% of the theoretical capacity by sintering the precursor materials at about 550°C [4]. This approach optimizes the synthesis conditions so that the formation of trivalent impurities is suppressed while the particle sizes are minimized. Other material processing strategies to increase the electronic conductivity of the LiMPO<sub>4</sub> electrode materials to technologically useful levels include coating the particles with a thin layer of carbon [35-40] or doping the compounds with metal ions supervalent to Li<sup>+</sup> [32]. The former strategy has received more attention in the literature.

There have been several investigations into the local structure of the LiMPO<sub>4</sub> compounds, especially as a function of lithium concentration; however, the majority of these investigations have focused on the transition metal ions using Mössbauer spectroscopy and X-ray absorption spectroscopy (XAS) [3,4,7,11,26,27,29,41]. Tucker *et al.* utilized <sup>7</sup>Li and <sup>31</sup>P magic angle spinning nuclear magnetic resonance spectroscopy (MAS-NMR) to investigate the local structure around the Li and P atoms in the LiMPO<sub>4</sub> series [42,43]. A number of researchers have shown that vibrational spectroscopy is very useful in probing fundamental lithium intercalation reactions in a variety of crystalline electrode materials [44-52]. For example, distinct phase changes could be identified in Li<sub>x</sub>Mn<sub>2</sub>O<sub>4</sub> (0 ≤ x ≤ 2) using infrared and Raman spectroscopy [47,50,51]. The vibrations of the PO<sub>4</sub><sup>3-</sup> anions are expected to be extremely sensitive to the presence of the Li<sup>+</sup> ions because they are coordinated to oxygen atoms that are covalently bonded to phosphorous atoms. Thus, a vibrational spectroscopic investigation into the LiMPO<sub>4</sub> compounds might provide a unique perspective on the lithium (de)insertion reactions that accompany cathode cycling. To this end, infrared and Raman spectra of LiMPO<sub>4</sub> (M = Fe, Mn, Co,

and Ni) and  $\text{NaFePO}_4$  are measured to explore the features of the vibrational spectra. The effect of lithium extraction is then investigated in  $\text{Li}_x\text{FePO}_4$  and  $\text{Li}_x(\text{Mn}_{0.5}\text{Fe}_{0.5})\text{PO}_4$  ( $0 \leq x \leq 1$ ) cathodes.

## 2.2 Experimental Methods

Samples of  $\text{LiFePO}_4$  are prepared by mixing stoichiometric quantities of  $\text{FeC}_2\text{O}_4 \cdot 2\text{H}_2\text{O}$ ,  $\text{Li}_2\text{CO}_3$ , and  $(\text{NH}_4)_2\text{HPO}_4$ . The mixture is heated at  $300^\circ\text{C}$  for  $\sim 3$  h, followed by heating at  $450^\circ\text{C}$  for 10 h. The sample is then cooled to room temperature, thoroughly ground, and pressed into pellets with a pressure of  $2.5 \times 10^7$  Pa. The pellets are then heated to  $800^\circ\text{C}$  for 24 h. All thermal treatments are conducted under an inert atmosphere of  $\text{N}_2$  to minimize the formation of  $\text{Fe}^{3+}$  impurities. The preparation of  $^6\text{LiFePO}_4$  is identical to the above procedure except lithium-6 acetate is substituted for lithium carbonate. To synthesize  $\text{LiNiPO}_4$  and  $\text{LiMnPO}_4$ , appropriate quantities of  $\text{Li}_2\text{CO}_3$ ,  $(\text{NH}_3)_2\text{HPO}_4$ , and either  $\text{NiCO}_3$  or  $\text{Mn}(\text{C}_2\text{H}_3\text{O}_2)_2$  are ground together and heated at  $125^\circ\text{C}$  for 24 h. Next, the precursor is thoroughly re-ground and heated at  $225^\circ\text{C}$  for 3 h, then at  $750^\circ\text{C}$  for 48 h ( $\text{LiMnPO}_4$ ) or 96 h ( $\text{LiNiPO}_4$ ). Both of the latter heating steps are performed under flowing nitrogen. The procedure of Lloris *et al.* is utilized to prepare  $\text{LiCoPO}_4$  [18]. In short, a  $\text{CoNH}_4\text{PO}_4$  precipitate is formed by mixing aqueous solutions of  $\text{CoCl}_2$ ,  $(\text{NH}_4)_2\text{HPO}_4$ , and  $\text{NH}_4\text{OH}$ . The product is reacted with  $\text{Li}_2\text{CO}_3$  at  $400^\circ\text{C}$  for 24 h, followed by  $700^\circ\text{C}$  for 96 h under static air. The purity of the as-synthesized materials is confirmed with powder XRD (Scintag X'Tra powder X-ray diffractometer).

Samples of  $\text{Li}(\text{Mn}_{0.5}\text{Fe}_{0.5})\text{PO}_4$  are prepared by the solid state reaction of  $\text{FeC}_2\text{O}_4 \cdot 2\text{H}_2\text{O}$ ,  $\text{Li}_2\text{CO}_3$ , and  $\text{NH}_4\text{H}_2\text{PO}_4$  under a flow of nitrogen. The starting materials are thoroughly ground together with 4 wt% cellulose acetate. The precursor is slowly heated to  $700^\circ\text{C}$  and annealed for 24 h before cooling to room temperature. The crystal structure is confirmed by powder XRD (STOE & Cie GmbH STADI powder diffractometer) using  $\text{Cu K}\alpha$  radiation. High purity  $\text{LiFePO}_4$  and  $\text{LiMnPO}_4$  is also obtained from Kerr-McGee Stored Power Company to compare with  $\text{Li}(\text{Mn}_{0.5}\text{Fe}_{0.5})\text{PO}_4$ .

Sodium ions are electrochemically inserted into the  $\text{FePO}_4$  structure to form  $\text{NaFePO}_4$ . Reacting  $\text{LiFePO}_4$  (Kerr-McGee sample) with an excess of  $\text{Br}_2$  in acetonitrile prepares the  $\text{FePO}_4$  precursor. Cathodes for this study are formulated from 65 wt%  $\text{FePO}_4$ , 16 wt% KS-6 graphite (Tim Cal), 16 wt% Super P carbon (3M), and 3 wt% Teflon. The resulting cathode paste is rolled into a thin sheet and cut into  $1.27 \text{ cm}^2$  circular disks. The total mass of each cathode is approximately 15 mg. Cells are constructed with these cathodes, a sodium metal anode, and an electrolyte consisting of 1 M  $\text{NaClO}_4$  in a 1:1 solution of propylene carbonate and ethylene carbonate. The cells are discharged using the galvanostatic intermittent titration technique (GITT) on an Arbin battery cycler (model number BT-20443). The test procedure involves discharging the cells at  $20 \mu\text{A cm}^{-2}$  until 5% of the theoretical capacity is achieved; the cell is then allowed to rest for 10 h. This process is repeated until the discharge voltage is less than 2.0 V.

The partially delithiated  $\text{Li}_x\text{FePO}_4$  ( $0 \leq x \leq 1$ ) is prepared by mixing  $\text{LiFePO}_4$  with an appropriate amount of  $\text{Br}_2$  in acetonitrile. The samples are stirred overnight, washed thoroughly with acetonitrile and acetone, dried under reduced pressure, and

stored under argon. Lithium ions are electrochemically extracted from  $\text{Li}(\text{Mn}_{0.5}\text{Fe}_{0.5})\text{PO}_4$  to form the  $\text{Li}_x(\text{Mn}_{0.5}\text{Fe}_{0.5})\text{PO}_4$  materials. To this end, cathodes are prepared from 87 wt% active material, 5 wt% KS-6 graphitic carbon (Tim Cal, Ltd.), 5 wt% Super P, and 3 wt% Teflon. The resulting mixture is then pressed into thin circular disks ( $0.6207 \text{ cm}^2$  and  $4.0 \pm 0.6 \text{ mg}$ ) and dried overnight at  $150^\circ\text{C}$  in a vacuum oven. Coin cells are constructed using a lithium metal anode and an electrolyte of  $1 \text{ M}$   $\text{LiPF}_6$  in a 1:1 solution of ethylene carbonate and diethyl carbonate. The cell potential is potentiostatically swept between 4.60 and 2.85 V at approximately  $55^\circ\text{C}$  using a  $0.5 \text{ mV/sec}$  rate ( $\sim 1\text{C}$ ). All of the cells undergo one complete cycle before being charged to the desired voltage. Next, the cells are disassembled under an argon atmosphere, washed twice with diethyl carbonate, dried under reduced pressure at room temperature, and stored under argon. Details concerning the instrumental procedures may be found in App. A.

## 2.3 Results and Discussion

### 2.3.1 $\text{LiMPO}_4$ ( $M = \text{Fe}, \text{Mn}, \text{Co}, \text{Ni}$ )

Powder XRD patterns for  $\text{LiMPO}_4$  ( $M = \text{Mn}, \text{Fe}, \text{Ni}, \text{and Co}$ ) are presented in Fig. 2-1. All of the reflections for each sample can be indexed to the  $Pnma$  ( $D_{2h}^{16}$ ) space group, and the lattice parameters for these materials are summarized in Table II-I. Indeed, the diffraction results agree very well with previously reported crystallographic data [11,16,53-60]. A representation of the  $\text{LiFePO}_4$  unit cell is presented in Fig. 2-2 ( $Z = 4$ ) to illustrate the global structure of the compound; the other three materials have similar structures. In these materials, the divalent transition metal ions are octahedrally

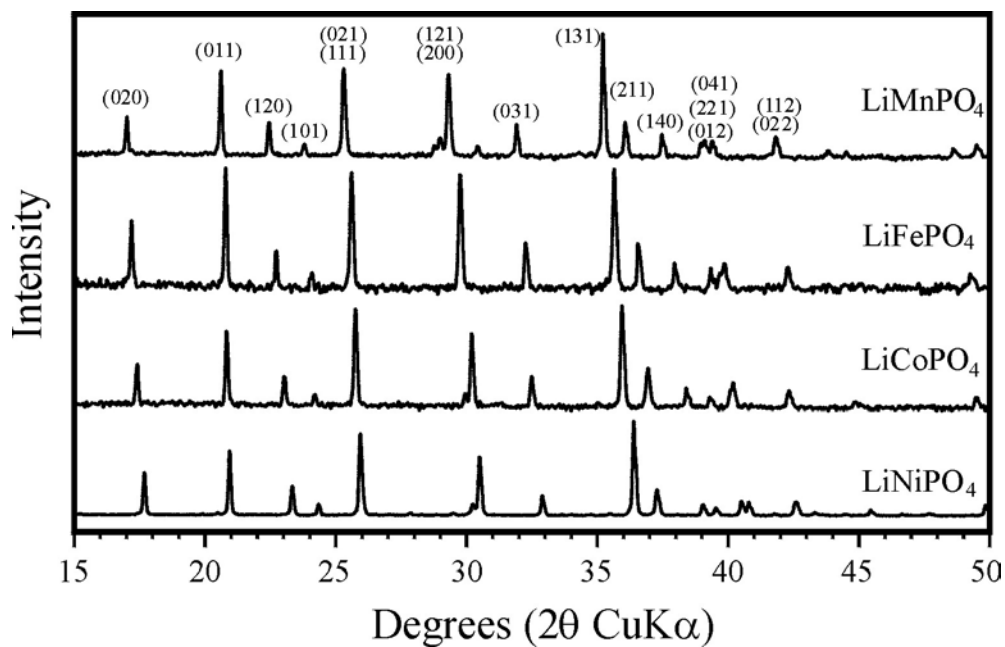


Figure 2-1: Powder XRD diffractograms of LiMPO<sub>4</sub> compounds.

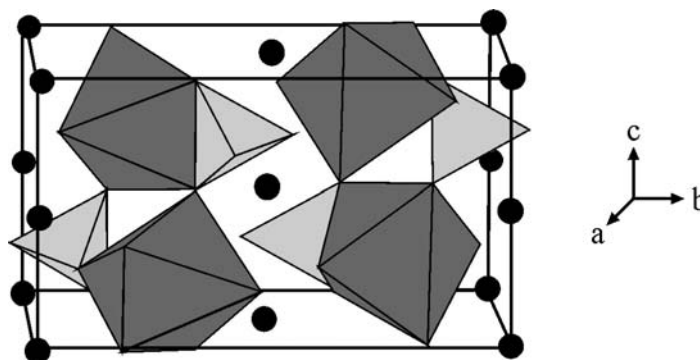


Figure 2-2: Representation of the phospho-olivine LiMPO<sub>4</sub> unit cell [2].

Table II-I: Lattice Parameters for LiMPO<sub>4</sub> Compounds

|                     | LiMnPO <sub>4</sub> | LiFePO <sub>4</sub> | LiCoPO <sub>4</sub> | LiNiPO <sub>4</sub> |
|---------------------|---------------------|---------------------|---------------------|---------------------|
| a (Å)               | 10.438(8)           | 10.318(3)           | 10.195(4)           | 10.030(8)           |
| b (Å)               | 6.097(3)            | 6.004(1)            | 5.927(6)            | 5.857(4)            |
| c (Å)               | 4.742(9)            | 4.692(7)            | 4.698(6)            | 4.680(3)            |
| V (Å <sup>3</sup> ) | 301.8(8)            | 290.7(2)            | 283.9(6)            | 274.9(9)            |

coordinated and occupy 4(c) Wyckoff sites ( $C_s$  symmetry) in the unit cell. These  $MO_6$  octahedra (shaded dark gray in Fig. 2-2) are interconnected with tetrahedrally coordinated  $P^{5+}$  cations (shaded light gray), which are also located on 4(c) sites, to form a 3-dimensional structure. Octahedrally coordinated  $Li^+$  ions (black circles) are situated on 4(a) Wyckoff sites ( $C_i$  symmetry) throughout the lattice.

Several laboratories have studied phospho-olivine materials with vibrational spectroscopy [61-63]; therefore, only a brief overview of the spectra will be provided for completeness. Early work by Paques-Ledent and Tarte focused on elucidating the atomic contributions for the vibrational modes of  $LiMPO_4$  ( $M = Mg, Ni, Co, Mn, Fe, \text{ and } Cd$ ) [61]. In particular, the authors focused on the first two compounds. The number and optical activity of the  $LiMPO_4$  vibrational modes depend on the site symmetry of the ions and the correlated motion of the ions in the unit cell. A factor group correlation of the vibrational modes for these materials may be found in Table II-II [61]. Although, the resulting normal modes are a mixture of different kinds of atomic motions, the vibrational modes of  $LiMPO_4$  may be easily divided into internal and external vibrations. Internal modes predominantly consist of intramolecular motions of the tetrahedral  $PO_4^{3-}$  anions and are typically denoted by Herzberg's notation for the fundamental vibrations of the isolated anion (i.e.,  $\nu_1-\nu_4$ ) [64]. In contrast, external modes (or lattice phonon modes) are primarily composed of translatory motions of the cations as well as whole-body translations and librations (pseudo-rotations) of the anions. In general, the separation of the vibrational modes into internal and external vibrations is justified because the force constants of the internal modes are much larger than the external modes [65]. Nevertheless, the approximation has been shown to break down for compounds that



**Table II-II:** Factor group correlation of the internal and external vibrations for LiFePO<sub>4</sub>

| Factor Group  | Number of Normal Modes       |                 |                 |                 |                                     |  |   |  | Total | Optical Activity                        |
|---|------------------------------|-----------------|-----------------|-----------------|-------------------------------------|--|---|--|-------|---|
|   | Internal Modes               |                 |                 |                 | External Modes                      |  |   |  |       |   |
|   | $\Gamma(\nu_1)$              | $\Gamma(\nu_2)$ | $\Gamma(\nu_3)$ | $\Gamma(\nu_4)$ | $\Gamma_{\text{tran}}(\text{Li}^+)$ | $\Gamma_{\text{tran}}(\text{Fe}^{2+})$ | $\Gamma_{\text{rot}}(\text{PO}_4^{3-})$ | $\Gamma_{\text{tran}}(\text{PO}_4^{3-})$ |       |   |
| D <sub>2h</sub>   | C <sub>s</sub> <sup>ZX</sup> |                 |                 |                 | C <sub>i</sub>                      | C <sub>s</sub> <sup>ZX</sup>           | C <sub>s</sub> <sup>ZX</sup>            | C <sub>s</sub> <sup>ZX</sup>             |       |   |
| A <sub>g</sub>  | 1                            | 1               | 2               | 2               | 0                                   | 2                                      | 1                                       | 2  | 11    | $\alpha_{xx}, \alpha_{yy}, \alpha_{zz}$ |
| B <sub>1g</sub>   | 0                            | 1               | 1               | 1               | 0                                   | 1                                      | 2                                       | 1  | 7     | $\alpha_{xy}$                           |
| B <sub>2g</sub>   | 1                            | 1               | 2               | 2               | 0                                   | 2                                      | 1                                       | 2  | 11    | $\alpha_{zx}$                           |
| B <sub>3g</sub>   | 0                            | 1               | 1               | 1               | 0                                   | 1                                      | 2                                       | 1  | 7     | $\alpha_{yz}$                           |
| A <sub>u</sub>  | 0                            | 1               | 1               | 1               | 3                                   | 1                                      | 2                                       | 1  | 10    | Inactive                                |
| B <sub>1u</sub>   | 1                            | 1               | 2               | 2               | 3                                   | 2                                      | 1                                       | 2  | 14    | $\mu_z$                                 |
| B <sub>2u</sub>   | 0                            | 1               | 1               | 1               | 3                                   | 1                                      | 2                                       | 1  | 10    | $\mu_y$                                 |
| B <sub>3u</sub>   | 1                            | 1               | 2               | 2               | 3                                   | 2                                      | 1                                       | 2  | 14    | $\mu_x$                                 |
| Acoustic Modes: $\Gamma_{\text{total}} = B_{1u} + B_{2u} + B_{3u}$  |                              |                 |                 |                 |                                     |  |   |  |       |   |
| Optical Modes: $\Gamma_{\text{total}} = 11A_g + 7B_{1g} + 11B_{2g} + 7B_{3g} + 10A_u + 13B_{1u} + 9B_{2u} + 13B_{3u}$ |                              |                 |                 |                 |                                     |  |   |  |       |   |

contain light cations, such as Li<sup>+</sup>. In those compounds, the translatory vibrations of the Li<sup>+</sup> cations (also known as Li<sup>+</sup> “cage modes”) may occur at high enough frequencies to mix with PO<sub>4</sub><sup>3-</sup> bending modes of matching symmetry. In the phospho-olivine structure, Li<sup>+</sup> ions occupy sites that contain an inversion center. Therefore, any mode involving Li<sup>+</sup> motion must be Raman inactive and infrared active (cf., Table II-II).

Infrared absorption spectra of LiMPO<sub>4</sub> (M = Mn, Fe, Co, and Ni) are presented in Fig. 2-3 to demonstrate the effect of the transition metal ion on the vibrational modes. The mid-IR region of the spectrum (1300–400 cm<sup>-1</sup>) consists mostly of intramolecular PO<sub>4</sub><sup>3-</sup> stretching ( $\nu_1$  and  $\nu_3$ ) and bending ( $\nu_4$ ) modes. Fortunately, the assignment of bands originating in the intramolecular stretching motions of the phosphate anion ( $\nu_1$  and  $\nu_3$ ) can be done with some degree of confidence because they are highly decoupled. For

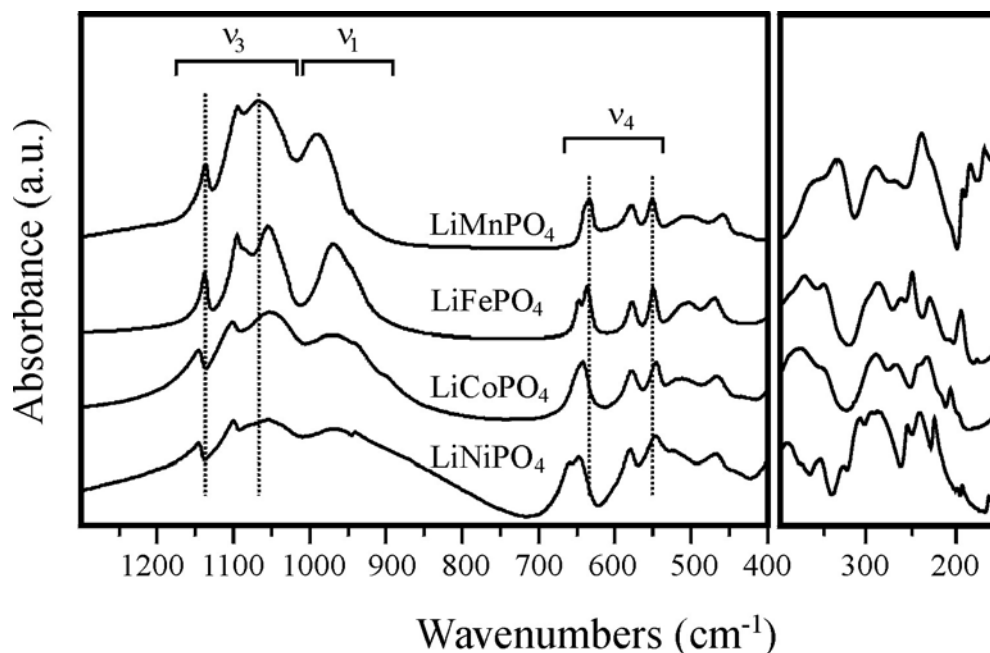


**Figure 2-3:** Infrared absorption spectra of LiMPO<sub>4</sub>. Dashed lines mark changes that occur when the transition metal ion is changed. Between 1300–400 cm<sup>-1</sup> and 400–150 cm<sup>-1</sup> spectra are collected with KBr (mid-IR) and Mylar (far-IR) beam splitters, respectively.

example, all of the samples contain three relatively broad bands near 1140, 1095, and 1070 cm<sup>-1</sup> that may be assigned to  $\nu_3$ . The bands between 700 and ~525 cm<sup>-1</sup> are assigned to  $\nu_4$ . Paques-Ledent and Tarte utilized <sup>6</sup>Li/<sup>7</sup>Li isotope shifts to show that the two bands between ~525 and 400 cm<sup>-1</sup> contain a significant amount of Li<sup>+</sup> motion in LiMgPO<sub>4</sub> and LiNiPO<sub>4</sub> [61]. Therefore, these bands are assigned to the Li<sup>+</sup> ion cage modes. The degree of mixing between the Li<sup>+</sup> ion cage modes and the PO<sub>4</sub><sup>3-</sup> bending modes in these bands will be explored in greater detail in Sec. 2.3.2.

Far-IR spectra of LiMPO<sub>4</sub> (M = Mn, Fe, Co, Ni) are also presented in Fig. 2-3 (400–150 cm<sup>-1</sup>). The bands between 400 and 350 cm<sup>-1</sup> probably consist mostly of antisymmetric PO<sub>4</sub><sup>3-</sup> bending vibrations ( $\nu_2$ ). However, an unambiguous assignment of these modes is somewhat problematic because these modes are likely mixed with lattice

phonon modes. For instance, the frequencies of the  $\nu_2$  bands depend on the transition metal ion. The external modes of  $\text{LiMPO}_4$  occur below  $300 \text{ cm}^{-1}$ . These vibrations consist of a complicated mixture of atomic motions. For this reason, they cannot be assigned with any degree of confidence without the aid of calculations or detailed isotopic substitution studies [61].

The major features of the spectra are preserved as the transition metal ion is changed; however, the frequencies of some of the bands depend on the nature of the  $\text{M}^{2+}$  ion. Paques-Ledent and Tarte suggested that the splitting of the  $\text{PO}_4^{3-}$  internal modes is related “not to a geometrical deformation...but to an unequal distribution of the bonding forces within the tetrahedral group” [61]. Furthermore, it has been demonstrated that the splitting of  $\nu_3$  increases with the second ionization energy of the transition metal ion in  $\text{LiMPO}_4$  [61,62]. A similar trend is expected for the  $\nu_4$  bands as the splitting of these

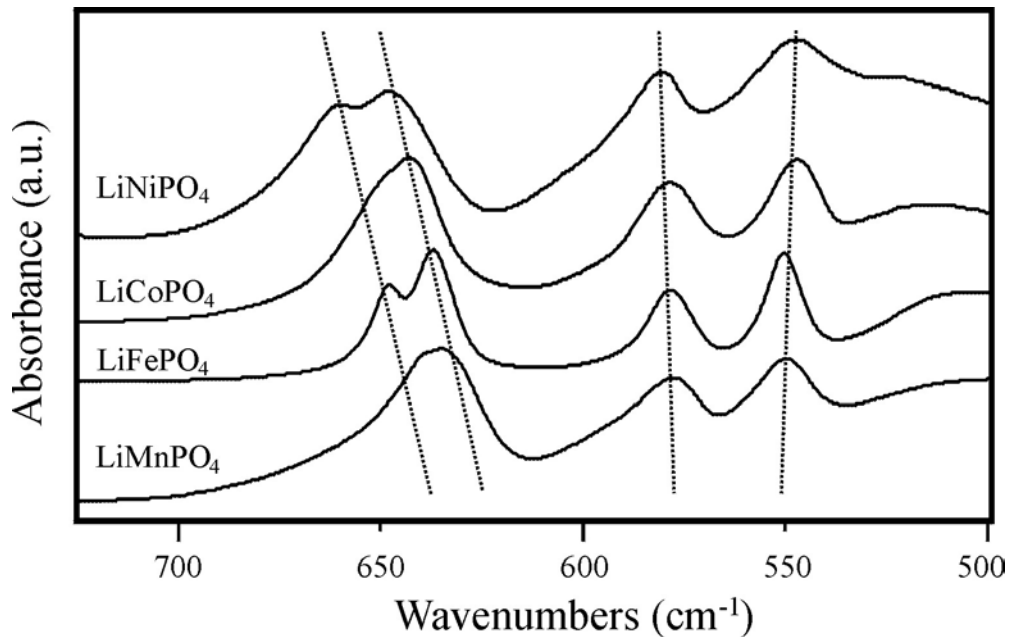


**Figure 2-4:** Infrared absorption spectra of  $\nu_4$  for  $\text{LiMPO}_4$ .

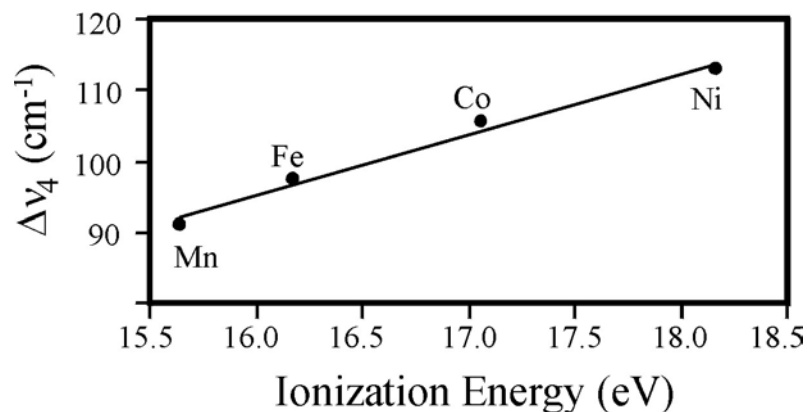


**Figure 2-5:** Linear correlation between the factor group splitting of  $\nu_4$  and the second ionization energy of the divalent transition metal ion in  $\text{LiMPO}_4$  ( $r = 0.9921$ ,  $p = 0.0079$ ).

modes increases as the transition metal ion changes from manganese to nickel (Fig. 2-4). Here, the factor group splitting is calculated by subtracting the frequencies of the highest and lowest bands in a given vibrational multiplet. For example, the splitting of  $\nu_4$  in  $\text{LiFePO}_4$ , as defined here, is  $98 \text{ cm}^{-1}$  ( $648 - 550 \text{ cm}^{-1}$ ). The splitting of the  $\nu_4$  modes may be fit to an empirical equation (Fig. 2-5) using values of the second ionization potential of the transition metal cations found in Ref. 66:

$$\Delta\nu_4 = 8.5759 E - 42.154 \quad \text{[Equation 2-1]}$$

where  $\Delta\nu_4$  is the factor group splitting of the  $\nu_4$  modes and  $E$  is the ionization energy of the  $\text{M}^{2+}$  ion in  $\text{LiMPO}_4$ . Transition metal ions that have a relatively large ionization potential form strong bonds with the oxygen atoms of the phosphate tetrahedra and result in greater factor group splitting effects for the  $\text{PO}_4^{3-}$  anions [61]. Thus, the  $\nu_4$  modes of  $\text{LiNiPO}_4$  exhibit greater splitting compared to  $\text{LiMnPO}_4$  because  $\text{Ni}^{2+}$  has larger ionization energy than  $\text{Mn}^{2+}$ .

Raman scattering spectra of the  $\text{LiMPO}_4$  ( $M = \text{Mn, Fe, Co, Ni}$ ) intramolecular stretching modes are presented in Fig. 2-6. The spectra are dominated by a very intense band near  $950 \text{ cm}^{-1}$  that is assigned to the  $A_g$  mode of  $\nu_1$ . Several weaker bands are identified between  $975$  and  $1125 \text{ cm}^{-1}$  in each of the samples. These are attributed to  $\nu_3$  modes. Group theory predicts  $\nu_4$  will yield six Raman normal modes ( $2A_g + B_{1g} + 2B_{2g} + B_{3g}$ ) and  $\nu_2$  will yield four Raman active vibrations ( $A_g + B_{1g} + B_{2g} + B_{3g}$ ) at the Brillouin zone center [61]. The  $\nu_4$  bands appear between  $750$  and  $550 \text{ cm}^{-1}$ . The origin of the  $730 \text{ cm}^{-1}$  band in  $\text{LiFePO}_4$  is not known since the frequency of this band is much higher expected for a  $\nu_4$  mode. Bands near  $450 \text{ cm}^{-1}$  are assigned to mostly  $\nu_2$  vibrations, and the Raman active external modes occur below  $400 \text{ cm}^{-1}$ . As discussed earlier, none of these modes consist of pure  $\text{PO}_4^{3-}$  motion. Instead, they are a complicated mixture of

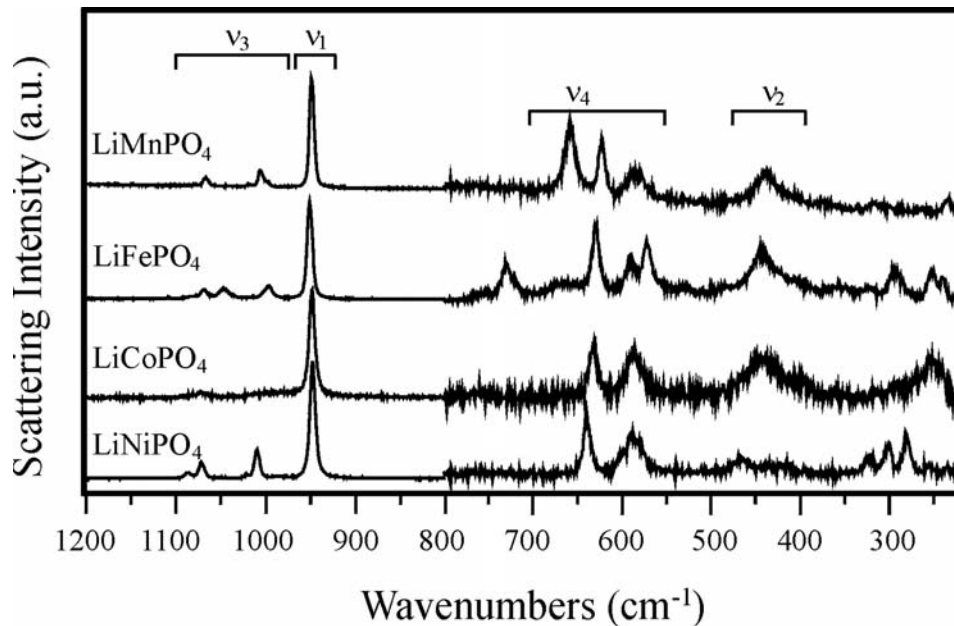


**Figure 2-6:** Raman scattering spectra of  $\text{LiMPO}_4$ . The spectra recorded below  $800 \text{ cm}^{-1}$  have been magnified.

atomic motions. Paraguassu *et al.* performed phonon calculations to assign the lower-frequency Raman bands in  $\text{LiMPO}_4$  ( $M = \text{Fe, Co, Ni}$ ); their results may be found in Ref. [63]. It is important to note that the  $\text{Li}^+$  ion cage modes do not appear in the Raman spectra ( $530$  to  $460 \text{ cm}^{-1}$ ), in accord with the theoretical predictions.

### 2.3.2 $\text{LiFePO}_4$ and $\text{NaFePO}_4$

The effect of the  $\text{Li}^+$  cations on the vibrational modes of  $\text{LiMPO}_4$  ( $M = \text{Mn, Fe, Co, Ni}$ ) is investigated by studying the vibrational spectra of  $^6\text{LiFePO}_4$ ,  $^7\text{LiFePO}_4$ , and  $\text{NaFePO}_4$ . Infrared and Raman spectra of  $^7\text{LiFePO}_4$  and  $^6\text{LiFePO}_4$  are presented in Figures 2-7 and 2-8, respectively. Most of the bands in the Raman spectra are not affected when the isotope is changed to lithium-6 (Figure 2-7). For example, there are no frequency shifts in the  $\nu_1$  and  $\nu_3$  bands. As expected, a significant amount of  $\text{Li}^+$  ion

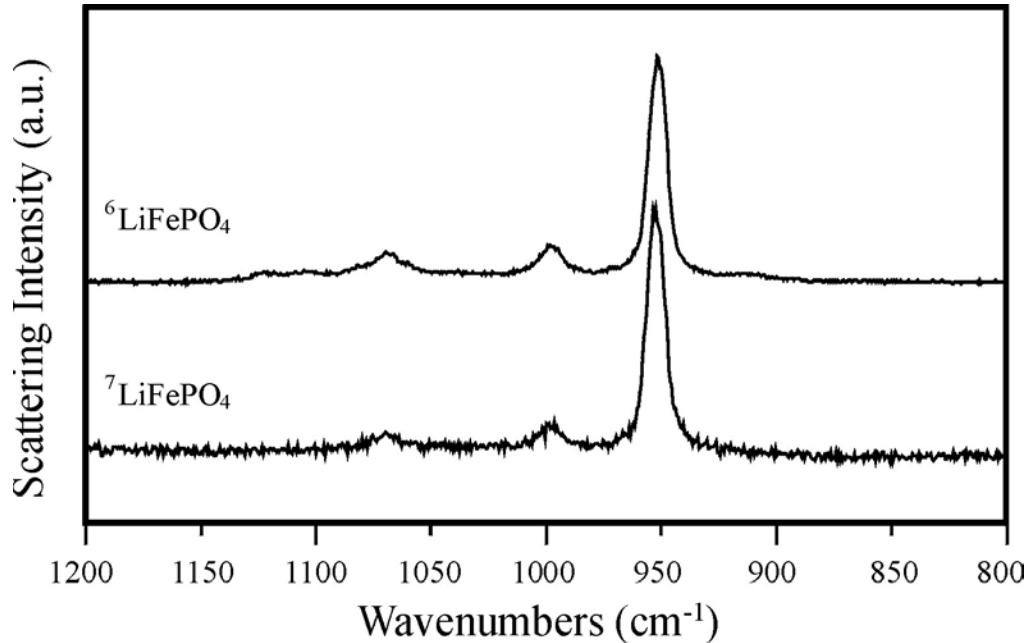


**Figure 2-7:** Raman scattering spectra of  $^6\text{LiFePO}_4$  and  $^7\text{LiFePO}_4$ .

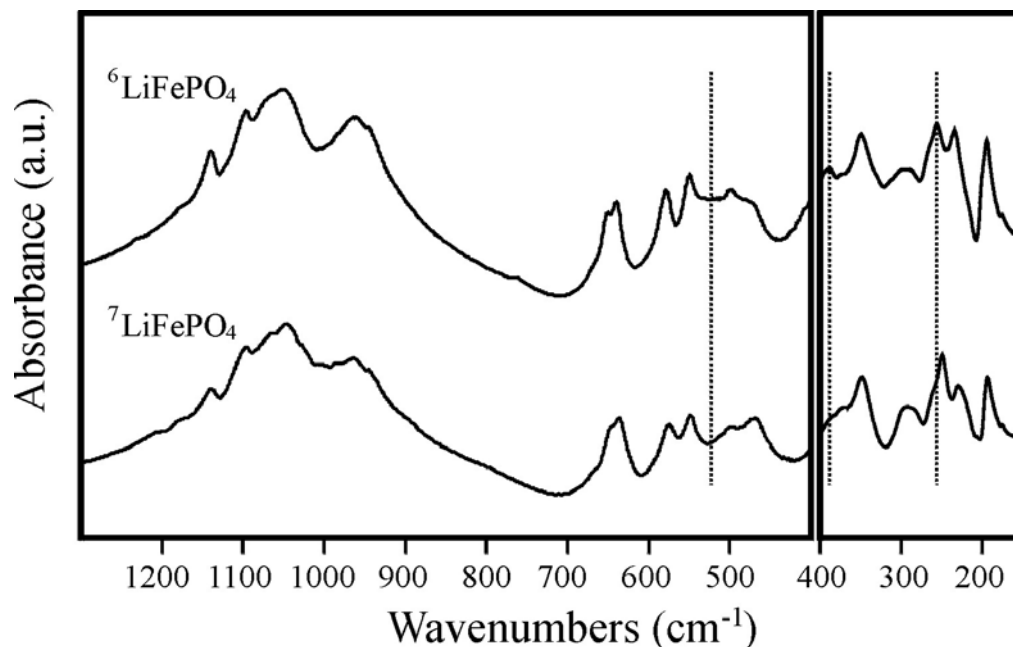


**Figure 2-8:** Infrared absorption spectra of  ${}^6\text{LiFePO}_4$  and  ${}^7\text{LiFePO}_4$ . Between 1300–400  $\text{cm}^{-1}$  and 400–150  $\text{cm}^{-1}$  spectra are collected with KBr (mid-IR) and Mylar (far-IR) beam splitters, respectively.

motion is detected in the bands between 575 to 465  $\text{cm}^{-1}$  in the infrared spectra as shown in Figure 2-8. Moreover, a few of the lattice modes are affected by the substitution of  ${}^6\text{Li}$  for  ${}^7\text{Li}$ .

Although the  ${}^6\text{Li}/{}^7\text{Li}$  isotope study clearly reveals bands that contain  $\text{Li}^+$  ion motion, the shifts are not large enough to determine the degree of coupling between the  $\text{Li}^+$  cage modes and the  $\text{PO}_4^{3-}$  bending modes. To this end, the vibrational spectrum of  $\text{LiFePO}_4$  is compared to  $\text{NaFePO}_4$ . Sodium ions have a larger mass than lithium ions so the  $\text{Na}^+$  ion cage modes should appear at lower frequencies than the  $\text{Li}^+$  ion cage modes. Two phases of  $\text{NaFePO}_4$  have been reported in the literature. Yakubovich *et al.* [67] and Birdson *et al.* [68] used XRD data to describe a phase of  $\text{NaFePO}_4$  that is isostructural with the phospho-olivine mineral maricite (space group  $Pnma$ ,  $D_{2h}^{16}$ ) [69]. The authors

also noted that this phase of NaFePO<sub>4</sub> is structurally analogous to LiFePO<sub>4</sub>.

Nevertheless, there are several important differences between LiFePO<sub>4</sub> and NaFePO<sub>4</sub>. In maricite-like NaFePO<sub>4</sub>, the PO<sub>4</sub><sup>3-</sup> anions occupy 4(c) sites, whereas the Na<sup>+</sup> and Fe<sup>2+</sup> cations occupy 4(c) and 4(a) sites, respectively. In contrast, the Li<sup>+</sup> ions reside on 4(c) sites and the Fe<sup>2+</sup> ions occupy 4(a) sites in LiFePO<sub>4</sub>. This is probably due to the larger ionic radius of Na<sup>+</sup> compared to Li<sup>+</sup>. Additionally, the average Na–O bond length in NaFePO<sub>4</sub> is significantly longer than the Li–O bonds in LiFePO<sub>4</sub> (2.46 Å compared to 2.14 Å), yet the average Fe–O and P–O bond lengths are nearly identical in the two compounds. The second phase of NaFePO<sub>4</sub> reported in the literature has distinctly different lattice parameters than those reported for maricite [70]. Furthermore, Paques-Ledent used vibrational spectroscopy to argue that this phase belongs to a crystal system with symmetry lower than D<sub>2h</sub> [70].

Fig. 2-9 shows GITT data for the electrochemical insertion of Na<sup>+</sup> ions into the FePO<sub>4</sub> structure. Sodium intercalation proceeds along a flat voltage plateau of 2.87 V vs. Na<sup>+</sup>/Na. The total first discharge capacity of the cell is 151 mAh/g, which is 85% of the theoretical capacity for NaFePO<sub>4</sub>. Therefore, the estimated stoichiometry from the electrochemical discharge curves is Na<sub>0.85</sub>FePO<sub>4</sub>, but the samples will be referred to as NaFePO<sub>4</sub> throughout the remainder of this chapter. Sodium ions could be reversibly extracted from the cathodes; however, this avenue of research is not the focus of this work and will not be discussed further.

Since the site symmetry of the monovalent cations is different for NaFePO<sub>4</sub> and LiFePO<sub>4</sub>, a factor group correlation of the internal and external vibrations is conducted for NaFePO<sub>4</sub>. The Brillouin zone center normal modes of maricite-like NaFePO<sub>4</sub> are



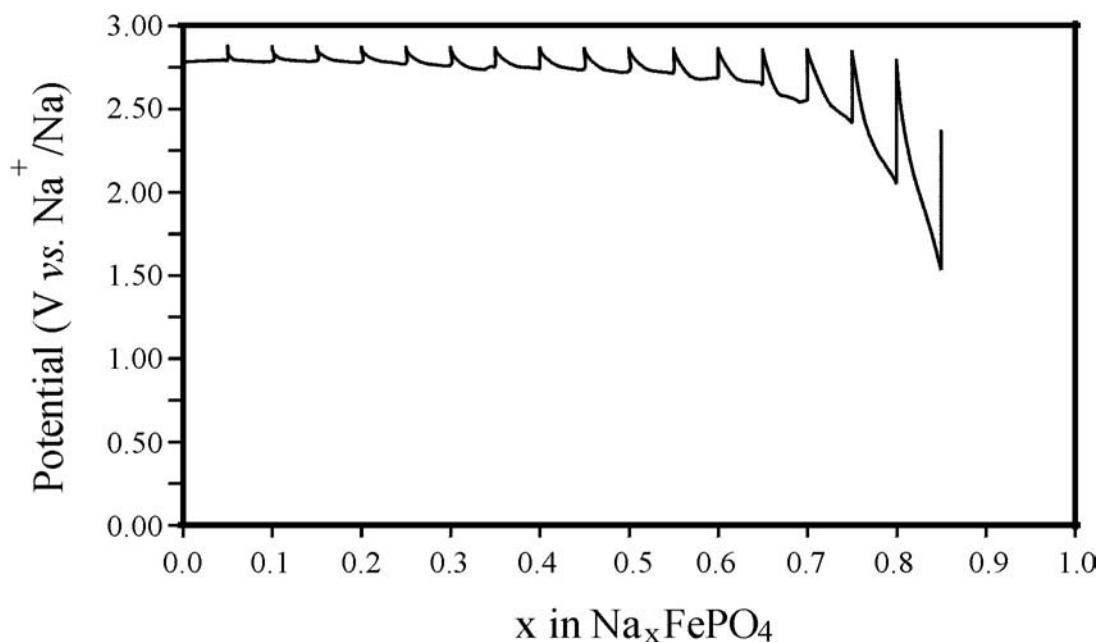


**Figure 2-9:** GITT data of the electrochemical insertion of Na<sup>+</sup> ions into FePO<sub>4</sub>.

distributed among the irreducible representations of the  $D_{2h}$  point group as described in Table II-III. The different site symmetries of the Li<sup>+</sup> and Na<sup>+</sup> ions will affect the selection rules for the translatory motions of the monovalent cations. In the LiFePO<sub>4</sub> structure, the Li<sup>+</sup> ion cage modes must be Raman inactive because the Li<sup>+</sup> ions occupy sites that contain a center of symmetry [61]. However, in the crystal structure of NaFePO<sub>4</sub>, the Na<sup>+</sup> and Fe<sup>2+</sup> cations are located on C<sub>s</sub> and C<sub>i</sub> sites, respectively. Consequently, modes involving Na<sup>+</sup> ions are either Raman- or IR-active, but vibrations containing Fe<sup>2+</sup> motion must be only IR-active. Fortunately, the PO<sub>4</sub><sup>3-</sup> anions occupy C<sub>s</sub> sites in both of the structures investigated; therefore, the factor group correlations of the internal modes are identical for LiFePO<sub>4</sub> and NaFePO<sub>4</sub>.

Infrared absorption spectra of the intramolecular stretching vibrations ( $\nu_1$  and  $\nu_3$ )

**Table II-III:** Factor group correlation of the internal and external vibrations for NaFePO<sub>4</sub>

| Number of Normal Modes |                              |               |               |               |                                     |  |   |  |       |   |
|------------------------|------------------------------|---------------|---------------|---------------|-------------------------------------|--|---|--|-------|---|
| Site Group             | Internal Modes               |               |               |               | External Modes                      |  |   |  | Total | Optical Activity                        |
|                        | $\Gamma(v_1)$                | $\Gamma(v_2)$ | $\Gamma(v_3)$ | $\Gamma(v_4)$ | $\Gamma_{\text{tran}}(\text{Na}^+)$ | $\Gamma_{\text{tran}}(\text{Fe}^{2+})$ | $\Gamma_{\text{rot}}(\text{PO}_4^{3-})$ | $\Gamma_{\text{tran}}(\text{PO}_4^{3-})$ |       |   |
| D <sub>2h</sub>        | C <sub>s</sub> <sup>ZX</sup> |               |               |               | C <sup>ZX</sup>                     | C <sub>i</sub>                         | C <sup>ZX</sup>                         | C <sup>ZX</sup>                          |       |   |
| A <sub>g</sub>         | 1                            | 1             | 2             | 2             | 2                                   | 0                                      | 1                                       | 2  | 11    | $\alpha_{xx}, \alpha_{yy}, \alpha_{zz}$ |
| B <sub>1g</sub>        | 0                            | 1             | 1             | 1             | 1                                   | 0                                      | 2                                       | 1  | 7     | $\alpha_{xy}$                           |
| B <sub>2g</sub>        | 1                            | 1             | 2             | 2             | 2                                   | 0                                      | 1                                       | 2  | 11    | $\alpha_{zx}$                           |
| B <sub>3g</sub>        | 0                            | 1             | 1             | 1             | 1                                   | 0                                      | 2                                       | 1  | 7     | $\alpha_{yz}$                           |
| A <sub>u</sub>         | 0                            | 1             | 1             | 1             | 1                                   | 3                                      | 2                                       | 1  | 10    | Inactive                                |
| B <sub>1u</sub>        | 1                            | 1             | 2             | 2             | 2                                   | 3                                      | 1                                       | 2  | 14    | $\mu_z$                                 |
| B <sub>2u</sub>        | 0                            | 1             | 1             | 1             | 1                                   | 3                                      | 2                                       | 1  | 10    | $\mu_y$                                 |
| B <sub>3u</sub>        | 1                            | 1             | 2             | 2             | 2                                   | 3                                      | 1                                       | 2  | 14    | $\mu_x$                                 |

Acoustic Modes:  $\Gamma_{\text{total}} = B_{1u} + B_{2u} + B_{3u}$

Optical Modes:  $\Gamma_{\text{total}} = 11A_g + 7B_{1g} + 11B_{2g} + 7B_{3g} + 10A_u + 13B_{1u} + 9B_{2u} + 13B_{3u}$

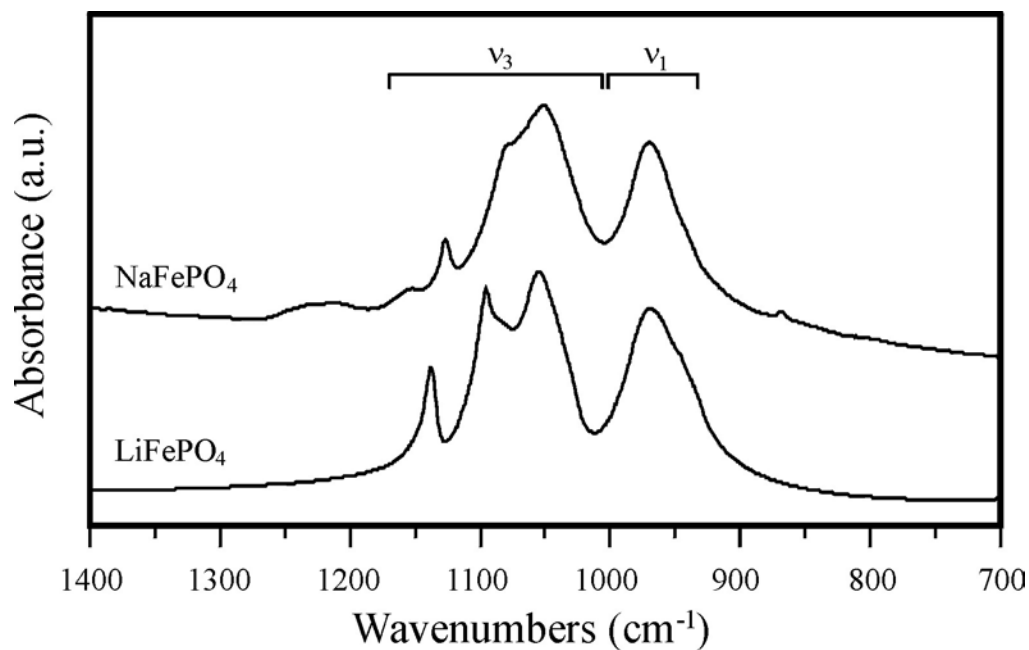
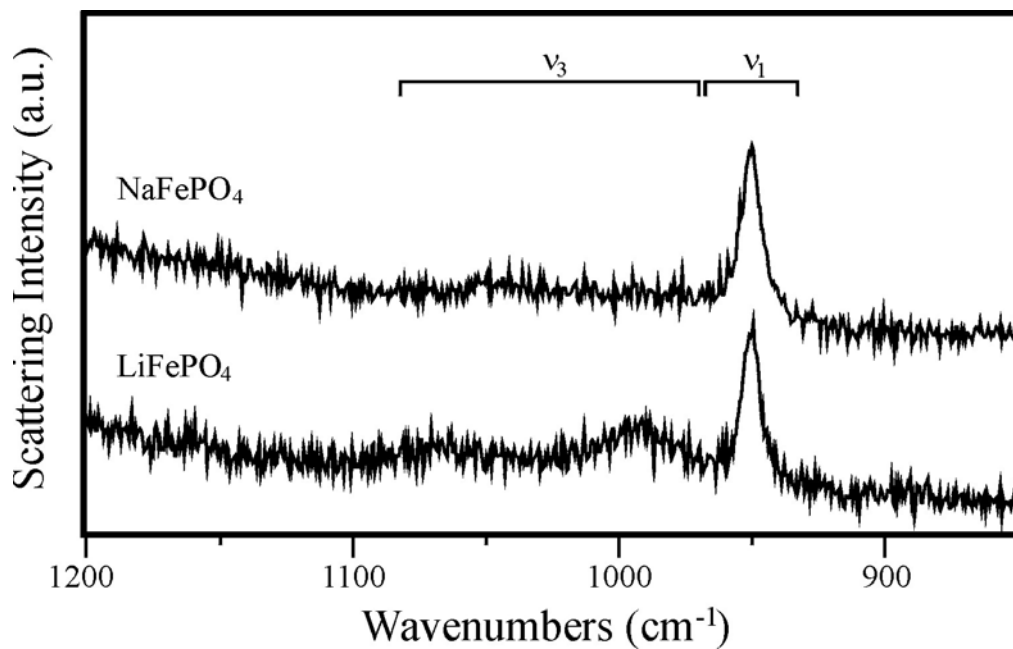


**Figure 2-10:** Infrared absorption spectra of v<sub>1</sub> and v<sub>3</sub> for LiFePO<sub>4</sub> and NaFePO<sub>4</sub>.

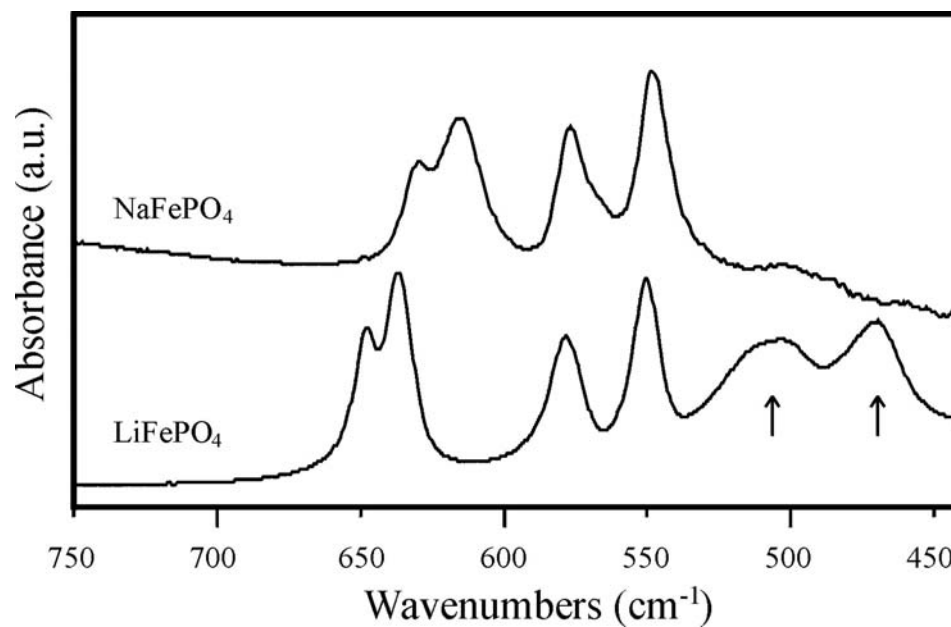
for  $\text{LiFePO}_4$  and  $\text{NaFePO}_4$  are provided in Fig. 2-10. The infrared spectrum of  $\text{NaFePO}_4$  is similar to that of  $\text{LiFePO}_4$ . The bands at 1052, 1080, and 1125  $\text{cm}^{-1}$  are assigned to  $\nu_3$  vibrations, and the  $\nu_1$  modes are identified at 972  $\text{cm}^{-1}$  and the 943  $\text{cm}^{-1}$  shoulder. The spectrum of  $\text{NaFePO}_4$  also contains several weak bands (e.g., the 1153  $\text{cm}^{-1}$  band) that might be due to small amounts of residual  $\text{FePO}_4$ . This is consistent with the electrochemical data that indicates there is a small quantity of  $\text{FePO}_4$  remaining in the sample. Raman spectra of  $\nu_1$  and  $\nu_3$  for  $\text{NaFePO}_4$  and  $\text{LiFePO}_4$  are also very similar to each other (Fig. 2-11). In both compounds the  $A_g$  mode of  $\nu_1$  occurs at 950  $\text{cm}^{-1}$ . Unfortunately, the conductive carbons used in the electrodes significantly decrease the intensity of these modes [71].

Fig. 2-12 shows infrared spectra of  $\text{LiFePO}_4$  and  $\text{NaFePO}_4$  between 750 and 450  $\text{cm}^{-1}$ . As with  $\nu_1$  and  $\nu_3$ , the relative intensities of the  $\nu_4$  bands are nearly identical in the two compounds. However, the frequencies of  $\nu_4$  are affected by the monovalent cations. Interestingly, the two bands between 525 and 450  $\text{cm}^{-1}$  in the infrared spectrum of  $\text{LiFePO}_4$  do not appear in the spectrum of  $\text{NaFePO}_4$ . Instead, there is only a very weak feature near 500  $\text{cm}^{-1}$ .

The infrared and Raman spectra of  $\text{LiFePO}_4$  have been extensively investigated in the literature [61-63], but there is only one report of the vibrational spectrum of  $\text{NaFePO}_4$  [70]. As discussed earlier, the structure of that phase of  $\text{NaFePO}_4$  [70] is different than the maricite-like  $\text{NaFePO}_4$  investigated by Yakubovich *et al.* [67] and Birdson *et al.* [68]. The infrared and Raman spectra of  $\text{NaFePO}_4$  published in Reference [70] do not agree with the spectra presented in Figs. 2-10 through 2-12. For example, the Raman spectrum of the electrochemically-synthesized  $\text{NaFePO}_4$  contains a single strong band (the  $\nu_1(A_g)$



**Figure 2-11:** Raman scattering spectra of  $\nu_1$  and  $\nu_3$  for LiFePO<sub>4</sub> and NaFePO<sub>4</sub>.



**Figure 2-12:** Infrared absorption spectra of  $\nu_4$  and the Li<sup>+</sup> ion cage modes for LiFePO<sub>4</sub> and NaFePO<sub>4</sub>. Arrows denote the Li<sup>+</sup> ion cage modes.

mode) and several bands that have weak scattering intensities (the  $\nu_3$  modes). In contrast, Raman spectra of the compounds presented in Reference 70 contain several intense bands between 900 and 1150  $\text{cm}^{-1}$ . This suggests that the electrochemically-synthesized  $\text{NaFePO}_4$  described in this paper has a different structure than the compound reported by Paques-Ledent [70].

The similar spectroscopic signatures of  $\text{NaFePO}_4$  and  $\text{LiFePO}_4$  as shown in Figs. 2-10 through 2-12, particularly the latter two figures, suggests that the  $\text{PO}_4^{3-}$  anions of the electrochemically-prepared sample have similar local structures as those in  $\text{LiFePO}_4$ . Popović *et al.* empirically established a linear correlation between the Raman stretching frequencies of a large number of inorganic phosphates and their P–O bond lengths [72]. In fact, the average P–O bond length is only 1.8 pm shorter in the structure of maricite-like  $\text{NaFePO}_4$  [67,68] compared to  $\text{LiFePO}_4$  [11]. The identical  $\nu_1$  frequencies and relative intensities of  $\text{NaFePO}_4$  and  $\text{LiFePO}_4$  in Fig. 2-11 strongly suggest that the potential energy environment of the phosphate anion in the electrochemically-prepared  $\text{NaFePO}_4$  is similar to that in both maricite and  $\text{LiFePO}_4$ .

The degenerate internal modes of the  $\text{PO}_4^{3-}$  anions may split whenever the symmetry of the electric crystal field is lower than the tetrahedral symmetry of the anion. Fortunately, the  $\text{PO}_4^{3-}$  anions occupy 4(c) Wyckoff sites in  $\text{LiFePO}_4$  and  $\text{NaFePO}_4$ ; hence, the selection rules are identical for the internal modes of these compounds. Approximately the same number of bands is detected in the infrared and Raman spectra of  $\text{NaFePO}_4$  and  $\text{LiFePO}_4$ . Moreover, the relative intensities of the intramolecular  $\text{PO}_4^{3-}$  bands are similar, but the factor group splitting of  $\nu_3$  and  $\nu_4$  is between 10 and 20  $\text{cm}^{-1}$  less for  $\text{NaFePO}_4$  than for  $\text{LiFePO}_4$ .

The magnitude of the splitting in a crystalline compound is controlled by specific interactions between the ions in the unit cell. Phosphate anions that interact strongly with neighboring cations will exhibit large factor group splitting effects. Crystallographic data show that the Fe–O bond lengths are nearly identical in the structures of NaFePO<sub>4</sub> and LiFePO<sub>4</sub>, but the Na–O bonds are longer than the Li–O bonds [11,67,68]. Thus, differences in the factor group splitting of the internal modes may be primarily due to interactions between the monovalent cations and the phosphate anions. Lithium ions have a relatively large charge density and can form stronger bonds with the PO<sub>4</sub><sup>3-</sup> anions than Na<sup>+</sup> ions. Therefore, the Li<sup>+</sup> ions exert a stronger perturbation on the vibrational modes of the PO<sub>4</sub><sup>3-</sup> anions, which results in greater factor group splitting effects for LiFePO<sub>4</sub> compared to NaFePO<sub>4</sub>.

The infrared spectrum of LiFePO<sub>4</sub> contains two broad bands centered at 506 and 470 cm<sup>-1</sup> (Fig. 2-12); however, there are no bands in this region for NaFePO<sub>4</sub>. Although isotopic substitution studies have shown that the 506 and 470 cm<sup>-1</sup> bands in LiFePO<sub>4</sub> contain a significant amount of lithium motion (see Ref. [61] and the discussion at the beginning of this section), the <sup>6</sup>Li/<sup>7</sup>Li isotope effect is not large enough to confidently assign these bands solely as Li<sup>+</sup> ion cage modes. That is, the isotope effect could not completely rule out the possibility that the Li<sup>+</sup> ion translatory motions are mixed with phosphate bending modes (e.g., ν<sub>2</sub> or ν<sub>4</sub>). Differences in the site symmetry of the monovalent cations cannot account for this disparity since the Na<sup>+</sup> and Li<sup>+</sup> ion translatory modes are infrared-active in both compounds. Sodium ions have a larger mass than Li<sup>+</sup> ions, so the Na<sup>+</sup> ion translatory modes are expected to occur at much lower frequencies than the corresponding Li<sup>+</sup> ion translatory modes. The similarity of the factor group

multiplets in  $\text{LiFePO}_4$  and  $\text{NaFePO}_4$  (viz., the four higher frequency modes of these compounds in Fig. 2-12) strongly argues that the 506 and 470  $\text{cm}^{-1}$  bands in the spectrum of  $\text{LiFePO}_4$  are not a mixture of  $\text{Li}^+$  ion translations and  $\nu_2$ . Instead, these bands are composed almost entirely of  $\text{Li}^+$  translations and may be assigned as  $\text{Li}^+$  ion cage modes with some degree of confidence.

### 2.3.3 $\text{Li}_x\text{FePO}_4$ ( $0 \leq x \leq 1$ ) Cathodes

Chemically delithiated  $\text{LiFePO}_4$  is prepared to investigate the sensitivity of the phosphate vibrations to lithium extraction. This provides a material that is free of conductive carbon and binder materials for the spectroscopic experiments. Cathodes prepared from the  $\text{LiFePO}_4$  gave a flat voltage of 3.6 V vs.  $\text{Li}^+/\text{Li}$  when charged. The first charge and discharge capacities are low compared to the 170 mAh/g theoretical capacity of  $\text{LiFePO}_4$  (76 and 59 mAh/g, respectively). This is not surprising since the electronic conductivity of this material is not enhanced by doping with metal ions or coating the particles with carbon. Additionally, relatively high sintering temperatures (800°C) are used in the preparation of this sample. This causes the growth of larger particles sizes, resulting in less than optimal cycling performance [4].

The lithium content of the  $\text{Li}_x\text{FePO}_4$  materials is analyzed by inductively coupled plasma-optical emission spectroscopy (ICP-OES). The following atomic ratios are found:  $\text{Li}_{1.00}\text{FePO}_4$ ,  $\text{Li}_{0.74}\text{FePO}_4$ ,  $\text{Li}_{0.38}\text{FePO}_4$ , and  $\text{Li}_{0.11}\text{FePO}_4$ . The “completely delithiated” material does contain residual  $\text{Li}^+$  ions even though the amount of bromine used in the extraction is several times greater than the amount needed to fully delithiate the sample. This is probably due to the slow diffusion of  $\text{Li}^+$  ions across the  $\text{LiFePO}_4$ -

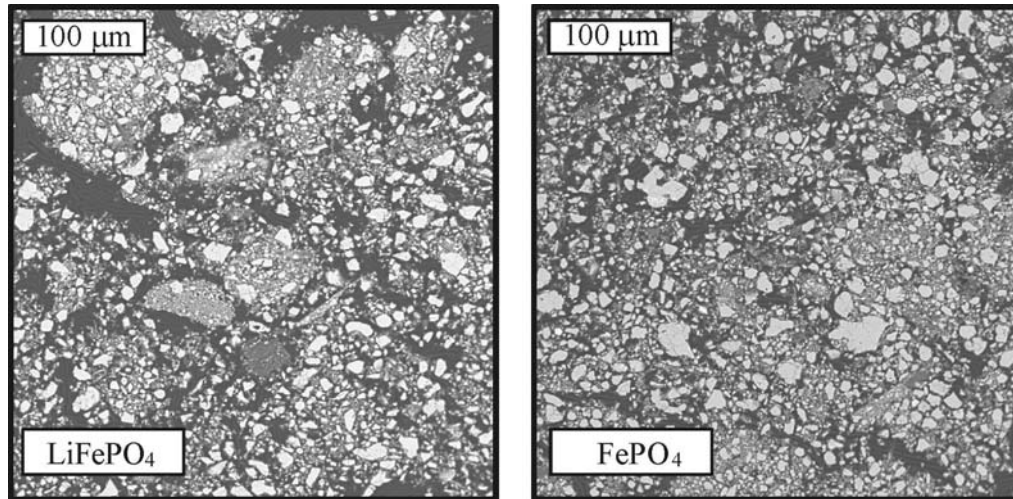


**Figure 2-13:** Electron microprobe images of  $\text{LiFePO}_4$  and  $\text{FePO}_4$  at 200x magnification.

$\text{FePO}_4$  interface [1]. For brevity, the  $\text{Li}_{0.11}\text{FePO}_4$  material will be referred to as  $\text{FePO}_4$ .

Sample heterogeneity is measured by comparing the iron and phosphorous contents in a number of the particles with wavelength dispersive spectrometry using an electron microprobe. Furthermore, the imaging capabilities of the electron microprobe are used to analyze the particle sizes and morphology of the  $\text{Li}_x\text{FePO}_4$  samples. Fig. 2-13 shows  $395 \mu\text{m} \times 395 \mu\text{m}$  images of the  $\text{LiFePO}_4$  and  $\text{FePO}_4$  samples. There are three distinct size domains in the sample: large grains, fine grains (light gray), and the epoxy in which the grains are impregnated (gray-black background). The larger particles are approximately  $10\text{-}20 \mu\text{m}$  in diameter and the fine intergranular particles are about  $1 \mu\text{m}$  in diameter. Magnification of the regions consisting of mostly the fine-grain material reveals that it is composed of distinct particles. The fine intergranular material is predominantly dispersed throughout the entire sample, but regions may be identified where the finer particles are in abundance. The size of the larger particles observed with



the electron microprobe agree very well with particle size distribution measurements for  $\text{LiFePO}_4$  prepared at 800 °C by Yamada *et al.* [4].

The observation of two different particle sizes in the sample is confirmed by examining  $\text{LiFePO}_4$  with an optical microscope. Estimates of the larger particles' diameters agree with the measurements from the electron microprobe. Moreover, the fine intergranular material is found, demonstrating that it is not a byproduct of the electron microprobe sample preparation. However, it is possible that the sample preparation does disintegrate some of the larger particles, which would enhance the amount of the fine intergranular material found by the electron microprobe. Because the two different particle sizes appear in all the  $\text{Li}_x\text{FePO}_4$  samples, including the as-synthesized  $\text{LiFePO}_4$ , it is unlikely that this results from the delithiation treatment.

The Fe/P ratio is calculated to determine if either of the two different particle sizes can be ascribed as an impurity, such as  $\text{Li}_3\text{PO}_4$  or  $\text{Fe}_2\text{O}_3$ . These values are presented in Table II-IV. It is not possible to isolate a large enough agglomeration of fine grain particles in all the samples to obtain a reasonable estimate of the Fe/P ratio, because the majority of the smaller particles are dispersed around the larger particles. The Fe/P ratio is found to be relatively constant as lithium is removed from the larger particles, further supporting the notion that delithiation does not significantly affect the iron or phosphorous amounts in the samples. Moreover, within a particular  $\text{Li}_x\text{FePO}_4$  sample,

**Table II-IV:** The calculated Fe/P ratios for  $\text{Li}_x\text{FePO}_4$  materials

|                      | $\text{LiFePO}_4$ | $\text{Li}_{0.74}\text{FePO}_4$ | $\text{Li}_{0.38}\text{FePO}_4$ | $\text{FePO}_4$ |
|----------------------|-------------------|---------------------------------|---------------------------------|-----------------|
| Large Particles      | 1.816             | 1.794                           | 1.752                           | 1.845           |
| Fine-Grain Particles | 1.818             | ---                             | 1.670                           | ---             |

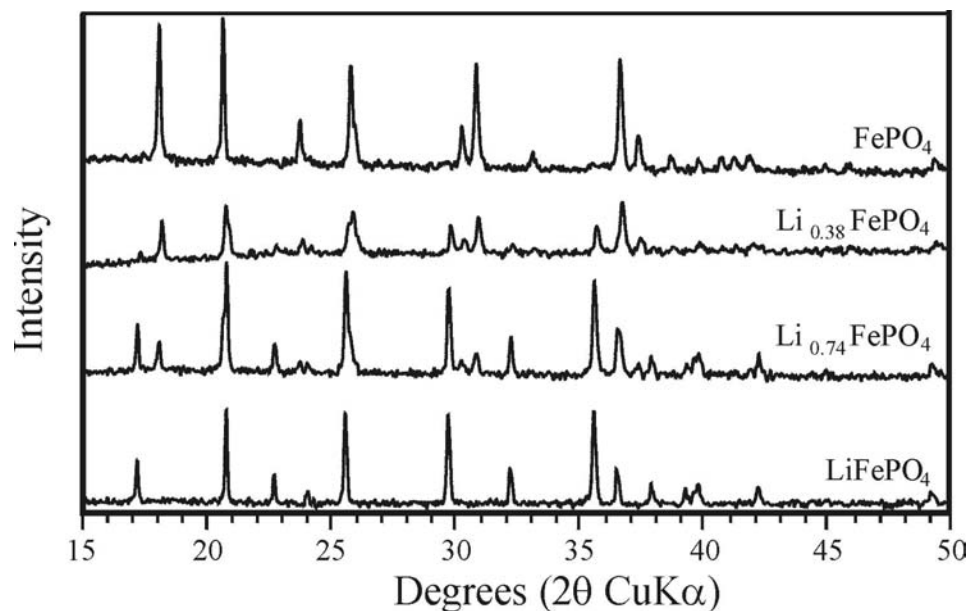


**Figure 2-14:** Powder XRD diffractograms of  $\text{Li}_x\text{FePO}_4$ .

the Fe/P ratio of a region that consists predominantly of the larger particles is similar to the ratio for a region that is mostly composed of the fine intergranular particles. This argues that both the large and fine particles are the same material, rather than one of them present as an impurity. However, the ratio does appear to depend slightly on the lithium concentration. This observation must be qualified because of the limited amount of data available. Unfortunately, the lithium content of the two different sizes cannot be determined, although it is reasonable to expect that the residual  $\text{Li}^+$  ions detected by ion chromatography reside in the core of the particles.

Powder XRD data of the four  $\text{Li}_x\text{FePO}_4$  materials are provided in Fig. 2-14. The diffractograms agree very well with the results of a chemical delithiation study of  $\text{LiFePO}_4$  by Padhi *et al.* [1], and two-phase behavior is clearly observed as  $\text{Li}^+$  ions are extracted from the sample. The end members of the series may be identified as the triphylite and heterosite phases, and the two middle diffractograms show mixtures of

these two phases. There is no XRD evidence of residual  $\text{LiFePO}_4$  in the fully delithiated phase even though the ion chromatography experiment reveals a small amount of lithium. The crystallite sizes of  $\text{Li}_x\text{FePO}_4$  are approximated using the Scherrer formula and values of 67 to 90 nm are obtained. These estimates are much smaller than the measurements obtained with the electron microprobe or the results of Yamada *et al.* [4]. It is well known that large particles are often agglomerations of much smaller particles. Thus, the particles observed with the electron microprobe are probably composed of crystallites ranging from 60 to 80 nm in size, as determined from the XRD data. It is also possible that the ferrous species in the sample would fluoresce with the  $\text{Cu K}\alpha$  radiation [73]. The higher backgrounds would prevent an accurate measurement of the full width at half the peaks intensity, thus giving slightly lower estimates of the crystallite sizes.

The lithium extraction mechanism is a topotactic process [1,11]; thus, any observed changes between the vibrational spectra of  $\text{LiFePO}_4$  and  $\text{FePO}_4$  are due solely to the presence of  $\text{Li}^+$  ions, rather than a change of the space group and the corresponding selection rules. Infrared and Raman spectra are shown in Figs. 2-15 and 2-16, respectively, to illustrate the effect of lithium extraction on  $\nu_1$  and  $\nu_3$ . In this spectral region, the infrared active bands are broad, overlapping features with some structure, whereas the Raman active bands are relatively narrow and well resolved. As lithium is extracted, the  $\nu_1$  and  $\nu_3$  bands appear to move apart in the infrared spectrum. In the  $\text{PO}_4^{3-}$  antisymmetric stretching region of  $\text{LiFePO}_4$ , the sharp but weak band at  $1096\text{ cm}^{-1}$  becomes the dominant band in  $\text{Li}_{0.74}\text{FePO}_4$  while the dominant band at  $1046\text{ cm}^{-1}$  in  $\text{LiFePO}_4$  becomes a weak shoulder in  $\text{Li}_{0.74}\text{FePO}_4$ . In  $\text{FePO}_4$ , the band maximum now occurs at  $1082\text{ cm}^{-1}$  with a broad, indistinct high frequency shoulder. The  $\text{PO}_4^{3-}$

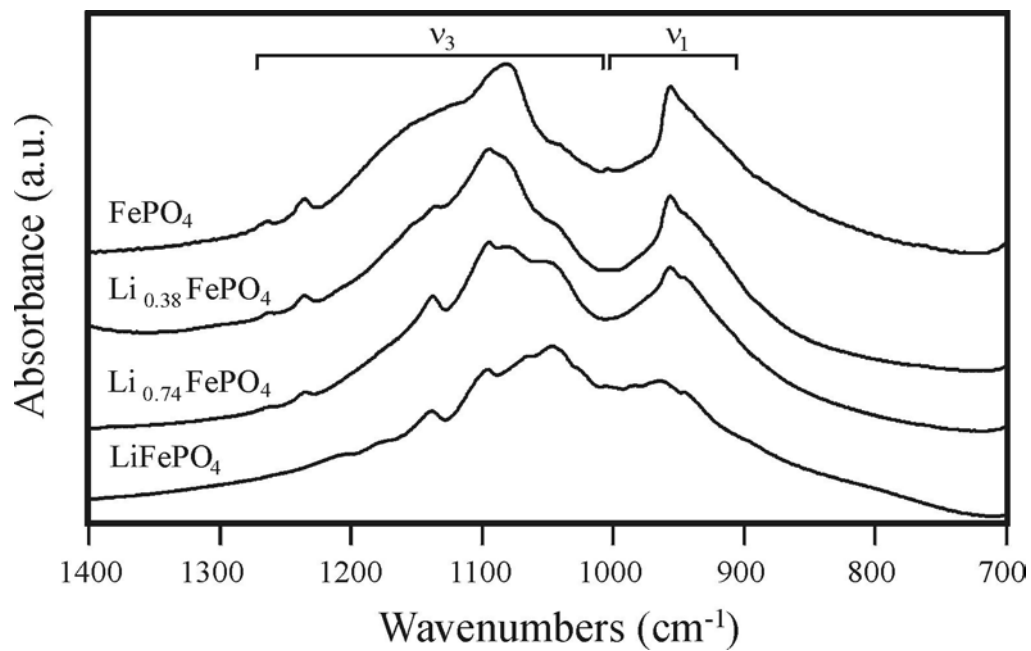


**Figure 2-15:** Infrared absorption spectra of  $\nu_1$  and  $\nu_3$  for  $\text{Li}_x\text{FePO}_4$ .

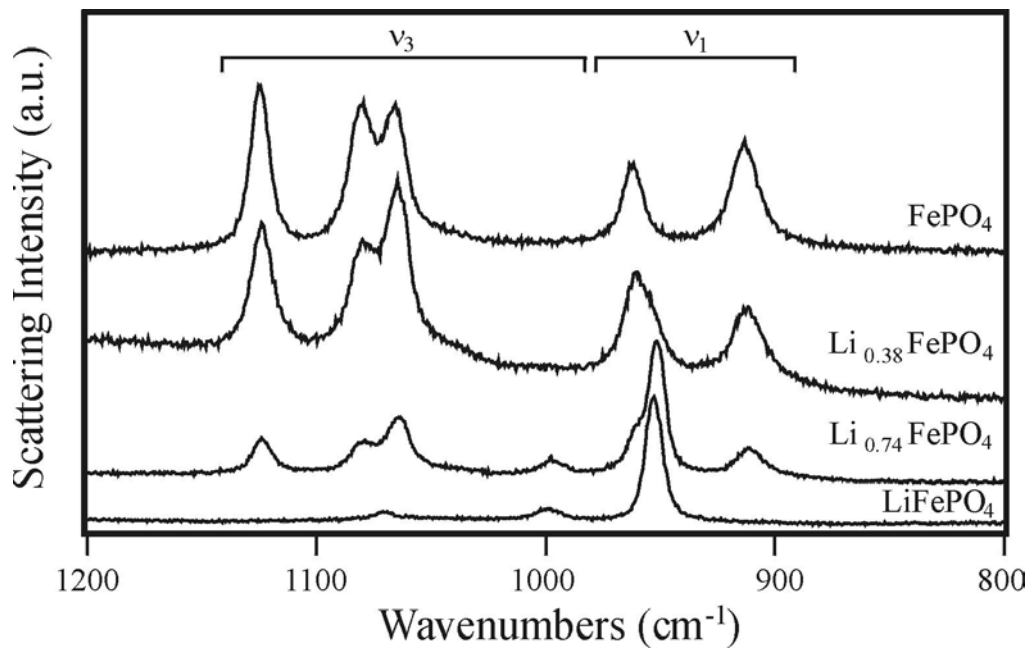
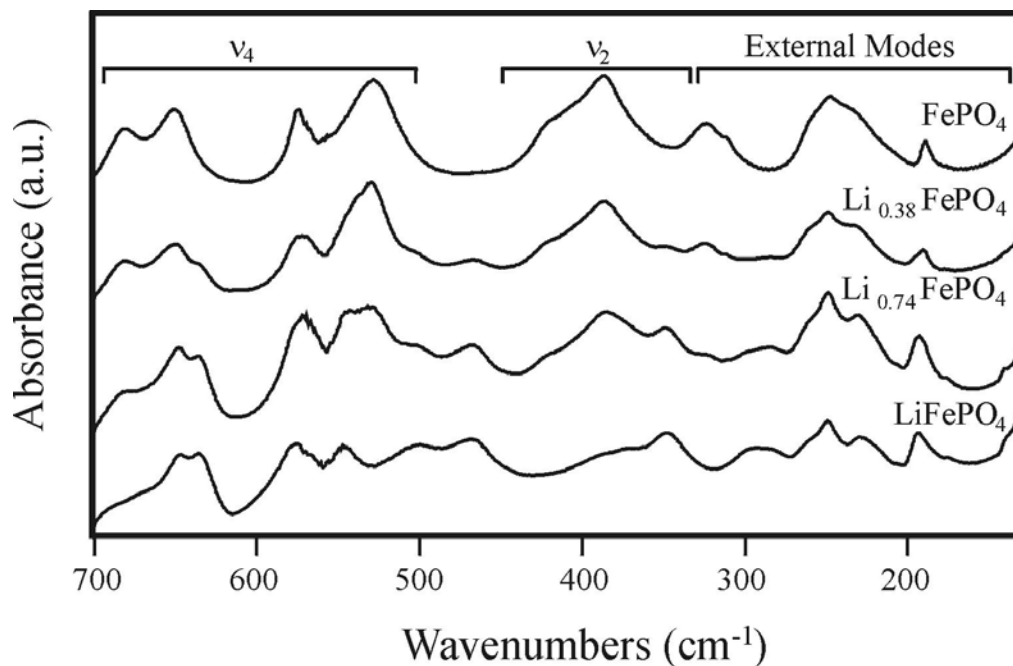


**Figure 2-16:** Raman scattering spectra of  $\nu_1$  and  $\nu_3$  for  $\text{Li}_x\text{FePO}_4$ .

symmetric stretching band in  $\text{LiFePO}_4$  at  $963\text{ cm}^{-1}$  appears at  $956\text{ cm}^{-1}$  in  $\text{FePO}_4$ .

In the Raman spectra of  $\text{Li}_x\text{FePO}_4$ , the  $\nu_1$  and  $\nu_3$  modes also appear to slightly separate as the  $\text{Li}^+$  ion concentration is decreased, which agrees with the infrared spectroscopic data. The most notable feature of the Raman spectra is the appearance of several bands in  $\text{FePO}_4$  that are not found in  $\text{LiFePO}_4$ . In particular, two new bands in the range of  $1050\text{-}1150\text{ cm}^{-1}$  appear and one band dramatically increases in intensity as lithium is extracted; these are assigned to the  $\nu_3$  antisymmetric stretching modes of the  $\text{PO}_4^{3-}$  anion in  $\text{FePO}_4$ . With the removal of about 25% of the lithium, new bands appear at  $1124$  and  $911\text{ cm}^{-1}$ . The band at  $1071\text{ cm}^{-1}$  is split into two components at  $1080$  and  $1064\text{ cm}^{-1}$ , and a shoulder is visible on the high frequency side of the intense  $\nu_1$  band. The  $911\text{ cm}^{-1}$  band continues to increase in intensity with lithium extraction. The spectrum with about 60% of the lithium removed is quite similar to the previous spectrum, except the intense  $\nu_3$  band is now a low frequency shoulder to the band at  $962\text{ cm}^{-1}$  and the  $\nu_3$  band at  $999\text{ cm}^{-1}$  is absent. The spectrum of the almost fully delithiated sample closely resembles that of the 60% delithiated sample, except for relative intensities changes in a few bands.

A factor group analysis of  $\text{FePO}_4$  (space group  $Pnma$ ) predicts  $\nu_1$  will yield two Raman-active vibrations ( $A_g + B_{2g}$ ) at the Brillouin zone center. The  $A_g$  mode of  $\text{LiFePO}_4$  is seen to shift to  $962\text{ cm}^{-1}$  in  $\text{FePO}_4$ . Additionally, a new band appears at  $911\text{ cm}^{-1}$  that is not present in  $\text{LiFePO}_4$ . Based on the similarity of frequency for the  $A_g$  mode in  $\text{LiFePO}_4$  and the  $962\text{ cm}^{-1}$  band, the bands at  $962$  and  $912\text{ cm}^{-1}$  in  $\text{FePO}_4$  are assigned to the  $A_g$  and  $B_{2g}$  modes of  $\nu_1$ , respectively.



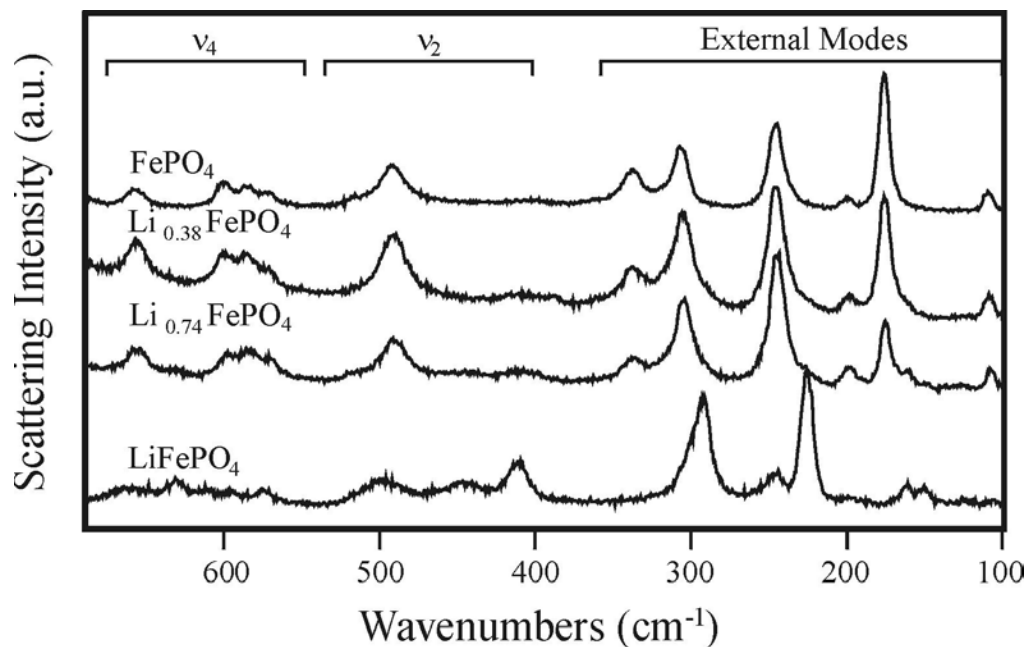
**Figure 2-17:** Infrared absorption spectra of  $\nu_4$ ,  $\nu_2$ , and the external modes for  $\text{Li}_x\text{FePO}_4$ .

Fig. 2-17 shows the infrared spectrum from 700 to 150  $\text{cm}^{-1}$  of the  $\text{Li}_x\text{FePO}_4$  samples. A factor group analysis of  $\text{LiFePO}_4$  predicts three and five infrared active modes for  $\nu_2$  and  $\nu_4$ , respectively [61]. Four of the  $\nu_4$  bands are clearly observed between 700 and  $\sim 525 \text{ cm}^{-1}$  while the  $\nu_2$  bands are thought to predominantly occur between 400 and  $350 \text{ cm}^{-1}$ . In the spectrum of  $\text{LiFePO}_4$ , there is a strong band at  $636 \text{ cm}^{-1}$  and a somewhat weaker band at  $647 \text{ cm}^{-1}$  with a high frequency shoulder. In  $\text{Li}_{0.74}\text{FePO}_4$ , the intensities are reversed, and a weak band appears at  $682 \text{ cm}^{-1}$ . The intensity of the two bands at  $647$  and  $682 \text{ cm}^{-1}$  continue to grow with decreasing  $\text{Li}^+$  ion concentration. The  $\nu_4$  region of  $\text{LiFePO}_4$  consists of a doublet at  $576$  and  $546 \text{ cm}^{-1}$ , whereas in  $\text{Li}_{0.74}\text{FePO}_4$  a third band appears at  $530 \text{ cm}^{-1}$ . The intensity of this third feature dramatically increases in  $\text{Li}_{0.38}\text{FePO}_4$  and becomes dominant in  $\text{FePO}_4$  while the band at  $546 \text{ cm}^{-1}$  essentially

vanishes. As expected, the lithium cage modes at 500 and 469  $\text{cm}^{-1}$  in the spectrum of  $\text{LiFePO}_4$  decrease in intensity with decreasing lithium concentration until they vanish in  $\text{FePO}_4$ .

Bands consisting mostly of  $\nu_2$ -type motion and the external modes are also affected by the extraction of lithium ions. In  $\text{LiFePO}_4$ , there is a band at 348  $\text{cm}^{-1}$  and a broad high frequency shoulder. As lithium is extracted from the sample, the intensity of the 348  $\text{cm}^{-1}$  band decreases as a band appears at 387  $\text{cm}^{-1}$ . In  $\text{FePO}_4$ , the 387  $\text{cm}^{-1}$  band dominates the region with a high frequency shoulder, and the 348  $\text{cm}^{-1}$  band is not found. A small band near 291  $\text{cm}^{-1}$  in  $\text{LiFePO}_4$  decreases in intensity with lithium extraction until it disappears in the  $\text{FePO}_4$  sample. Furthermore, two bands concurrently appear at 324 and 312  $\text{cm}^{-1}$  as  $\text{Li}^+$  ions are removed, and the 229  $\text{cm}^{-1}$  band in  $\text{LiFePO}_4$  becomes a low frequency shoulder on the band at 249  $\text{cm}^{-1}$  in  $\text{FePO}_4$ . The majority of the bands below 250  $\text{cm}^{-1}$  do not appear to be greatly affected by lithium extraction.

Raman spectra of  $\text{Li}_x\text{FePO}_4$  are reported in Fig. 2-18 for the lower frequency region. In contrast to Fig. 2-16, many of the bands belonging to  $\nu_2$  and  $\nu_4$  in the Raman spectrum of  $\text{LiFePO}_4$  appear to be weak and poorly resolved. Six weak bands found between 800 and 550  $\text{cm}^{-1}$  are assigned to mostly  $\nu_4$  vibrations with some contribution from  $\nu_2$ . Three bands at 410, 447, and 499  $\text{cm}^{-1}$  along with a high frequency shoulder to the 499  $\text{cm}^{-1}$  band are probably the four Raman active vibrations of  $\nu_2$ . As in the infrared spectrum, no assignment will be attempted for the lower-frequency Raman bands. The  $\text{LiFePO}_4$   $\nu_4$  bands (viz., 631, 610, and 582  $\text{cm}^{-1}$ ) lose intensity with progressive delithiation. At the same time, bands at 695 (not shown), 657, 599, 585, and 582  $\text{cm}^{-1}$  increase in intensity. The three bands in  $\text{LiFePO}_4$  that belong predominantly to  $\nu_2$  are



**Figure 2-18:** Raman scattering spectra of  $\nu_4$ ,  $\nu_2$ , and the external modes for  $\text{Li}_x\text{FePO}_4$ .

seen to decrease in intensity as a band at  $492\text{ cm}^{-1}$  appears in the  $\text{Li}_{0.74}\text{FePO}_4$  sample. The intensity of this band continues to increase until it is the dominant band in  $\text{Li}_{0.38}\text{FePO}_4$  and  $\text{FePO}_4$ . Very weak bands are found in the Raman spectrum of  $\text{FePO}_4$  at  $516$  and  $406\text{ cm}^{-1}$  that are possibly the components of  $\nu_2$  in  $\text{FePO}_4$  or are remnants of  $\text{LiFePO}_4$ .

Numerous changes are found in the Raman bands of the lattice modes. The  $292\text{ cm}^{-1}$  band is one of the dominant features of  $\text{LiFePO}_4$ , however it is non-existent in the  $\text{Li}_{0.74}\text{FePO}_4$  material. Instead, two bands appear at slightly higher frequencies. A similar trend is observed for the other dominant  $\text{LiFePO}_4$  band at  $225\text{ cm}^{-1}$ . The removal of about 25% of the lithium is sufficient to cause this band to essentially vanish and significantly enhance the intensity of the  $245\text{ cm}^{-1}$  feature. In  $\text{LiFePO}_4$ , only two very weak bands are resolved below  $200\text{ cm}^{-1}$ , but a strong band appears in the delithiated



samples at  $176\text{ cm}^{-1}$ . Further delithiation of the  $\text{Li}_{0.74}\text{FePO}_4$  sample produces changes in the relative intensities of the bands in this region, but the frequencies remain unaltered.

Both the infrared and Raman spectra of the internal modes of the  $\text{PO}_4^{3-}$  anion undergo numerous changes as lithium is extracted. To understand why the internal modes of the  $\text{PO}_4^{3-}$  anion are so sensitive to  $\text{Li}^+$  ions, it is necessary to consider how these groups are structurally related to the lithium and iron ions [1,2]. The crystal structure of  $\text{FePO}_4$  is very similar to the  $\text{LiFePO}_4$  compound [1,11]. Both compounds belong to the *Pnma* space group and have nearly identical P–O bond lengths; however, the average Fe–O bond length contracts from  $2.17\text{ \AA}$  in  $\text{LiFePO}_4$  to  $2.04\text{ \AA}$  in  $\text{FePO}_4$ . The oxygen atoms that define the lithium and iron octahedral units in  $\text{LiFePO}_4$  are covalently bonded to phosphorous atoms, forming the distorted tetrahedral  $\text{PO}_4^{3-}$  groups. Consequently, the local environment of a  $\text{Li}^+$  ion may be viewed as being surrounded by four  $\text{PO}_4^{3-}$  anions. The vibrational potential energy of the  $\text{PO}_4^{3-}$  anions is affected by the lithium and iron ions. When  $\text{Li}^+$  ions are extracted, the iron ions necessarily increase their oxidation state to  $\text{Fe}^{3+}$ . Together, the removal of the  $\text{Li}^+$  ions and the increase in the oxidation state of the ferrous ion would significantly change the vibrational potential energy of the  $\text{PO}_4^{3-}$  groups. This would produce marked changes in both the Raman and IR band intensities and frequencies of the  $\text{PO}_4^{3-}$  groups, which are dependent on the lithium content.

A comparison of the Raman and infrared spectra of pure  $\text{LiFePO}_4$  to  $\text{FePO}_4$  (see Figs. 2-15 through 2-18) reveals distinct changes in several band frequencies and intensities that occur through a redistribution of electron density in the P–O bonds in

response to the removal of lithium. This redistribution produces differences in the effective force constants (frequencies), polarizability derivatives (Raman intensities), and dipole moment derivatives (infrared intensities) of  $\text{FePO}_4$  compared to  $\text{LiFePO}_4$ . For example, Fig. 2-19 compares the  $\nu_4$  bands of  $\text{FePO}_4$ ,  $\text{LiFePO}_4$ , and  $\text{NaFePO}_4$ . The splitting of the  $\nu_4$  components of  $\text{FePO}_4$  ( $149 \text{ cm}^{-1}$ ) is considerably larger than the splitting of  $\nu_4$  for  $\text{LiFePO}_4$  ( $98 \text{ cm}^{-1}$ ) or  $\text{NaFePO}_4$  ( $82 \text{ cm}^{-1}$ ). However, it is smaller than what would be predicted from the ionization potential of the  $\text{Fe}^{3+}$  ions and equation 2-1 ( $211 \text{ cm}^{-1}$ ). This disparity is possibly due to the greater covalency of the Fe–O bonds in  $\text{FePO}_4$  [74] and the lack of monovalent cations on the 4(a) sites in the unit cell of  $\text{FePO}_4$ .

Generally speaking, the spectroscopic data (Figs. 2-15 through 2-18) taken together reveal only gradual changes in the infrared band intensities as lithium is

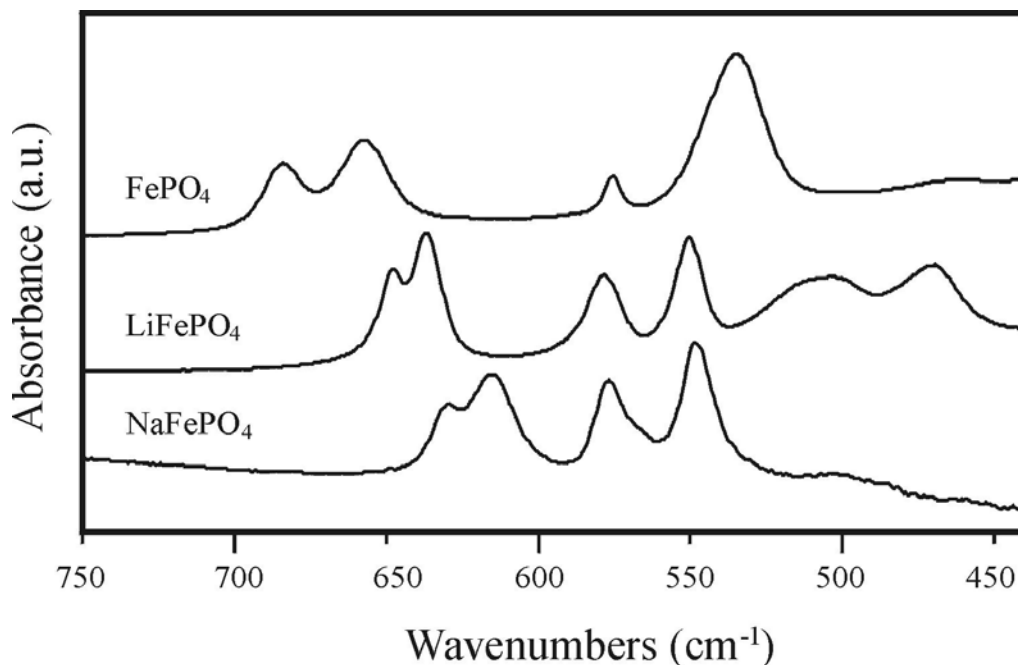


**Figure 2-19:** Infrared absorption spectra of  $\nu_4$  and the  $\text{Li}^+$  ion cage modes for  $\text{LiFePO}_4$ ,  $\text{NaFePO}_4$ , and  $\text{FePO}_4$ .

extracted, while the Raman bands undergo dramatic changes in the first delithiation step ( $\text{LiFePO}_4$  to  $\text{Li}_{0.74}\text{FePO}_4$ ). The difference between the infrared and Raman spectral intensities at the same degree of delithiation, specifically the difference in the relative amounts of  $\text{LiFePO}_4$  and  $\text{FePO}_4$  seen by the same technique, can be understood by considering the optical skin effect of the  $\text{Li}_x\text{FePO}_4$  particles. Electromagnetic radiation is exponentially attenuated as it passes through an absorbing sample, and the effective penetration depth of the wave is proportional to the wavelength of the light and the optical constants of the sample [75]. Although the optical constants of  $\text{LiFePO}_4$  and  $\text{FePO}_4$  are not known at the frequency of the excitation laser, the dark color of the  $\text{Li}_x\text{FePO}_4$  particles must be due to low-lying electronic absorptions in the visible region of the spectrum. The wavelength of the Raman excitation laser is 532 nm or 0.532  $\mu\text{m}$ , and a typical penetration depth is in the range of one-fourth to one-half the wavelength of the light. Thus, the Raman laser beam experiences a very significant skin effect and penetrates only a fraction of a micron into the  $\text{Li}_x\text{FePO}_4$  particles. By contrast, the infrared beam passes completely through the particles in most of the infrared region and is significantly attenuated only in the center of the strongest absorption bands.

A number of workers have shown that the delithiation of  $\text{LiFePO}_4$  to  $\text{FePO}_4$  proceeds by a shrinking-core mechanism [1,12,13,76]. That is, the surface of the  $\text{LiFePO}_4$  particles becomes encased with a thin shell of lithium deficient  $\text{FePO}_4$  when the sample is charged, and progressive delithiation causes the shell to grow inward via a two-phase reaction until the  $\text{LiFePO}_4$  core is consumed. The infrared spectroscopic measurements show a gradual decrease in the intensities of the  $\text{LiFePO}_4$  bands and a gradual increase in the intensities of the  $\text{FePO}_4$  bands because the infrared beam is

sampling the entire particle. In contrast, more dramatic changes are observed in the Raman spectra in the early stages of delithiation because the excitation beam primarily sees the thin FePO<sub>4</sub> shell, due to the skin effect.

If the delithiation process occurred by a single-phase pathway, then the bands in the infrared and Raman spectra should gradually shift in frequency as lithium is extracted. This type of behavior is not evident in the spectra. Instead, spectra at intermediate lithium concentrations appear to be a superposition of the spectra of pure LiFePO<sub>4</sub> and pure FePO<sub>4</sub> with the relative intensities of each component governed by the extent of delithiation at the effective penetration depth of the sampling beam. This observation supports the two-phase delithiation process originally proposed by Padhi *et al.* [1] and confirms the ability of vibrational spectroscopic techniques to discriminate between a single-phase transition and a two-phase transition in phosphate-based electrode materials. The most dramatic example of this is seen in the Raman spectra of Fig. 2-16. In Li<sub>0.38</sub>FePO<sub>4</sub> and Li<sub>0.74</sub>FePO<sub>4</sub>, bands belonging to  $\nu_1$  and  $\nu_3$  of FePO<sub>4</sub> may be identified along with the analogous LiFePO<sub>4</sub> bands. As lithium is extracted, the LiFePO<sub>4</sub> bands decrease in intensity while the FePO<sub>4</sub> bands increase in intensity, yet the frequencies of the bands do not appear to depend on the lithium content. Similar features may be observed in the infrared spectra, however they are not as obvious as the Raman spectra.

#### 2.3.4 $Li_x(Mn_yFe_{1-y})PO_4$ ( $0 \leq x, y \leq 1$ ) Cathodes

Raman spectroscopic measurements of Li(Mn<sub>0.5</sub>Fe<sub>0.5</sub>)PO<sub>4</sub> are presented in Fig. 2-20. Two broad bands at approximately 1595 and 1342 cm<sup>-1</sup> dominate the spectrum.

These bands are due to a carbon coating on the surface of the particles. Hexagonal graphite crystallizes in the  $P6_3/mmc$  ( $D_{6h}^4$ ) space group [77]. At the Brillouin zone center, the vibrational modes of crystalline graphite are distributed among the following irreducible representations of the  $D_{6h}$  point group:

$$\Gamma = A_{2u} + 2B_{2g} + E_{1u} + 2E_{2g}$$

Only the two  $E_{2g}$  modes are Raman-active in first-order scattering experiments [77].

These vibrational modes correspond to the in-plane motion of the carbon atoms and have been observed at 42 and 1581 ( $G$  band)  $\text{cm}^{-1}$  [78]. Several researchers have reported additional bands in the Raman spectrum of microcrystalline graphite between 1318 to 1355  $\text{cm}^{-1}$  ( $D$  band) and at 1623  $\text{cm}^{-1}$  ( $D'$  band) [77-80]. These bands are thought to be non-zero-center phonons that arise from the crystal boundary regions of microcrystalline

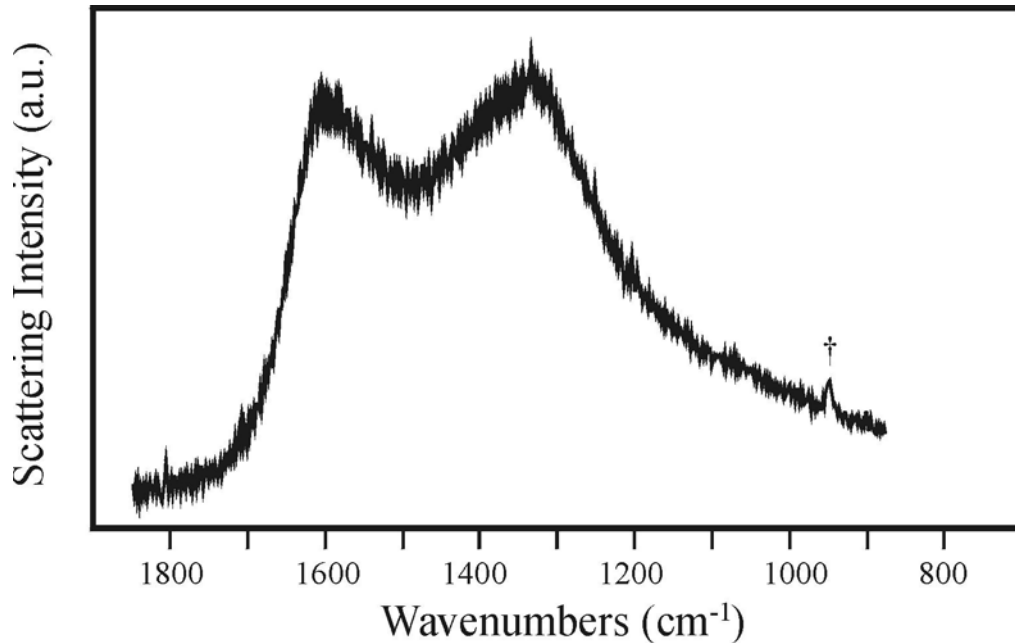


**Figure 2-20:** Raman scattering spectrum of carbon-coated  $\text{Li}(\text{Mn}_{0.5}\text{Fe}_{0.5})\text{PO}_4$ .

The dagger ( $\dagger$ ) denotes the  $\nu_1(A_g)$  mode.

graphite. Tuinstra and Koenig [77] and Nikiel and Jagodzinski [80] have shown that the integrated intensity ratio of the G and D bands is inversely proportional to the intraplane crystallite size,  $L_a$ , in polycrystalline graphite. The linewidths of the G, D, and D' bands are also somewhat dependant on  $L_a$  [80].

Doeff *et al.* characterized a series of carbon-coated  $\text{LiFePO}_4$  compounds with Raman spectroscopy and determined that the electrochemical discharge capacity of the materials strongly depends on the integrated intensity ratio of the D and G bands and the relative amount of  $\text{sp}^2$ - and  $\text{sp}^3$ -hybridized carbon [71]. Materials that had a low D/G ratio were predominantly composed of  $\text{sp}^2$ -type carbon and gave the best electrochemical performance. Wagner *et al.* [81] and Ramsteiner and Wagner [82] utilized resonance Raman spectroscopy to probe the relative abundance of  $\text{sp}^2$ - and  $\text{sp}^3$ -hybridized carbon in amorphous carbon and microcrystalline graphite. The resonance Raman technique is sensitive to the electronic  $\pi$ - $\pi^*$  transition that occurs between 3.5 and 6.5 eV for  $\text{sp}^2$ -bonded carbon atoms [81]. Although resonance Raman experiments were not performed on the  $\text{Li}(\text{Mn}_{0.5}\text{Fe}_{0.5})\text{PO}_4$  samples, the bands at 1595 and 1342  $\text{cm}^{-1}$  in Fig. 2-19 closely resemble the bands of carbon-coated  $\text{LiFePO}_4$  (sample 3A) from Doeff *et al.* [71] and the microcrystalline graphite, which is predominately  $\text{sp}^2$ -hybridized carbon, from Wagner *et al.* [81]. Therefore, it is reasonable to conclude that the  $\text{Li}(\text{Mn}_{0.5}\text{Fe}_{0.5})\text{PO}_4$  particles are coated with a thin layer of disordered graphite that is composed mostly of  $\text{sp}^2$ -coordinated carbon atoms.

Fig. 2-20 also contains a weak band at 948  $\text{cm}^{-1}$  that is assigned to  $\nu_1(\text{A}_g)$  mode for  $\text{Li}(\text{Mn}_{0.5}\text{Fe}_{0.5})\text{PO}_4$ . Although the intensity of the  $\nu_1$  band in  $\text{Li}(\text{Mn}_{0.5}\text{Fe}_{0.5})\text{PO}_4$  is

much weaker than the corresponding bands in other  $\text{LiMPO}_4$  ( $M = \text{Mn, Fe, Co, and Ni}$ ) systems, the frequencies are very similar (see [55,61] and Sec. 2.3.1). This suggests that the P-O bond lengths of  $\text{Li}(\text{Mn}_{0.5}\text{Fe}_{0.5})\text{PO}_4$  are similar to those in  $\text{LiFePO}_4$  and  $\text{LiMnPO}_4$  [72]. The relatively weak intensity of the band in  $\text{Li}(\text{Mn}_{0.5}\text{Fe}_{0.5})\text{PO}_4$  is probably due to the optical skin effect of the carbon-coated  $\text{Li}(\text{Mn}_{0.5}\text{Fe}_{0.5})\text{PO}_4$  particles [75]. In these experiments, the wavelength of the Raman excitation laser is 532 nm. Therefore, the Raman laser beam penetrates only a fraction of a micron into the particles, and the scattering volume predominantly contains the graphite surface layer and only a small amount of the  $\text{Li}(\text{Mn}_{0.5}\text{Fe}_{0.5})\text{PO}_4$  material.

Infrared spectra of the intramolecular stretching modes ( $\nu_1$  and  $\nu_3$ ) for  $\text{Li}(\text{Mn}_y\text{Fe}_{1-y})\text{PO}_4$  ( $0 \leq y \leq 1$ ) are presented in Fig. 2-21. The infrared spectrum of  $\text{Li}(\text{Mn}_{0.5}\text{Fe}_{0.5})\text{PO}_4$  is intermediate between  $\text{LiFePO}_4$  and  $\text{LiMnPO}_4$ , and two-mode

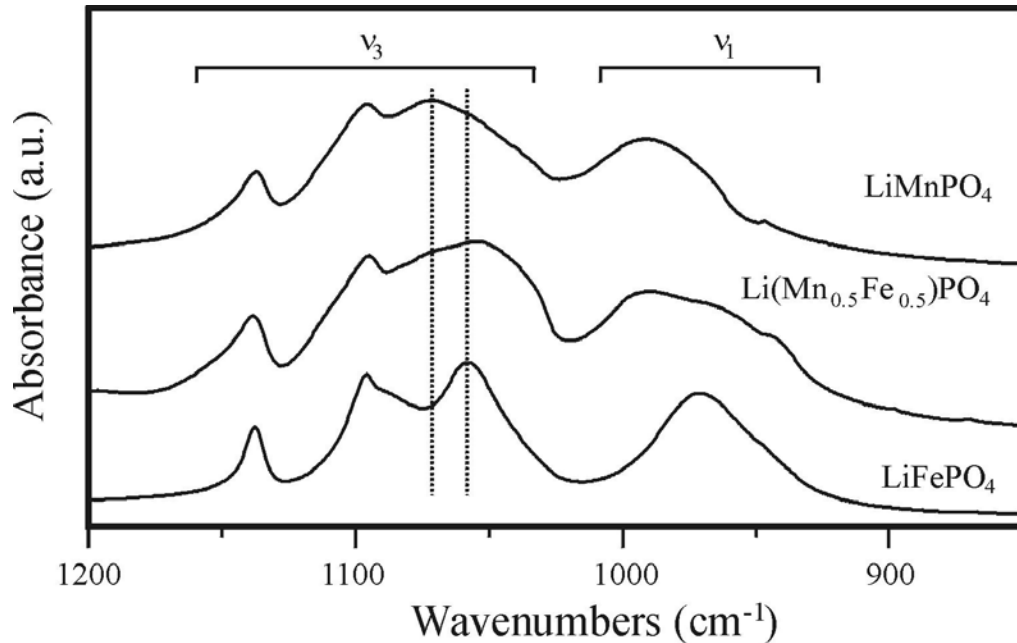


**Figure 2-21:** Infrared absorption spectra of  $\nu_1$  and  $\nu_3$  for  $\text{Li}(\text{Mn}_y\text{Fe}_{1-y})\text{PO}_4$  ( $y = 0, 0.5, 1$ ). The dashed lines denote the two-mode behavior in  $\nu_3$ .

behavior can be clearly identified in the  $\text{PO}_4^{3-}$  intramolecular stretching region. In two-mode behavior, the vibrational spectrum of an intermediate composition in a solid solution series is essentially a superposition of the spectra of the two end-members, and the intensities of the bands are governed by the composition of the material [83]. For example, there are two bands at 1067 and 1053  $\text{cm}^{-1}$  in the spectrum of  $\text{Li}(\text{Mn}_{0.5}\text{Fe}_{0.5})\text{PO}_4$  instead of a single band at the mean frequency of the respective  $\nu_3$  components. This type of behavior is characteristic of well-localized vibrations. Two-mode behavior may be contrasted with one-mode behavior where “a single band (more or less broadened) is observed throughout the series of solid solutions, at a frequency which is roughly a weighted average of the frequencies of the end-members” [83].

Fig. 2-22 contains infrared spectra of  $\text{Li}(\text{Mn}_y\text{Fe}_{1-y})\text{PO}_4$  between 700 and 450  $\text{cm}^{-1}$ . Four bands ranging in frequency from 550 to 650  $\text{cm}^{-1}$  are assigned to antisymmetric  $\text{PO}_4^{3-}$  bending vibrations ( $\nu_4$ ). The bands near 500 and 465  $\text{cm}^{-1}$  are assigned to  $\text{Li}^+$  ion “cage modes” [61]. Unlike the stretching modes in Fig. 2-21, the lithium cage modes and  $\nu_4$  do not exhibit two-mode behavior throughout the  $\text{Li}(\text{Mn}_y\text{Fe}_{1-y})\text{PO}_4$  solid-solution series. Instead, the frequencies of these bands depend on the concentration of the  $\text{Fe}^{2+}$  ions. For instance, the two bands at 648 and 637  $\text{cm}^{-1}$  in the spectrum of  $\text{LiFePO}_4$  grow together and shift to lower frequencies as the  $\text{Mn}^{2+}$  concentration is increased. Although none of the phosphate vibrations consist purely of phosphorous and oxygen motion, the  $\text{PO}_4^{3-}$  bending modes generally contain more  $\text{M}^{2+}$  ( $\text{M} = \text{Fe}$  or  $\text{Mn}$ ) and  $\text{Li}^+$  motion than the stretching modes. Therefore,  $\nu_1$  and  $\nu_3$  are more localized than  $\nu_4$  and the  $\text{Li}^+$  cage modes and exhibit two-mode behavior while the lower frequency modes do not [83].



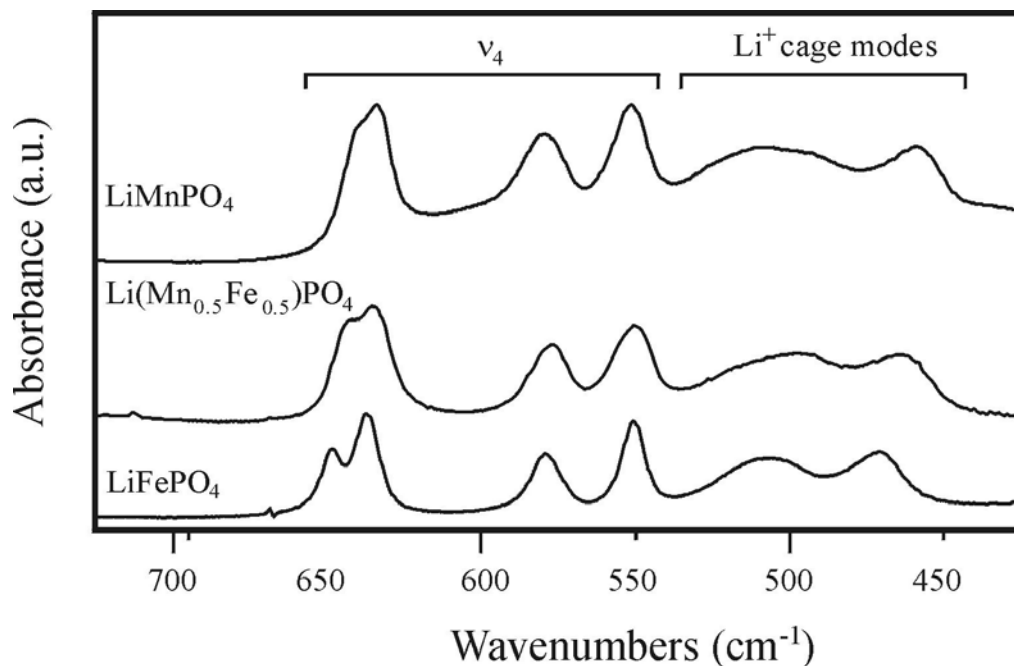


**Figure 2-22:** Infrared absorption spectra of  $\nu_4$  and the  $\text{Li}^+$  ion cage modes for  $\text{Li}(\text{Mn}_y\text{Fe}_{1-y})\text{PO}_4$  ( $y = 0, 0.5, 1$ ). The arrows denote the  $\text{Li}^+$  ion cage modes.

Fig. 2-23 contains a CV scan of the  $\text{Li}(\text{Mn}_{0.5}\text{Fe}_{0.5})\text{PO}_4$  cells. On the anodic sweep, two peaks appear at 3.70 and 4.20 V that correspond to the  $\text{Fe}^{2+}/\text{Fe}^{3+}$  and  $\text{Mn}^{2+}/\text{Mn}^{3+}$  redox couples, respectively [1]. The slight increase in current between 4.50 and 4.60 is likely due to electrolyte decomposition. Cells typically delivered capacities of 135 mAh/g. For simplicity, samples charged to 4.60 V are referred to as  $(\text{Mn}_{0.5}\text{Fe}_{0.5})\text{PO}_4$  even though there are residual  $\text{Li}^+$  ions in the particles. During the cathodic sweep, the  $\text{Mn}^{3+}$  cations were reduced to  $\text{Mn}^{2+}$  at 3.80 V. This is followed by the reduction of  $\text{Fe}^{3+}$  to  $\text{Fe}^{2+}$  at 3.30 V [1].

Infrared absorption spectra of  $\nu_1$  and  $\nu_3$  for  $\text{Li}_x(\text{Mn}_{0.5}\text{Fe}_{0.5})\text{PO}_4$  cathodes and  $\text{FePO}_4$  are presented in Fig. 2-24. Only minor spectral changes occur when  $\text{Fe}^{2+}$  is oxidized to  $\text{Fe}^{3+}$  (the initial OCV to 3.95 V) in the  $\text{Li}_x(\text{Mn}_{0.5}\text{Fe}_{0.5})\text{PO}_4$  cathodes. For

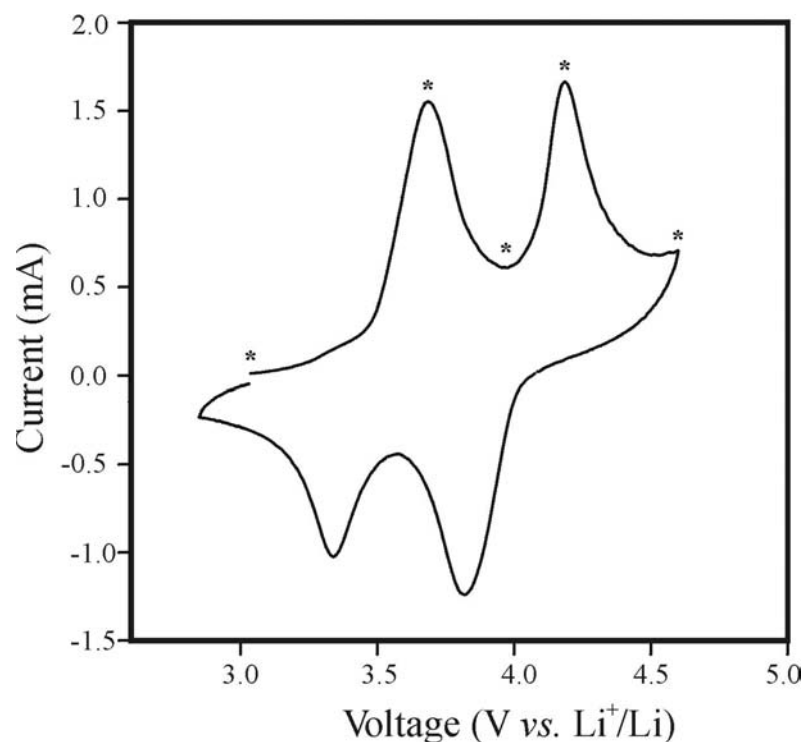


**Figure 2-23:** Cyclic voltammogram of Li(Mn<sub>0.5</sub>Fe<sub>0.5</sub>)PO<sub>4</sub> between 2.85 and 4.6 V (0.5 mV/sec). The asterisks (\*) denote points where cells were disassembled for spectroscopic measurements of the cathode material.

example, a high frequency shoulder appears on the 1137 cm<sup>-1</sup> band. However, the  $\nu_1$  and  $\nu_3$  modes undergo dramatic changes during the Mn<sup>2+</sup>/Mn<sup>3+</sup> redox couple (3.95 to 4.60 V). For instance, the two bands at 1076 and 1040 cm<sup>-1</sup> replace the asymmetric band near 1060 cm<sup>-1</sup>, while the three bands at 989, 968, and 944 cm<sup>-1</sup> collapse into two bands at 972 and 929 cm<sup>-1</sup>. There are several differences in the vibrational spectrum of (Mn<sub>0.5</sub>Fe<sub>0.5</sub>)PO<sub>4</sub> and FePO<sub>4</sub>. The most intense  $\nu_3$  mode of (Mn<sub>0.5</sub>Fe<sub>0.5</sub>)PO<sub>4</sub> is at 1076 cm<sup>-1</sup>, whereas the band is centered at 1099 cm<sup>-1</sup> in the spectrum of FePO<sub>4</sub>. The bandwidths of  $\nu_1$  and  $\nu_3$  are also dependant on the lithium concentration over the Mn<sup>2+</sup>/Mn<sup>3+</sup> redox couple. Indeed, the (Mn<sub>0.5</sub>Fe<sub>0.5</sub>)PO<sub>4</sub> bands are much broader than the corresponding FePO<sub>4</sub> bands.

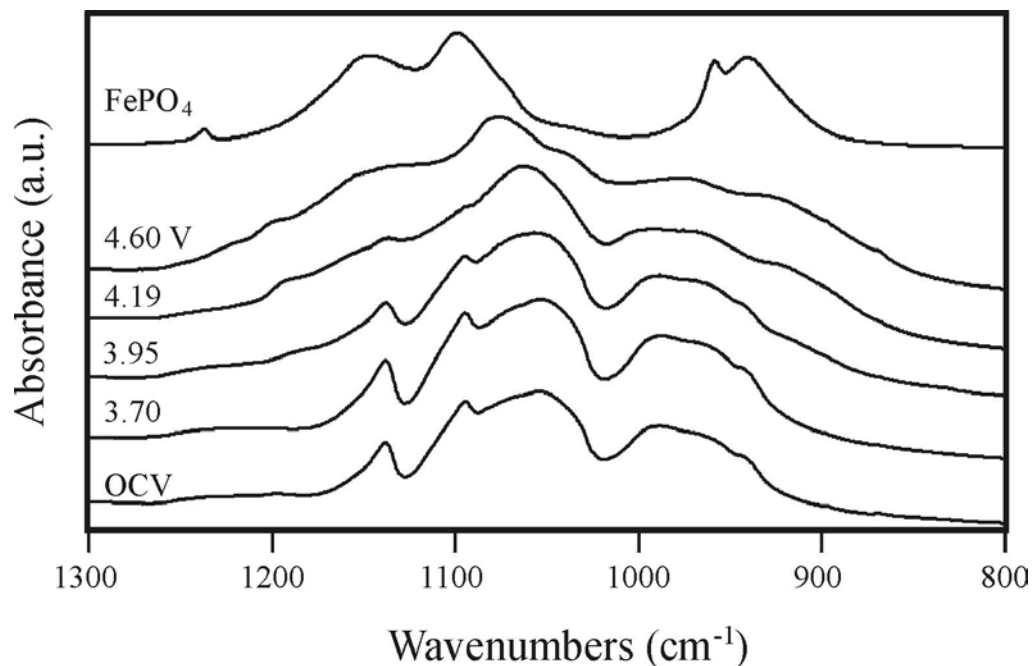


**Figure 2-24:** Infrared absorption spectra of  $\nu_1$  and  $\nu_3$  for  $\text{Li}_x(\text{Mn}_{0.5}\text{Fe}_{0.5})\text{PO}_4$  at various states of charge and  $\text{FePO}_4$ .

Similar changes are observed for the  $\nu_4$  and  $\text{Li}^+$  ion cage modes in Fig. 2-25. Only minor spectral changes in the infrared bands are observed during the  $\text{Fe}^{2+}/\text{Fe}^{3+}$  redox couple, but rather dramatic changes occur during the  $\text{Mn}^{2+}/\text{Mn}^{3+}$  couple. For example, the intensity of the  $496\text{ cm}^{-1}$  band diminishes slightly when the cells are charged to 3.95 V, but the band at  $661\text{ cm}^{-1}$  increases in intensity at the expense of the  $642\text{ cm}^{-1}$  band. A new band appears at  $532\text{ cm}^{-1}$  that gradually replaces the  $577$  and  $551\text{ cm}^{-1}$  bands between 3.95 and 4.6 V. Additionally, the  $661$  and  $642\text{ cm}^{-1}$  bands become a single band centered near  $650\text{ cm}^{-1}$  in the spectrum of  $(\text{Mn}_{0.5}\text{Fe}_{0.5})\text{PO}_4$ . The  $\text{Li}^+$  cage modes essentially vanish during the  $\text{Mn}^{2+}/\text{Mn}^{3+}$  redox couple leaving a weak feature near  $460\text{ cm}^{-1}$  in the 4.6 V sample. This is probably due to the residual  $\text{Li}^+$  ions in the  $(\text{Mn}_{0.5}\text{Fe}_{0.5})\text{PO}_4$  particles.

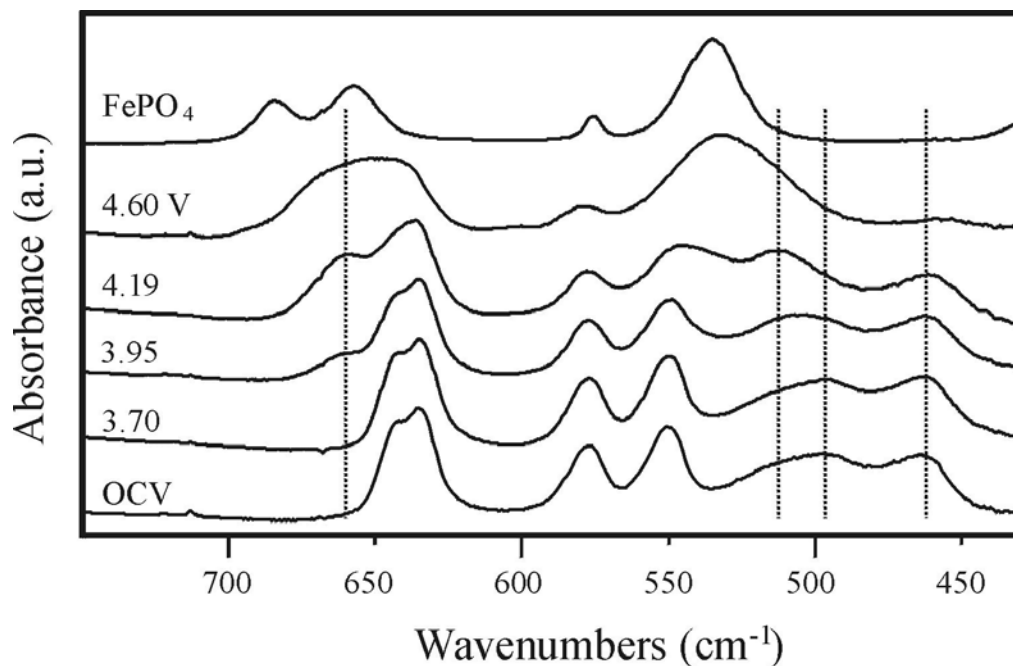


**Figure 2-25:** Infrared absorption spectra of  $\nu_4$  and the lithium cage modes for  $\text{Li}_x(\text{Mn}_{0.5}\text{Fe}_{0.5})\text{PO}_4$  at various states of charge and  $\text{FePO}_4$ .

Two conflicting models have been proposed to explain the delithiation mechanism during the  $\text{Fe}^{2+}/\text{Fe}^{3+}$  redox couple in  $\text{Li}(\text{Mn}_y\text{Fe}_{1-y})\text{PO}_4$  solid solutions. Bramnik *et al.* used high resolution synchrotron XRD data to suggest a two-phase mechanism in  $\text{Li}(\text{Mn}_{0.6}\text{Fe}_{0.4})\text{PO}_4$  [31], whereas Yamada *et al.* described single-phase transitions in a series of  $\text{Li}(\text{Mn}_y\text{Fe}_{1-y})\text{PO}_4$  materials [3]. Unfortunately, the infrared spectra presented in Figs. 2-24 and 2-25 cannot be used to distinguish between these mechanisms because the spectra undergo small changes throughout most of the  $\text{Fe}^{2+}/\text{Fe}^{3+}$  redox couple. This behavior is quite different than the  $\text{Li}_x\text{FePO}_4$  system where  $\text{FePO}_4$  bands appeared early in the delithiation process and continued to increase at the expense of the  $\text{LiFePO}_4$  bands. Spectral differences between  $\text{Li}_x\text{FePO}_4$  and  $\text{Li}_x(\text{Mn}_{0.5}\text{Fe}_{0.5})\text{PO}_4$  at approximately the same level of delithiation must be due to the presence of the  $\text{Mn}^{2+}$

ions. In  $\text{Li}(\text{Mn}_{0.5}^{\text{II}}\text{Fe}_{0.5}^{\text{II}})\text{PO}_4$ , the  $\text{Mn}^{2+}$  and  $\text{Fe}^{2+}$  ions are randomly distributed among symmetrically equivalent 4(c) sites; thus, there are a number of possible coordination environments for the  $\text{PO}_4^{3-}$  anions. During the first electrochemical plateau, the  $\text{Fe}^{2+}$  ions are oxidized to  $\text{Fe}^{3+}$  leaving the  $\text{PO}_4^{3-}$  anions coordinated to  $\text{Li}^+$ ,  $\text{Mn}^{2+}$ , and  $\text{Fe}^{3+}$  ions. In contrast, particles of  $\text{Li}_x\text{FePO}_4$  consist of a  $\text{LiFePO}_4$  core encased within a shell of lithium deficient  $\text{FePO}_4$  [1,11]; in  $\text{FePO}_4$ , the  $\text{PO}_4^{3-}$  anions are only coordinated to  $\text{Fe}^{3+}$  ions. The lack of spectral changes in Figs. 2-24 and 2-25 suggests that the local structure about the  $\text{PO}_4^{3-}$  anions in  $\text{Li}_x(\text{Mn}_{0.5}\text{Fe}_{0.5})\text{PO}_4$  does not change significantly during the  $\text{Fe}^{2+}/\text{Fe}^{3+}$  redox couple. This is probably because the  $\text{Li}^+$  and  $\text{Mn}^{2+}$  ions cause the potential energy environment of the  $\text{PO}_4^{3-}$  anions in  $\text{Li}_{0.5}(\text{Mn}_{0.5}^{\text{II}}\text{Fe}_{0.5}^{\text{II}})\text{PO}_4$  to be more similar to those in  $\text{Li}(\text{Mn}_{0.5}^{\text{II}}\text{Fe}_{0.5}^{\text{II}})\text{PO}_4$  than in  $\text{FePO}_4$ .

Both Yamada *et al.* [3] and Bramnik *et al.* [31] described a two-phase delithiation mechanism between  $\text{Li}_{0.5}(\text{Mn}_{0.5}^{\text{II}}\text{Fe}_{0.5}^{\text{III}})\text{PO}_4$  and  $(\text{Mn}_{0.5}^{\text{III}}\text{Fe}_{0.5}^{\text{III}})\text{PO}_4$ . The infrared spectra presented in Figs. 2-24 and 2-25 support this model. Between 3.95 and 4.60 V, several new bands appear and increase in intensity as the  $\text{Mn}^{2+}$  ions are oxidized to  $\text{Mn}^{3+}$ . This behavior is identical to the spectral behavior observed for the two-phase delithiation of  $\text{LiFePO}_4$  (see Sec. 2.3.3). Indeed, the frequencies of these modes are very similar to those of  $\text{FePO}_4$ . This is because the local structure of  $(\text{Mn}_{0.5}^{\text{III}}\text{Fe}_{0.5}^{\text{III}})\text{PO}_4$  becomes very similar to  $\text{FePO}_4$  when the sample is fully delithiated. Both compounds contain  $\text{PO}_4^{3-}$  anions that are coordinated only to trivalent transition metal ions.

Above 3.95 V, the  $(\text{Mn}_{0.5}\text{Fe}_{0.5})\text{PO}_4$  bandwidths in Figs. 2-24 and 2-25 become quite large compared to  $\text{FePO}_4$ . This indicates that there is a higher degree of disorder around the phosphate anions in  $(\text{Mn}_{0.5}\text{Fe}_{0.5})\text{PO}_4$  than in  $\text{FePO}_4$ . Previous experiments using extended X-ray absorption fine structure measurements have clearly shown that the local structure around the manganese cations becomes distorted when the  $\text{Mn}^{2+}$  ions are oxidized to  $\text{Mn}^{3+}$  [3,26]. This is due to a strong electron-lattice interaction (Jahn-Teller effect) on the  $\text{Mn}^{3+}$  ions in the  $(\text{Mn}_y\text{Fe}_{1-y})\text{PO}_4$  materials. The oxygen atoms forming the  $\text{MnO}_6$  octahedra are covalently bonded to phosphorous atoms in the phospho-olivine materials. Therefore, the local deformations in the manganese octahedra will directly influence the  $\text{PO}_4^{3-}$  vibrational modes through the covalent P–O bonds and result in the significant band broadening observed for the  $\text{PO}_4^{3-}$  anions of  $(\text{Mn}_{0.5}\text{Fe}_{0.5})\text{PO}_4$ .

## 2.4 Conclusions

Infrared and Raman spectroscopy are utilized to investigate the local structure of  $\text{LiMPO}_4$  ( $\text{M} = \text{Mn}, \text{Fe}, \text{Co}, \text{and Ni}$ ) and  $\text{NaFePO}_4$ . The factor group splitting of the intramolecular  $\text{PO}_4^{3-}$  vibrations is affected by the nature of the transition metal ion in  $\text{LiMPO}_4$  compounds. Previous workers have shown that specific interactions between the ions in the unit cell influence the magnitude of the factor group splitting of  $\nu_3$  [61,62]. The second ionization energy of the transition metal ion in  $\text{LiMPO}_4$  ( $\text{M} = \text{Fe}, \text{Mn}, \text{Co}, \text{Ni}$ ) is also correlated to the splitting of  $\nu_4$  (cf., Fig. 2-5).

Spectroscopic studies of  $\text{NaFePO}_4$  and  $\text{LiFePO}_4$  suggest that the compound prepared by the electrochemical insertion of  $\text{Na}^+$  ions into  $\text{FePO}_4$  is structurally related to

LiFePO<sub>4</sub> and the mineral maricite. Moreover, the Raman-active A<sub>g</sub> mode of  $\nu_1$  occurs at the same frequency for both NaFePO<sub>4</sub> and LiFePO<sub>4</sub> because the average P–O bond length is nearly identical in the two compounds. The factor group splitting of the intramolecular PO<sub>4</sub><sup>3-</sup> vibrations is between 10 and 20 cm<sup>-1</sup> less for NaFePO<sub>4</sub> than for LiFePO<sub>4</sub>. The vibrational modes of the anions are more perturbed in LiFePO<sub>4</sub> and exhibit larger factor group splitting effects compared to NaFePO<sub>4</sub> because the Li<sup>+</sup> ions have a larger charge density than Na<sup>+</sup> ions and can form stronger coordinative bonds with the PO<sub>4</sub><sup>3-</sup> anions. The similarity of the factor group multiplets in both LiFePO<sub>4</sub> and NaFePO<sub>4</sub>, particularly in the PO<sub>4</sub><sup>3-</sup> bending region, strongly suggests that the 506 and 470 cm<sup>-1</sup> bands in LiFePO<sub>4</sub> are not a mixture of Li<sup>+</sup> translations and PO<sub>4</sub><sup>3-</sup> bending motions. Rather, these bands may be assigned to Li<sup>+</sup> ion cage modes with some degree of confidence.

The imaging capability of the electron microprobe provides a good means to explore the morphology and particle size distribution of Li<sub>x</sub>FePO<sub>4</sub> samples. Furthermore, an elemental analysis of the various regions in the samples using wavelength dispersive spectrometry allows an investigation into the homogeneity of the sample. The results of this study show that the sample is relatively homogeneous with respect to iron and phosphorous but there is a relatively large distribution of particle sizes. The sample is primarily composed of larger particles (10-20  $\mu\text{m}$  in diameter) and much finer sized particles ( $\sim 1 \mu\text{m}$ ), with some distribution of particle sizes between these two classes.

Raman and infrared spectroscopic measurements of Li<sub>x</sub>FePO<sub>4</sub> ( $0 \leq x \leq 1$ ) demonstrate that the intramolecular vibrations of the PO<sub>4</sub><sup>3-</sup> anions are very sensitive to the presence of Li<sup>+</sup> ions. This arises in part because the removal of Li<sup>+</sup> ions and the

necessary oxidation of the  $\text{Fe}^{2+}$  ions cause a redistribution of electron density in the P–O bonds of the  $\text{PO}_4^{3-}$  anions. This redistribution changes the effective force constants (frequencies), dipole moment derivatives (IR intensities) and polarizability derivatives (Raman intensities) in  $\text{LiFePO}_4$  cathodes. For example, the Raman-active  $\nu_3$  bands are much more intense in  $\text{FePO}_4$  compared to  $\text{LiFePO}_4$ . Moreover, the factor group splitting of the  $\text{FePO}_4$   $\nu_4$  modes is quite large. In fact, the magnitude of the splitting is greater than what would be predicted from the ionization energy of the  $\text{Fe}^{3+}$  ions.

The delithiation of  $\text{LiFePO}_4$  is thought to proceed according to a two-phase model, [1,11] with a layer of  $\text{FePO}_4$  forming around each  $\text{LiFePO}_4$  particle as  $\text{Li}^+$  ions are extracted. The distance from the center of the particle to the boundary between the  $\text{FePO}_4$  and  $\text{LiFePO}_4$  phases decreases as the cathode material is charged. Consequently, the surface area of the interface decreases as the lithium concentration decreases, thus inhibiting  $\text{Li}^+$  ion diffusion [1,11,76,84]. The infrared and Raman spectra presented in Figs. 2-15 to 2-18 clearly support this model. If delithiation proceeded through a single phase, then the frequencies of the bands would shift, dependent on the  $\text{Li}^+$  ion concentration. However, the band intensities of each phase change with no apparent frequency shifts as the lithium is extracted. As noted earlier, the intensities in the Raman spectra are mediated by the optical skin effect. Differences in the penetration depths for the two spectroscopic techniques yield microscopic information concerning the delithiation process in the particles on two different spatial scales.

The local structure of  $\text{Li}_x(\text{Mn}_y\text{Fe}_{1-y})\text{PO}_4$  ( $0 \leq x, y \leq 1$ ) is also explored with vibrational spectroscopy. Raman spectra of the carbon-coated  $\text{Li}(\text{Mn}_{0.5}\text{Fe}_{0.5})\text{PO}_4$  particles are dominated by two intense bands that are assigned to the G and D bands of



graphite. The relative intensities of these bands suggest that the particles are predominately covered with disordered,  $sp^2$ -coordinated carbon atoms. The Raman spectrum also contains a weak band at  $948\text{ cm}^{-1}$  that is assigned to the  $A_g$  mode of  $\nu_1$ . The frequency of this band agrees very well with previous Raman spectroscopic measurements of  $\nu_1$  in other phospho-olivine  $\text{LiMPO}_4$  systems [55,61] and indicates that the P–O bond lengths do not change significantly in  $\text{Li}(\text{Mn}_y\text{Fe}_{1-y})\text{PO}_4$  solid solutions [72].

The infrared spectrum of  $\text{Li}(\text{Mn}_{0.5}\text{Fe}_{0.5})\text{PO}_4$  is intermediate between  $\text{LiFePO}_4$  and  $\text{LiMnPO}_4$ , and two-mode behavior could be clearly identified in the  $\text{PO}_4^{3-}$  intramolecular stretching region ( $\nu_1$  and  $\nu_3$ ). However, the  $\text{Li}^+$  cage modes and  $\nu_4$  did not exhibit this behavior. Instead, the frequencies of these bands depend on the concentration of the  $\text{Fe}^{2+}$  ions. For example, the  $\text{Li}^+$  cage mode at  $470\text{ cm}^{-1}$  in the spectrum of  $\text{LiFePO}_4$  shifts to  $459\text{ cm}^{-1}$  as the  $\text{Mn}^{2+}$  concentration is increased in  $\text{Li}(\text{Mn}_y\text{Fe}_{1-y})\text{PO}_4$ . The  $\nu_1$  and  $\nu_3$  vibrations are more localized than  $\nu_4$  and the  $\text{Li}^+$  cage modes; hence, they exhibit two-mode behavior while the latter bands do not.

The  $\text{PO}_4^{3-}$  vibrations of the  $\text{Li}(\text{Mn}_{0.5}\text{Fe}_{0.5})\text{PO}_4$  solid-solution are sensitive to lithium extraction. There are only minor changes for a few of the bands during the  $\text{Fe}^{2+}/\text{Fe}^{3+}$  redox couple. However, significant changes occur in the  $\text{PO}_4^{3-}$  vibrations and  $\text{Li}^+$  cage modes during the  $\text{Mn}^{2+}/\text{Mn}^{3+}$  redox couple. The infrared spectra indicate that the local structure of the  $\text{PO}_4^{3-}$  anions does not change significantly during the  $\text{Fe}^{2+}/\text{Fe}^{3+}$  redox couple. This is possibly due to the coordination of the  $\text{PO}_4^{3-}$  anions by  $\text{Li}^+$  and  $\text{Mn}^{2+}$  ions in addition to the  $\text{Fe}^{3+}$  ions. Moreover, the infrared spectra confirm a two-

phase mechanism for the oxidation of  $\text{Mn}^{2+}$  to  $\text{Mn}^{3+}$  between 3.95 and 4.60 V vs.  $\text{Li}^+/\text{Li}$ . The bandwidths of the  $\text{Li}_x(\text{Mn}_{0.5}\text{Fe}_{0.5})\text{PO}_4$  modes also show some dependence on the lithium concentration. In fact, the  $(\text{Mn}_{0.5}\text{Fe}_{0.5})\text{PO}_4$  bands are much broader than the corresponding bands for  $\text{FePO}_4$ . This indicates that the  $\text{PO}_4^{3-}$  anions are more disordered in  $(\text{Mn}_{0.5}\text{Fe}_{0.5})\text{PO}_4$  compared to  $\text{FePO}_4$ . The local disorder in the  $\text{PO}_4^{3-}$  anions is probably due to local deformations in the  $\text{MnO}_6$  octahedra induced by the Jahn-Teller active  $\text{Mn}^{3+}$  ions in  $(\text{Mn}_{0.5}\text{Fe}_{0.5})\text{PO}_4$ .

## 2.5 References

- [1] A. K. Padhi, K. S. Nanjundaswamy and J. B. Goodenough, *J. Electrochem. Soc.*, **144**, (1997) 1188-1194.
- [2] A. K. Padhi, K. S. Nanjundaswamy, C. Masquelier, S. Okada and J. B. Goodenough, *J. Electrochem. Soc.*, **144**, (1997) 1609-1613.
- [3] A. Yamada, Y. Kudo and K.-Y. Liu, *J. Electrochem. Soc.*, **148**, (2001) A1153-A1158.
- [4] A. Yamada, S. C. Chung and K. Hinokuma, *J. Electrochem. Soc.*, **148**, (2001) A224-A229.
- [5] S. Okada, S. Sawa, M. Egashira, J.-I. Yamaki, M. Tabuchi, H. Kageyama, T. Konishi and A. Yoshino, *J. Power Sources*, **97-98**, (2001) 430-432.
- [6] G. Li, H. Azuma and M. Tohda, *Electrochem. Solid-State Lett.*, **5**, (2002) A135-A137.
- [7] S. Okada, S.-I. Sawa, Y. Uebou, M. Egashira, J.-I. Yamaki, M. Tabuchi, H. Kobayashi, K. Fukumi and H. Kageyama, *Electrochemistry*, **71**, (2003) 1136-1138.

- [8] K. Amine, H. Yasuda and M. Yamachi, *Electrochem. Solid-State Lett.*, **3**, (2000) 178-179.
- [9] M. Piana, M. Arrabito, S. Bodoardo, A. D'Epifanio, D. Satolli, F. Croce and B. Scrosati, *Ionics*, **8**, (2002)
- [10] M. S. Whittingham, *Chem. Rev.*, **104**, (2001) 4271-4301.
- [11] A. S. Andersson, B. Kalska, L. Häggström and J. O. Thomas, *Solid State Ionics*, **130**, (2000) 41-52.
- [12] V. Srinivasan and J. Newman, *J. Electrochem. Soc.*, **151**, (2004) A1517-A1529.
- [13] A. Yamada, H. Koizumi, N. Sonoyama and R. Kanno, *Electrochem. Solid-State Lett.*, **8**, (2005) A409-A413.
- [14] C. Delacourt, P. Poizot, J.-M. Tarascon and C. Masquelier, *Nat. Mater.*, **4**, (2005) 254-260.
- [15] C. Delacourt, P. Poizot, M. Morcrette, J.-M. Tarascon and C. Masquelier, *Chem. Mater.*, **16**, (2004) 93-99.
- [16] M. Yonemura, A. Yamada, Y. Takei, N. Sonoyama and R. Kanno, *J. Electrochem. Soc.*, **151**, (2004) A1352-A1356.
- [17] C. Delacourt, L. Laffont, R. Bouchet, C. Wurm, J.-B. Leriche, M. Morcrette, J.-M. Tarascon and C. Masquelier, *J. Electrochem. Soc.*, **152**, (2005) A913-A921.
- [18] J. M. Lloris, C. Pérez Vicente and J. L. Tirado, *Electrochem. Solid-State Lett.*, **5**, (2002) A234-A237.
- [19] K. Tadanaga, F. Mizuno, A. Hayashi, T. Minami and M. Tatsumisago, *Electrochemistry*, **71**, (2003) 1192-1195.
- [20] A. Eftekhari, *J. Electrochem. Soc.*, **151**, (2004) A1456-A1460.
- [21] N. N. Bramnik, K. G. Bramnik, C. Baetz and H. Ehrenberg, *J. Power Sources*, **145**, (2005) 74-81.
- [22] F. Zhou, M. Cococcioni, K. Kang and G. Ceder, *Electrochem. Commun.*, **6**, (2004) 1144-1148.

- [23] J. Wolfenstine and J. Allen, *J. Power Sources*, **142**, (2005) 389-390.
- [24] J.-M. Tarascon and D. Guyomard, *Solid State Ionics*, **69**, (1994) 293-305.
- [25] J. Wolfenstine and J. Allen, *J. Power Sources*, **136**, (2004) 150-153.
- [26] A. Yamada and S.-C. Chung, *J. Electrochem. Soc.*, **148**, (2001) A960-A967.
- [27] A. Yamada, Y. Kudo and K.-Y. Liu, *J. Electrochem. Soc.*, **148**, (2001) A747-A754.
- [28] G. Li, H. Azuma and M. Tohda, *J. Electrochem. Soc.*, **149**, (2002) A743-A747.
- [29] G. Li, Y. Kudo, K.-Y. Liu, H. Azuma and M. Tohda, *J. Electrochem. Soc.*, **149**, (2002) A1414-A1418.
- [30] A. Yamada, M. Hosoya, S.-C. Chung, Y. Kudo, K. Hinokuma, K.-Y. Liu and Y. Nishi, *J. Power Sources*, **119-121**, (2003) 232-238.
- [31] N. N. Bramnik, K. G. Bramnik, K. Nikolowski, M. Hinterstein, C. Baehtz and H. Ehrenberg, *Electrochem. Solid-State Lett.*, **8**, (2005) A379-A381.
- [32] S.-Y. Chung, J. T. Bloking and Y.-M. Chiang, *Nat. Mater.*, **1**, (2002) 123-128.
- [33] S.-Y. Chung and Y.-M. Chiang, *Electrochem. Solid-State Lett.*, **6**, (2003) A278-A281.
- [34] H. Tukamoto and A. R. West, *J. Electrochem. Soc.*, **144**, (1997) 3164-3168.
- [35] N. Ravet, J. B. Goodenough, S. Besner, M. Simoneau, P. Hovington and M. Armand, *Electrochem. Soc. Meet. Abs.*, **99-2**, Honolulu, HI, (Oct. 17-22, 1999), No. 127.
- [36] P. P. Prosini, D. Zane and M. Pasquali, *Electrochim. Acta*, **46**, (2001) 3517-3523.
- [37] H. Huang, S.-C. Yin and L. F. Nazar, *Electrochem. Solid-State Lett.*, **4**, (2001) A170-A172.
- [38] Z. Chen and J. R. Dahn, *J. Electrochem. Soc.*, **149**, (2002) A1184-A1189.
- [39] S. Franger, F. Le Cras, C. Bourbon and H. Rouault, *Electrochem. Solid-State Lett.*, **5**, (2002) A231-A233.

- [40] J. Barker, M. Y. Saidi and J. L. Swoyer, *Electrochem. Solid-State Lett.*, **6**, (2003) A53-A55.
- [41] O. Haas, A. Deb, E. J. Cairns and A. Wokaun, *J. Electrochem. Soc.*, **152**, (2005) A191-A196.
- [42] M. C. Tucker, M. M. Doeff, T. J. Richardson, R. Fiñones, J. A. Reimer and E. J. Cairnes, *Electrochem. Solid-State Lett.*, **5**, (2002) A95-A98.
- [43] M. C. Tucker, M. M. Doeff, T. J. Richardson, R. Fiñones, E. J. Cairns and J. A. Reimer, *J. Am. Chem. Soc.*, **124**, (2002) 3832-3833.
- [44] E. Cazzanelli, E. Mariotto, S. Passerini and W. H. Smyrl, *J. Non-cryst. Solids*, **208**, (1996) 89-98.
- [45] E. Cazzanelli, G. Marriotto, S. Passerini and F. Decker, *Solid State Ionics*, **70-71**, (1994) 412-416.
- [46] W. Huang and R. Frech, *J. Electrochem. Soc.*, **145**, (1998) 765-770.
- [47] W. Huang and R. Frech, *J. Power Sources*, **81-82**, (1999) 616-620.
- [48] T. Itoh, H. Sato, T. Nishina, T. Matue and I. Uchida, *J. Power Sources*, **68**, (1997) 333-337.
- [49] C. Julien, M. Massot, C. Perez-Vicente, E. Haro-Poniatowski, G. A. Nazri and A. Rougier, *Mat. Res. Soc. Symp. Proc.*, **496**, (1998) 415-420.
- [50] C. Julien, C. Perez-Vicente and G.A. Nazri, *Ionics*, **2**, (1996) 468-473.
- [51] T. J. Richardson, S. J. Wen, K. A. Striebel, P. N. Ross Jr. and E. J. Cairns, *Mater. Res. Bull.*, **32**, (1997) 609-618.
- [52] A. Šurca and B. Orel, *Electrochim. Acta*, **44**, (1999) 3051-3057.
- [53] S. Geller and J. L. Durand, *Acta Cryst.*, **13**, (1960) 325-331.
- [54] R. E. Newnham, R. P. Santoro and M. J. Redman, *Phys. Chem. Solids*, **26**, (1965) 445-447.

- [55] O. García-Moreno, M. Alvarez-Vega, F. García-Alvarado, J. García-Jaca, J. M. Gallardo-Amores, M. L. Sanjuán and U. Amador, *Chem. Mater.*, **13**, (2001) 1570-1576.
- [56] V. A. Streltsov, E. L. Belokoneva, V. G. Tsirelson and N. K. Hansen, *Acta Cryst.*, **B49**, (1993) 147-153.
- [57] G. Rousse, J. Rodriguez-Carvajal, S. Patoux and C. Masquelier, *Chem. Mater.*, **15**, (2003) 4082-4090.
- [58] F. Kubel, *Z. Kristallogr.*, **209**, (1994) 755.
- [59] I. Abrahams and K. S. Eason, *Acta Cryst.*, **C49**, (1993) 925-926.
- [60] S. A. Warda and S.-L. Lee, *Z. Kristallogr.*, **212**, (1997)
- [61] M. T. Paques-Ledent and P. Tarte, *Spectrochim. Acta*, **30A**, (1974) 673-689.
- [62] A. A. Salah, P. Jozwiak, J. Garbarczyk, K. Benkhoucha, K. Zaghrib, F. Gendron and C. M. Julien, *J. Power Sources*, **140**, (2005) 370-375.
- [63] W. Paraguassu, P. T. C. Freire, V. Lemos, S. M. Lala, L. A. Montoro and J. M. Rosolen, *J. Raman Spectrosc.*, **36**, (2005) 213-220.
- [64] G. Herzberg, *Molecular Spectra and Molecular Structure: II. Infrared and Raman Spectra of Polyatomic Molecules*, 1<sup>st</sup> ed., Van Nostrand Reinhold Company: New York (1945) pp 259.
- [65] A. Rulmont, R. Cahay, M. Liégeois-Duyckaerts and P. Tarte, *Eur. J. Solid State Inorg. Chem.*, **28**, (1991) 207-219.
- [66] J. E. Huheey, E. A. Keiter and R. L. Keiter, *Inorganic Chemistry: Principles of Structure and Reactivity*, 4<sup>th</sup> ed., Harper Collins: (1993) pp 36-37.
- [67] O. V. Yakubovich, E. L. Belokoneva, V. G. Tsirel'son and V. S. Urusov, *Vestn. Mosk. Univ., Ser. 4: Geol.*, **6**, (1992) 54-65.
- [68] J. N. Birdson, S. E. Quinlan and P. R. Tremaine, *Chem. Mater.*, **10**, (1998) 763-768.
- [69] Y. Le Page and G. Donnay, *Can. Mineral.*, **15**, (1977) 518-521.

- [70] M. T. Paques-Ledent, *Rev. Chim. Miner.*, **10**, (1973) 785-794.
- [71] M. Doeff, Y. Hu, F. McLarnon and R. Kostecki, *Electrochem. Solid-State Lett.*, **6**, (2003) A207-A209.
- [72] L. Popović, D. de Waal and J. C. A. Boeyens, *J. Raman Spectrosc.*, **36**, (2005) 2-11.
- [73] B. D. Cullity, *Elements of X-ray Diffraction*, 2<sup>nd</sup> ed., Addison-Wesley Publishing Company, Inc: Reading (1978) pp 178.
- [74] P. Tang and N. A. W. Holzwarth, *Phys. Rev. B*, **68**, (2003) 165107.
- [75] M. Born and E. Wolf, *Principles of Optics: Electromagnetic Theory of Propagation, Interference, and Diffraction of Light*, 4<sup>th</sup> ed., Pergamon Press: Oxford (1970) pp 614.
- [76] A. S. Andersson and J. O. Thomas, *J. Power Sources*, **97-98**, (2001) 498-502.
- [77] F. Tuinstra and J. L. Koenig, *J. Chem. Phys.*, **53**, (1970) 1126-1130.
- [78] K. Sinha and J. Menéndez, *Phys. Rev. B*, **41**, (1990) 10845-10847.
- [79] R. J. Nemanich and S. A. Solin, *Phys. Rev. B*, **20**, (1979) 392-401.
- [80] L. Nikiel and P. W. Jagodzinski, *Carbon*, **31**, (1993) 1313-1317.
- [81] J. Wagner, M. Ramsteiner, C. Wild and P. Koidl, *Phys. Rev. B*, **40**, (1989) 1817-1824.
- [82] M. Ramsteiner and J. Wagner, *Appl. Phys. Lett.*, **51**, (1987) 1355-1357.
- [83] P. Tarte, A. Rulmont, M. Liégeois-Duykaerts, R. Cahay and J. M. Winand, *Solid State Ionics*, **42**, (1990) 177-196.
- [84] P. P. Prosini, M. Lisi, D. Zane and M. Pasquali, *Solid State Ionics*, **148**, (2002) 45-51.

## Chapter 3: LISICON $\text{Li}_3\text{V}_2(\text{PO}_4)_3$ and $\text{LiTi}_2(\text{PO}_4)_3$ CATHODES

---

*Christopher M. Burba and Roger Frech, Solid State Ionics, Submitted (2005)\**

*Christopher M. Burba and Roger Frech, Solid State Ionics, Submitted (2005)\**

### 3.1 Introduction

A number of vanadium and titanium phosphate compounds have been explored as potential cathode materials because of their high energy densities [1-20]. For example, Azmi *et al.* [7] conducted a comprehensive survey of the electrochemical performance for the seven known phases of  $\text{VOPO}_4$ , and discovered that the performance of  $\text{VOPO}_4$  cathodes critically depends on the initial phase of the compound. In addition, Barker *et al.* [21] investigated  $\text{LiVFPO}_4$  and Davies *et al.* [22] studied vanadium phosphate glasses as novel cathodes for rechargeable lithium cells. Furthermore, spinel  $\text{Li}_4\text{Ti}_5\text{O}_{12}$  has garnered significant interest as an anode material because of its excellent coulombic efficiency [23-25]. Nonetheless, LISICON-like phases of  $\text{Li}_3\text{M}_2(\text{PO}_3)_2$  ( $\text{M} = \text{V}$  and  $\text{Ti}$ ) have attracted most of the attention [11-15,17-20,26-32]. These compounds have a  $\text{Na}_3\text{Zr}_2\text{Si}_2\text{PO}_{12}$ -type structure [33], and have good ionic conductivity and competitive redox potentials. Many of the compounds crystallize in a rhombohedral crystal system; however, some materials in this family exhibit a monoclinic distortion. The  $\text{Li}_3\text{M}_2(\text{PO}_4)_3$  structure consist of an extended 3-dimensional network of corner-sharing  $\text{MO}_6$  octahedra and  $\text{PO}_4$  tetrahedra (hereafter denoted as  $[\text{M}_2(\text{PO}_4)_3]_{\infty}^{3-}$ ) with lithium ions occupying the interstitial sites of the structure. The  $[\text{M}_2(\text{PO}_4)_3]_{\infty}^{3-}$  network provides a robust framework to withstand repeated lithium (de)intercalation cycles. Moreover, the

\*© Elsevier, Inc. (2005).



polyatomic anions generate an inductive effect, which lowers the energy of the transition metal redox couple with respect to the Fermi level of lithium. Unfortunately, the covalent P–O bonds also results in low intrinsic electronic conductivities for these compounds. Thus, “smart” processing strategies, such as carbon-coating of the electrode particles, have been explored to compensate for this problem. For example, Huang *et al.* obtained excellent reversibility at high rates from nanostructured  $\text{Li}_3\text{V}_2(\text{PO}_4)_3$ /carbon cathodes [17].

Most research efforts focused on the thermodynamically stable phase of  $\text{Li}_3\text{V}_2(\text{PO}_4)_3$  (denoted A- $\text{Li}_3\text{V}_2(\text{PO}_4)_3$ ) [11,14,17-19]. This compound has a monoclinic crystal structure and is isostructural to several other  $\text{Li}_3\text{M}_2(\text{PO}_4)_3$  (M = Sc, Fe, and Cr) materials [14,17,34]. All three  $\text{Li}^+$  ions may be reversibly extracted from A- $\text{Li}_3\text{V}_2(\text{PO}_4)_3$  over four two-phase electrochemical plateaus to yield a theoretical capacity of 197 mAh/g [14]. Experimental measurements of the equilibrium potential show that the first two  $\text{Li}^+$  ions may be easily extracted from the compound, but the third  $\text{Li}^+$  ion is kinetically hindered and exhibits large polarization effects [18,20]. When the sample is discharged, solid solution behavior is observed for the first two reinserted  $\text{Li}^+$  ions, yet two-phase behavior occurs when the last  $\text{Li}^+$  ion is reinserted [14,18,20]. Two phase changes occur when A- $\text{Li}_3\text{V}_2(\text{PO}_4)_3$  is heated to 300°C [ $\alpha$  (monoclinic A-form)  $\leftrightarrow$   $\beta$  (orthorhombic)  $\leftrightarrow$   $\gamma$  (orthorhombic)] [16,30,31], and Sato *et al.* [31] successfully stabilized the high temperature orthorhombic phase by doping the structure with zirconium to form  $\text{Li}_{2.6}(\text{V}_{0.8}\text{Zr}_{0.2})_2(\text{PO}_4)_3$ . These compounds deliver up to 104 mAh/g at modest rates along two electrochemical plateaus at 3.7 and 4.1 V vs.  $\text{Li}^+/\text{Li}$ .

Rhombohedral  $\text{Li}_3\text{V}_2(\text{PO}_4)_3$  (denoted B-  $\text{Li}_3\text{V}_2(\text{PO}_4)_3$ ) has also been studied [12,15,20], but this phase is not accessible by direct solid-state synthesis. Gopalakrishnan and Rangan [35] first synthesized B- $\text{Li}_3\text{V}_2(\text{PO}_4)_3$  by oxidizing rhombohedral  $\text{Na}_3\text{V}_2(\text{PO}_4)_3$  with  $\text{Cl}_2$  in  $\text{CHCl}_3$  to form  $\text{V}_2(\text{PO}_4)_3$ ; this product was then reduced with  $\text{LiI}$ . However, the phase is also accessible by direct ion exchange from  $\text{Na}_3\text{V}_2(\text{PO}_4)_3$  [15]. Electrochemical measurements show that two  $\text{Li}^+$  ions may be reversibly extracted from B- $\text{Li}_3\text{V}_2(\text{PO}_4)_3$  over a flat electrochemical plateau at 3.76 V vs.  $\text{Li}^+/\text{Li}$ . This corresponds to a theoretical capacity of 131 mAh/g [15]. The electrochemical performance of rhombohedral  $\text{LiTi}_2(\text{PO}_4)_3$  is similar to the vanadium analog, and two  $\text{Li}^+$  ions may be intercalated into  $\text{LiTi}_2(\text{PO}_4)_3$  along a flat voltage plateau at 2.48 V to form  $\text{Li}_3\text{Ti}_2(\text{PO}_4)_3$  [26-28].

Most investigations of A- and B- $\text{Li}_3\text{V}_2(\text{PO}_4)_3$  and  $\text{LiTi}_2(\text{PO}_4)_3$  cathodes have employed electrochemical voltage measurements to map the energy of the  $\text{M}^{3+}/\text{M}^{4+}$  redox couple ( $\text{M} = \text{Ti}$  or  $\text{V}$ ) as a function of lithium content [11-18,20,27,28] or neutron and X-ray diffraction (XRD) techniques to probe the global structure of the materials [14-20,26-28]. For example, Gaubicher *et al.* [15] and Morcrette *et al.* [20] utilized powder XRD to establish a structural phase change from  $R\bar{3} (S_6^2)$  to  $R\bar{3}c (D_{3d}^6)$  in B- $\text{Li}_x\text{V}_2(\text{PO}_4)_3$  cathodes. The structural transformations that occur upon lithium intercalation into  $\text{LiTi}_2(\text{PO}_4)_3$  are analogous to those for B- $\text{Li}_x\text{V}_2(\text{PO}_4)_3$  [27,28]. A number of authors have also shown that delithiation of A- $\text{Li}_3\text{V}_2(\text{PO}_4)_3$  is topotactic and all of the intermediate compositions belong to the  $P2_1/n (C_{2h}^5)$  space group [15-20]. Investigations into the local structure of A- and B- $\text{Li}_x\text{V}_2(\text{PO}_4)_3$  and  $\text{Li}_x\text{Ti}_2(\text{PO}_4)_3$  have almost exclusively used  $^7\text{Li}$  or  $^{31}\text{P}$  NMR techniques [15,18,19,26]. For example, Yin *et al.* utilized a combination

of  $^7\text{Li}$  NMR and neutron diffraction to suggest that charge ordering on the  $\text{V}^{n+}$  sites and  $\text{Li}^+$  ordering/disordering among the lattice sites could account for all of the complex features in the voltage-composition curve of  $\text{A-Li}_x\text{V}_2(\text{PO}_4)_3$ , including the voltage hysteresis observed during the solid-solution domain [18,19].

In Chapter 2, vibrational spectroscopy was shown to be extremely valuable in probing fundamental lithium intercalation reactions for  $\text{Li}_x\text{FePO}_4$  and  $\text{Li}_x(\text{Mn}_y\text{Fe}_{1-y})\text{PO}_4$ . Indeed, the vibrations of the phosphate anions are extremely sensitive to the presence of the lithium ions and the oxidation state of the transition metal ions. A large number of NASICON-type compounds have been investigated with infrared and Raman spectroscopy. These materials include  $\text{M}^{\text{I}}_3\text{M}^{\text{II}}_2(\text{PO}_4)_3$  and  $\text{M}^{\text{I}}_3\text{M}^{\text{II}}_2(\text{PO}_4)_y(\text{AsO}_4)_{1-y}$  ( $\text{M}^{\text{I}} = \text{Li, Na}$  and  $\text{M}^{\text{II}} = \text{Cr, Fe, In, Sc}$ ) as well as  $\text{M}^{\text{I}}\text{M}^{\text{IV}}_2(\text{PO}_4)_3$  ( $\text{M}^{\text{I}} = \text{Li, Na, K, Rb, Cs, Tl}$  and  $\text{M}^{\text{II}} = \text{Ge, Sn, Ti, Zr, Hf}$ ) [36-42]. However, there are few reports where vibrational spectroscopy is used to probe these compounds as a function of lithium content. Varadaraju *et al.* performed the first vibrational spectroscopic characterization of lithium insertion into  $\text{LiTi}_2(\text{PO}_4)_3$  [43], but the spectral changes are only briefly discussed and neither the infrared nor the Raman spectra are included in their communication. In addition, Pikel *et al.* [44] investigated  $\text{Li}_{2x}\text{Mn}_{0.5-x}\text{Ti}_2(\text{PO}_4)_3$  ( $x = 0, 0.25, \text{ and } 0.5$ ) with infrared and Raman spectroscopy. In that system, the vibrational modes of the  $\text{PO}_4^{3-}$  anions are strongly affected by the presence of  $\text{Mn}^{2+}$  ions. Spectroscopic investigations into the vanadium phosphates have been mostly limited to vanadium phosphate glasses [22,45] or  $\text{VOPO}_4$  materials [46,47]. In  $\text{Li}_x\text{M}_2(\text{PO}_4)_3$ , the lithium and transition metal cations are coordinated to the tetrahedral  $\text{PO}_4^{3-}$  anions via  $\text{M-O-P}$  bonds; hence, any changes in the  $\text{Li-O}$  or  $\text{M-O}$  interactions will directly affect the vibrational modes of the

$\text{PO}_4^{3-}$  anions. Therefore, a careful vibrational spectroscopic investigation may provide a unique perspective on the electrochemical reactions accompanying  $\text{Li}^+$  (de)insertion into/from  $\text{Li}_x\text{M}_2(\text{PO}_4)_3$  ( $\text{M} = \text{V}$  or  $\text{Ti}$ ) and complement the existing electrochemical, diffraction, and NMR studies.

### 3.2 Experimental Methods

Monoclinic  $\text{Li}_3\text{V}_2(\text{PO}_4)_3$  (A-form) is prepared by mixing stoichiometric quantities of  $\text{Li}_2\text{CO}_3$ ,  $\text{V}_2\text{O}_5$ , and  $\text{NH}_4\text{H}_2\text{PO}_4$ . The precursor is heated at  $300^\circ\text{C}$  for 1 h to decompose the organic constituents and then further annealed at  $900^\circ\text{C}$  for 18 h. The thermal steps are performed under a flowing atmosphere of 10%  $\text{H}_2$  and 90%  $\text{N}_2$ . The product is then passed through a  $43\ \mu\text{m}$  sieve to remove the larger aggregates. Rhombohedral  $\text{Li}_3\text{V}_2(\text{PO}_4)_3$  (B-form) is prepared by ion exchange from  $\text{Na}_3\text{V}_2(\text{PO}_4)_3$ . The procedure to make  $\text{Na}_3\text{V}_2(\text{PO}_4)_3$  is identical to that of monoclinic  $\text{Li}_3\text{V}_2(\text{PO}_4)_3$  except  $\text{Na}_2\text{CO}_3$  is substituted for  $\text{Li}_2\text{CO}_3$ . The ion exchange is performed by suspending 4.11 g of  $\text{Na}_3\text{V}_2(\text{PO}_4)_3$  in 250 ml of a 1 M aqueous solution of  $\text{LiNO}_3$  by magnetic stirring. The resulting material is washed with water and then dried at  $60^\circ\text{C}$ . B- $\text{LiV}_2(\text{PO}_4)_3$  is chemically synthesized by reacting B- $\text{Li}_3\text{V}_2(\text{PO}_4)_3$  with excess  $\text{Br}_2$  in acetonitrile. Vitreous samples of vanadium phosphate are synthesized from  $\text{V}_2\text{O}_5$  and  $(\text{NH}_4)_2\text{HPO}_4$  with a nominal V:P mole ratio of 2:3. The precursor is intimately mixed and then heated at  $300^\circ\text{C}$  for approximately 4 h to decompose the organic constituents. The sample is then crushed and subsequently heated at  $1100^\circ\text{C}$  ( $25^\circ\text{C}/\text{min}$  rate) under a static air atmosphere. After heating for 1 h, the melt is quenched on a metal plate cooled to 77K.

Samples of  $\text{LiTi}_2(\text{PO}_4)_3$  are prepared by the solid-state reaction of stoichiometric quantities of  $\text{Li}_2\text{CO}_3$ ,  $\text{TiO}_2$ , and  $(\text{NH}_4)_2\text{HPO}_4$ . The reagents are ground together with an agate mortar and pestle and slowly heated to  $1000^\circ\text{C}$ . The sample is then held at that temperature for 48 h.

Phase purity of the crystalline samples is verified with powder XRD using a Scintag X'Tra XRD system (Cu  $K\alpha$  radiation with a rate of  $0.50^\circ/\text{s}$ ). Wavelength dispersive spectrometry (SX50 electron probe microanalyzer) is used to characterize the V:P ratios of A- and B- $\text{Li}_3\text{V}_2(\text{PO}_4)_3$ . The electron imaging capability of the electron microprobe also provides information about the particle sizes and morphology of the materials. Detailed sample preparation procedures for the electron microprobe may be found in App. A-2.

Samples containing different lithium concentrations are electrochemically prepared from A- and B- $\text{Li}_3\text{V}_2(\text{PO}_4)_3$  and  $\text{LiTi}_2(\text{PO}_4)_3$ . To this end, cathodes are prepared by mixing 87 wt% active material, 5 wt% KS-6 graphite (Tim Cal), 5 wt% Super P carbon (3M), and 3 wt% Teflon. The resulting cathode paste is rolled into a thin sheet and cut into  $1.27\text{ cm}^2$  circular disks. The mass of the vanadium containing cathodes is approximately 15 mg each, whereas the titanium containing cathodes are  $22 \pm 3$  mg. Cells are constructed with the above cathodes, a lithium metal anode, and an electrolyte consisting of 1 M  $\text{LiPF}_6$  in a 1:1 solution of diethyl carbonate and ethylene carbonate. Electrochemical testing is performed on an Arbin battery cycler. The vanadium cells are cycled at a constant current density of  $0.1\text{ mA}/\text{cm}^2$ . However, the  $\text{LiTi}_2(\text{PO}_4)_3$  cells are discharged using the galvanostatic intermittent titration technique (GITT). This technique entails discharging the cells at a current density of  $0.1\text{ mA}/\text{cm}^2$  until  $0.05\text{ Li}^+$

ions per formula unit are inserted into the cathode. The cell potential is then monitored during a rest step, and the process is repeated until the desired cathode composition is achieved. Afterwards, the cells are disassembled under argon, washed twice with diethyl carbonate, dried overnight, and stored under argon. Specific details concerning the spectroscopic analysis may be found in App. A-5 and A-6.

### 3.3 Results

#### 3.3.1 Powder X-Ray Diffraction

Powder XRD patterns of  $\text{Na}_3\text{V}_2(\text{PO}_4)_3$ , A- $\text{Li}_3\text{V}_2(\text{PO}_4)_3$ , B- $\text{Li}_3\text{V}_2(\text{PO}_4)_3$ , and  $\text{LiTi}_2(\text{PO}_4)_3$  are presented in Fig. 3-1. All four samples are crystalline and the diffractograms match previously published results for these systems. A- and B- $\text{Li}_3\text{V}_2(\text{PO}_4)_3$  crystallize in the  $P2_1/n$  ( $C_{2h}^5$ ) and  $R\bar{3}$  ( $S_6^2$ ), space groups, respectively [14,15]. Both  $\text{Na}_3\text{V}_2(\text{PO}_4)_3$  and  $\text{LiTi}_2(\text{PO}_4)_3$  may be indexed in the rhombohedral crystal system ( $R\bar{3}c$ ,  $D_{3d}^6$ ) [26-28,48], and Miller indices for some of the most intense reflections are noted on the figure. Lattice parameters of the compounds are calculated by least squares analysis of the XRD data and may be found in Table III-I.

#### 3.3.2 Electron Microprobe Analysis

A Scherrer calculation is performed on the powder XRD data of the vanadium containing compounds, and the approximate diameters of the crystallite domains are determined to be 72, 86, and 46 nm for  $\text{Na}_3\text{V}_2(\text{PO}_4)_3$ , A- $\text{Li}_3\text{V}_2(\text{PO}_4)_3$ , and B- $\text{Li}_3\text{V}_2(\text{PO}_4)_3$ , respectively. The average crystallite sizes are much smaller than the particle sizes

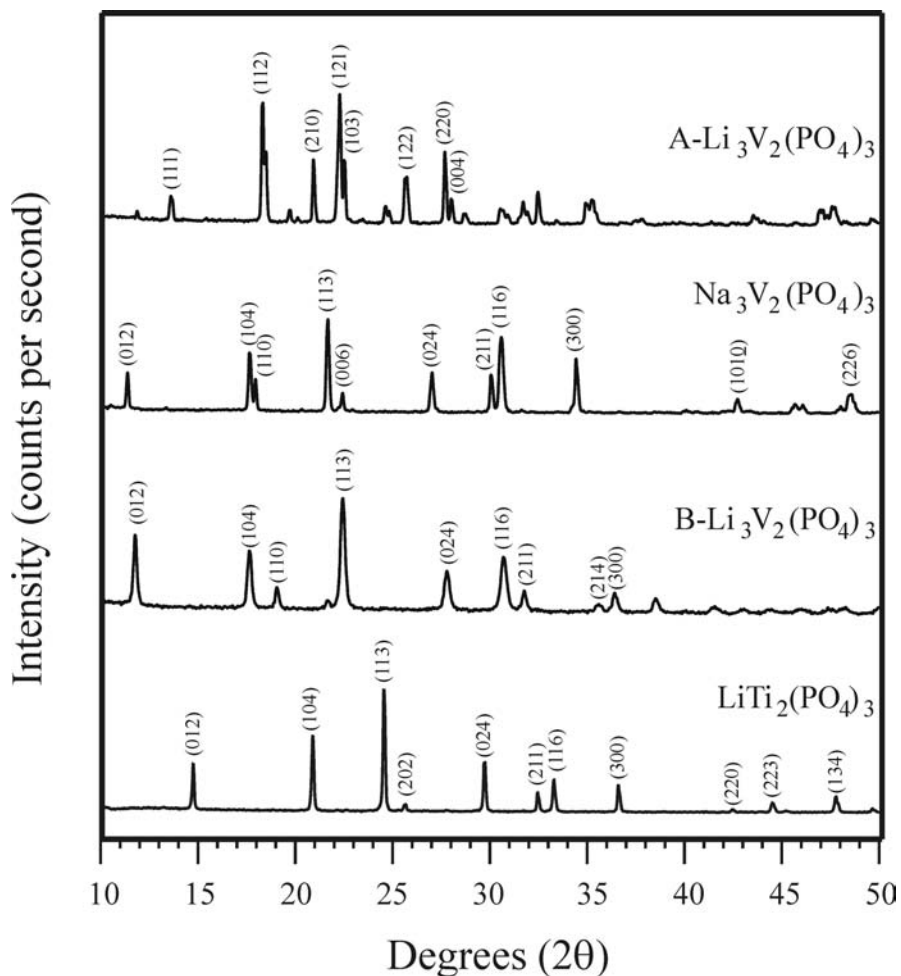


**Figure 3-1:** Powder XRD patterns for A- and B- $\text{Li}_3\text{V}_2(\text{PO}_4)_3$ ,  $\text{Na}_3\text{V}_2(\text{PO}_4)_3$ , and  $\text{LiTi}_2(\text{PO}_4)_3$ .

**Table III-I:** Lattice parameters of A- and B-  $\text{Li}_3\text{V}_2(\text{PO}_4)_3$ ,  $\text{Na}_3\text{V}_2(\text{PO}_4)_3$ , and  $\text{LiTi}_2(\text{PO}_4)_3$

|                  | A- $\text{Li}_3\text{V}_2(\text{PO}_4)_3$ | B- $\text{Li}_3\text{V}_2(\text{PO}_4)_3$ | $\text{Na}_3\text{V}_2(\text{PO}_4)_3$ | $\text{LiTi}_2(\text{PO}_4)_3$ |
|------------------|---|---|--|--------------------------------|
| Crystal System   | Monoclinic                                | Rhombohedral                              | Rhombohedral                           | Rhombohedral                   |
| $a$ (Å)          | 8.623(7)                                  | 8.317(3)                                  | 8.744(0)                               | 8.458(6)                       |
| $b$ (Å)          | 8.584(9)                                  |   |  |                                |
| $c$ (Å)          | 12.029(4)                                 | 22.450(1)                                 | 21.784(5)                              | 20.90(4)                       |
| $\beta$          | 89.86(6) $^\circ$                         |   |  |                                |
| Volume (Å $^3$ ) | 890.6                                     | 1345                                      | 1442                                   | 1295                           |

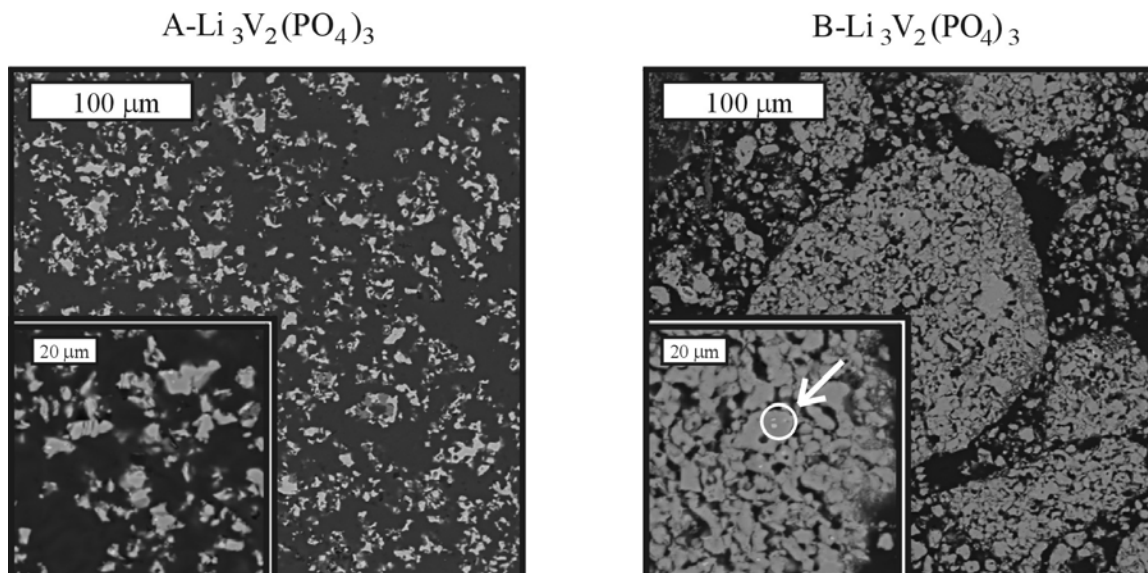


**Figure 3-2:** Electron microprobe images of A- and B- $\text{Li}_3\text{V}_2(\text{PO}_4)_3$  at a magnification of 250x (inset: 1000x).

observed with the imaging capabilities of an electron microprobe (Fig. 3-2). For example, most of the particles of A- $\text{Li}_3\text{V}_2(\text{PO}_4)_3$  observed with the electron microprobe are between 5 and 20  $\mu\text{m}$ . It is not uncommon for small crystallites to aggregate into larger particles. Thus, particles observed with the electron microprobe are probably composed of smaller crystallites detected with X-ray diffraction.

There are two distinct size domains in B- $\text{Li}_3\text{V}_2(\text{PO}_4)_3$ . The smaller particles of B- $\text{Li}_3\text{V}_2(\text{PO}_4)_3$  are approximately the same size as those found in A- $\text{Li}_3\text{V}_2(\text{PO}_4)_3$ . However, B- $\text{Li}_3\text{V}_2(\text{PO}_4)_3$  also contains much larger particles that range from 50 to 100  $\mu\text{m}$  in diameter. Magnification of the larger particles (the inset in Fig. 3-2) shows that these regions are actually dense clusters of the smaller particles. The formation of these domains might be due to the ion exchange reaction used in the preparation of B- $\text{Li}_3\text{V}_2(\text{PO}_4)_3$  from  $\text{Na}_3\text{V}_2(\text{PO}_4)_3$ .



The phosphorous and vanadium contents of A- and B-Li<sub>3</sub>V<sub>2</sub>(PO<sub>4</sub>)<sub>3</sub> are analyzed with the electron microprobe. The V:P ratio for A-Li<sub>3</sub>V<sub>2</sub>(PO<sub>4</sub>)<sub>3</sub> is 0.652, which is very close to the theoretical value (0.667). Compositional analysis of B-Li<sub>3</sub>V<sub>2</sub>(PO<sub>4</sub>)<sub>3</sub> shows that the ion exchange is successful, as Na<sup>+</sup> ions constitute less than 3 wt% of the sample. However, the V:P ratio of the B-Li<sub>3</sub>V<sub>2</sub>(PO<sub>4</sub>)<sub>3</sub> clusters (measured with a 20 μm spot) is 0.842. This value is much higher than expected, but the V:P ratio falls to 0.750 when smaller domains are analyzed with a 3 μm spot. The electron microprobe is also able to resolve very small regions of unreacted V<sub>2</sub>O<sub>5</sub> in the samples. These regions usually appear as bright spots embedded in the main phase of the sample. Two of these regions are highlighted in the inset image of B-Li<sub>3</sub>V<sub>2</sub>(PO<sub>4</sub>)<sub>3</sub>. It should be noted that the residual V<sub>2</sub>O<sub>5</sub> impurities are not detected with powder XRD.

### 3.3.3 Symmetry-based Analysis of the Vibrational Modes

The optically-active normal modes of A- and B-Li<sub>3</sub>V<sub>2</sub>(PO<sub>4</sub>)<sub>3</sub> are distributed among the following irreducible representations of the C<sub>2h</sub> and S<sub>6</sub> point groups respectively, at the Brillouin zone center:

$$\Gamma_{\text{A-Li}_3\text{V}_2(\text{PO}_4)_3} = 60\text{A}_g + 60\text{E}_g + 59\text{A}_u + 58\text{E}_u \quad [\text{Equation 3-1}]$$

$$\Gamma_{\text{B-Li}_3\text{V}_2(\text{PO}_4)_3} = 20\text{A}_g + 20\text{E}_g + 19\text{A}_u + 19\text{E}_u \quad [\text{Equation 3-2}]$$

The analysis predicts 120 Raman-active modes and 117 IR-active modes for A-Li<sub>3</sub>V<sub>2</sub>(PO<sub>4</sub>)<sub>3</sub>, while 40 Raman-active and 38 IR-active modes are expected for B-Li<sub>3</sub>V<sub>2</sub>(PO<sub>4</sub>)<sub>3</sub>. Since lithium extraction from A-Li<sub>3</sub>V<sub>2</sub>(PO<sub>4</sub>)<sub>3</sub> is a topotactic process, the space group of the compound remains the same throughout the A-Li<sub>x</sub>V<sub>2</sub>(PO<sub>4</sub>)<sub>3</sub> (0 ≤ x ≤ 3) series. Consequently, any changes in the vibrational modes accompanying delithiation

**Table III-II:** A factor group correlation of the  $\text{PO}_4^{3-}$  internal modes for monoclinic  $\text{Li}_x\text{V}_2(\text{PO}_4)_3$  and rhombohedral  $\text{Li}_x\text{M}_2(\text{PO}_4)_3$  ( $x = 1, 3$  and  $\text{M} = \text{V}, \text{Ti}$ )

|                 | Monoclinic $\text{Li}_x\text{V}_2(\text{PO}_4)_3$ | Rhombohedral $\text{LiM}_2(\text{PO}_4)_3$             | Rhombohedral $\text{Li}_3\text{M}_2(\text{PO}_4)_3$ |
|-----------------|---|--|---|
|                 | Site Symmetry: $C_1$                              | Site Symmetry: $C_2$                                   | Site Symmetry: $C_1$                                |
| $\Gamma(\nu_1)$ | $3A_g + 3B_g + 3A_u + 3B_u$                       | $A_{1g} + E_g + A_{1u} + E_u$                          | $A_g + B_g + A_u + B_u$                             |
| $\Gamma(\nu_2)$ | $6A_g + 6B_g + 6A_u + 6B_u$                       | $2A_{1g} + 2E_g + 2A_{1u} + 2E_u$                      | $2A_g + 2B_g + 2A_u + 2B_u$                         |
| $\Gamma(\nu_3)$ | $9A_g + 9B_g + 9A_u + 9B_u$                       | $A_{1g} + 2A_{2g} + 3E_g + A_{1u}$<br>$2A_{2u} + 3E_u$ | $3A_g + 3B_g + 3A_u + 3B_u$                         |
| $\Gamma(\nu_4)$ | $9A_g + 9B_g + 9A_u + 9B_u$                       | $A_{1g} + 2A_{2g} + 3E_g + A_{1u}$<br>$2A_{2u} + 3E_u$ | $3A_g + 3B_g + 3A_u + 3B_u$                         |

must solely be due to the presence of the  $\text{Li}^+$  ions and the oxidation state of the  $\text{V}^{n+}$  ions.

The extraction of lithium from  $\text{B-Li}_3\text{V}_2(\text{PO}_4)_3$  to form  $\text{B-LiV}_2(\text{PO}_4)_4$  induces a phase

change from  $R\bar{3}$  to  $R\bar{3}c$ . A factor group correlation of the normal modes for B-

$\text{LiV}_2(\text{PO}_4)_3$  (space group  $D_{3d}^6$ ) yields

$$\Gamma_{\text{B-LiV}_2(\text{PO}_4)_3} = 8A_{1g} + 9A_{2g} + 17E_g + 9A_{1u} + 9A_{2u} + 18E_u \quad [\text{Equation 3-3}]$$

after the three acoustic modes are subtracted. Here, the  $A_{1u}$  modes are optically inactive

so the analysis predicts 34 Raman-active modes and 27 IR-active modes. The site

symmetries of the  $\text{Li}^+$ ,  $\text{Ti}^{n+}$  ( $n = 3$  or  $4$ ), and  $\text{PO}_4^{3-}$  ions in  $\text{LiTi}_2(\text{PO}_4)_3$  and  $\text{Li}_3\text{Ti}_2(\text{PO}_4)_3$

are identical to those of  $\text{B-LiV}_2(\text{PO}_4)_3$  and  $\text{B-Li}_3\text{V}_2(\text{PO}_4)_3$ . Thus, the factor group

analyses of the  $\text{Li}_x\text{Ti}_2(\text{PO}_4)_3$  compounds are the same as the  $\text{B-Li}_x\text{V}_2(\text{PO}_4)_3$  materials

[36,37,44]. The predicted number of internal modes for  $\text{A-Li}_3\text{V}_2(\text{PO}_4)_3$ ,  $\text{B-Li}_x\text{V}_2(\text{PO}_4)_3$ ,

and  $\text{Li}_x\text{Ti}_2(\text{PO}_4)_3$  ( $x = 1$  and  $3$ ) are presented in Table III-II.

### 3.3.4 Raman Spectroscopy

#### 3.3.4.1 Pure Materials – The Raman scattering spectrum of the intramolecular $\text{PO}_4^{3-}$

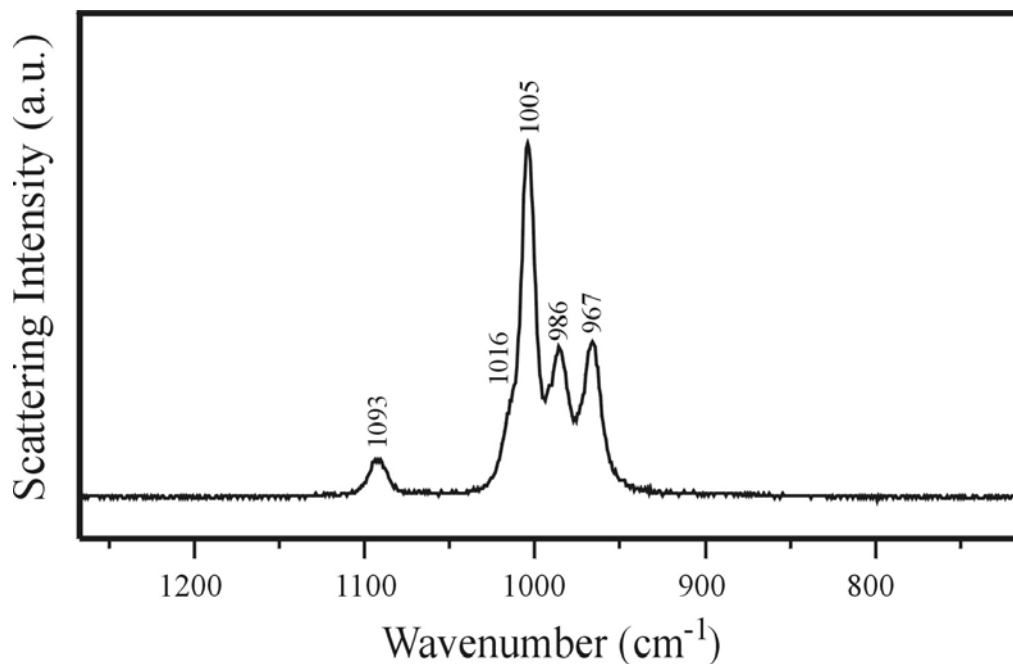


**Figure 3-3:** Raman scattering spectrum of  $\nu_1$  and  $\nu_3$  for  $\text{LiTi}_2(\text{PO}_4)_3$ . The numbers correspond to the band frequencies.

stretching modes ( $\nu_1$  and  $\nu_3$ ) of  $\text{LiTi}_2(\text{PO}_4)_3$  is presented in Fig. 3-3. The spectrum is dominated by three intense bands at 1005, 986, and 967  $\text{cm}^{-1}$  and a weaker band at 1093  $\text{cm}^{-1}$ . A high frequency shoulder on the 1005  $\text{cm}^{-1}$  band may also be resolved near 1016  $\text{cm}^{-1}$ . At the Brillouin zone center, group theory predicts  $\nu_1$  will yield two Raman active modes ( $A_{1g} + E_g$ ), whereas  $\nu_3$  will give six Raman active vibrations ( $A_{1g} + 2A_{2g} + 3E_g$ ) for this compound (see Table III-II). It is tempting to assign the two bands at 986 and 967  $\text{cm}^{-1}$  to  $\nu_1$  and the bands at 1093, 1016, and 1005  $\text{cm}^{-1}$  to  $\nu_3$  since the  $\text{PO}_4^{3-}$  symmetric stretching modes typically occur at lower frequencies than the antisymmetric modes [49]. However, the relatively large scattering intensity of the 1005  $\text{cm}^{-1}$  band makes such an assignment questionable. Usually the symmetric stretching modes, especially the  $A_{1g}$  mode of  $\nu_1$ , have large Raman scattering cross sections. Consequently, they are often the most intense bands in this region of the spectrum [37]. Although it is

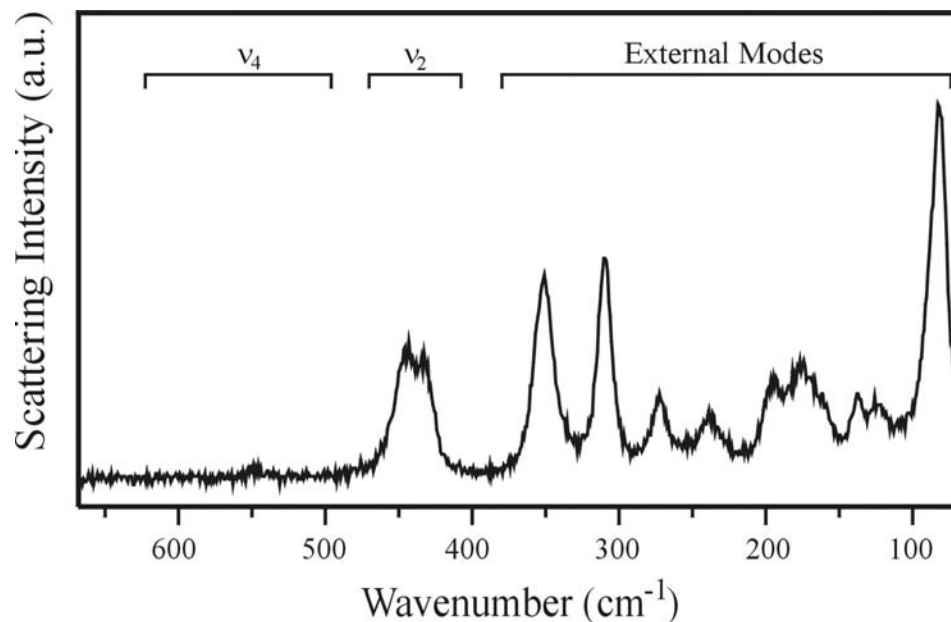


**Figure 3-4:** Raman scattering spectrum of  $\text{LiTi}_2(\text{PO}_4)_3$ .

not uncommon for highly distorted  $\text{PO}_4^{3-}$  anions to produce  $\nu_1$  and  $\nu_3$  bands of comparable intensity (e.g., see the Raman spectrum of  $\text{FePO}_4$  in Chapter 2, Section 2.3.3), the  $\text{PO}_4^{3-}$  anions in  $\text{LiTi}_2(\text{PO}_3)_4$  are regular [26]. In fact, the P–O bond lengths are almost identical in these compounds [26]. Therefore, the very intense band at  $1005 \text{ cm}^{-1}$  is tentatively assigned to predominately  $\nu_1$  motions based on its intensity.

A Raman spectrum of  $\text{LiTi}_2(\text{PO}_4)_3$  between  $650$  and  $75 \text{ cm}^{-1}$  is provided in Fig. 3-4. The antisymmetric  $\text{PO}_4^{3-}$  bending modes ( $\nu_4$ ) are assigned to the very weak bands above  $500 \text{ cm}^{-1}$ , while the bands at  $442$  and  $432 \text{ cm}^{-1}$  are thought to consist mostly of symmetric  $\text{PO}_4^{3-}$  bending motions ( $\nu_2$ ). The highly symmetrical  $\text{PO}_4^{3-}$  anions in  $\text{LiTi}_2(\text{PO}_4)_3$  results in larger intensities for  $\nu_2$  compared to  $\nu_4$ , further supporting the assignment of the strong Raman band at  $1005 \text{ cm}^{-1}$  in Fig. 3-3 to  $\nu_1$ .

The external modes occur below  $\sim 350 \text{ cm}^{-1}$  in the Raman spectrum of  $\text{LiTi}_2(\text{PO}_4)_3$ . In general, it is extremely difficult to assign bands in this region of the spectrum because the modes are highly mixed, consisting of different types of atomic motion. Numerous researchers have had varying degrees of success in assigning these bands through isotopic substitution studies or by comparing a series of isostructural compounds (e.g.,  $\text{LiM}_2(\text{PO}_4)_3$  where  $M = \text{Ge}, \text{Sn}, \text{Ti}, \text{Zr}, \text{Hf}$ ) [37,38,40]. Tarte *et al.* [37] utilized these strategies to identify  $M^{4+}$  translational modes near  $265$  and  $122 \text{ cm}^{-1}$  in a series of  $M^I M^{IV}_2(\text{PO}_4)_3$  compounds. Furthermore, the authors assigned the bands near  $320, 285\text{-}295, 160\text{-}170$  and  $75 \text{ cm}^{-1}$  to  $\text{PO}_4^{3-}$  translational or librational motions [37]. The Raman spectra of  $\text{LiTi}_2(\text{PO}_4)_3$  in Fig. 3-4 and the Raman spectra in Ref. [37] are very similar; hence, the bands at  $270, 137,$  and  $125 \text{ cm}^{-1}$  in the Raman spectrum of  $\text{LiTi}_2(\text{PO}_4)_3$  are tentatively assigned to translational vibrations of the  $\text{Ti}^{4+}$  ions, while the bands at  $348, 308, 233, 193, 172,$  and  $82 \text{ cm}^{-1}$  are assigned to modes that predominantly contain  $\text{PO}_4^{3-}$  motions. Selection rules forbid  $\text{Li}^+$  ion cage modes from being Raman active since  $\text{Li}^+$  ions occupy sites with  $S_6$  symmetry in  $\text{LiTi}_2(\text{PO}_4)_3$ .

Raman scattering spectra of the  $\text{PO}_4^{3-}$  intramolecular stretching vibrations ( $\nu_1$  and  $\nu_3$ ) for A- and B- $\text{Li}_3\text{V}_2(\text{PO}_4)_3$  are presented in Fig. 3-5. The spectra of A- and B- $\text{Li}_3\text{V}_2(\text{PO}_4)_3$  consist of much weaker bands than  $\text{LiTi}_2(\text{PO}_4)_3$ . Four broad bands may be resolved in the spectrum of A- $\text{Li}_3\text{V}_2(\text{PO}_4)_3$  at  $973, 1011, 1055,$  and  $1142 \text{ cm}^{-1}$ , but the bands in B- $\text{Li}_3\text{V}_2(\text{PO}_4)_3$  are much less distinct with the most intense band appearing at  $1021 \text{ cm}^{-1}$  and a broad low-frequency shoulder near  $890 \text{ cm}^{-1}$ . Although the frequencies of the bands in Fig. 3-5 are similar to the Raman spectra of the related systems [36,38-40,42,50], the intensities are much weaker. Indeed, the weak Raman intensities are

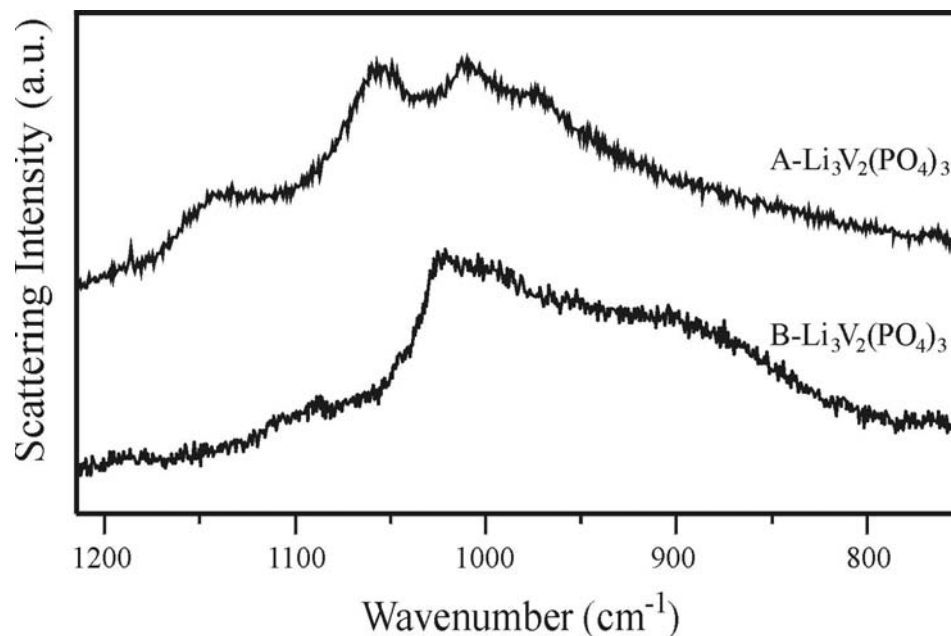


**Figure 3-5:** Raman scattering spectra of A- and B- $\text{Li}_3\text{V}_2(\text{PO}_4)_3$ .

surprising since some of the  $\text{PO}_4^{3-}$  vibrations, especially  $\nu_1$ , typically have large polarizability derivatives and hence strong Raman bands. It is possible that the weak Raman intensities are due a thin disordered surface layer on the particles. Both A- and B- $\text{Li}_3\text{V}_2(\text{PO}_4)_3$  are dark olive green, and samples with a dark coloration often suffer from a significant optical skin effect due to low-lying electronic bands (see discussion in Sec. 2.3.3). Consequently, the laser beam penetrates only a very small distance into the darkly colored particles, and predominantly samples the surface layer. In contrast,  $\text{LiTi}_2(\text{PO}_4)_3$  is white; thus, the excitation laser beam penetrates further in the material resulting in a larger scattering volume. This might explain the weak Raman band intensities even though the XRD data (Fig. 3-1) indicate that the vanadium samples are crystalline. Unfortunately, the low scattering intensities of the vanadium materials will not permit a detailed investigation of lithium (de)intercalation.

3.3.4.2  $\text{Li}_x\text{Ti}_2(\text{PO}_4)_3$  – GITT curves of lithium insertion into  $\text{LiTi}_2(\text{PO}_4)_3$  are provided in Fig. 3-6. Several different research groups have used voltage-composition curves to investigate lithium insertion into this material [26-28], and the results in Fig. 3-6 most closely match the electrochemical data of Delmas and coworkers [26,27]. Lithium ions are inserted into the compound along a quasi-equilibrium potential of 2.5 V vs.  $\text{Li}^+/\text{Li}$ . A high degree of polarization occurs for  $x > 2$  in  $\text{Li}_x\text{Ti}_2(\text{PO}_4)_3$ . Significant polarization is also reported in the early work of Delmas *et al.* [27], but Patoux *et al.* [28] found that the cell polarization strongly depends on the electrode preparation. For instance, little cell polarization is observed when the electrode material is mechanically ball-milled with conductive carbon.

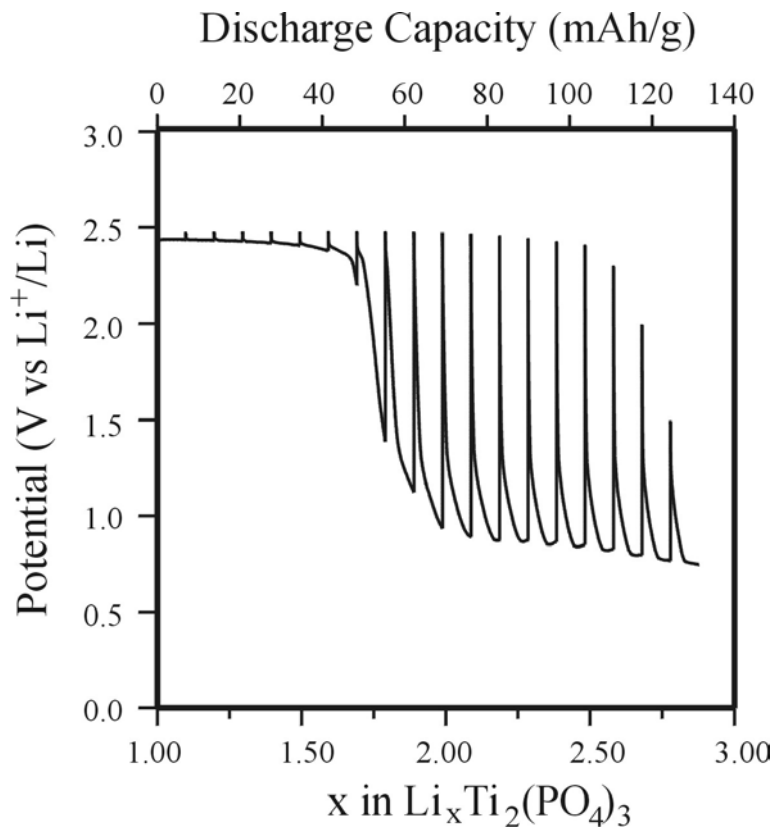


**Figure 3-6:** GITT data for the electrochemical insertion of  $\text{Li}^+$  into  $\text{LiTi}_2(\text{PO}_4)_3$ .

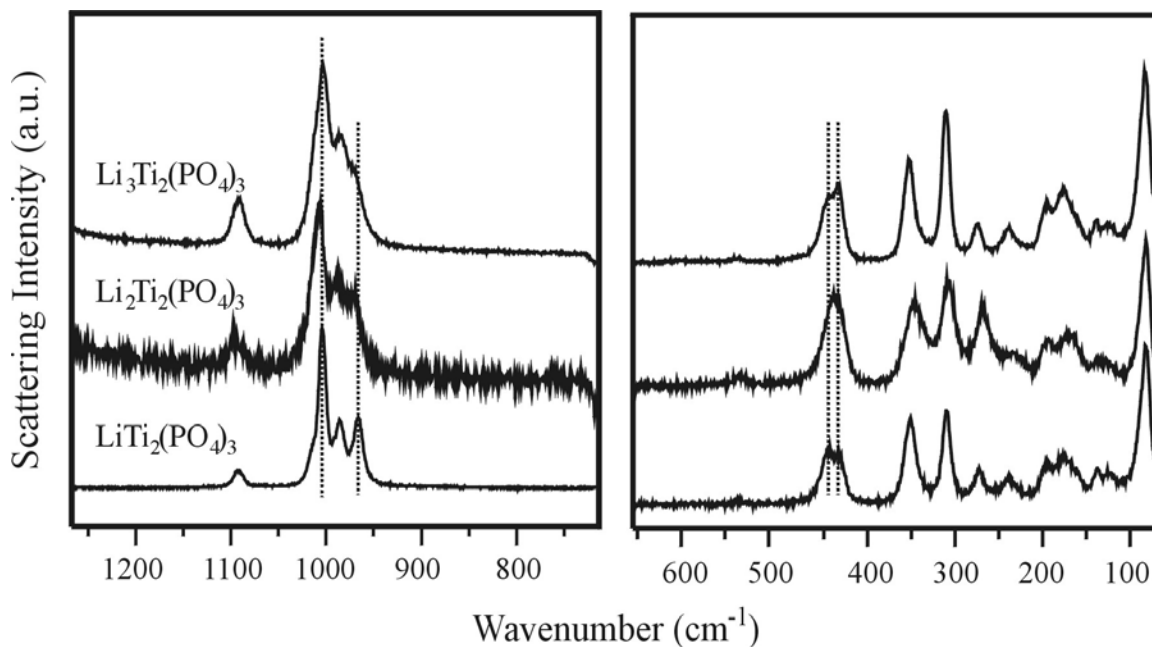


**Figure 3-7:** Raman scattering spectra of  $\text{Li}_x\text{Ti}_2(\text{PO}_4)_3$ . Dashed lines mark some intensity changes as lithium is inserted into the compound.

Raman spectra of  $\text{Li}_x\text{Ti}_2(\text{PO}_4)_3$  ( $x = 1, 2$ , and  $3$ ) are presented in Fig. 3-7. The frequencies of the stretching vibrations ( $1200\text{--}900\text{ cm}^{-1}$ ) do not appear to be affected by the insertion of  $\text{Li}^+$  ions. Nevertheless, the intensity of the  $967\text{ cm}^{-1}$  band diminishes slightly and the  $1093\text{ cm}^{-1}$  band increases in intensity with increasing lithium content. Lithium intercalation produces several noticeable changes in  $\nu_4$ ,  $\nu_2$ , and the external modes. For example, the  $433\text{ cm}^{-1}$  band of  $\nu_2$  increases in intensity at the expense of the  $442\text{ cm}^{-1}$  band, and the frequencies of most of the external modes increase between  $2\text{--}6\text{ cm}^{-1}$  when  $\text{LiTi}_2(\text{PO}_4)_3$  is converted into  $\text{Li}_3\text{Ti}_2(\text{PO}_4)_3$ . In addition, the intensities of several bands are affected by lithium insertion. For instance, the  $348$  and  $308\text{ cm}^{-1}$  bands have approximately the same intensity in  $\text{LiTi}_2(\text{PO}_4)_3$ , but the  $310\text{ cm}^{-1}$  is more intense than the  $353\text{ cm}^{-1}$  band in  $\text{Li}_3\text{Ti}_2(\text{PO}_4)_3$ . All of the bands appear to broaden somewhat as



lithium intercalation proceeds. This might indicate some degree of local disordering about the  $\text{PO}_4^{3-}$  anions as  $\text{Li}^+$  is inserted into the cathode.

### 3.3.5 Infrared Spectroscopy

**3.3.5.1 Pure Materials** – Infrared absorption spectra of A- and B- $\text{Li}_3\text{V}_2(\text{PO}_4)_3$ , B- $\text{Na}_3\text{V}_2(\text{PO}_4)_3$ , and  $\text{LiTi}_2(\text{PO}_4)_3$  are presented in Fig. 3-8. In general, the spectra of all four compounds agree very well with previously published data on related  $(\text{M}^{\text{I}})_3(\text{M}^{\text{II}})_2(\text{PO}_4)_3$  and  $(\text{M}^{\text{I}})_3(\text{M}^{\text{II}})_2(\text{PO}_4)_y(\text{AsO}_4)_{1-y}$  ( $\text{M}^{\text{I}} = \text{Li, Na}$  and  $\text{M}^{\text{II}} = \text{Cr, Fe, In, Sc, Ti}$ ) systems [36,38-40,42,44,50]. Intense, overlapping bands ranging from 700 to 1400  $\text{cm}^{-1}$  dominate each mid-IR spectrum (1500–400  $\text{cm}^{-1}$ ). Weaker bands occur between 700 and 450  $\text{cm}^{-1}$  of Fig. 3-8. The former bands are assigned to  $\nu_1$  and  $\nu_3$ , whereas bands in the latter region

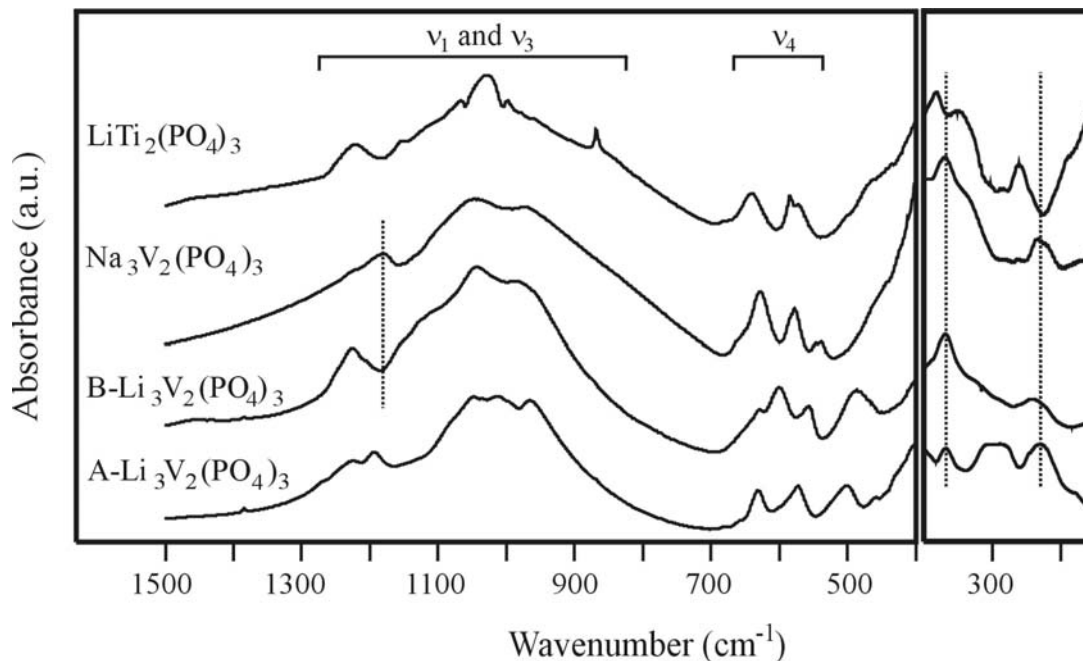


**Figure 3-8:** Infrared absorption spectra of A- and B- $\text{Li}_3\text{V}_2(\text{PO}_4)_3$ ,  $\text{Na}_3\text{V}_2(\text{PO}_4)_3$ , and  $\text{LiTi}_2(\text{PO}_4)_3$ . Between 1500–400  $\text{cm}^{-1}$  and 400–150  $\text{cm}^{-1}$  spectra are collected with KBr (mid-IR) and Mylar (far-IR) beamsplitters, respectively.

are assigned to  $\nu_4$ . Lattice modes and the  $\nu_2$  vibrations are observed below  $400\text{ cm}^{-1}$ .

Nine bands may be easily identified in the  $\text{PO}_4^{3-}$  stretching region and six bands are observed in the  $\text{PO}_4^{3-}$  bending region in the infrared spectrum of  $\text{A-Li}_3\text{V}_2(\text{PO}_4)_3$ . Fewer bands are observed in the mid-IR spectra of  $\text{B-Li}_3\text{V}_2(\text{PO}_4)_3$  and  $\text{Na}_3\text{V}_2(\text{PO}_4)_3$  than  $\text{A-Li}_3\text{V}_2(\text{PO}_4)_3$ . This is consistent with the predictions from the factor group analysis in Table III-II. Namely,  $\text{A-Li}_3\text{V}_2(\text{PO}_4)_3$  is of a lower symmetry than either  $\text{Na}_3\text{V}_2(\text{PO}_4)_3$  or  $\text{B-Li}_3\text{V}_2(\text{PO}_4)_3$  thereby producing a larger set of vibrational modes. The discrepancy between the number of experimentally detected bands and the theoretical predictions is probably due to coincidental band overlap in the very broad  $\nu_1$  and  $\nu_3$  region and weak dipole moment derivatives for some of the factor group multiplets.

The infrared spectrum of  $\text{LiTi}_2(\text{PO}_4)_3$  (Fig. 3-8) contains a sharp band at  $869\text{ cm}^{-1}$  and broad features between  $700$  and  $850\text{ cm}^{-1}$ . The frequencies of these bands are somewhat lower than expected for  $\text{PO}_4^{3-}$  stretching modes. In fact, bands in this region of the spectrum are often due to condensed phosphate groups such as  $\text{P}_2\text{O}_7^{4-}$  or extended polyphosphate structures [37]. However, there are no bands near  $750\text{ cm}^{-1}$  in the infrared spectrum to indicate the presence of bridging P–O–P groups. Raman spectroscopy is particularly useful in identifying condensed phosphates as the P–O–P bending motions yield intense bands between  $700$  and  $800\text{ cm}^{-1}$  in the Raman spectrum. The lack of any spectral activity in this region of Fig. 3-3 coupled with the absence of any impurity phases detected with powder XRD (Fig. 3-1) strongly argues that the  $\text{LiTi}_2(\text{PO}_4)_3$  sample does not contain a significant fraction of condensed phosphate groups.

There are several noteworthy differences between the spectrum of  $\text{Na}_3\text{V}_2(\text{PO}_4)_3$  and  $\text{B-Li}_3\text{V}_2(\text{PO}_4)_3$ . For instance, a band at  $1180\text{ cm}^{-1}$  in  $\text{B-Na}_3\text{V}_2(\text{PO}_4)_3$  shifts to  $1226$

$\text{cm}^{-1}$  in  $\text{B-Li}_3\text{V}_2(\text{PO}_4)_3$  (denoted with a dashed line on Fig. 3-8), and the bandwidth of the  $1045 \text{ cm}^{-1}$  band becomes smaller when  $\text{Na}^+$  is exchanged for  $\text{Li}^+$ . Differences in frequencies of some  $\nu_3$  modes may be primarily due to interactions between the monovalent cations and the phosphate anions. Lithium ions have a larger charge density than  $\text{Na}^+$  ions and can form stronger bonds with the  $\text{PO}_4^{3-}$  anions than  $\text{Na}^+$ . Therefore, the  $\text{Li}^+$  ions exert a stronger perturbation on the vibrational modes of the  $\text{PO}_4^{3-}$  anions, which results in greater factor group splitting effects for  $\text{B-Li}_3\text{V}_2(\text{PO}_4)_3$  compared to  $\text{Na}_3\text{V}_2(\text{PO}_4)_3$ .

A new band also appears at  $488 \text{ cm}^{-1}$  in  $\text{B-Li}_3\text{V}_2(\text{PO}_4)_3$  that was not present in  $\text{Na}_3\text{V}_2(\text{PO}_4)_3$ . The frequency and relative intensity of this band is very similar to the  $502 \text{ cm}^{-1}$  band in the spectrum of  $\text{A-Li}_3\text{V}_2(\text{PO}_4)_3$ . Similar bands have been observed in infrared spectra of monoclinic  $\text{Li}_3\text{M}_2(\text{PO}_4)_3$  ( $\text{M} = \text{Sc}$  and  $\text{Fe}$ ) [38,40] and orthorhombic  $\text{LiMPO}_4$  ( $\text{M} = \text{Mn}$ ,  $\text{Fe}$ ,  $\text{Co}$ ,  $\text{Ni}$ ) compounds [51,52]. In fact,  $^6\text{Li}/^7\text{Li}$  isotope shifts were effectively used to argue that this band is a  $\text{Li}^+$  ion cage mode in the monoclinic [38,40] and orthorhombic materials [51]. The strong similarities in the frequencies and relative intensities between the  $488 \text{ cm}^{-1}$  band in the infrared spectrum of  $\text{B-Li}_3\text{V}_2(\text{PO}_4)_3$  and the  $\text{Li}^+$  ion cage modes in  $\text{Li}_3\text{Sc}_2(\text{PO}_4)_3$  and  $\text{LiMPO}_4$  (cf., Fig. 3-8 to Refs. [38,40,51]) suggests that this band is probably also a  $\text{Li}^+$  ion cage mode. Tarte *et al.* [37] was unable to identify any band in the infrared spectrum of  $\text{LiTi}_2(\text{PO}_4)_3$  (between  $150\text{-}350 \text{ cm}^{-1}$ ) that contained a large amount of  $\text{Li}^+$  ion motion with  $^6\text{Li}/^7\text{Li}$  isotope shifts even though these modes are infrared active for  $\text{LiTi}_2(\text{PO}_4)_3$ .

The vanadium containing compounds all have similar features below  $450 \text{ cm}^{-1}$ , especially for the rhombohedral materials. For example, the bands between  $425$  and  $300$

$\text{cm}^{-1}$  occur at essentially the same frequency in each material. The far-IR spectrum of  $\text{LiTi}_2(\text{PO}_4)_3$  also contains at least three intense bands at 464, 381, and  $348 \text{ cm}^{-1}$ . However, the lower frequency band occurs at somewhat higher frequencies than in either  $\text{Na}_3\text{V}_2(\text{PO}_4)_3$  or  $\text{B-Li}_3\text{V}_2(\text{PO}_4)_3$ . There is some disagreement concerning the assignment of the bands below  $400 \text{ cm}^{-1}$ . The  $\nu_2$  modes are expected to occur at these frequencies; however, it is difficult to assign these modes with confidence because some of the external modes may also occur at these frequencies. Furthermore, Barj *et al.* [36] assigned the bands between 200 and  $250 \text{ cm}^{-1}$  to either translatory or librational motions of the phosphate anions in  $\text{Na}_3\text{M}_2(\text{PO}_4)_3$  ( $\text{M} = \text{Fe}$  and  $\text{Cr}$ ) compounds, yet Tarte *et al.* [37] assigned these bands to predominantly  $\text{M}^{4+}$  translatory motions. The dependence of the  $\sim 225 \text{ cm}^{-1}$  band on the nature of the transition metal ion (Fig. 3-8) strongly indicates that this band contains a large amount of vanadium or titanium motion.

3.3.5.2 Monoclinic  $\text{Li}_x\text{V}_2(\text{PO}_4)_3$  – Electrochemical data for  $\text{A-Li}_3\text{V}_2(\text{PO}_4)_3$  are presented in Fig. 3-9. The results agree very well with previous voltage measurements for this system [12-14]. All three  $\text{Li}^+$  ions may be extracted over four two-phase voltage plateaus. The solid solution regime is followed by two-phase transitions when the third  $\text{Li}^+$  ion is reinserted (region V).

*Ex situ* mid-IR spectra of  $\text{A-Li}_x\text{V}_2(\text{PO}_4)_3$  ( $0 \leq x \leq 3$ ) are collected at various points along the electrochemical curves and are presented in Fig. 3-10. The stretching and bending modes of the  $\text{PO}_4^{3-}$  anions are affected when the cells are charged from their open circuit voltage (OCV) to 3.90 V. For example, the  $573 \text{ cm}^{-1}$  band vanishes and the  $501 \text{ cm}^{-1}$  band becomes a high frequency shoulder on a band at  $473 \text{ cm}^{-1}$ . Moreover, five

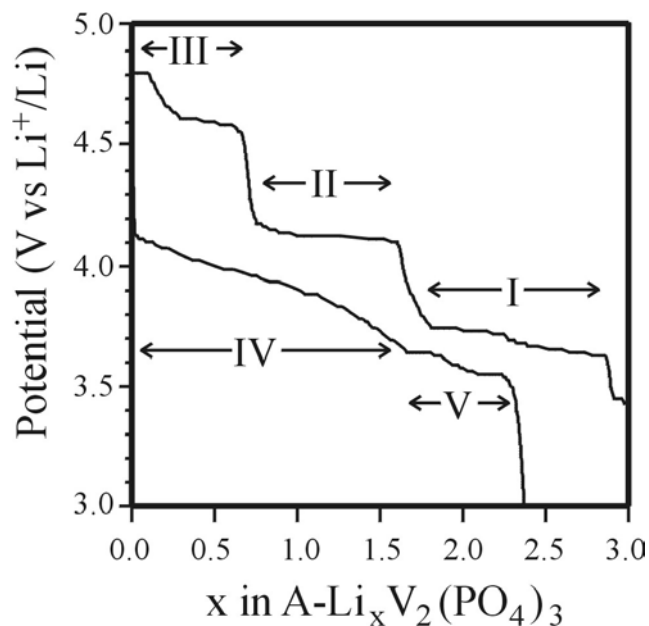


**Figure 3-9:** Electrochemical cycling of A-Li<sub>3</sub>V<sub>2</sub>(PO<sub>4</sub>)<sub>3</sub>.

$\nu_3$  modes may be resolved in the 3.66 V sample (1083, 1048, 1035, 1015, and 994  $\text{cm}^{-1}$ ), whereas only three bands at 1083, 1045 and 1021  $\text{cm}^{-1}$  are identified at 3.90 V.

Continuing to charge the cells to 4.09 V produces subtle changes in the  $\text{PO}_4^{3-}$  stretching modes, particularly for  $\nu_3$ . For instance, in the 3.90 V sample there are a number of bands between 1270 and 1100  $\text{cm}^{-1}$ , but there are only three bands (1256, 1230, and 1163  $\text{cm}^{-1}$ ) in the 4.09 V sample. At 4.35 V the cells enter the final electrochemical plateau. At this voltage, two bands at 618 and 595  $\text{cm}^{-1}$  replace the two  $\nu_4$  bands at 664 and 644  $\text{cm}^{-1}$ . Minor frequency shifts are observed for some of the lower intensity bending vibrations when the cells are charged to 4.60 V, and further charging to 4.80 V causes significant broadening in all  $\text{PO}_4^{3-}$  bands. In general, the spectral changes that occurred during  $\text{Li}^+$  extraction are reversed upon reinsertion of the  $\text{Li}^+$  ions. Indeed, the infrared spectra measured during the first discharge are very similar to the spectra recorded when

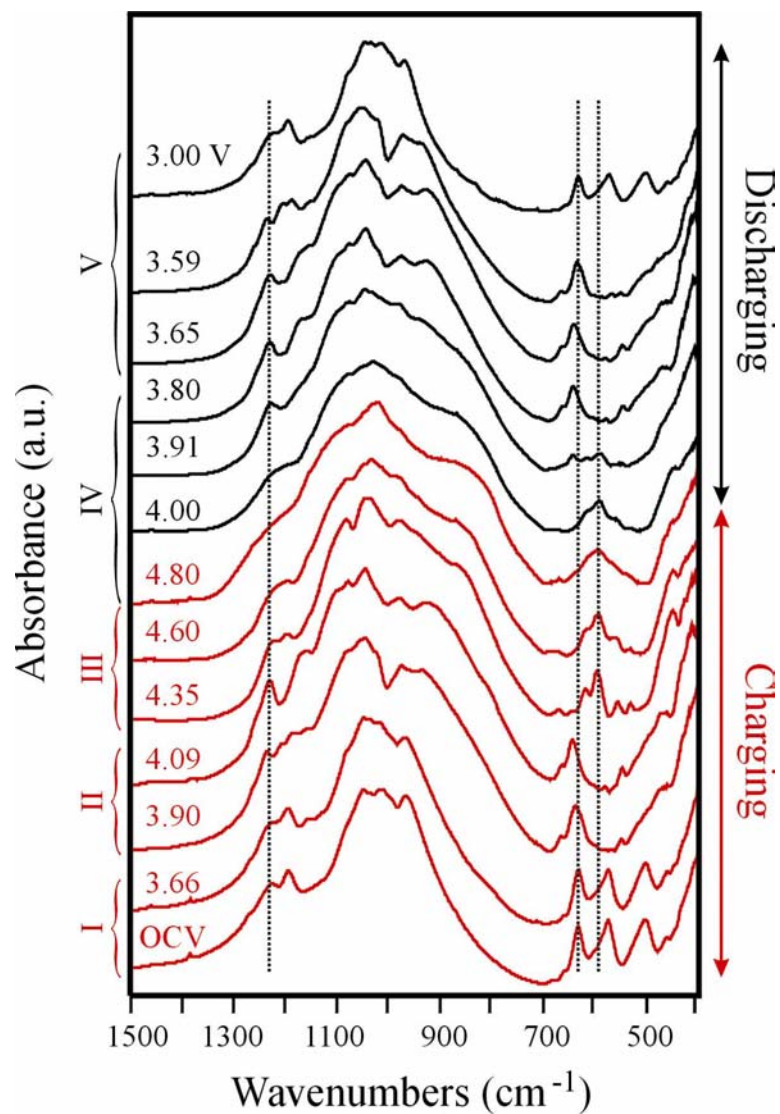


**Figure 3-10:** Infrared absorption spectra of  $A\text{-Li}_x\text{V}_2(\text{PO}_4)_3$  recorded at different points along the first cycle (black = discharge step and red = charge step). The Roman numerals correspond to the different regions of Fig. 3-9.

the cells were charged to 4.80 V. The infrared spectrum of the fully discharged sample (3.00 V) is very close to the spectrum of the pristine material.

3.3.5.3 Rhombohedral  $\text{Li}_x\text{V}_2(\text{PO}_4)_3$  – Fig. 3-11 contains electrochemical cycling data for  $\text{B-Li}_3\text{V}_2(\text{PO}_4)_3$ . The charging and discharging curves agree very well with the previously published data of Gaubicher *et al.* [15] and Morcrette *et al.* [20].

Approximately two  $\text{Li}^+$  ions could be electrochemically extracted over a single voltage plateau. Some polarization is exhibited in the cells for lithium concentrations between 1.75 and 1.25, and fully charged samples are obtained after the cathodes are potentiostatically charged at 4.30 V. Lithium ions may be electrochemically reinserted into  $\text{B-LiV}_2(\text{PO}_4)_3$  over a single voltage plateau at approximately 3.70 V.

*Ex situ* mid-IR spectra are recorded at various points along the charging and discharging curves of  $\text{B-Li}_3\text{V}_2(\text{PO}_4)_3$ , and these spectra are presented in Fig. 3-12. Minor

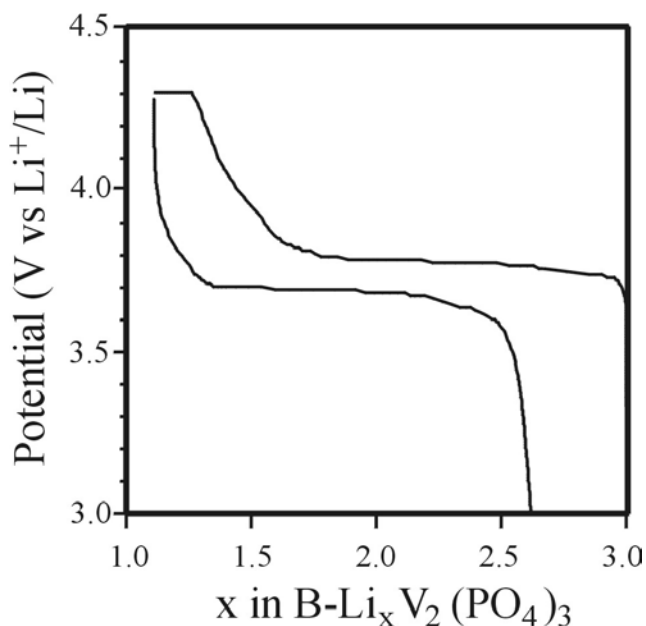


**Figure 3-11:** Electrochemical cycling of  $\text{B-Li}_3\text{V}_2(\text{PO}_4)_3$ .

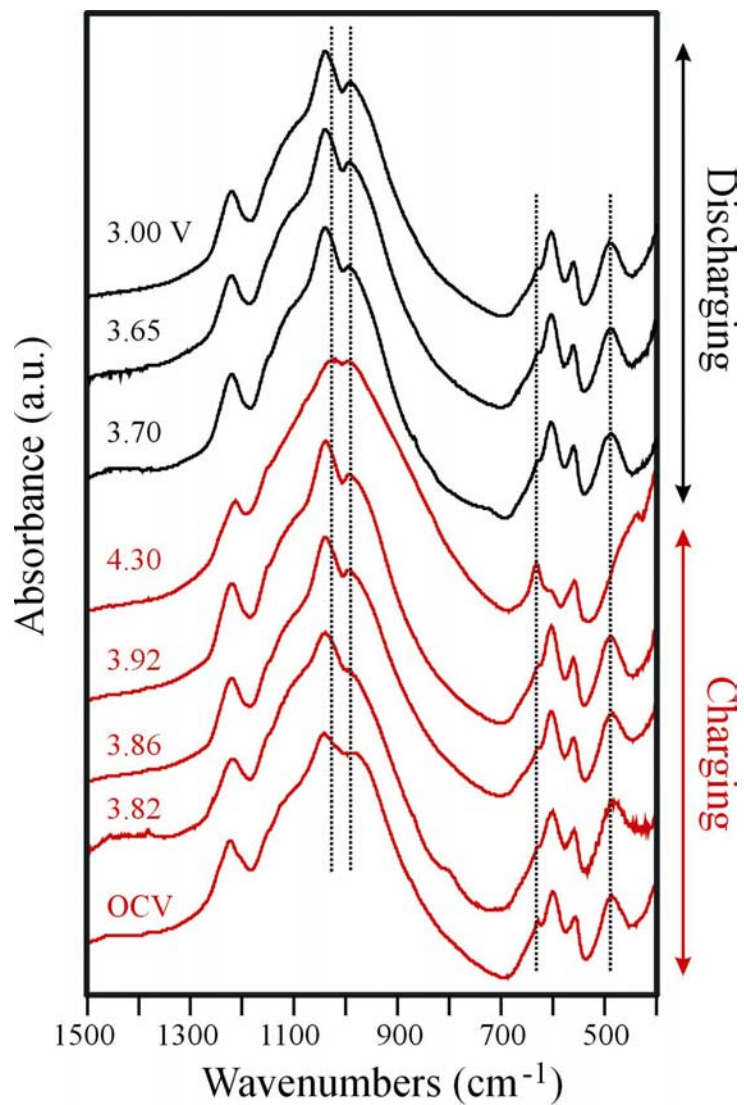


**Figure 3-12:** Infrared absorption spectra of  $B\text{-Li}_x\text{V}_2(\text{PO}_4)_3$  recorded at different points along the first cycle (black = discharge step and red = charge step).



changes occur in the infrared spectra when the samples are charged to 3.92 V. For example, the frequencies and intensities of the bands between 700 and 450  $\text{cm}^{-1}$  undergo small changes over this potential range. For example, the 488  $\text{cm}^{-1}$  band slightly decreases in intensity with respect to the 600  $\text{cm}^{-1}$  band. When the voltage is further increased to 4.30 V the relative intensities of the bands near 630 and 600  $\text{cm}^{-1}$  are reversed and a new band at 438  $\text{cm}^{-1}$  engulfs the band at 488  $\text{cm}^{-1}$ . The  $\text{PO}_4^{3-}$  stretching modes are also affected by the extraction of  $\text{Li}^+$  ions. For instance, the bands at 1044 and 970  $\text{cm}^{-1}$  in  $\text{B-Li}_3\text{V}_2(\text{PO}_4)_3$  begin to converge when the cells are charged to 4.30 V, and the  $\nu_3$  component at 1226  $\text{cm}^{-1}$  in the uncharged material shifts to 1216  $\text{cm}^{-1}$  in the 4.30 V sample.

Dramatic spectral changes occur when the cells are discharged from 4.30 to 3.70 V. For instance, the relative intensities of the bands at 629 and 604  $\text{cm}^{-1}$  invert, and the band at 488  $\text{cm}^{-1}$  suddenly reappears. Additionally, the 1027  $\text{cm}^{-1}$  band shifts to 1041  $\text{cm}^{-1}$  as the relative intensity of the 995  $\text{cm}^{-1}$  band decreases. The infrared spectra remain essentially unchanged as more  $\text{Li}^+$  ions are re-inserted into the cathode. The infrared spectrum of the fully discharged sample (3.00 V) does not match that of the pristine material; however, this might be because the composition of the 3.00 V sample is  $\text{Li}_{2.62}\text{V}_2(\text{PO}_4)_3$  rather than  $\text{Li}_3\text{V}_2(\text{PO}_4)_3$ .

3.3.5.4  $\text{Li}_x\text{Ti}_2(\text{PO}_4)_3$  – The frequencies and relative intensities of the  $\nu_1$  and  $\nu_3$  modes are marginally affected by the insertion of  $\text{Li}^+$  ions (Fig. 3-13). For example, the 1222  $\text{cm}^{-1}$  band in  $\text{LiTi}_2(\text{PO}_4)_3$  shifts to 1213  $\text{cm}^{-1}$  in  $\text{Li}_3\text{Ti}_2(\text{PO}_4)_3$ . In addition, the intensity of the 869  $\text{cm}^{-1}$  band decreases between  $\text{LiTi}_2(\text{PO}_4)_3$  and  $\text{Li}_2\text{Ti}_2(\text{PO}_4)_3$ , and all of the stretching

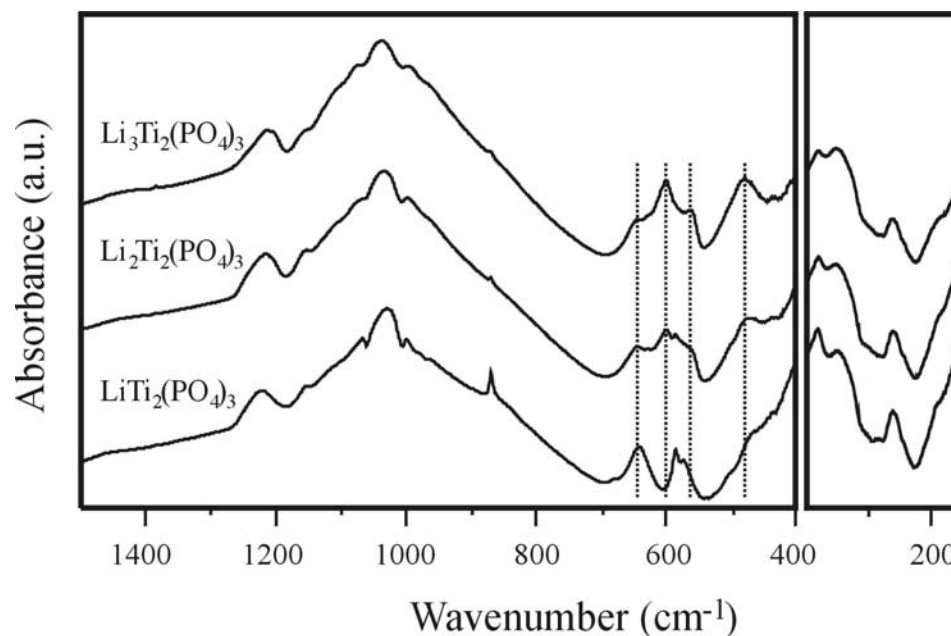


**Figure 3-13:** Infrared absorption spectra of  $\text{Li}_x\text{Ti}_2(\text{PO}_4)_3$ . Between  $1500\text{--}400\text{ cm}^{-1}$  and  $400\text{--}150\text{ cm}^{-1}$  spectra are collected with KBr (mid-IR) and Mylar (far-IR) beamsplitters, respectively.

modes in the infrared spectra appear to broaden with lithium intercalation. The band broadening of  $\nu_1$  and  $\nu_3$  in Fig. 3-13 agrees with the broadening observed in the Raman spectra (Fig. 3-7). As noted earlier, this is probably due to a small degree of disordering in the  $\text{PO}_4^{3-}$  anions as lithium is inserted in the compound. The  $\nu_2$  and  $\nu_4$  modes are more sensitive to lithium insertion than the stretching modes. For example, a new band appears at  $600\text{ cm}^{-1}$  in  $\text{Li}_2\text{Ti}_2(\text{PO}_4)_3$ , which becomes the dominant feature of the  $\nu_4$  vibrational multiplet when the cells are fully discharged. In addition, new bands may be easily discerned in the infrared spectrum of  $\text{Li}_3\text{Ti}_2(\text{PO}_4)_3$  at  $643$ ,  $600$ , and  $561\text{ cm}^{-1}$ . In particular, a new band at  $478\text{ cm}^{-1}$  appears in  $\text{Li}_2\text{Ti}_2(\text{PO}_4)_3$  and increases in intensity with further lithium insertion. The frequency and relative intensity of this band is very similar to the  $\text{Li}^+$  cage modes of A- and B- $\text{Li}_3\text{V}_2(\text{PO}_4)_3$ ; therefore, the  $478\text{ cm}^{-1}$  band is assigned as a  $\text{Li}^+$  cage mode of  $\text{Li}_3\text{Ti}_2(\text{PO}_4)_3$ .

## 3.4 Discussion

### 3.4.1 Monoclinic $\text{Li}_x\text{V}_2(\text{PO}_4)_3$

For ease of discussion, samples of  $\text{A-Li}_x\text{V}_2(\text{PO}_4)_3$  prepared by deinserting  $\text{Li}^+$  ions (charging) are denoted  $\text{D-Li}_x\text{V}_2(\text{PO}_4)_3$  and samples that are synthesized by reinserting  $\text{Li}^+$  ions into the empty  $[\text{V}_2(\text{PO}_4)_3]_\infty^{3-}$  framework (discharging) are identified as  $\text{R-Li}_x\text{V}_2(\text{PO}_4)_3$ . Furthermore, the  $\text{Li}^+$  sites are labeled according to the conventions established by Yin *et al.* [19].

The intramolecular stretching and bending vibrations of the  $\text{PO}_4^{3-}$  anions are sensitive to the extraction of  $\text{Li}^+$  ions in the cathodes. Indeed, these spectral changes are particularly obvious in the bending modes (see Fig. 3-10 between 700 and 400  $\text{cm}^{-1}$ ). Based on these changes, the infrared spectra may be grouped into several distinct regions on the voltage-composition curve (viz., I-V of Fig. 3-9). Although the space group of the compound does not change throughout the entire lithium deintercalation process [18-20], powder neutron diffraction experiments by Yin and co-workers reveal significant differences in the lithium and vanadium coordination environments and Li–O and V–O bond lengths in each of these compositional domains; specific details concerning these changes may be found in Ref. [19].

Since the lithium and vanadium cations are coordinated to the oxygen atoms of the  $\text{PO}_4^{3-}$  anions, any variations in the Li–O and V–O bonding geometry will directly affect the vibrational modes of the  $\text{PO}_4^{3-}$  anions. Therefore, the observed differences in the frequencies and intensities of the intramolecular  $\text{PO}_4^{3-}$  stretching and bending modes in each region are probably due to subtle changes in the  $\text{Li}^+$  ion coordination number and

the Li–O and V–O bond distances for each intermediate composition. For example, the infrared spectra of the 3.90 and 4.35 V samples are dissimilar (Fig. 3-10) because the lithium and vanadium cations are coordinated to the  $\text{PO}_4^{3-}$  anions differently in these two materials. The 3.90 V sample has an estimated composition of  $\text{D-Li}_{2.1}\text{V}_2(\text{PO}_4)_3$ . In this material, the  $\text{Li}^+$  ions are distributed between two pseudosymmetric, four-coordinate sites [Li(1) and Li(2b)] and the  $\text{V}^{3+}/\text{V}^{4+}$  ions are charged ordered along the (010) axis [19]. However, in the 4.35 V sample ( $\text{D-Li}_{0.9}\text{V}_2(\text{PO}_4)_3$ ), the remaining  $\text{Li}^+$  ion is in a distorted trigonal bipyramid [Li(2c)] that is related to the Li(2) site from  $\text{A-Li}_3\text{V}_2(\text{PO}_4)_3$ , and the average V–O bond length has slightly decreased [19].

A number of researchers have detected a slight loss of crystallinity in fully charged  $\text{A-V}_2(\text{PO}_4)_3$  with powder neutron and X-ray diffraction methods [13,19]. Infrared spectroscopy is very sensitive to the local environment of the  $\text{PO}_4^{3-}$  anions (i.e., the immediate potential energy environment of the  $\text{PO}_4^{3-}$  ion), and might be useful in investigating the structure of  $\text{A-V}_2(\text{PO}_4)_3$ . Pronounced band broadening is observed when the final  $\text{Li}^+$  ion is extracted (4.35 to 4.80 V in Fig. 3-10). This suggests that the  $\text{PO}_4^{3-}$  anions become locally disordered even though the global structure of the compound remains crystalline according to the diffraction experiments [19,20]. The local structure of  $\text{A-V}_2(\text{PO}_4)_3$  is further investigated by comparing it to a  $\text{V}_2\text{O}_5\text{-P}_2\text{O}_5$  glass of the same composition (Fig. 3-14). The infrared spectrum of the vitreous sample contains a very broad band centered near  $1210\text{ cm}^{-1}$  and four other bands at 1079, 1031, 912, and  $750\text{ cm}^{-1}$  (indicated by dashed lines in the figure). These results are consistent with previous spectroscopic investigations into  $\text{V}_2\text{O}_5\text{-P}_2\text{O}_5$  glasses with the same nominal composition

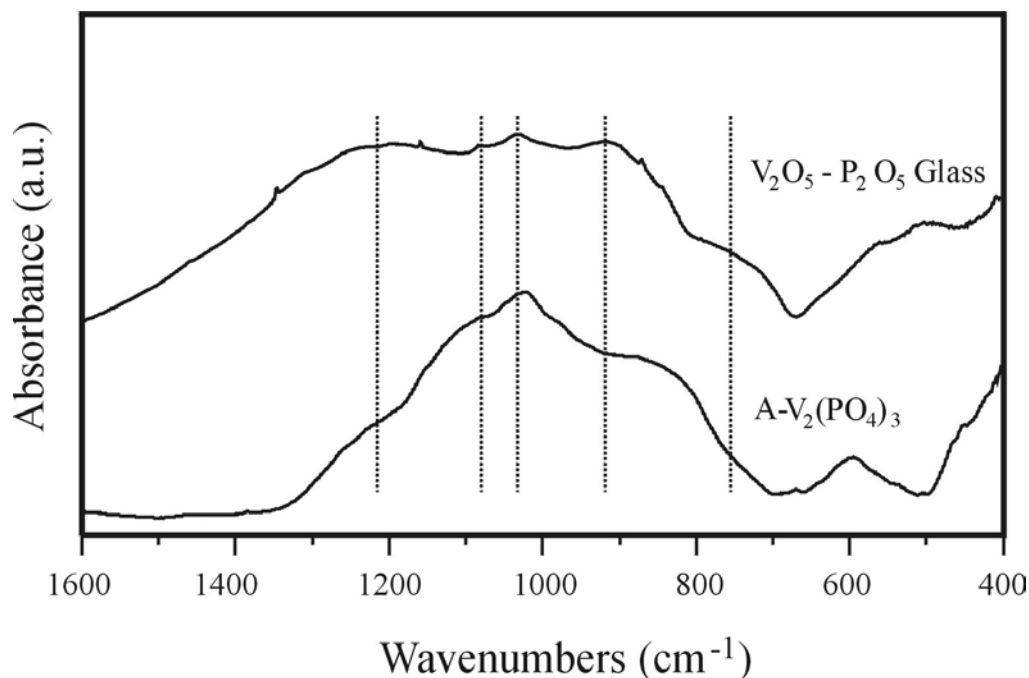


**Figure 3-14:** Infrared absorption spectra of  $A-V_2(PO_4)_3$  and a  $V_2O_5-P_2O_5$  glass with a nominal composition of 2:3.

[22]. The frequencies of the  $PO_4^{3-}$  stretching modes for  $A-V_2(PO_4)_3$  and  $V_2O_5-P_2O_5$  are similar between 1300 and 950  $cm^{-1}$ ; however, the relative intensity of the 1210  $cm^{-1}$  band is much smaller in  $A-V_2(PO_4)_3$  compared to the vitreous sample. There are some differences in the frequencies and intensities of the stretching vibrations between 950 and 750  $cm^{-1}$ , and the bending modes are dissimilar in the two compounds. Bending modes are often more sensitive to subtle changes in the local environment of the  $PO_4^{3-}$  anions than stretching modes, and the spectroscopic differences in these vibrations suggest that the local structure of  $A-V_2(PO_4)_3$  is quite different from the  $V_2O_5-P_2O_5$  glass. The bandwidths are also much larger for the glass compared to  $A-V_2(PO_4)_3$ . This indicates much less disorder in  $A-V_2(PO_4)_3$  compared to the vitreous material. This is probably related to the global structure that is retained in the delithiated compound.

Single-phase behavior is observed when the first two  $\text{Li}^+$  ions are reinserted into the empty  $[\text{V}_2(\text{PO}_4)]_\infty^{3-}$  framework (region IV in Fig. 3-9). In the early stages of lithium intercalation, the vibrational multiplet structure of the  $\text{PO}_4^{3-}$  vibrations begins to reappear (Fig. 3-10) indicating that the  $\text{PO}_4^{3-}$  anions become more ordered. The 4.00 V spectrum (prepared by  $\text{Li}^+$  insertion) is very similar to the 4.60 V spectrum from region III. At these compositions ( $x < 1$ ), crystallographic data indicate that  $\text{Li}^+$  ions are distributed between a four-coordinate site (similar to Li(1) in  $\text{D-Li}_2\text{V}_2(\text{PO}_4)_3$ ) and a five-coordinate site that is nearly identical to the L(2c) site in  $\text{D-LiV}_2(\text{PO}_4)_3$  [19]. According to  $^7\text{Li}$  NMR data of  $\text{R-Li}_x\text{V}_2(\text{PO}_4)_3$ , Li(2c) sites have a greater population than Li(1) sites over the compositional range  $0 \leq x \leq 1.25$  [19]. Consequently, the spectra recorded at 4.00 and 4.60 V contain very similar features due to the similar local environments of the  $\text{PO}_4^{3-}$  anions in these two compounds.

Discharging to 3.91 V produces a material with an approximate composition of  $\text{R-LiV}_2(\text{PO}_4)_3$ . Here,  $^7\text{Li}$  NMR data suggest that  $\text{Li}^+$  ions are randomly distributed over Li(1) and Li(2c) sites with occupation factors of 0.4 and 0.6, respectively [19]. Since these two sites are each characteristic of a different sample composition (viz.,  $x = 1.0$  and 2.0 in  $\text{D-Li}_x\text{V}_2(\text{PO}_4)_3$ ), the infrared spectrum of the 3.91 V material appears as a superposition of the  $\text{D-Li}_{0.9}\text{V}_2(\text{PO}_4)_3$  (4.35 V) and  $\text{D-Li}_{2.1}\text{V}_2(\text{PO}_4)_3$  (3.90 V) spectra with the relative intensities of the bands governed by the site occupancy of the  $\text{Li}^+$  ions.

At  $x \approx 1.25$ , the site occupation factors became equal and further lithium intercalation fills both sites at the same rate [19]. Moreover, powder neutron diffraction and  $^7\text{Li}$  NMR data show that the five-coordinate Li(2c) site converts into the four-coordinate Li(2b) site, leaving  $\text{R-Li}_2\text{V}_2(\text{PO}_4)_3$  indistinguishable from  $\text{D-Li}_2\text{V}_2(\text{PO}_4)_3$  [19].

Indeed, the infrared spectra of the 3.59 and 3.66 V samples are quite similar. Two-phase behavior then resumes for lithium concentrations greater than  $x = 2$  (region V on Fig. 3-9). The infrared data are consistent with this model in that the spectra from region V are very similar to the spectra recorded in regions I and II. Moreover, the spectrum of the fully discharged sample (R- $\text{Li}_{2.4}\text{V}_2(\text{PO}_4)_3$ ) is identical to the spectrum of D- $\text{Li}_{2.5}\text{V}_2(\text{PO}_4)_3$  (3.66 V sample), further highlighting the excellent reversibility of this system.

### 3.4.2 Rhombohedral $\text{Li}_x\text{V}_2(\text{PO}_4)_3$ and $\text{Li}_x\text{Ti}_2(\text{PO}_4)_3$

Gaubicher *et al.* [15] and Morcrette *et al.* [20] used diffraction techniques to suggest similar  $\text{Li}^+$  extraction mechanisms for B- $\text{Li}_3\text{V}_2(\text{PO}_4)_3$  and  $\text{LiTi}_2(\text{PO}_4)_3$ .

Therefore, a spectroscopic comparison between the two compounds may be interesting. Infrared spectra of the  $\text{Li}_x\text{Ti}_2(\text{PO}_4)_3$  and B- $\text{Li}_x\text{V}_2(\text{PO}_4)_3$  end-members ( $x = 1$

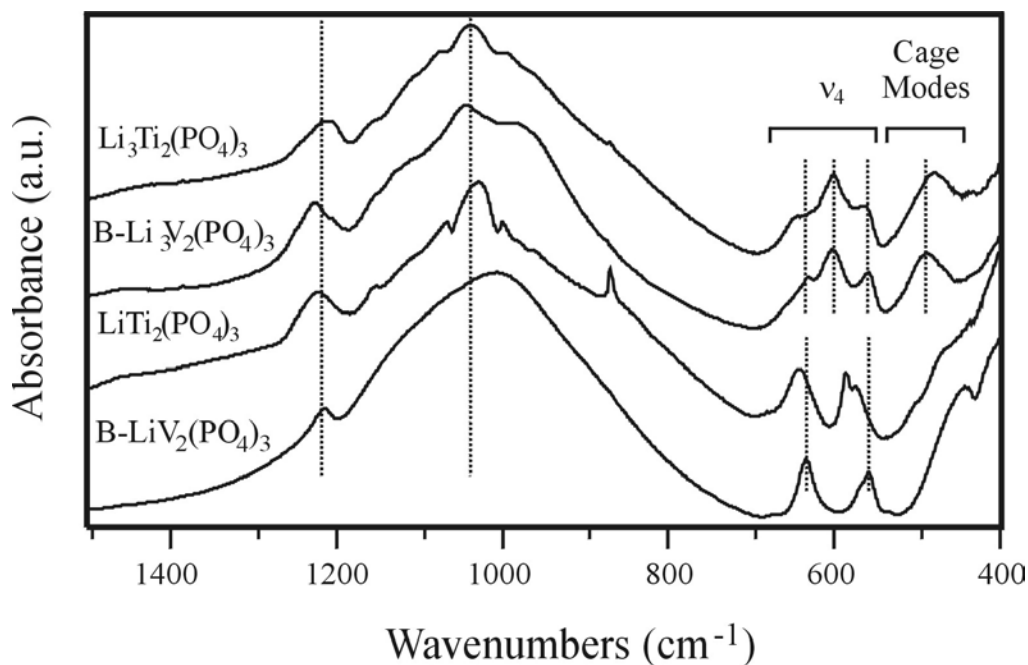


**Figure 3-15:** Infrared absorption spectra comparing  $\text{Li}_x\text{Ti}_2(\text{PO}_4)_3$  and B- $\text{Li}_x\text{V}_2(\text{PO}_4)_3$  where  $x = 1$  and 3.

and 3) are presented in Fig. 3-15. There are strong similarities between the spectra of these two materials, especially between 400 and 700  $\text{cm}^{-1}$ . Both of the fully intercalated compounds contain  $\text{Li}^+$  ion cage modes in the infrared spectra (478  $\text{cm}^{-1}$  for  $\text{Li}_3\text{Ti}_2(\text{PO}_4)_3$  and 488  $\text{cm}^{-1}$  for  $\text{B-Li}_3\text{V}_2(\text{PO}_4)_3$ ). In these two compounds, all three  $\text{Li}^+$  ions reside in highly distorted tetrahedral sites within the 8-coordinate M(2) cavities. These tetrahedral sites are denoted as M(3) to distinguish them from the larger M(2) cavities. Aatiq *et al.* [26] used nuclear difference Fourier maps calculated from neutron diffraction data to precisely determine the  $\text{Li}^+$  ion positions in  $\text{Li}_3\text{Ti}_2(\text{PO}_4)_3$ . They discovered that the  $\text{Li}^+$  ions are distributed between two slightly different M(3) subsites within the M(2) cavities with occupation factors of 2/3 and 1/3. A similar distribution of  $\text{Li}^+$  ions is expected for  $\text{B-Li}_3\text{V}_2(\text{PO}_4)_3$ . Therefore, the  $\text{Li}^+$  ion cage modes of  $\text{Li}_3\text{M}_2(\text{PO}_4)_3$ , which are detected with infrared spectroscopy, may be assigned to  $\text{Li}^+$  ions that occupy these sites. The similar frequencies and relative intensities indicate that the potential energy distributions of the  $\text{Li}^+$  ions are very similar in the two compounds. Even though the  $\text{Li}^+$  ion cage modes of  $\text{Li}_3\text{Ti}_2(\text{PO}_4)_3$  are both Raman and IR active ( $3A_g + 3E_g + 3A_u + 3E_u$ ), corresponding bands do not appear in the Raman spectrum of  $\text{Li}_3\text{Ti}_2(\text{PO}_4)_3$  (see Fig. 3-4). This is because  $\text{Li}^+$  translatory modes typically have negligible polarizability derivatives and hence small Raman intensities. Here the  $\text{Li}^+$  ion cage modes are distributed among the irreducible representations of the  $S_6$  point group, which is isomorphic to the factor group of  $\text{Li}_3\text{Ti}_2(\text{PO}_4)_3$ .

Electrochemical cycling data has shown that only two of the three  $\text{Li}^+$  ions may be reversibly extracted from rhombohedral  $\text{Li}_3\text{M}_2(\text{PO}_4)_3$  to form  $\text{LiM}_2(\text{PO}_4)_3$ . Crystallographic data suggest that the extraction of two of the  $\text{Li}^+$  ions from the M(3)



sites causes the remaining  $\text{Li}^+$  ion to depopulate the M(3) sites and migrate to an octahedral M(1) site [15,20]. The Li–O bond lengths are known to be longer for  $\text{Li}^+$  ions that occupy octahedral sites than those in the tetrahedral sites [26]. Thus, lithium translatory motions of the  $\text{Li}^+$  ions that occupy the M(1) sites are expected to have somewhat weaker force constants. Consequently, these modes will probably appear at lower frequencies, possibly overlapping or mixing with the  $\nu_2$  bands.

Cell polarization is detected in the electrochemical data between 3.92 and 4.30 V for  $\text{B-Li}_x\text{V}_2(\text{PO}_4)_3$  ( $1.0 \leq x \leq 1.5$ ; see Fig. 3-11 and Refs. [12,15,20]). This is accompanied by a rapid decrease in the intensity of the  $488 \text{ cm}^{-1}$  band in the infrared spectra. First principles calculations by Morgan *et al.* [12] identified a small increase in potential due to  $\text{Li}^+$  ion ordering over M(1) and M(3) at the composition  $\text{B-Li}_{1.5}\text{V}_2(\text{PO}_4)_3$ . Therefore, the disappearance of the  $488 \text{ cm}^{-1}$  band and the increase in cell polarization might be due to the migration of  $\text{Li}^+$  from the M(3) sites to the M(1) sites between 3.92 and 4.30 V. Re-inserting lithium reverses these spectral changes, and the infrared spectra are consistent with the shift of the  $\text{Li}^+$  ions from M(1) back to M(3) between 4.30 and 3.70 V (Fig. 3-12). The lack of significant cell polarization upon discharging, especially between 4.30 and 3.70 V, might indicate that it is easier to shift  $\text{Li}^+$  ions from M(1) to M(3) compared to the reverse process accompanying the charging step.

In the titanium system,  $\text{Li}^+$  ion cage modes appear much earlier in the lithium intercalation process (cf. Fig. 3-12 to Fig. 3-13). Thus, lithium reorganization in  $\text{Li}_x\text{Ti}_2(\text{PO}_4)_3$  might occur at higher lithium concentrations than  $\text{Li}_x\text{V}_2(\text{PO}_4)_3$ . It is tempting to correlate the spectral changes with the significant cell polarization detected in Fig. 3-6. However, Patoux and Masquelier have shown that cell polarization can be

affected by ball milling the compound with carbon [28]. Therefore, it is unclear whether the appearance of the  $\text{Li}^+$  ion cage modes is correlated to the cell polarization of this material. Ball milling is believed to enhance electrode performance by fracturing the particles and creating fresh surfaces. It is also known that milling with carbon can improve electrode conductivity [53]. However, other effects of mechanical milling are unknown. It is possible that the energetic shocks associated with ball milling will also affect the crystallinity or structure of the compound. For example, the introduction of defects has been reported in other ball-milled samples [54]. At any rate, the spectroscopic data clearly show that lithium reorganization is somewhat different between  $\text{LiTi}_2(\text{PO}_4)_3$  and  $\text{B-LiV}_2(\text{PO}_4)_3$ .

The stretching and bending modes of the  $\text{PO}_4^{3-}$  anions are also strongly affected throughout the charging process (see Figs. 3-12 and 3-13). Most of the spectral changes occur in the  $\text{PO}_4^{3-}$  bending modes, especially  $\nu_4$ . This is because  $\nu_1$  and  $\nu_3$  are more localized vibrations than the  $\text{PO}_4^{3-}$  bending modes [55]. Consequently, the latter modes are much more sensitive to small structural changes in the unit cell and provide a more sensitive probe of the phosphate framework during cycling. Differences in the vibrational modes of the  $\text{PO}_4^{3-}$  anions are probably due to changes in the effective force constants and dipole moment derivatives of the P–O bonds, which accompany the removal of  $\text{Li}^+$  ions from the structure and the concomitant oxidation of  $\text{M}^{3+}$  ions to  $\text{M}^{4+}$ .

Powder XRD data has shown that the electrochemical insertion of  $\text{Li}^+$  into rhombohedral  $\text{LiM}_2(\text{PO}_4)_3$  is a two-phase process between  $\text{LiM}_2(\text{PO}_4)_3$  and  $\text{Li}_3\text{M}_2(\text{PO}_4)_3$  [15,20,26-28]. The spectroscopic data in Figs. 3-7, 3-12, and 3-13 are consistent with this model. If lithium intercalation proceeded by a single-phase mechanism, the

frequencies and intensities of the vibrational modes would depend on the concentration of the  $\text{Li}^+$  ions. However, in a two-phase model the frequencies of the modes are expected to be independent of the lithium concentration, yet the intensities of each band would be governed by the amount of each phase present in the sample. For instance, in the two-phase delithiation of  $\text{LiFePO}_4$ , bands characteristic of  $\text{LiFePO}_4$  gradually decreased in intensity at the expense of the  $\text{FePO}_4$  bands (see Chapter 2).

A two-phase mechanism for lithium insertion is clearly observed in the infrared and Raman spectra of  $\text{Li}_x\text{Ti}_2(\text{PO}_4)_3$ . For example, consider the  $\nu_4$  modes in Fig. 3-13. As  $\text{LiTi}_2(\text{PO}_4)_3$  is discharged, bands characteristic of  $\text{Li}_3\text{Ti}_2(\text{PO}_4)_3$  appear and gradually replace the  $\text{LiTi}_2(\text{PO}_4)_3$  bands. This is particularly clear in the  $\nu_4$  region of the infrared spectra (denoted with dashed lines in the figure). Four  $\nu_4$  bands are observed in the spectrum of  $\text{LiTi}_2(\text{PO}_4)_3$  at 573, 585, 643, and 680  $\text{cm}^{-1}$ . When the cells are discharged to form  $\text{Li}_2\text{Ti}_2(\text{PO}_4)_3$ , the infrared spectrum becomes intermediate between  $\text{LiTi}_2(\text{PO}_4)_3$  and  $\text{Li}_3\text{Ti}_2(\text{PO}_4)_3$ . For example, new bands appear in the spectrum of  $\text{Li}_2\text{Ti}_2(\text{PO}_4)_3$  at 479, 561, and 600  $\text{cm}^{-1}$ , but bands characteristic of  $\text{LiTi}_2(\text{PO}_4)_3$  are still discernable (e.g., the 585  $\text{cm}^{-1}$  band). Further discharging to form  $\text{Li}_3\text{Ti}_2(\text{PO}_4)_3$  causes the  $\text{LiTi}_2(\text{PO}_4)_3$  bands to vanish, leaving three  $\nu_4$  bands and a new band near 478  $\text{cm}^{-1}$  that are characteristic of  $\text{Li}_3\text{Ti}_2(\text{PO}_4)_3$ .

### 3.5 Conclusions

Powder XRD and an electron microprobe is used to characterize the particle sizes of monoclinic and rhombohedral  $\text{Li}_3\text{V}_2(\text{PO}_4)_3$  (A- and B-forms, respectively). The

particles sizes measured with the electron microprobe are much larger than the average crystallite domain sizes estimated from the XRD data. This is probably because the larger particles are aggregates of the smaller crystallites. Furthermore, two distinct size domains are detected in B-Li<sub>3</sub>V<sub>2</sub>(PO<sub>4</sub>)<sub>3</sub>. The smaller particles of B-Li<sub>3</sub>V<sub>2</sub>(PO<sub>4</sub>)<sub>3</sub> are approximately the same size as those found in A-Li<sub>3</sub>V<sub>2</sub>(PO<sub>4</sub>)<sub>3</sub>. However, B-Li<sub>3</sub>V<sub>2</sub>(PO<sub>4</sub>)<sub>3</sub> also contains much larger domains. Magnification of these regions shows that they are actually dense clusters of smaller particles. Wavelength dispersive spectrometry is used to calculate the V:P ratio of the samples; both materials have V:P ratios near the theoretical value. It is also demonstrated that very small regions of unreacted V<sub>2</sub>O<sub>5</sub> can be detected with the electron microprobe.

Infrared and Raman spectra of A- and B-Li<sub>3</sub>V<sub>2</sub>(PO<sub>4</sub>)<sub>3</sub> and rhombohedral LiTi<sub>2</sub>(PO<sub>4</sub>)<sub>3</sub> are similar to previous spectroscopic data from related systems. Unfortunately, the Raman band intensities are very weak for A- and B-Li<sub>x</sub>V<sub>2</sub>(PO<sub>4</sub>)<sub>3</sub> cathodes, and Raman spectroscopy could not be used to investigate lithium intercalation in those systems. The weak Raman intensities might be due to a thin disordered layer on the surface of the particles. Since the samples are darkly colored, the excitation laser beam suffers a severe optical skin effect and can only penetrate a very small distance into the particles. Thus, the laser predominantly samples the surface of the particles. On the contrary, the optical skin effect of LiTi<sub>2</sub>(PO<sub>4</sub>)<sub>3</sub> is not as severe since the samples are white in color. Consequently, Raman spectra of Li<sub>x</sub>Ti<sub>2</sub>(PO<sub>4</sub>)<sub>3</sub> (1 ≤ x ≤ 3) could be measured.

The PO<sub>4</sub><sup>3-</sup> intramolecular vibrations of A-Li<sub>3</sub>V<sub>2</sub>(PO<sub>4</sub>)<sub>3</sub> are very sensitive to the extraction of Li<sup>+</sup> ions. Changes in the frequencies and intensities of the PO<sub>4</sub><sup>3-</sup> bands are

due to subtle changes in the  $\text{Li}^+$  ion coordination number and the Li–O and V–O bond distances. Infrared spectra recorded throughout the solid solution regime are essentially a superposition of the D- $\text{Li}_{0.9}\text{V}_2(\text{PO}_4)_3$  (4.35 V) and D- $\text{Li}_{2.1}\text{V}_2(\text{PO}_4)_3$  (3.90 V) spectra with the relative intensities of the bands governed by the site occupancy of the  $\text{Li}^+$  ions. The infrared spectrum of the fully discharged sample matches that of the pristine cathode, highlighting the excellent reversibility of this material.

Pronounced band broadening is observed in the infrared spectrum of A- $\text{Li}_x\text{V}_2(\text{PO}_4)_3$  as  $x \rightarrow 0$ . This suggests that the  $\text{PO}_4^{3-}$  anions become locally disordered when the compound is fully delithiated even though the global structure of the compound is retained [19,20]. The local structure of A- $\text{V}_2(\text{PO}_4)_3$  is compared to a  $\text{V}_2\text{O}_5\text{-P}_2\text{O}_5$  glass of the same composition. A comparison of the bandwidths indicates that there is much less disorder in A- $\text{V}_2(\text{PO}_4)_3$  than the vitreous material. Furthermore, the frequencies and intensities of the high frequency stretching modes are relatively similar for the two compounds, but there are numerous differences between the bending and low frequency stretching modes. This is because bending modes are less localized than the stretching modes and are more sensitive to the local structure surrounding the anions.

The vibrational modes of B- $\text{Li}_3\text{V}_2(\text{PO}_4)_3$  and  $\text{LiTi}_2(\text{PO}_4)_3$  are also sensitive to lithium (de)insertion. This is particularly evident for the  $\nu_4$  modes in the infrared spectrum of B- $\text{Li}_x\text{V}_2(\text{PO}_4)_3$  and  $\text{Li}_x\text{Ti}_2(\text{PO}_4)_3$  and, to a lesser extent, the  $\nu_2$  modes in the Raman spectrum of  $\text{Li}_x\text{Ti}_2(\text{PO}_4)_3$ . Spectral changes in the  $\text{PO}_4^{3-}$  modes are probably due to changes in the effective force constants and dipole moment derivatives of the P–O bonds that accompany the removal of  $\text{Li}^+$  ions and the associated oxidation of the  $\text{M}^{3+}$  ions. The frequencies of the vibrational modes do not depend on the concentration of the

$\text{Li}^+$  ions in the cathode material. Instead, the  $\text{Li}_3\text{M}_2(\text{PO}_4)_3$  bands appear and increase in intensity at the expense of  $\text{LiM}_2(\text{PO}_4)_3$  bands. This type of behavior is indicative of a two-phase mechanism for the electrochemical insertion of  $\text{Li}^+$  into  $\text{LiTi}_2(\text{PO}_4)_3$ .

Lithium cage modes are identified in the infrared spectra of  $\text{B-Li}_3\text{V}_2(\text{PO}_4)_3$  and  $\text{Li}_3\text{Ti}_2(\text{PO}_4)_3$ . These modes are assigned to the vibrations of  $\text{Li}^+$  ions that occupy the M(3) sub-sites of the structure. Spectral changes in these modes are consistent with the migration of  $\text{Li}^+$  ions from the M(3) sites to the M(1) sites between 3.92 and 4.30 V for  $\text{B-Li}_x\text{V}_2(\text{PO}_4)_3$  cathodes. Over this voltage interval the cells experience some cell polarization, which may be related to the reorganization of the  $\text{Li}^+$  ions. The infrared spectra and electrochemical data show that  $\text{Li}^+$  ions migrate back to the M(3) sites relatively early in the discharge step (between 4.30 and 3.70 V). On the contrary, infrared spectra of  $\text{Li}_x\text{Ti}_2(\text{PO}_4)_3$  indicate a different compositional range for lithium reorganization. The  $\text{Li}^+$  cage modes have measurable intensity at  $\text{Li}_2\text{Ti}_2(\text{PO}_4)_3$ , which might suggest that lithium reorganization occurs at higher lithium concentrations than the vanadium system.

### 3.6 References

- [1] K. Yoshida, K. Toda, K. Uematsu and M. Sato, *Key Eng. Mater.*, **157-158**, (1999) 289-295.
- [2] J. Gaubicher, T. Le Mercier, Y. Chabre, J. Angenault and M. Quarton, *J. Electrochem. Soc.*, **146**, (1999) 4375-4379.
- [3] T. A. Kerr, J. Gaubicher and L. F. Nazar, *Electrochem. Solid-State Lett.*, **3**, (2000) 460-462.

- [4] N. Dupré, J. Gaubicher, J. Angenault, G. Wallez and M. Quarton, *J. Power Sources*, **97-98**, (2004) 532-534.
- [5] N. Dupré, J. Gaubicher, T. Le Mercier, G. Wallez, J. Angenault and M. Quarton, *Solid State Ionics*, **140**, (2001) 209-221.
- [6] B. M. Azmi, T. Ishihara, H. Nishiguchi and Y. Takita, *Electrochim. Acta*, **48**, (2002) 165-170.
- [7] B. M. Azmi, T. Ishihara, H. Nishiguchi and Y. Takita, *J. Power Sources*, **119-121**, (2003) 273-277.
- [8] N. Dupré, J. Gaubicher, J. Angenault and M. Quarton, *J. Solid State Electrochem.*, **8**, (2004) 322-329.
- [9] J. Barker, M. Y. Saïdi and J. L. Swoyer, *J. Electrochem. Soc.*, **151**, (2004) A796-A800.
- [10] N. Dupré, G. Wallez, J. Gaubicher and M. Quarton, *J. Solid State Chem.*, **177**, (2004) 2896-2902.
- [11] D. Morgan, G. Ceder, M. Y. Saïdi, J. Barker, J. Swoyer, H. Huang and G. Adamson, *J. Power Sources*, **119-121**, (2003) 755-759.
- [12] D. Morgan, G. Cedar, M. Y. Saïdi, J. Barker, J. Swoyer, H. Huang and G. Adamson, *Chem. Mater.*, **14**, (2002) 4684-4693.
- [13] M. Y. Saïdi, J. Barker, H. Huang, J. L. Swoyer and G. Adamson, *J. Power Sources*, **119-121**, (2003) 266-272.
- [14] M. Y. Saïdi, J. Barker, H. Huang, J. L. Swoyer and G. Adamson, *Electrochem. Solid-State Lett.*, **5**, (2002) A149-A151.
- [15] J. Gaubicher, C. Wurm, G. Goward, C. Masquelier and L. Nazar, *Chem. Mater.*, **12**, (2000) 3240-3242.
- [16] S. Patoux, C. Wurm, M. Morcrette, G. Rouse and C. Masquelier, *J. Power Sources*, **119-121**, (2003) 279-284.
- [17] H. Huang, S.-C. Yin, T. Kerr, N. Taylor and L. F. Nazar, *Adv. Mater.*, **14**, (2002) 1525-1528.
- [18] S.-C. Yin, H. Grondy, P. Strobel, H. Huang and L. F. Nazar, *J. Am. Chem. Soc.*, **125**, (2003) 326-327.

- [19] S.-C. Yin, H. Grondey, P. Strobel, M. Anne and L. F. Nazar, *J. Am. Chem. Soc.*, **125**, (2003) 10402-10411.
- [20] M. Morcrette, J.-B. Leriche, S. Patoux, C. Wurm and C. Masquelier, *Electrochem. Solid-State Lett.*, **6**, (2003) A80-A84.
- [21] J. Barker, M. Y. Saïdi and J. L. Swoyer, *J. Electrochem. Soc.*, **150**, (2003) A1394-A1398.
- [22] A. Davies, R. J. Hobson, M. J. Hudson, W. J. Macklin and R. J. Neat, *J. Mater. Chem.*, **4**, (1994) 113-118.
- [23] T. Ohzuku, A. Ueda and N. Yamamoto, *J. Electrochem. Soc.*, **142**, (1995) 1431-1435.
- [24] T. Ohzuku, A. Ueda, N. Yamamoto and Y. Iwakoshi, *J. Power Sources*, **54**, (1995) 99-102.
- [25] S. Scharner, W. Weppner and P. Schmid-Beurmann, *J. Electrochem. Soc.*, **146**, (1999) 857-861.
- [26] A. Aatiq, M. Ménétrier, L. Croguennec, E. Suard and C. Delmas, *J. Mater. Chem.*, **12**, (2002) 2972-2978.
- [27] C. Delmas, A. Nadiri and J. L. Soubeyroux, *Solid State Ionics*, **28-30**, (1988) 419-423.
- [28] S. Patoux and C. Masquelier, *Chem. Mater.*, **14**, (2002) 5057-5068.
- [29] S. Okada, H. Arai, K. Asakura, Y. Sakurai, J. Yamaki, K. S. Nanjundaswamy, A. K. Pahdi, C. Masquelier and J. B. Goodenough, *Prog. Batteries & Battery Mater.*, **16**, (1997) 302-308.
- [30] H. Ohkawa, K. Yoshida, M. Saito, K. Uematsu, K. Toda and M. Sato, *Chem. Lett.*, **10**, (1999) 1017-1018.
- [31] M. Sato, H. Ohkawa, K. Yoshida, M. Saito, K. Uematsu and K. Toda, *Solid State Ionics*, **135**, (2000) 137-142.
- [32] G. X. Wang, D. H. Bradhurst, S. X. Dou and H. K. Liu, *J. Power Sources*, **124**, (2003) 231-236.
- [33] H. Y.-P. Hong, *Mater. Res. Bull.*, **11**, (1976) 173-182.
- [34] A. B. Bykov, A. P. Chirkin, L. N. Demyanets, S. N. Doronin, E. A. Genkina, A. K. Ivanov-Shits, I. P. Kondratyul, B. A. Maksimov, O. K. Mel'nikov, L. N.



- Muradyan, V. I. Simonov and V. A. Timofeeva, *Solid State Ionics*, **38**, (1990) 31-52.
- [35] J. Gopalakrishnan and K. Kasthuri Rangan, *Chem. Mater.*, **4**, (1992) 745-747.
- [36] M. Barj, G. Lucazeau and C. Delmas, *J. Solid State Chem.*, **100**, (1992) 141-150.
- [37] P. Tarte, A. Rulmont and C. Merckaert-Ansay, *Spectrochim. Acta A*, **42**, (1986) 1009-1016.
- [38] V. V. Kravchenko, V. I. Michailov and S. E. Segaryov, *Solid State Ionics*, **50**, (1992) 19-30.
- [39] M. Barj, H. Perthuis and P. Colomban, *Solid State Ionics*, **9 & 10**, (1983) 845-850.
- [40] S. E. Sigaryov, *Mat. Sci. Eng.*, **B13**, (1992) 121-123.
- [41] G. Butt, N. Sammes, G. Tompsett, A. Smirnova and O. Yamamoto, *J. Power Sources*, **134**, (2004) 72-79.
- [42] J.-M. Winand, A. Rulmont and P. Tarte, *J. Solid State Chem.*, **87**, (1990) 83-94.
- [43] U. V. Varadaraju, K. A. Thomas, B. Sivasankar and G. V. Subba Rao, *J. Chem. Soc., Chem. Commun.*, (1987) 814-815.
- [44] R. Pikel, D. de Waal, A. Aatiq and A. El Jazouli, *Mater. Res. Bull.*, **33**, (1998) 955-961.
- [45] G. W. Anderson and J. L. Verble, *J. Appl. Phys.*, **50**, (1979) 2765-2767.
- [46] R. N. Bhargava and R. A. Condrate, *Appl. Spectrosc.*, **31**, (1977) 230-236.
- [47] F. Ben Abdelouahab, R. Olier, N. Guilhaume, F. Lefebvre and J. C. Volta, *J. Catal.*, **134**, (1992) 151-167.
- [48] C. Delmas, R. Olazcuaga, F. Cherkaoui, R. Brochu and G. Le Flem, *C. R. Acad. Sc. Paris*, **287**, (1978) 169-171.
- [49] A. Rulmont, R. Cahay, M. Liégeois-Duyckaerts and P. Tarte, *Eur. J. Solid State Inorg. Chem.*, **28**, (1991) 207-219.
- [50] M. Barj, H. Perthuis and P. Colomban, *Solid State Ionics*, **11**, (1983) 157-177.
- [51] M. T. Paques-Ledent and P. Tarte, *Spectrochim. Acta*, **30A**, (1974) 673-689.
- [52] A. A. Salah, P. Jozwiak, J. Garbarczyk, K. Benkhouja, K. Zaghieb, F. Gendron and C. M. Julien, *J. Power Sources*, **140**, (2005) 370-375.

- [53] J.-M. Tarascon, M. Morcrette, J. Saint, L. Aymard and R. Janot, *C. R. Chimie*, **8**, (2005) 17-26.
- [54] M. R. Palacin, G. Rousse, M. Morcrette, L. Dupont, C. Masquelier, Y. Chabre, M. Hervieu and J.-M. Tarascon, *J. Power Sources*, **97-98**, (2001) 398-401.
- [55] P. Tarte, A. Rulmont, M. Liégeois-Duykaerts, R. Cahay and J. M. Winand, *Solid State Ionics*, **42**, (1990) 177-196.

## Chapter 4: TIN PHOSPHATE ANODES

*Christopher M. Burba and Roger Frech, J. Electrochem. Soc., 152 (6) A1233-A1240 (2005)\**

---

### 4.1 Introduction

Currently, most commercial  $\text{Li}^+$  ion rocking chair batteries employ a graphitic anode because it provides reasonably good electrochemical performance. However, there are extensive research efforts to identify higher capacity anodes with better electrochemical performance than graphite. Tin has been targeted as a potential anode material because of its high gravimetric (993 mAh/g) and volumetric (7232 mAh/ml) theoretical capacities compared to crystalline graphite (372 mAh/g and 837 mAh/ml). Here, lithium and tin form alloys up to a maximum composition of  $\text{Li}_{22}\text{Sn}_5$  [1,2]. However, the alloying process is accompanied by a tremendous volume expansion that causes particle cracking and disintegration [3,4]. This significantly reduces the practical capacity of tin anodes and ultimately leads to poor long-term cycling performance.

Composite tin-based anodes have been suggested as one way to overcome the poor performance of tin anodes. These materials first react irreversibly with lithium to form domains of metallic tin embedded in an inorganic matrix; second, lithium reversibly alloys with the tin domains [5]. The inorganic matrix helps to preserve the particles' structural integrity during the extreme volume fluctuations that accompany the alloying process [6]. With this strategy, some of the anode's capacity is sacrificed for better cycling performance. Since there are virtually no restrictions on the constituents that may be used in the composite tin-based materials, a large number of compounds have been

\*© The Electrochemical Society, Inc. (2004). All rights reserved.

explored [5,7-15]. The majority of the amorphous compounds studied are  $\text{SnB}_x\text{P}_y\text{O}_z$  glasses, while  $\text{SnO}$ ,  $\text{SnO}_2$ ,  $\text{Sn}_2\text{P}_2\text{O}_7$ ,  $\text{Sn}_3(\text{PO}_4)_2$  and  $\text{LiSn}_2(\text{PO}_4)_3$  are some examples of the crystalline compounds. Unfortunately, there is a tremendous irreversible capacity on the first discharge that is associated with the formation of the inorganic matrices. This constitutes a major problem in implementing this family of anodes as commercial replacements for graphite. In order to address this concern, it is necessary to have a complete understanding of the fundamental reactions that occur during the formation of the inorganic phase.

A variety of techniques have been used to investigate the reaction of lithium with composite tin-based anodes. For example, the formation of metallic tin and lithium-tin alloys in  $\text{SnO}$  has been unambiguously observed with X-ray diffraction (XRD) experiments [5]. Nuclear magnetic resonance [15,16] and  $^{119}\text{Sn}$  Mössbauer [14,15,17] spectroscopy have also been used to characterize the tin and lithium sites in several composite materials. Courtney *et al.* [17] clearly demonstrated the formation of  $\text{Li}_x\text{Sn}$  phases in  $\text{SnO}$  and  $\text{SnO}:0.25 \text{B}_2\text{O}_3:0.25 \text{P}_2\text{O}_5$  with  $^{119}\text{Sn}$  Mössbauer spectroscopy, and Gejke *et al.* [10-12] utilized micro-Raman and diffuse reflectance infrared spectroscopies to investigate a family of vitreous  $\text{SnB}_x\text{P}_y\text{O}_z$  compounds. The specific constituents composing the inorganic matrices of the discharged glasses could be easily deduced from the vibrational spectra. In this chapter, the inorganic matrices and metallic domains that form during the first discharge of crystalline  $\text{LiSn}_2(\text{PO}_4)_3$  and  $\text{Sn}_3(\text{PO}_4)_2$  are investigated. Infrared spectroscopy is used to probe the inorganic matrices that form and differential scanning calorimetry (DSC) gives insight into the metallic domains.

## 4.2 Experimental Methods

Samples of triclinic  $\text{LiSn}_2(\text{PO}_4)_3$  (space group  $P\bar{1}$ ,  $C_i'$ ) are synthesized from stoichiometric amounts of  $\text{SnO}_2$ ,  $\text{Li}_2\text{CO}_3$ , and  $(\text{NH}_4)_2\text{HPO}_4$ . The precursors are heated under static air at  $400^\circ\text{C}$  (3h) and then raised at a  $10^\circ\text{C}/\text{min}$  rate to  $1250^\circ\text{C}$  (48h). X-ray diffractograms of the resulting powder reveal a mixture of  $P\bar{1}$  and  $R\bar{3}c$  phases.

Converting the sample to the thermodynamically stable  $P\bar{1}$  phase [18] is achieved by applying pressure ( $\sim 1.4 \times 10^8$  Pa) with a KBr pellet press. The  $\text{Sn}_3(\text{PO}_4)_2$  samples are synthesized by heating a mixture of  $\text{SnO}_2$  and  $(\text{NH}_4)_2\text{HPO}_4$  at  $300^\circ\text{C}$  for 6h and then at  $450^\circ\text{C}$  overnight. The sample is then further annealed for 2h at  $600^\circ\text{C}$  to produce monoclinic  $\text{Sn}_3(\text{PO}_4)_2$  (space group  $P2_1/c$ ,  $C_{2h}^5$ ). All thermal treatments for  $\text{Sn}_3(\text{PO}_4)_2$  are performed under a flowing atmosphere of 5%  $\text{H}_2$  and 95% Ar.

The lithiated samples are created by discharging  $\text{LiSn}_2(\text{PO}_4)_3$  and  $\text{Sn}_3(\text{PO}_4)_3$  electrodes to the appropriate state of charge. To accomplish this, electrodes are prepared by mixing 87 wt% active material, 5 wt% KS-6 graphitic carbon (Tim Cal, Ltd.), 5 wt% Ketjen black, and 3 wt% Teflon. The resulting mixture is then pressed into a thin sheet. Circular disks are cut from the sheet ( $1.27 \text{ cm}^2$  and  $16 \pm 4$  mg) and dried at  $150^\circ\text{C}$  overnight in a vacuum oven. Size 2430 coin cells are constructed using a lithium metal anode and an electrolyte of 1 M  $\text{LiPF}_6$  in a 1:1 mixture of ethylene carbonate and dimethyl carbonate. Samples are discharged galvanostatically with an Arbin battery cycler at  $0.20 \text{ mA}/\text{cm}^2$  until the desired voltage is achieved. Afterwards, the coin cells are disassembled and the cathodes are washed twice with DMC, dried under reduced

pressure at approximately 100°C, and stored under an argon atmosphere. Details of the instrumental procedures may be found in App. A.

### 4.3 Results

#### 4.3.1 Particle Size and Surface Area Measurements

Particle size distributions are presented in Fig. 4-1 for the as-synthesized  $\text{LiSn}_2(\text{PO}_4)_3$  and  $\text{Sn}_3(\text{PO}_4)_2$  powders. The synthetic procedures employed in this study produced powders having a broad range of particle sizes. For example,  $\text{LiSn}_2(\text{PO}_4)_3$  is characterized by three distinct peaks at 26.34, 6.024, and 0.907  $\mu\text{m}$ . Approximately 58% of the sample has a mean particle size of 6.024  $\mu\text{m}$ , while the peak centered at 26.34  $\mu\text{m}$

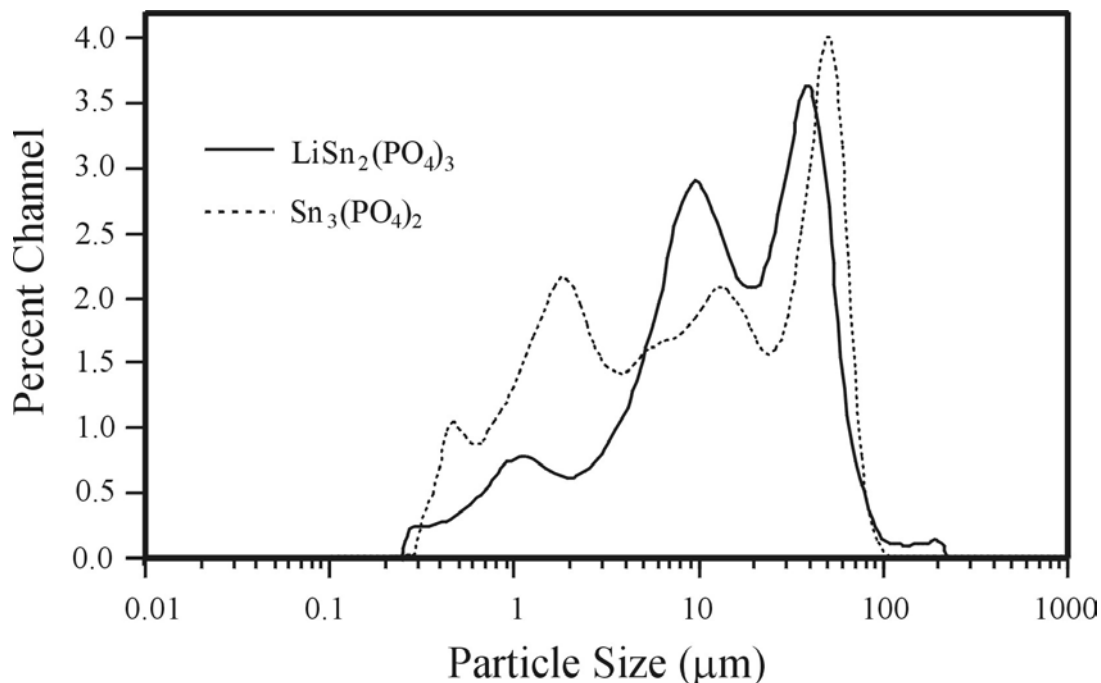


**Figure 4-1:** Particle size analyses of the as-synthesized  $\text{LiSn}_2(\text{PO}_4)_3$  and  $\text{Sn}_3(\text{PO}_4)_2$  powders.

comprises 23% of the sample. The remaining 19% of  $\text{LiSn}_2(\text{PO}_4)_3$  has a mean diameter of 0.907  $\mu\text{m}$ . In contrast, the  $\text{Sn}_3(\text{PO}_4)_2$  powder has at least four peaks and the dominant feature occurs at 26.81  $\mu\text{m}$  (32% of the sample). Two broad peaks at 5.449 and 0.861  $\mu\text{m}$  account for 33% and 29% of the sample, respectively. Additionally, there is a small fraction (6%) that has a mean diameter of 226 nm.

Although there are significant differences in the particle size distributions of the two materials, the overall mean particle diameters are similar (9.724  $\mu\text{m}$  for  $\text{LiSn}_2(\text{PO}_4)_3$  and 10.641  $\mu\text{m}$  for  $\text{Sn}_3(\text{PO}_4)_2$ ). Thus, the two materials should have similar surface areas. The Brunauer-Emmett-Teller (BET) method was used to estimate surface areas of the samples from  $\text{N}_2$  adsorption-desorption isotherms. Indeed, the measured surface areas are very close for the two compounds: 1.4  $\text{m}^2/\text{g}$  ( $\text{LiSn}_2(\text{PO}_4)_3$ ) and 1.2  $\text{m}^2/\text{g}$  ( $\text{Sn}_3(\text{PO}_4)_2$ ).

#### 4.3.2 Electrochemical Data

Electrochemical discharge curves of  $\text{LiSn}_2(\text{PO}_4)_3$  and  $\text{Sn}_3(\text{PO}_4)_2$  are presented in Fig. 4-2. Behm and Irvine [13] have previously reported the electrochemical performance of  $\text{LiSn}_2(\text{PO}_4)_3$  and  $\text{Sn}_2(\text{PO}_4)_3$ , and the curves presented in Fig. 4-2 agree well with their findings. Upon discharging, the  $\text{Sn}_3(\text{PO}_4)_2$  cells enter a voltage plateau at approximately 1.76 V vs.  $\text{Li}^+/\text{Li}$ . This plateau ends when the Li/Sn ratio is  $\sim 2$ .

Afterwards, the cell voltage precipitously drops to 0.9 V, and then gradually decreases to 0.01 V. The  $\text{Sn}_3(\text{PO}_4)_2$  electrodes gave a full discharge capacity of 1121 mAh/g (Li/Sn = 7.61) and the  $\text{LiSn}_2(\text{PO}_4)_3$  cells exhibit similar discharge behavior. Initially, the cells have a 1.32 V plateau that ends when the Li/Sn ratio is  $\sim 4$ . Following a small plateau near 0.9 V, the voltage slowly decreases to 0.01 V. The total discharge capacity for

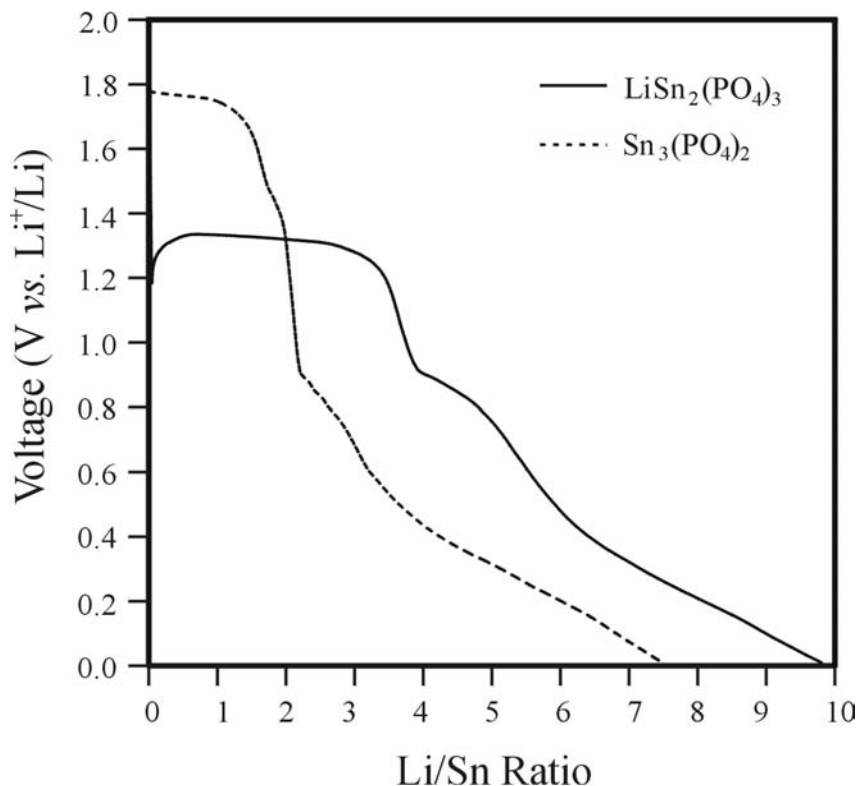


**Figure 4-2:** The first electrochemical discharge of  $\text{LiSn}_2(\text{PO}_4)_3$  and  $\text{Sn}_3(\text{PO}_4)_2$  electrodes.

the  $\text{LiSn}_2(\text{PO}_4)_3$  material is 993 mAh/g, which corresponds to a Li/Sn ratio of 9.80.

The bulk resistivities of  $\text{LiSn}_2(\text{PO}_4)_3$  and  $\text{Sn}_3(\text{PO}_4)_2$  are measured before and after discharging. DC methods are used to estimate the bulk resistivities of pure  $\text{LiSn}_2(\text{PO}_4)_3$  and  $\text{Sn}_3(\text{PO}_4)_2$  because the materials exceeded the range of the impedance analyzer. Both of the materials had very high intrinsic resistivities ( $\sim 2 \times 10^{10} \Omega \text{ cm}$  for  $\text{LiSn}_2(\text{PO}_4)_3$  and  $>10^{10} \Omega \text{ cm}$  for  $\text{Sn}_3(\text{PO}_4)_2$ ). Impedance data are collected for both of the fully discharged samples. Complex plane plots of the impedance data for the two compounds give single semicircles that are attributed to the electronic conductivity of the samples. From these data, the bulk resistivities of the fully discharged  $\text{LiSn}_2(\text{PO}_4)_3$  and  $\text{Sn}_3(\text{PO}_4)_2$  materials are  $5.6 \times 10^4$  and  $7.9 \times 10^4 \Omega \text{ cm}$ , respectively. This indicates that the bulk resistivities of



$\text{LiSn}_2(\text{PO}_4)_3$  and  $\text{Sn}_3(\text{PO}_4)_2$  decrease by approximately six orders of magnitude when discharged to 0.01 V.

#### 4.3.3 Powder X-Ray Diffraction Data

The XRD data of the crystalline compounds (Fig. 4-3) are in excellent agreement with previously published data [13,18,19]. The small peak at  $30.8^\circ$  ( $2\theta$ ) in the  $\text{Sn}_3(\text{PO}_4)_2$  diffractogram may belong to the (200) reflection of metallic tin. Other metallic tin reflections are not clearly observed because they overlap  $\text{Sn}_3(\text{PO}_4)_2$  reflections. The

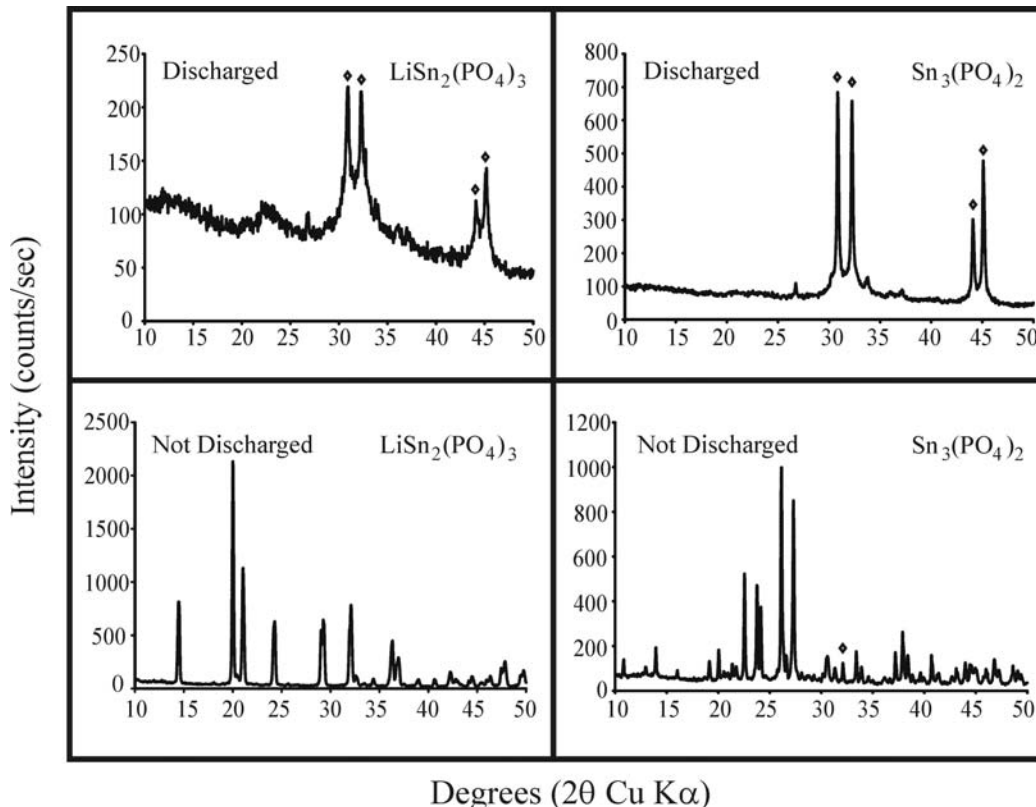


**Figure 4-3:** X-ray diffractograms (10-50°, 0.50°/min) of  $\text{LiSn}_2(\text{PO}_4)_3$  and  $\text{Sn}_3(\text{PO}_4)_2$  before and after discharging to 0.01 V. The peaks marked with an open diamond (◇) are indexed to metallic tin. All of the other peaks belong to  $\text{LiSn}_2(\text{PO}_4)_3$  or  $\text{Sn}_3(\text{PO}_4)_2$ .

presence of metallic tin in  $\text{Sn}_3(\text{PO}_4)_2$  probably results from the reducing conditions employed in the preparation of the sample. Inserting  $\text{Li}^+$  ions into  $\text{LiSn}_2(\text{PO}_4)_3$  and  $\text{Sn}_3(\text{PO}_4)_2$  results in the complete destruction in the crystallinity of the materials. This is evidenced by the lack of any reflections resembling the original structures in the discharged samples. Both of the discharged electrodes exhibit peaks that are indicative of  $\beta$ -Sn (white tin). The grain size of the tin domains may be estimated with the Scherrer formula. The fully discharged  $\text{Sn}_3(\text{PO}_4)_2$  has larger tin domains (37 nm) compared to the fully discharged  $\text{LiSn}_2(\text{PO}_4)_3$  (16 nm). Additionally, there is a small peak in  $\text{LiSn}_2(\text{PO}_4)_3$  at  $22.7^\circ$  that might be related to Li-Sn alloys, but there is no analogous feature in the discharged  $\text{Sn}_3(\text{PO}_4)_2$ . The small peak at  $26.7^\circ$  is due to the graphitic carbons used in preparing the electrodes.

#### *4.3.4 Symmetry-Based Analysis of the Vibrational Modes*

A factor group correlation [20] of the  $\text{PO}_4^{3-}$  intramolecular vibrations for  $\text{LiSn}_2(\text{PO}_4)_3$  ( $Z = 2$ ) and  $\text{Sn}_3(\text{PO}_4)_2$  ( $Z = 6$ ) is given in Table IV-I. The analysis predicts 27 IR and 27 Raman active modes for  $\text{LiSn}_2(\text{PO}_4)_3$ , while 36 IR and 36 Raman modes are expected for  $\text{Sn}_3(\text{PO}_4)_2$ . Of course, fewer bands will actually be detected in the experimentally measured vibrational spectra due to coincidental overlap of the factor group multiplets or weak dipole moment and polarizability derivatives for some of the modes. Infrared absorption and Raman scattering spectra of  $\text{LiSn}_2(\text{PO}_4)_3$  and  $\text{Sn}_3(\text{PO}_4)_2$  are present in Figs. 4-4 and 4-5, respectively. Fortunately, the assignment of bands originating in the intramolecular vibrations of the phosphate anion can be done with a high degree of confidence because they are decoupled from the lattice phonon modes.

**Table IV-I:** Factor group correlation of the intramolecular  $\text{PO}_4^{3-}$  modes in  $\text{LiSn}_2(\text{PO}_4)_3$  and  $\text{Sn}_3(\text{PO}_4)_2$

|                | $\text{LiSn}_2(\text{PO}_4)_3$ |            |              | $\text{Sn}_3(\text{PO}_4)_2$                |            |              |
|----------------|--------------------------------|------------|--------------|---|------------|--------------|
|                | Point Group                    | Site Group | Factor Group | Point Group                                 | Site Group | Factor Group |
|                | $T_d$                          | $C_1$      | $C_i$        | $T_d$                                       | $C_1$      | $C_{2h}$     |
| $\nu_1$        | A                              |            | $A_g$        | A   |            | $A_g$        |
| $\nu_2$        | E                              | A          | $A_u$        | E   | A          | $B_g$        |
| $\nu_3, \nu_4$ | $F_2$                          |            | $A_u$        | $F_2$                                       |            | $A_u$        |
|                |                                |            | $A_u$        |   |            | $B_u$        |
|                | $\Gamma(\nu_1) = 3A_g + 3A_u$  |            |              | $\Gamma(\nu_1) = 2A_g + 2B_g + 2A_u + 2B_u$ |            |              |
|                | $\Gamma(\nu_2) = 6A_g + 6A_u$  |            |              | $\Gamma(\nu_2) = 4A_g + 4B_g + 4A_u + 4B_u$ |            |              |
|                | $\Gamma(\nu_3) = 9A_g + 9A_u$  |            |              | $\Gamma(\nu_3) = 6A_g + 6B_g + 6A_u + 6B_u$ |            |              |
|                | $\Gamma(\nu_4) = 9A_g + 9A_u$  |            |              | $\Gamma(\nu_4) = 6A_g + 6B_g + 6A_u + 6B_u$ |            |              |

The intramolecular  $\text{PO}_4^{3-}$  stretching modes ( $\nu_1$  and  $\nu_3$ ) occur between 1250 and 900  $\text{cm}^{-1}$ , and the bending modes ( $\nu_2$  and  $\nu_4$ ) appear between 650 and 450  $\text{cm}^{-1}$ . The theoretical analysis predicts that  $\nu_1(\text{PO}_4^{3-})$  will yield three IR active modes in  $\text{LiSn}_2(\text{PO}_4)_3$ ; these modes are assigned to the bands at 1014, 991, and 976  $\text{cm}^{-1}$  in the infrared spectrum. Nine IR-active normal modes are expected for the  $\text{PO}_4^{3-}$  antisymmetric stretching motions,  $\nu_3(\text{PO}_4^{3-})$ , and six of these modes are identified between 1035 and 1300  $\text{cm}^{-1}$  in Fig. 4-4. The separation of  $\nu_1(\text{PO}_4^{3-})$  and  $\nu_3(\text{PO}_4^{3-})$  is not as clear in the Raman spectrum of  $\text{LiSn}_2(\text{PO}_4)_3$  as it is in the infrared spectrum, so band assignments are not attempted for these vibrations. Nevertheless, the  $\nu_1(\text{PO}_4^{3-})$  modes are expected to occur at lower frequencies than  $\nu_3(\text{PO}_4^{3-})$ , therefore the bands between 984 and 967  $\text{cm}^{-1}$  probably

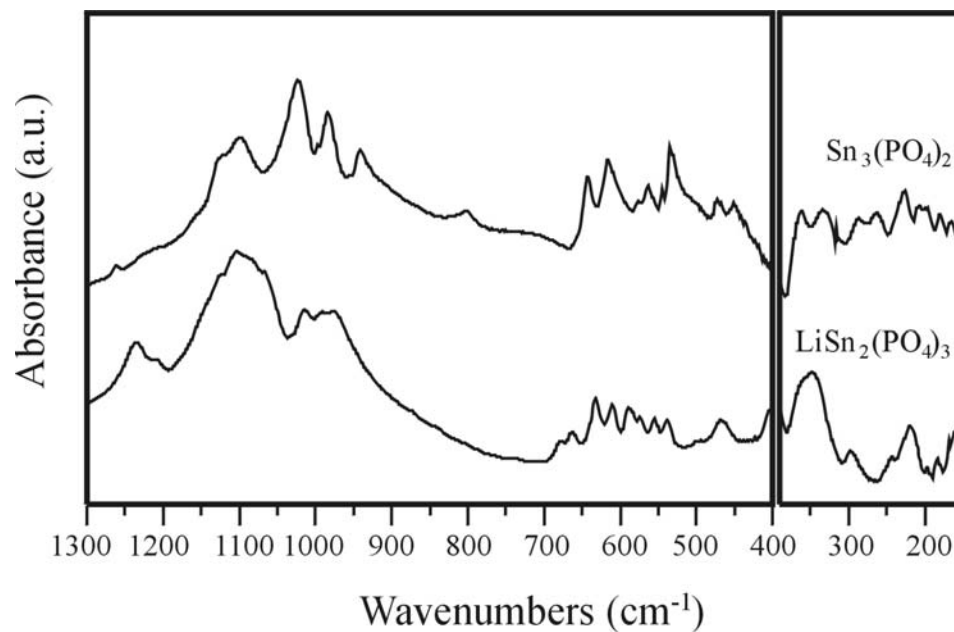


**Figure 4-4:** Infrared absorption spectra of  $\text{LiSn}_2(\text{PO}_4)_3$  and  $\text{Sn}_3(\text{PO}_4)_2$ . Between  $1300\text{--}400 \text{ cm}^{-1}$  and  $400\text{--}150 \text{ cm}^{-1}$  spectra are collected with KBr (mid-IR) and Mylar (far-IR) beamsplitters, respectively.

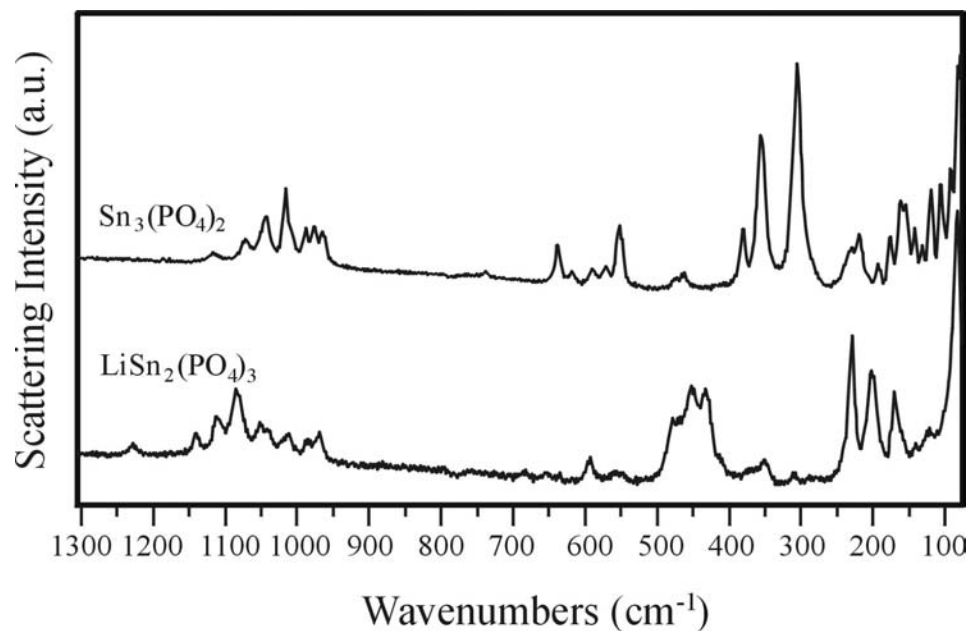


**Figure 4-5:** Raman scattering spectra of  $\text{LiSn}_2(\text{PO}_4)_3$  and  $\text{Sn}_3(\text{PO}_4)_2$ .

contain more  $\nu_1(\text{PO}_4^{3-})$  motion than the higher frequency bands.

Nine distinct bands between 680 and 490  $\text{cm}^{-1}$  in the infrared spectrum of  $\text{LiSn}_2(\text{PO}_4)_3$  (Fig. 4-4) may be assigned as primarily  $\nu_2(\text{PO}_4^{3-})$  vibrations, and three bands at 467, 434, 393  $\text{cm}^{-1}$ , a shoulder at 408  $\text{cm}^{-1}$ , and two overlapping bands at 345 and 365  $\text{cm}^{-1}$  are assigned to  $\nu_4(\text{PO}_4^{3-})$  modes. In the corresponding Raman spectrum (Fig. 4-5), the  $\nu_4(\text{PO}_4^{3-})$  bands have very small relative intensities compared to the  $\nu_2(\text{PO}_4^{3-})$  modes. In fact, only two weak bands at 593 and 555  $\text{cm}^{-1}$  are observed for  $\nu_4(\text{PO}_4^{3-})$ . In contrast, at least four overlapping bands are assigned to  $\nu_2(\text{PO}_4^{3-})$ .

Theory and experiment agree well for the intramolecular stretching modes of the  $\text{PO}_4^{3-}$  anion in  $\text{Sn}_3(\text{PO}_4)_2$ . However, it is difficult to assign bands in the  $\nu_2(\text{PO}_4^{3-})$  and  $\nu_4(\text{PO}_4^{3-})$  regions in this material. Apella *et al.* [21] have previously measured the mid-IR spectrum of  $\text{Sn}_3(\text{PO}_4)_2$ , and their proposed band assignments are adopted for this chapter. Overall, the mid-IR spectrum of  $\text{Sn}_3(\text{PO}_4)_2$  is quite similar to the previously published results, with only minor differences in intensity for a few of the bands. The  $\nu_4(\text{PO}_4^{3-})$  modes are more intense than the  $\nu_2(\text{PO}_4^{3-})$  modes in the Raman spectrum of this system.

Lattice phonon modes are identified in the spectra of both compounds at lower frequencies (cf., Figs. 4-4 and 4-5). These vibrations are composed of librations and translations of the  $\text{PO}_4^{3-}$  anion and translatory motions of the  $\text{Li}^+$  and  $\text{Sn}^{n+}$  ( $n = 2$  or  $4$ ) cations. Typically, these modes consist of a complicated mixture of atomic motions, and it is difficult to determine which motions are involved in a particular band. Even though

the lattice phonon modes of  $\text{LiSn}_2(\text{PO}_4)_3$  and  $\text{Sn}_3(\text{PO}_4)_2$  contain a rich vibrational structure, it is sufficient for this chapter simply to identify these bands as lattice modes.

#### 4.3.5 Infrared Spectra during $\text{Li}^+$ Ion Insertion

Mid-IR spectra of  $\text{LiSn}_2(\text{PO}_4)_3$  at different states of discharge are presented in Fig. 4-6. The intensities and frequencies of the  $\text{PO}_4^{3-}$  stretching and bending vibrations are clearly affected by  $\text{Li}^+$  insertion. For example, when cells are discharged to 1.00 V, the  $\nu_1(\text{PO}_4^{3-})$  and  $\nu_3(\text{PO}_4^{3-})$  bands collapse into a broad band centered at  $1039\text{ cm}^{-1}$  with a shoulder at  $984\text{ cm}^{-1}$ ; furthermore, weak bands begin to appear at 1505, 1427, and  $863\text{ cm}^{-1}$ . Simultaneously, the  $\nu_4(\text{PO}_4^{3-})$  bands become a single band at  $589\text{ cm}^{-1}$ , and two broad bands appear below  $500\text{ cm}^{-1}$ . At 0.40 V, the  $1039\text{ cm}^{-1}$  band has essentially

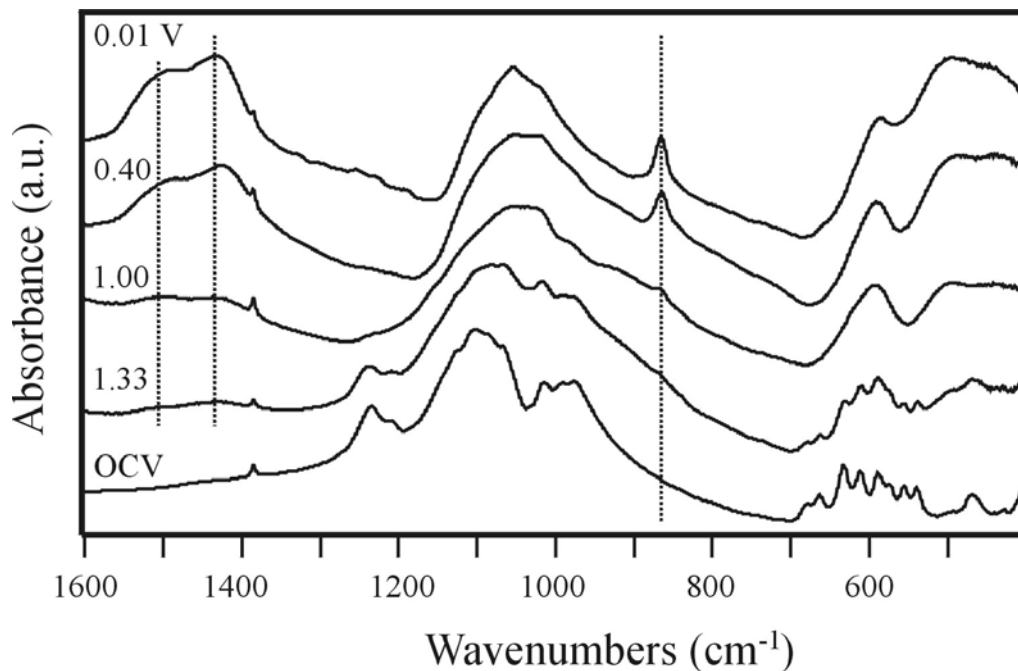


**Figure 4-6:** Mid-IR spectra of  $\text{LiSn}_2(\text{PO}_4)_3$  at various states of discharge. The dashed lines mark the appearance of the  $\text{CO}_3^{2-}$  bands.

absorbed the  $984\text{ cm}^{-1}$  shoulder, while bands at  $498$  and  $438\text{ cm}^{-1}$  continue to increase in intensity compared to the  $589\text{ cm}^{-1}$  band. The  $1505$ ,  $1427$ , and  $863\text{ cm}^{-1}$  bands substantially increase in intensity when  $\text{LiSn}_2(\text{PO}_4)_3$  is discharged to  $0.40\text{ V}$ . These bands are assigned to the intramolecular vibrations of  $\text{CO}_3^{2-}$  species. Specifically, the bands at  $1505$  and  $1427\text{ cm}^{-1}$  are assigned to  $\text{CO}_3^{2-}$  stretching modes,  $\nu_3(\text{CO}_3^{2-})$  and  $\nu_1(\text{CO}_3^{2-})$ , and the  $863\text{ cm}^{-1}$  band is attributed to the  $\text{CO}_3^{2-}$  out-of-plane deformation,  $\nu_2(\text{CO}_3^{2-})$ . The  $\text{CO}_3^{2-}$  antisymmetric bending modes,  $\nu_4(\text{CO}_3^{2-})$ , are expected to occur below  $700\text{ cm}^{-1}$ , and the increased intensity of the bands below  $500\text{ cm}^{-1}$  is probably related to the appearance of the carbonate species. However, an unambiguous assignment is impossible because the phosphate bending modes occur at similar frequencies. The  $\text{CO}_3^{2-}$  bands are due to solvent molecules that decompose on the surface of the tin anodes. This will be further discussed in greater detail in Sec. 4.4.2. Further discharging to  $0.01\text{ V}$  only results in minor intensity changes for some of the bands.

Far-infrared spectra of the  $\text{LiSn}_2(\text{PO}_4)_3$  series may be found in Fig. 4-7. Some modest spectral changes result when cells are discharged to  $1.33\text{ V}$ . For example, the intensity of the  $345\text{ cm}^{-1}$  band slightly increases while the intensity of the  $365\text{ cm}^{-1}$  band remains constant. The lattice modes are not significantly affected over this voltage range. However, startling changes occur in the far-IR spectra when cells are discharged to  $1.00\text{ V}$ : all of the lattice modes completely vanish. Additionally, bands at  $393$  and  $345\text{ cm}^{-1}$  greatly diminish in intensity. There are no further spectral changes evident in the far-IR spectra when cells are discharged to  $0.01\text{ V}$ .

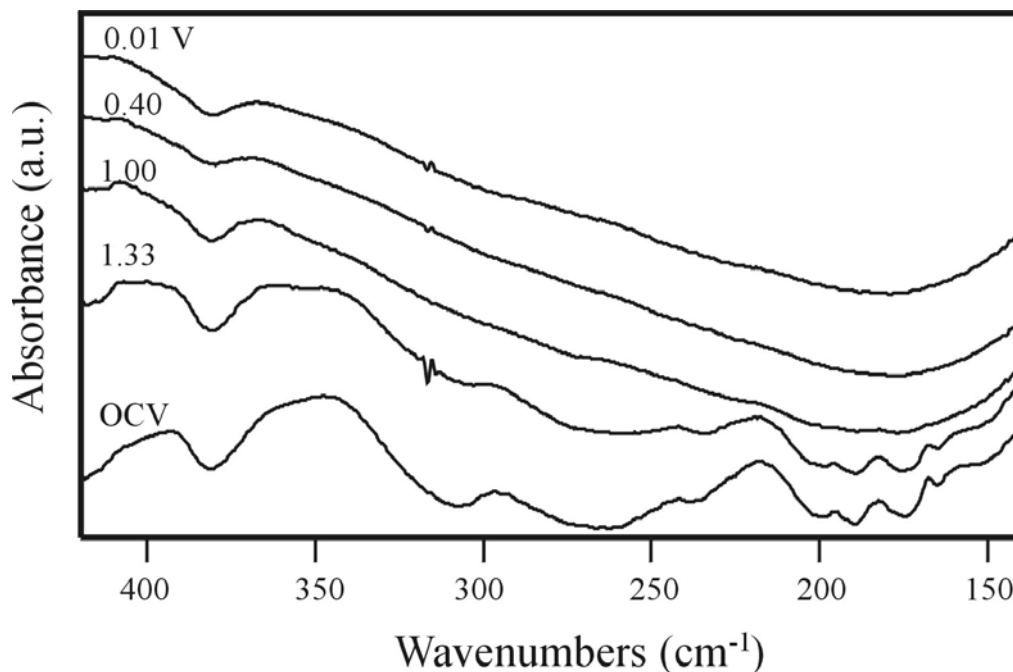


**Figure 4-7:** Far-IR spectra of  $\text{LiSn}_2(\text{PO}_4)_3$  at various states of discharge.

The corresponding  $\text{Sn}_3(\text{PO}_4)_2$  mid-IR spectra are presented in Fig. 4-8. The  $\text{Sn}_3(\text{PO}_4)_2$  spectra progress in a similar fashion as the  $\text{LiSn}_2(\text{PO}_4)_3$  series. As before, the factor group multiplets of  $\nu_1(\text{PO}_4^{3-})$  and  $\nu_3(\text{PO}_4^{3-})$  become less distinct with progressive lithium insertion. These bands eventually collapse into a single band at  $1061\text{ cm}^{-1}$  (1.00 V). The  $\nu_2(\text{PO}_4^{3-})$  and  $\nu_4(\text{PO}_4^{3-})$  bands are also affected over this voltage interval. The complicated vibrational structure of the  $\text{Sn}_3(\text{PO}_4)_2$  bending modes is degraded as cells are discharged, leaving a single band at  $591\text{ cm}^{-1}$  and a very broad band at  $477\text{ cm}^{-1}$ . Bands consistent with the formation of  $\text{CO}_3^{2-}$  species form when the  $\text{Sn}_3(\text{PO}_4)_2$  electrodes are discharged to 1.00 V. The frequencies of the  $\text{CO}_3^{2-}$  bands are similar to those observed in the  $\text{LiSn}_2(\text{PO}_4)_3$  system. At 0.70 V, the band centered at  $477\text{ cm}^{-1}$  greatly increases in intensity compared to the  $591\text{ cm}^{-1}$  band, and a  $1022\text{ cm}^{-1}$  shoulder appears on the 1061



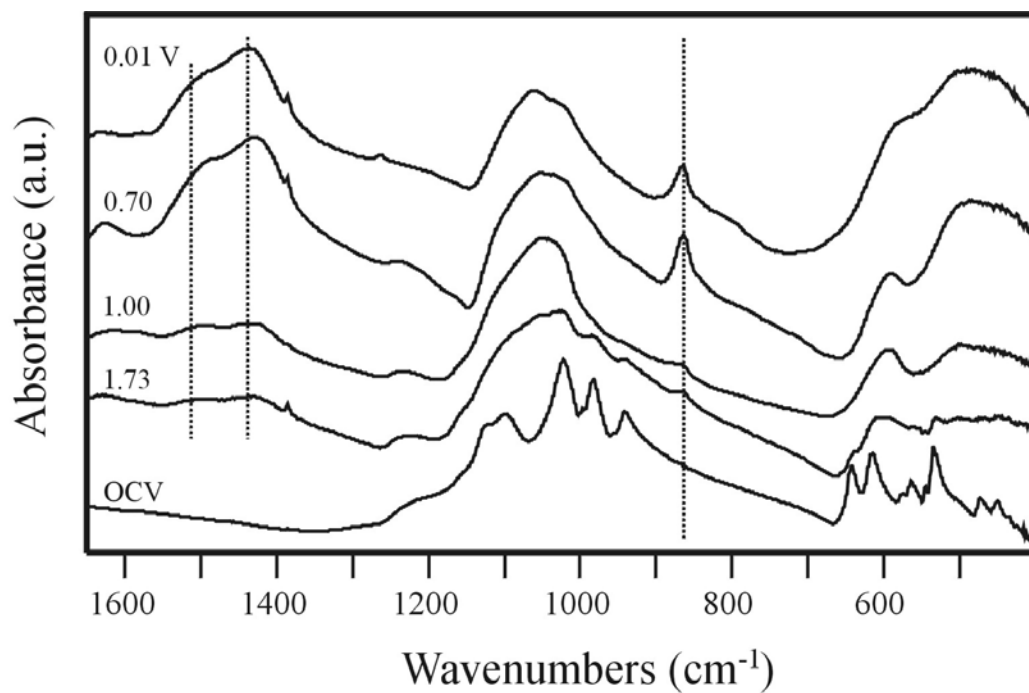


**Figure 4-8:** Mid-IR spectra of  $\text{Sn}_3(\text{PO}_4)_2$  at various states of discharge. The dashed lines mark the appearance of the  $\text{CO}_3^{2-}$  bands.

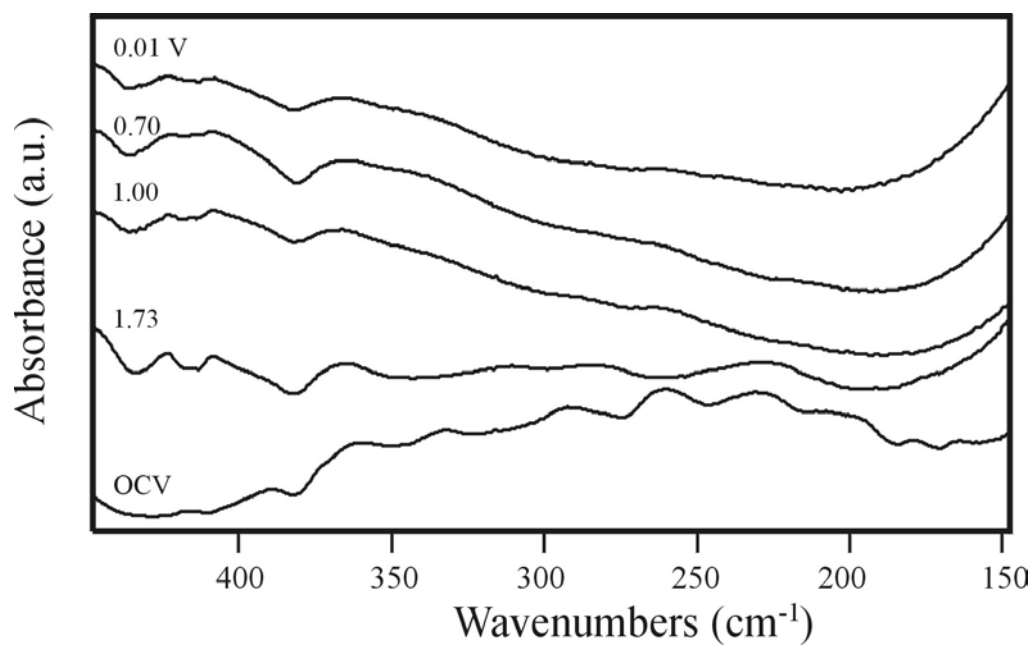


**Figure 4-9:** Far-IR spectra of  $\text{Sn}_3(\text{PO}_4)_2$  at various states of discharge.

$\text{cm}^{-1}$  band. Additionally, the  $\text{CO}_3^{2-}$  bands dramatically increase in intensity (e.g., the band at  $865 \text{ cm}^{-1}$ ). No major spectroscopic changes occur when discharging continues to 0.01 V. Far-IR spectra of  $\text{Sn}_3(\text{PO}_4)_2$  at various stages of discharge are shown in Fig. 4-9. The far-IR spectra change in a similar fashion as the  $\text{LiSn}_2(\text{PO}_4)_3$  series with one exception: the  $\text{Sn}_3(\text{PO}_4)_2$  lattice modes begin to disappear before 1.00 V. However, at 1.00 V all the vibrational features below  $300 \text{ cm}^{-1}$  are destroyed.

#### 4.3.6 Differential Scanning Calorimetry

Thermal measurements are performed on  $\text{LiSn}_2(\text{PO}_4)_3$  and  $\text{Sn}_3(\text{PO}_4)_2$  at various states of discharge, and the resulting data for the two systems are given in Fig. 4-10. The first and second thermal scans for each compound are recorded in the figure. DSC scans for  $\text{LiSn}_2(\text{PO}_4)_3$  and  $\text{Sn}_3(\text{PO}_4)_2$  electrodes prior to lithium insertion are relatively featureless. However, discharging either compound produces complicated exothermic peaks near  $225^\circ\text{C}$  and endothermic features above  $250^\circ\text{C}$ . These features all vanish when the temperature range is scanned a second time. Thus, these thermal transitions are irreversible.

Before the  $\text{Sn}_3(\text{PO}_4)_2$  electrodes are discharged, a very small endothermic transition at  $231^\circ\text{C}$  may be identified, which is attributed to the melting of tin [2]. Prior to discharging, there is no evidence for metallic tin in the  $\text{LiSn}_2(\text{PO}_4)_3$  electrodes. Discharging  $\text{Sn}_3(\text{PO}_4)_2$  cells to 1.00 V does not affect the magnitude of the  $231^\circ\text{C}$  thermal transition. However, the size of the peak is significantly enhanced between 1.00 and 0.70 V. By way of comparison, a metallic tin peak appears between 1.00 and 0.40 V for  $\text{LiSn}_2(\text{PO}_4)_3$ . When the  $\text{LiSn}_2(\text{PO}_4)_3$  and  $\text{Sn}_3(\text{PO}_4)_2$  cells are discharged further, broad

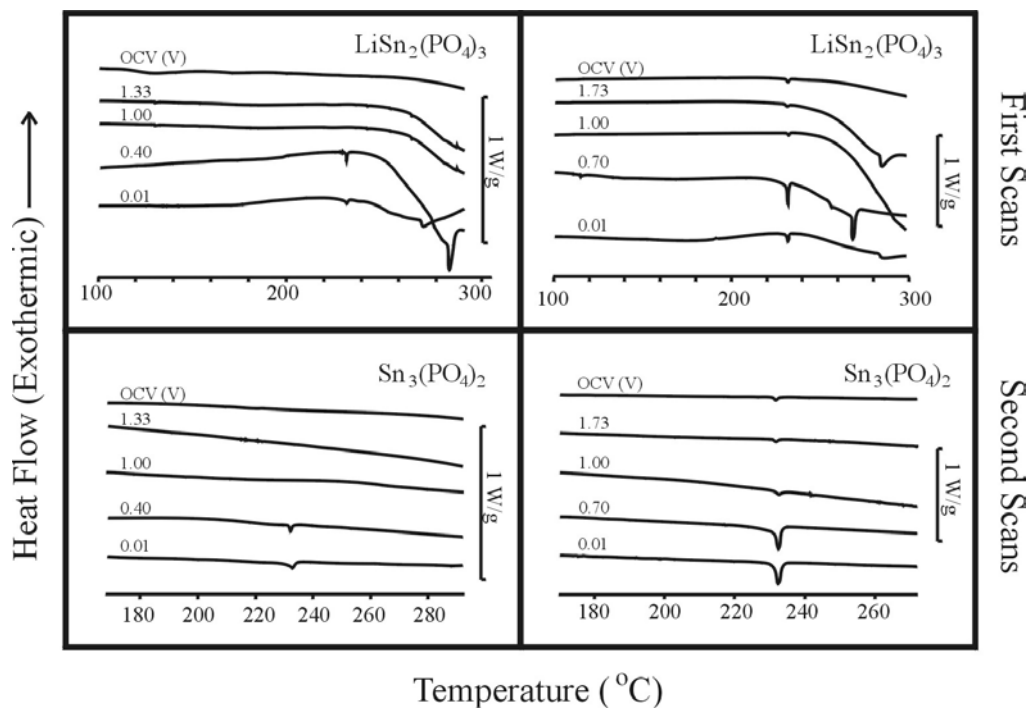


**Figure 4-10:** First and second DSC heating curves for  $\text{LiSn}_2(\text{PO}_4)_3$  and  $\text{Sn}_3(\text{PO}_4)_2$  as a function of voltage.

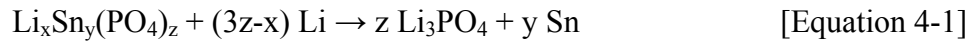
exothermic peaks at  $225^\circ\text{C}$  engulf the tin peaks. Fortunately, the exothermic features are irreversible, and the magnitude of tin thermal transition may be observed with the second thermal scans. There is a slight decrease in the magnitude of the tin peaks between 1.00 and 0.01 V for both samples.

## 4.4 Discussion

### 4.4.1 Impedance and X-Ray Diffraction Data

It is well known that phosphate-based electrodes have an intrinsically low conductivity [22]. For typical phosphate-based electrodes, such as  $\text{LiFePO}_4$ , electrochemical cycling is not expected to greatly enhance the conductivity of the

material. However, the bulk resistivities of  $\text{LiSn}_2(\text{PO}_4)_3$  and  $\text{Sn}_3(\text{PO}_4)_2$  decrease by six orders of magnitude when they are discharged to 0.01 V. This may be explained with an alloying theory proposed by Courtney and Dahn [5]. According to the theory, the first major plateau in the electrochemical data [13] is due to the irreversible formation of metallic tin within an inorganic matrix. The inorganic matrix is composed of the other constituents of the composite cathode material; e.g., in  $\text{SnO}$ , the inorganic matrix would primarily consist of  $\text{Li}_2\text{O}$ . For  $\text{LiSn}_2(\text{PO}_4)_3$ , the first plateau extends from 1.4 to 1.1 V, whereas this plateau ranges from 1.8 to 1.2 V for  $\text{Sn}_3(\text{PO}_4)_2$ . Subsequently, lithium and tin reversibly alloy along a second plateau that extends to 0.01 V. Based on the alloying theory, the following two equations are expected to govern the reaction of lithium with a general lithium-tin-phosphate compound:



Here, the inorganic matrix would be composed of  $\text{Li}_3\text{PO}_4$ . Therefore, the electrochemical reactions involved in discharging  $\text{LiSn}_2(\text{PO}_4)_3$  and  $\text{Sn}_3(\text{PO}_4)_2$  are different than those controlling other transition metal phosphate electrodes (e.g., intercalation of  $\text{Li}^+$  ions into orthorhombic  $\text{FePO}_4$  or rhombohedral  $\text{LiV}_2(\text{PO}_4)_3$ ). The formation of metallic species significantly improves the electronic conductivity of the anode material; hence, the bulk resistivities of the fully discharged  $\text{LiSn}_2(\text{PO}_4)_3$  and  $\text{Sn}_3(\text{PO}_4)_2$  electrodes are much lower than the parent materials.

A comparison of XRD data for  $\text{LiSn}_2(\text{PO}_4)_3$  and  $\text{Sn}_3(\text{PO}_4)_2$  before and after discharging clearly demonstrates that the samples' crystalline nature is completely destroyed with the insertion of  $\text{Li}^+$  ions, and both discharged samples have peaks that

may be assigned to  $\beta$ -Sn (white tin). The tin peaks are more intense in the discharged  $\text{Sn}_3(\text{PO}_4)_2$  sample than in the discharged  $\text{LiSn}_2(\text{PO}_4)_3$ . This suggests that larger domains of tin are produced in  $\text{Sn}_3(\text{PO}_4)_2$  than in  $\text{LiSn}_2(\text{PO}_4)_3$ . It has been shown that the “spectator atom” to tin ratio is critical for controlling the growth of large domains of tin [5,23,24]. Spectator atoms are defined as any other atomic species in the material that is not involved in the reversible alloying reactions. The size of the tin domains at equilibrium is inversely proportional to this ratio [24]. Although this formalism is defined for electrodes that have been cycled many times, it is possible that differences in the sizes of the tin domains produced on the first discharge of  $\text{LiSn}_2(\text{PO}_4)_3$  and  $\text{Sn}_3(\text{PO}_4)_2$  – and the relative differences in the XRD data – may also be understood in terms of the ratio.  $\text{LiSn}_2(\text{PO}_4)_3$  has a much larger spectator atom to tin ratio than  $\text{Sn}_3(\text{PO}_4)_2$  (8.00 compared to 3.33). Therefore, discharging  $\text{Sn}_3(\text{PO}_4)_2$  produces a material that is more concentrated with respect to tin. Tin aggregation is expected to be more severe in a material that has a higher concentration of tin. Thus, the  $\text{Sn}_3(\text{PO}_4)_2$  anodes produce larger tin domains than  $\text{LiSn}_2(\text{PO}_4)_3$  even though the materials have only undergone the first discharge.

There is very little XRD evidence of Li-Sn phases at these voltages. Similar findings have been reported for three related systems:  $\text{Sn}_2\text{BPO}_6$  and  $\text{Sn}_2\text{P}_2\text{O}_7$  glasses [12] and crystalline  $\text{Sn}_2\text{P}_2\text{O}_7$  [9]. In these systems, XRD measurements reveal either poorly resolved peaks or no features indicative of Li-Sn alloys. Previous research into other composite tin oxide-based materials demonstrated that Li-Sn alloys could be detected with XRD. For example, relatively broad and intense peaks developed at  $22^\circ$  and  $38^\circ$  in SnO that are assigned to Li-Sn phases [12]. The apparent lack of Li-Sn alloy peaks in the

X-ray diffractograms of discharged  $\text{LiSn}_2(\text{PO}_4)_3$  and  $\text{Sn}_3(\text{PO}_4)_2$  (Fig. 4-3) is not surprising since the samples have been exposed to the atmosphere during XRD data acquisition. This likely had a deleterious affect on the Li-Sn alloy domains.

#### 4.4.2 Vibrational Spectroscopy

The discharge mechanism of a number of tin-based polyanionic systems has been investigated with vibrational spectroscopy. Raman and diffuse reflectance infrared spectroscopies have been extensively used to study the reaction of lithium with  $\text{Sn}_2\text{BPO}_6$  and  $\text{Sn}_2\text{P}_2\text{O}_7$  [10,12] as well as  $\text{Sn}_2\text{B}_3\text{O}_{6.5}$  and  $\text{Sn}_2\text{B}_2\text{AlO}_{6.5}$  [11] glasses. Xiao *et al.* [9] investigated crystalline and amorphous forms of  $\text{Sn}_2\text{P}_2\text{O}_7$  with transmission mid-IR spectroscopy. In all the examples cited,  $\text{Li}^+$  ions irreversibly react with the polyatomic anions of the compounds to form an inorganic matrix. For example, the reaction of lithium with  $\text{Sn}_2\text{P}_2\text{O}_7$  produces  $\text{Li}_3\text{PO}_4$  [12], while  $\text{Li}_3\text{BO}_3$  results from  $\text{Sn}_2\text{B}_3\text{O}_{6.5}$  [11]. Therefore, in the  $\text{LiSn}_2(\text{PO}_4)_3$  and  $\text{Sn}_3(\text{PO}_4)_2$  systems,  $\text{Li}_3\text{PO}_4$  is expected to be the principle component of the inorganic matrices that form.

During the first discharge plateau, mid-IR data (Figs. 4-6 and 4-8) reveal a gradual degradation of the intramolecular  $\text{PO}_4^{3-}$  stretching and bending modes for both  $\text{LiSn}_2(\text{PO}_4)_3$  and  $\text{Sn}_3(\text{PO}_4)_2$ . For example, the bands belonging to  $\nu_1(\text{PO}_4^{3-})$  and  $\nu_3(\text{PO}_4^{3-})$  collapse into a single band when either material is discharged to 1.00 V. This band is consistent with the formation of  $\text{Li}_3\text{PO}_4$ . Moreover, the breadth of the  $\text{Li}_3\text{PO}_4$  bands suggests that the phosphate anions become disordered as lithium is inserted into the electrodes. Analogous conclusions may be drawn from far-IR data over the same voltage

interval (Fig. 4-7 and 4-9; OCV  $\rightarrow$  1.00 V). When  $\text{LiSn}_2(\text{PO}_4)_3$  and  $\text{Sn}_3(\text{PO}_4)_2$  are discharged to 1.00 V, the  $\nu_2(\text{PO}_4^{3-})$  bands also broaden and shift to higher frequencies. However, the complete loss of spectral intensity for all the lattice modes is the most striking feature of the vibrational spectra. Long-range translational order is crucial for a lattice mode to have measurable intensity (for example, see reference [25] and the citations therein). The disappearance of lattice modes below 1.00 V is due to the disordering of the phosphate anions, which accompanies lithium insertion. The disordered nature of the compounds is consistent with the XRD data for the  $\text{LiSn}_2(\text{PO}_4)_3$  and  $\text{Sn}_3(\text{PO}_4)_2$  systems.

According to the alloy model, lithium and tin reversibly react to form Li-Sn compounds along the second voltage plateau (1.00  $\rightarrow$  0.01 V) [5]. The formation of Li-Sn alloys is not expected to affect the local environment of the phosphate anions in the  $\text{Li}_3\text{PO}_4$  matrix. Indeed, only minor changes in mid-IR band intensities occur when  $\text{LiSn}_2(\text{PO}_4)_3$  and  $\text{Sn}_3(\text{PO}_4)_2$  are discharged from 1.00 to 0.01 V (cf., Fig. 4-6 and 4-8). Additionally, the far-IR spectra remain essentially featureless over this voltage range, suggesting that the  $\text{Li}_3\text{PO}_4$  matrix remains disordered throughout the alloying process. This is not surprising since the inorganic matrix is electrochemically inert and only serves to conduct  $\text{Li}^+$  ions to the metallic tin domains [5].

There is strong spectroscopic evidence for the formation of carbonate species in  $\text{LiSn}_2(\text{PO}_4)_3$  and  $\text{Sn}_3(\text{PO}_4)_2$  electrodes discharged below 1.00 V. The appearance of the carbonate species is also reflected in the electrochemical data for the two systems. Differential capacity plots can often illuminate very subtle details of a voltage-capacity curve; therefore, differential capacity curves were constructed for  $\text{LiSn}_2(\text{PO}_4)_3$  and

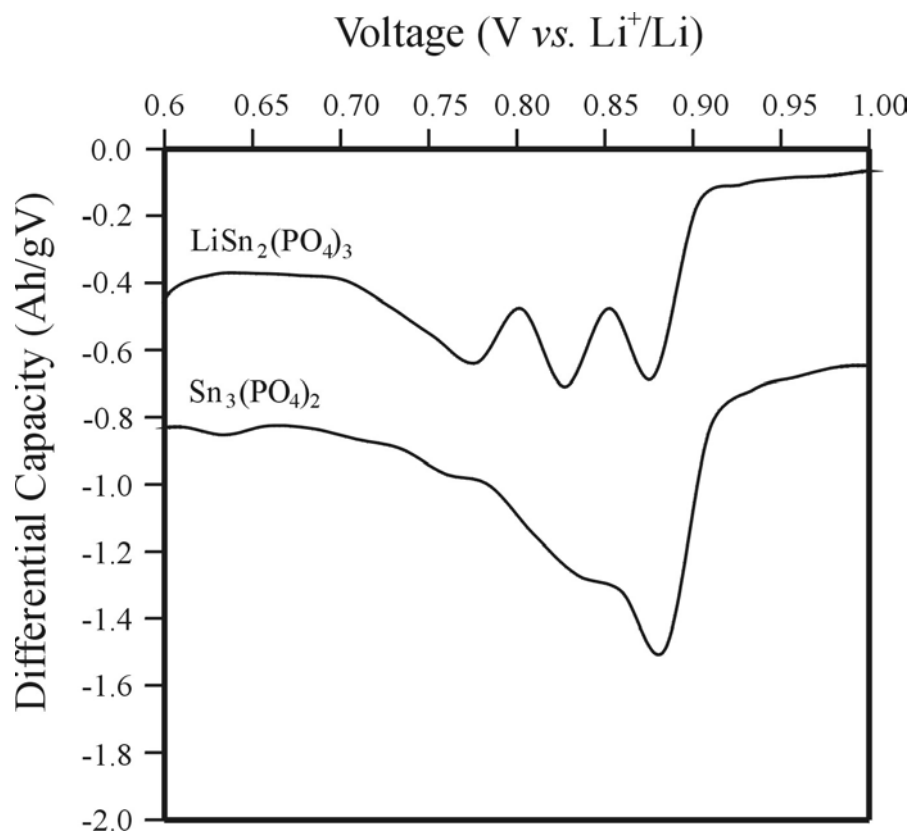


**Figure 4-11:** Differential capacity plots for  $\text{LiSn}_2(\text{PO}_4)_3$  and  $\text{Sn}_3(\text{PO}_4)_2$  between 0.60 and 1.00 V. The  $\text{LiSn}_2(\text{PO}_4)_3$  curve is displaced by  $-0.50 \text{ Ah/gV}$ .

$\text{Sn}_3(\text{PO}_4)_2$  between 1.00 and 0.60 V (Fig. 4-11). Both  $\text{LiSn}_2(\text{PO}_4)_3$  and  $\text{Sn}_3(\text{PO}_4)_2$  exhibit peaks within this voltage range, even though the peaks are relatively unresolved in the  $\text{LiSn}_2(\text{PO}_4)_3$  system compared to  $\text{Sn}_3(\text{PO}_4)_2$ . Behm and Irvine attributed these peaks to a passivation layer that forms on the conductive carbons in the electrodes [13]. However, carbonate bands appeared in infrared spectra of fully discharged  $\text{LiSn}_2(\text{PO}_4)_3$  and  $\text{Sn}_3(\text{PO}_4)_2$  electrodes that did not contain carbon. This suggests that the carbonate species primarily form on the active material present in the electrodes.

Beattie *et al.* [26] and Beaulieu *et al.* [6] described an anomalous, irreversible capacity for tin-based anodes that are charged above 0.80 V. In order to explain this



phenomenon, they speculated that electrolyte decomposition is catalyzed by metallic tin surfaces [26]. The carbonate species observed in the infrared spectra of discharged  $\text{LiSn}_2(\text{PO}_4)_3$  and  $\text{Sn}_3(\text{PO}_4)_2$  are hypothesized to form according to a similar mechanism. At 1.00 V, most of the tin cations have been reduced to metallic tin, but the Li-Sn alloys have not yet formed [27]. Between 1.00 V and  $\sim 0.8$  V, the electrolyte is in contact with the metallic tin in the electrode, and the tin facilitates the decomposition of the electrolyte to either  $\text{Li}_2\text{CO}_3$  or  $\text{LiRCO}_3$ . The differential capacity data indicates that these reactions cease at  $\sim 0.70$  V, which is after the formation of the first Li-Sn alloy phase ( $\text{Li}_2\text{Sn}_5$ ) [27]. It has been argued that lithium-tin alloys probably do not catalyze the decomposition of the electrolyte as efficiently as pure tin [26]. Hence, the intensities of the  $\text{CO}_3^{2-}$  bands remain unchanged as  $\text{LiSn}_2(\text{PO}_4)_3$  and  $\text{Sn}_3(\text{PO}_4)_2$  are discharged to 0.01 V.

Based on the above discussion, it is reasonable to assume that the carbonate species form on the surface of the  $\text{LiSn}_2(\text{PO}_4)_3$  and  $\text{Sn}_3(\text{PO}_4)_2$  particles. Thus, the amount of carbonate formed would be a function of the particle size and surface area of the particles. The synthesis conditions employed in this study produced a broad range of particle sizes (Fig. 4-1), yet most of the  $\text{LiSn}_2(\text{PO}_4)_3$  and  $\text{Sn}_2(\text{PO}_4)_3$  particles have approximately the same surface area and a mean diameter greater than 1  $\mu\text{m}$ .

Consequently, the relative intensities of the  $\text{CO}_3^{2-}$  bands are similar for the two systems.

Beattie *et al.* suggests “the layer of decomposed electrolyte... serves to inhibit the diffusion of  $\text{Li}^+$ , decreasing the overall capacity in subsequent cycles” [26]. Therefore, it is probably desirable to suppress the formation of the carbonate species on the first discharge. This could be accomplished either by controlling the discharge rate for the first cycle [6] or optimizing the particle sizes and surface areas of the materials.

#### 4.4.3 Thermal Data

The origin of the 225 and 250-300°C thermal transitions is not immediately clear. It is known that a solid electrolyte interphase (SEI) layer will develop on the surface of graphite when it is discharged to 0.01 V, and DSC measurements of lithiated graphite yield peaks that are similar to the features noted in the first thermal scans in Fig. 4-10 [28]. It is tempting to attribute the peaks in the DSC data to the formation of the carbonate species since they both develop at approximately the same voltage. However, discharging from 1.00 to 0.01 V produces dramatic changes in the DSC peaks, while the carbonate species remain unchanged according to the infrared spectroscopic data. This makes such an association tenuous. Moreover, Wagner *et al.* [29] has shown that the electrolyte decomposition mechanism is different for alloy- and graphite-based anodes. More research is required to understand the origin and nature of the DSC peaks and determine whether or not they are related to the carbonate species detected with infrared spectroscopy.

It is quite unusual that some regions of tin do not form Li-Sn alloys. There is only one report in the literature of tin persisting to very low voltages (*in situ* XRD study of  $\text{Sn}_2\text{BPO}_6$ ) [12], among the numerous phosphate- and borophosphate-based anode materials that have been investigated with *ex situ* and *in situ* XRD [9,12,24]. The Li-Sn binary phase diagram has been extensively researched [1,2], and the Li-Sn alloys that form between Sn and  $\text{Li}_{22}\text{Sn}_5$  melt at high temperatures. In fact, the melting points of Li-Sn alloys that have a lithium concentration greater than LiSn are beyond the thermal range of our DSC instrument. Thus, one would not expect to find large melting endotherms after the Li-Sn alloys form. The amount of metallic tin in the electrodes can

be approximated from the integrated intensity of the DSC data and the enthalpy of fusion for tin found in Ref. [30]. These calculations indicate that only a small amount of the tin expected from Eq. 4-1 is detected at 0.40 V for  $\text{LiSn}_2(\text{PO}_4)_3$  and 0.70 V for  $\text{Sn}_3(\text{PO}_4)_2$ . At these voltages, both of the materials are below the potential at which Li-Sn alloys form [27]. Thus, the tin endotherms in the DSC data are not a measurement of the total amount of metallic tin formed, but the amount of residual, unalloyed tin within the samples. Discharging to 0.01 V causes a slight decrease in the magnitude of the tin endothermic peaks because more of the residual tin is alloyed. The DSC data indicate that  $\text{Sn}_3(\text{PO}_4)_2$  contains larger domains of residual tin than  $\text{LiSn}_2(\text{PO}_4)_3$  at 0.01 V. This agrees well with the approximate grain sizes for the tin domains calculated from the XRD data (37 nm for  $\text{Sn}_3(\text{PO}_4)_2$  and 17 nm for  $\text{LiSn}_2(\text{PO}_4)_3$ ).

The following picture emerges when all the data are considered together. At 1.00 V, the tin cations in  $\text{LiSn}_2(\text{PO}_4)_3$  and  $\text{Sn}_3(\text{PO}_4)_2$  have been completely reduced to form tin atoms dispersed throughout a disordered  $\text{Li}_3\text{PO}_4$  matrix. At this voltage, the tin atoms have not begun to significantly aggregate into metallic tin domains; hence, there is not a measurable thermal transition in the DSC data. Metallic domains begin to develop when the materials are discharged below 1.00 V. The alloying peaks in the differential capacity data indicate that this is more severe for  $\text{Sn}_3(\text{PO}_4)_2$  than  $\text{LiSn}_2(\text{PO}_4)_3$ . It appears that the Li-Sn domains are smaller and less organized for  $\text{LiSn}_2(\text{PO}_4)_3$ , an observation that is similar to reports on other  $\text{SnB}_x\text{P}_y\text{O}_z$  systems [24]. The high capacities of the compounds below 0.80 V suggests that alloys with a high lithium concentration form in these anodes. The  $\text{Li}^+$  ions probably undergo slow diffusion in the electrode materials, leaving some of the metallic tin in the center of the larger aggregates unalloyed.

## 4.5 Conclusions

The first discharge of crystalline  $\text{LiSn}_2(\text{PO}_4)_3$  and  $\text{Sn}_3(\text{PO}_4)_2$  has been investigated with infrared spectroscopy, XRD, DSC, and impedance spectroscopy. The vibrational spectroscopic data may be explained in terms of an alloying model. In the original compounds,  $\text{PO}_4^{3-}$  intramolecular vibrations and lattice modes are clearly recognized in the infrared spectra. A factor group correlation explains the vibrational structure of phosphate anions for the pristine materials. The  $\text{PO}_4^{3-}$  bands become broad and the factor group vibrational multiplet structure is lost when  $\text{LiSn}_2(\text{PO}_4)_3$  or  $\text{Sn}_3(\text{PO}_4)_2$  is irreversibly reacted with lithium (Figs. 4-6 and 4-8; OCV  $\rightarrow$  1.00 V). In addition, the lattice modes vanish over this voltage range (Figs. 4-7 and 4-9). These spectral data argue that inserting  $\text{Li}^+$  ions into  $\text{LiSn}_2(\text{PO}_4)_3$  and  $\text{Sn}_3(\text{PO}_4)_2$  destroys the translational symmetry of the crystalline compounds and produces an inorganic matrix consisting primarily of disordered  $\text{Li}_3\text{PO}_4$ . Below 1.00 V, the  $\text{Li}_3\text{PO}_4$  bands are not significantly affected by lithium insertion. At these voltages lithium ions alloy with tin and do not react further with the inorganic matrix.

Bands that are assigned to  $\text{CO}_3^{2-}$  species appear rather suddenly in the mid-IR spectra of  $\text{LiSn}_2(\text{PO}_4)_3$  and  $\text{Sn}_3(\text{PO}_4)_2$ . Simultaneously, peaks appear in the differential capacity curves roughly between 1.00 and 0.80 V for both samples. It is known that above 0.80 V the electrolyte system will decompose on metallic tin [6,26], and a similar decomposition reaction is thought to produce the  $\text{CO}_3^{2-}$  species during the first discharge of  $\text{LiSn}_2(\text{PO}_4)_3$  and  $\text{Sn}_3(\text{PO}_4)_2$ . The intensities of the  $\text{CO}_3^{2-}$  bands are not affected by the

formation of Li-Sn alloys at low voltages. DSC measurements of the compounds as a function of voltage reveal the formation of thermally irreversible endothermic and exothermic peaks that might be related to the carbonate species. Similar DSC features have been reported in the literature when SEI layers form on graphite at low voltages [28]. However, the correlation between the peaks in the DSC data and the appearance of the  $\text{CO}_3^{2-}$  bands in the mid-IR spectra has yet to be established.

The conductivity of  $\text{LiSn}_2(\text{PO}_4)_3$  and  $\text{Sn}_3(\text{PO}_4)_2$  samples dramatically increases when the electrodes are discharged to 0.01 V. This is consistent with the formation of Sn and Li-Sn alloy domains. Further XRD measurements confirm the complete destruction of the host material's crystallinity. Metallic tin is detected with XRD and DSC measurements at very low voltages. It is thought that these regions of tin are small amounts of residual, unalloyed tin in the core of the alloy domains. Differences in the relative amount of tin detected by DSC and XRD for  $\text{LiSn}_2(\text{PO}_4)_3$  and  $\text{Sn}_3(\text{PO}_4)_2$  have been explained in terms of the spectator atom to tin ratio of the parent compounds.

Unfortunately, the Li-Sn alloys have melting points that exceed the capabilities of our DSC instrument, and there is essentially no clear XRD evidence for the existence of Li-Sn alloys in the discharged samples. The lack of prominent Li-Sn alloy peaks in the XRD data does not necessarily indicate that Li-Sn alloys do not form in the  $\text{LiSn}_2(\text{PO}_4)_3$  and  $\text{Sn}_3(\text{PO}_4)_2$  systems. There is strong electrochemical evidence that these compounds form alloys below  $\sim 0.8$  V [13]. Techniques that are more sensitive to the presence of Li-Sn domains, such as  $^{119}\text{Sn}$  Mössbauer spectroscopy [14,17], should be employed to fully understand the nature of the alloys that form in  $\text{LiSn}_2(\text{PO}_4)_3$  and  $\text{Sn}_3(\text{PO}_4)_2$ .

## 4.6 References

- [1] W. Gasiior, Z. Moser and W. Zakulski, *J. Non-cryst. Solids*, **205-207**, (1996) 379-382.
- [2] J. Sangster and C. W. Bale, *J. Phase Equilibria*, **19**, (1998) 70-75.
- [3] J. O. Besenhard, P. Komenda, A. Paxinos, E. Wudy and M. Josowicz, *Solid State Ionics*, **18-19**, (1986) 823-827.
- [4] M. Winter and J. O. Besenhard, *Electrochim. Acta*, **45**, (1999) 31-50.
- [5] I. A. Courtney and J. R. Dahn, *J. Electrochem. Soc.*, **144**, (1997) 2045-2052.
- [6] L. Y. Beaulieu, S. D. Beattie, T. D. Hatchard and J. R. Dahn, *J. Electrochem. Soc.*, **150**, (2003) A419-A424.
- [7] Y. Idota, M. Mishima, Y. Miyaki, K. Tadahiko and T. Miyasaka, *U. S. Pat. Appl.*, **5,618,640**, (1994).
- [8] Y. Idota, T. Kubota, A. Matsufuji, Y. Maekawa and T. Miyasaka, *Science*, **276**, (1997) 1395-1397.
- [9] Y. W. Xiao, J. Y. Lee, A. S. Yu and Z. L. Liu, *J. Electrochem. Soc.*, **146**, (1999) 3623-3629.
- [10] C. Gejke, E. Zanghellini, L. Börjesson, L. Fransson and K. Edström, "Lithium Insertion in Sn-P and Sn-B-P Oxide Glasses," in *Lithium Batteries*, S. Surampudi, R. A. Marsh, Z. Ogumi and J. Prakash, Eds., **PV 99-25** The Electrochemistry Society Proceedings Series: Pennington, (2000) 144-149.
- [11] C. Gejke, E. Zanghellini, L. Fransson, K. Edström and L. Börjesson, *J. Power Sources*, **97-98**, (2001) 226-228.
- [12] C. Gejke, E. Zanghellini, L. Börjesson, L. Fransson and K. Edström, *J. Phys. Chem. Solids*, **62**, (2001) 1213-1218.
- [13] M. Behm and J. T. S. Irvine, *Electrochim. Acta*, **47**, (2002) 1727-1738.
- [14] F. Robert, F. Morato, J. Chouvin, L. Aldon, P. E. Lippens, J. O. Fourcade, J.-. Jumas, B. Simon and P. Biensan, *J. Power Sources*, **119-121**, (2003) 581-584.
- [15] A. Hayashi, M. Nakai, M. Tatsumisago, T. Minami and M. Katada, *J. Electrochem. Soc.*, **150**, (2003) A582-A587.

- [16] Y. Wang, J. Sakamoto, C. K. Huang, S. Surampudi and S. G. Greenbaum, *Solid State Ionics*, **110**, (1998) 167-172.
- [17] I. A. Courtney, R. A. Dunlap and J. R. Dahn, *Electrochim. Acta*, **45**, (1999) 51-58.
- [18] E. Morin, J. Angenault, J. C. Couturier, M. Quarton, H. He and J. Klinowski, *Eur. J. Solid State Inorg. Chem.*, **34**, (1997) 947-958.
- [19] M. Mathew, L. W. Schroeder and T. H. Jordan, *Acta Cryst.*, **B33**, (1977) 1812-1816.
- [20] W. G. Fately, F. R. Dollish, N. T. McDevitt and F. F. Bentley, *Infrared and Raman Selection Rules for Molecular and Lattice Vibrations: The Correlation Method*, John Wiley & Sons: New York (1972).
- [21] M. C. Apella, E. J. Baran, S. B. Etcheverry and R. C. Mercader, *Monatsch. Chem.*, **114**, (1983) 1149-1159.
- [22] J.-M. Tarascon and M. Armand, *Nature*, **414**, (2001) 359-367.
- [23] I. A. Courtney and J. R. Dahn, *J. Electrochem. Soc.*, **144**, (1997) 2943-2948.
- [24] I. A. Courtney, W. R. McKinnon and J. R. Dahn, *J. Electrochem. Soc.*, **146**, (1999) 59-68.
- [25] P. Dean, *Rev. Modern. Phys.*, **44**, (1972) 127-168.
- [26] S. D. Beattie, T. Hatchard, A. Bonakdarpour, K. C. Hewitt and J. R. Dahn, *J. Electrochem. Soc.*, **150**, (2003) A701-A705.
- [27] I. A. Courtney, J. S. Tse, O. Mao, J. Hafner and J. R. Dahn, *Phys. Rev. B*, **58**, (1998) 15583-15588.
- [28] A. M. Andersson, M. Herstedt, A. G. Bishop and K. Edström, *Electrochim. Acta*, **47**, (2002) 1885-1898.
- [29] M. R. Wagner, P. R. Raimann, A. Trifonova, K.-C. Moeller, J. O. Besenhard and M. Winter, *Electrochem. Solid-State Lett.*, **7**, (2004) A201-A205.
- [30] R. C. Weast, Ed., *Handbook of Chemistry and Physics*, 55<sup>th</sup> ed., CRC Press: Cleveland, (1974), pp. B-148.

## Chapter 5: *IN SITU* VIBRATIONAL SPECTROSCOPIC STUDIES

---

*Christopher M. Burba and Roger Frech, Appl. Spectrosc., Accepted (2005)\**

*Christopher M. Burba and Roger Frech, Electrochim. Acta, Submitted (2005)†*

### 5.1 Introduction

Secondary lithium ion batteries are widely used in electronic devices such as cell phones, laptop computers, and personal digital assistants (PDAs) primarily because  $\text{Li}^+$  ion batteries have higher energy densities than competing rechargeable energy storage technologies (e.g., alkaline or lead-acid batteries) [1]. Commercial  $\text{Li}^+$  ion cells typically employ a carbonaceous anode, an oxide-based cathode (such as  $\text{LiCoO}_2$  or spinel  $\text{LiMn}_2\text{O}_4$ ), and a nonaqueous or polymeric electrolyte system. However, there are intense efforts to develop alternative high performance electrodes that are superior to the current technologies in terms of energy density, cyclability, safety, and ecological impact. In developing new electrode materials, it is critical that the fundamental reactions that occur inside the electrode materials and at the electrode/electrolyte interface be understood very well. It is particularly desirable to probe the cells *in situ* since exposure to the atmosphere might affect some of the interfacial and/or bulk properties. To this end, *in situ* vibrational spectroscopy has proven to be extremely valuable in investigating lithium batteries.

Initial *in situ* Raman spectroscopic studies focused on the intercalation of lithium ions into various oxide-based cathodes (viz.,  $\text{Li}_x\text{CoO}_2$ ,  $\text{Li}_x\text{Mn}_2\text{O}_4$ , and  $\text{Li}_x\text{V}_2\text{O}_5$ ) [2-5] and

\*© The Society for Applied Spectroscopy (2005). All rights reserved.

†© Elsevier, Inc. (2005).



graphitic anodes [6-8]. The technique has also been refined to allow spectroscopic investigations of single electrode particles during cell operation [9-11]. Several workers also report detailed spectro-topographic measurements of the cells [10-14]. For instance, Rey *et al.* examined a functioning  $\text{Li|P(EO)}_{20}\text{Li(SO}_2\text{CF}_3)_2\text{|V}_2\text{O}_5$  cell with *in situ* Raman microspectrometry and could detect structural changes in the  $\text{V}_2\text{O}_5$  cathode, concentration gradients in the polymer electrolyte, and polluting agents formed at the lithium-electrolyte interface [14].

Most *in situ* infrared experiments use diffuse reflection FTIR spectroscopy (DRIFTS) or attenuated total reflectance (ATR) FTIR spectroscopy. These techniques have been extensively used to study solid electrolyte interphase (SEI) formation on graphitic anodes in lithium batteries (e.g., see Ref. [15]). Unfortunately, DRIFTS and ATR spectroscopic methods often suffer from low reflectance intensities and broad, overlapping bands, which can introduce additional complexities when analyzing the spectroscopic data. Moreover, ATR crystals are usually very expensive and susceptible to attack from the harsh conditions inside a nonaqueous lithium battery [16].

In general, *in situ* vibrational spectroscopy requires the construction of specialized cells that are often structurally dissimilar to “normal” electrochemical cells. More importantly, the number of *in situ* cells available is usually limited by construction costs; thus, routine usage of the techniques is severely hampered for most laboratories. In this chapter, conventional coin cells are modified to facilitate routine *in situ* Raman spectroelectrochemical measurements of electrodes in lithium batteries. This approach will enable researchers to easily construct cells for *in situ* Raman spectroscopy in addition to cells that are used in normal electrochemical evaluations. Furthermore, a new

cell design is described to facilitate *in situ* transmission FTIR spectroelectrochemistry. This will extend *in situ* infrared spectroscopy of battery materials to allow new experiments that may not be easily performed with *in situ* reflection FTIR spectroelectrochemistry.

To test these cell designs, *in situ* Raman spectroelectrochemical measurements are conducted on Li//V<sub>2</sub>O<sub>5</sub> cells. Several different research groups have characterized lithium insertion into V<sub>2</sub>O<sub>5</sub> with Raman spectroscopy, and the resulting data provide a good benchmark for this experiment [2,17,18]. Preliminary electrochemical measurements of the modified coin cells are also compared to “normal” cells. The new *in situ* transmission FTIR spectroelectrochemical cell evaluated with Li//Li<sub>x</sub>FePO<sub>4</sub> half-cells. The intramolecular vibrations of the PO<sub>4</sub><sup>3-</sup> anions are known to be very sensitive to the presence of Li<sup>+</sup> ions and the oxidation state of the iron ions (e.g., see Chapter 2, Section 2.3.3). Therefore, this system will provide a good test of the capabilities of the *in situ* transmission infrared spectroelectrochemical cell.

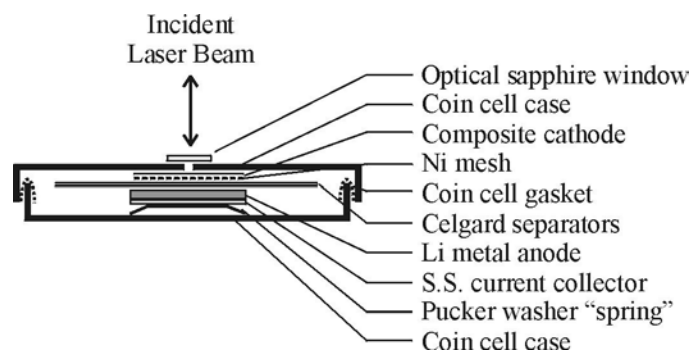
It is important to note that Cai *et al.* employed an analogous cell modification in investigating an alkaline Zn-MnO<sub>2</sub> AA-type cell [19]. Furthermore, Migge *et al.* measured lithium intercalation into graphite with an *in situ* Raman spectroelectrochemical cell design that is very similar to the one described in this chapter [20]. Although their *in situ* cells are not compared to unmodified ones, any credit for first adapting industrial cells for *in situ* Raman spectroscopy should be given to these authors.

## 5.2 *In Situ* Raman Spectroelectrochemistry

### 5.2.1 *In Situ* Raman Spectroelectrochemical Cell

5.2.1.1 Cathode Preparation – Composite cathodes are prepared by mixing 87 wt% V<sub>2</sub>O<sub>5</sub> (Aldrich), 5 wt% KS-6 graphite (Tim Cal), 5 wt% Super P carbon (3M), and 3 wt% Teflon. The resulting cathode paste is rolled into a thin sheet and cut into 1.27 cm<sup>2</sup> circular disks. The total mass of each cathode is approximately 15 mg. A thin sheet of Ni MicroMesh (50.8 μm thick, ca. 8 wires/mm and 14.7 μm/wire) is pressed into the composite cathode to improve electronic conductivity throughout the electrode. Modified and “normal” electrochemical cells are constructed in an analogous fashion. Size 2430 coin cells are constructed with the above cathodes, a lithium metal anode (Aldrich), two pieces of a porous polyethylene separator (Celgard 2700), a Whatman GF glass microfiber separator and an electrolyte consisting of 1 M LiPF<sub>6</sub> in a 1:1 solution of diethyl carbonate and ethylene carbonate.

5.2.2.2 Spectroelectrochemical Cell Design – A pictorial representation of the *in situ* Raman spectroelectrochemical coin cells is shown in Schematic 5-1. In short, the cells are very similar to the unmodified coin cells except for a 2 mm diameter hole that is drilled into the coin cell casing prior to cell assembly. After the coin cell is crimped closed, an optically transparent sapphire window (13 mm × 1 mm) is attached over the hole. The window is lightly pressed against the coin cells with a C-clamp and affixed in place with an epoxy resin.



**Scheme 5-1:** A diagram of the modified *in situ* Raman spectroelectrochemical cell (not drawn to scale).

5.2.2.3 Electrochemical and Spectroscopic Experiments – Cells are galvanostatically discharged at 0.01 mA/cm between 1.5 and 3.7 V vs.  $\text{Li}^+/\text{Li}$ . During the first cycle, the coin cells are discharged to the desired potential and then potentiostatically held at that potential until the current is less than 30  $\mu\text{A}$  or 24 h has elapsed. Afterwards, the electrochemical performance of the two cell types is evaluated by cycling the cells at a rate of 0.01 mA/cm with trickle charge/discharge steps (1 h duration) at the cutoff voltages.

Details concerning the Raman spectroscopic measurements are contained in App. A.6. Unfortunately, it is not possible to simultaneously cycle the cells and collect *in situ* Raman spectroscopy under an environmentally controlled atmosphere. Therefore, some of the cells have been exposed to the ambient atmosphere.

### 5.2.2 Lithium Insertion into $\text{V}_2\text{O}_5$ Cathodes

5.2.2.1 Electrochemistry – Crystalline  $\text{V}_2\text{O}_5$  belongs to the orthorhombic crystal system (space group  $Pmnm$ ,  $D_{2h}^{13}$ ) [21]. The vanadium ions occupy distorted trigonal bipyramids

that form edge-shared chains along [001]. The chains are linked together by corner-sharing vertices in [100], forming sheets in the  $xz$  plane. Previous research has shown that lithium intercalation into  $V_2O_5$  can occur along four electrochemical plateaus between 3.5 and 1.5 V vs.  $Li^+/Li$  until a maximum composition of  $Li_3V_2O_5$  is reached (442 mAh/g theoretical capacity) [22-25]. Several phase changes transpire during these electrochemical plateaus:  $\alpha$  ( $x < 0.1$ ),  $\epsilon$  ( $0.35 \leq x \leq 0.7$ ),  $\delta$  ( $0.9 \leq x \leq 1.0$ ),  $\gamma$  ( $1.0 \leq x \leq 1.8$ ), and  $\omega$  ( $x > 1.8$ ), where  $x$  refers to the number of  $Li^+$  ions per  $V_2O_5$  formula unit ( $Li_xV_2O_5$ ) [25]. Although the  $\alpha$ - and  $\epsilon$ - $Li_xV_2O_5$  structural phase changes are reversible upon lithium extraction, transformation to the  $\gamma$ -phase is irreversible and occurs slowly throughout the  $1.0 < x < 1.8$  composition domain [25-27]. That is, the  $\alpha$ - and  $\epsilon$ -phases are not recovered when the cells are charged. The  $\delta$ -phase gradually transforms into the  $\gamma$ -phase during the 2.4 V plateau, and deep discharging produces  $\omega$ - $Li_3V_2O_5$ , which has a simple rock salt structure and belongs to the cubic crystal system. West *et al.* demonstrated that these phase changes also depend on the cell temperature during cycling [24,28]. Several workers have extensively explored the electrochemical performance of  $\gamma$ - $LiV_2O_5$  [4,25,29]. Chemical and electrochemical extraction or insertion of  $Li^+$  results in new phases:  $\gamma'$ - $V_2O_5$  and  $\zeta$ - $Li_2V_2O_5$ , respectively [29,30]. The  $\gamma'$ - $V_2O_5$  and  $\zeta$ - $Li_2V_2O_5$  phases are both structurally related to  $\gamma$ - $LiV_2O_5$ .

The first cycle of the *in situ* and unmodified  $Li//V_2O_5$  coin cells are presented in Fig. 5-1. Both cells exhibit four electrochemical plateaus at 3.4, 3.2, 2.3 and 2.0 V when discharged, giving a specific capacity of approximately 400 mAh/g. Upon charging, the voltage-composition curves for both cell types show solid solution behavior. Here, the

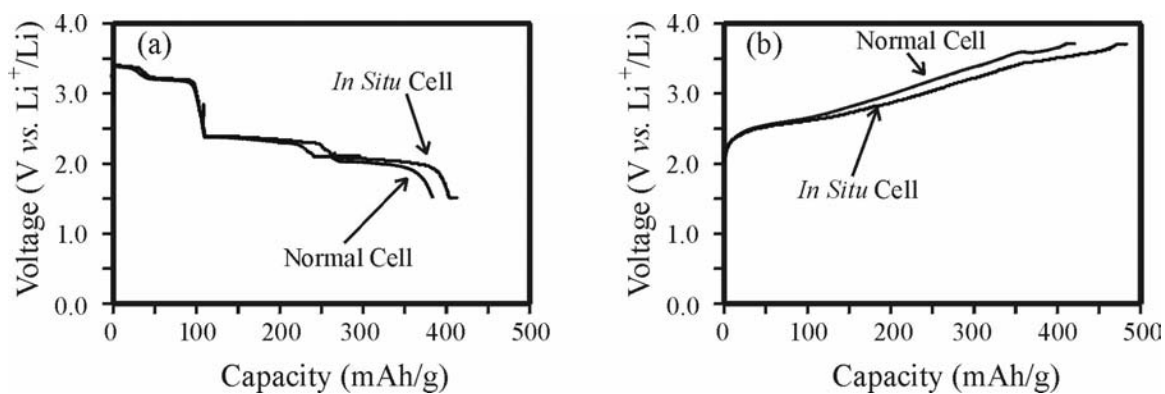


**Figure 5-1:** Electrochemical (a) discharging and (b) charging curves for *in situ* Raman spectroelectrochemical and normal cells.

cells gradually increase in potential as  $\text{Li}^+$  ions are extracted from the cathodes [24,25,28]. The solid solution behavior is caused by the loss of crystallinity associated with the insertion of three  $\text{Li}^+$  ions into the parent structure [28].

Cycling performance of *in situ* and unmodified coin cells is presented in Fig. 5-2. Both cells have very high initial discharge capacities but experience a rapid decrease in discharge capacity between the first and second cycles. For example, the discharge capacity of the unmodified cells falls from 398 to 309 mAh/g between cycle numbers one and two. Afterwards, the discharge capacity fades by about 3 mAh/(g cycle) between the third and eighth cycle to reach a value of approximately 260 mAh/g. The cycling performance of *in situ* coin cells mimics the cycling data of the unmodified ones. It is well known that  $\text{V}_2\text{O}_5$ -based cathodes experience rapid fade when discharged below 2.3 V. Several mechanisms for capacity fade have been proposed for  $\text{Li}_x\text{V}_2\text{O}_5$  compounds: chemical grinding [29], irreversible structural changes [24], and the formation of  $\text{VO}^{2+}$  impurities [22]. However, most of the initial capacity loss is probably due to irreversible

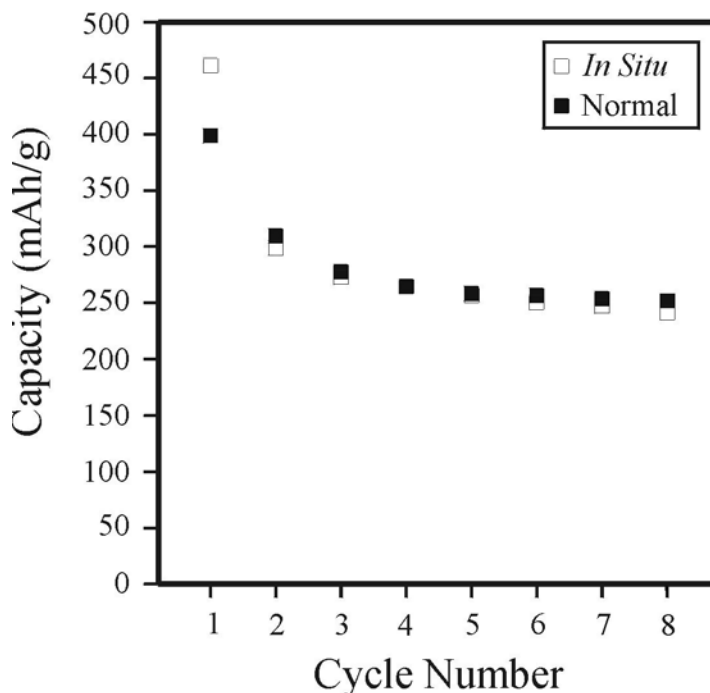


**Figure 5-2:** Effect of cell type on discharge capacity.

damage of the  $V_2O_5$  structure upon deep discharge to 1.5 V. Therefore, it is not surprising that these cells exhibit a 35% decrease in discharge capacity over the first eight cycles.

The electrochemical performance of the *in situ* Raman cells closely matches the unmodified coin cells when cycled under an inert atmosphere; however, moisture poisoning is detected when the *in situ* cells are cycled under ambient conditions. This appears as a long trickle charge/discharge step following the galvanostatic charging or discharging processes and somewhat lower capacities. Most likely, this is due to slow diffusion of water through the seals of the optical windows. It is not uncommon for *in situ* Raman spectroelectrochemical cells to have a relatively short lifetime of operation under ambient atmospheric conditions (e.g., see Ref. [10]) so these results are not surprising.

5.2.2.2 Raman Spectroscopy – A number of researchers have used Raman spectroscopy to characterize crystalline  $\text{Li}_x\text{V}_2\text{O}_5$  materials [2,4,17,18,31]. For example, Abello *et al.* conducted careful polarized Raman spectroscopic investigations of crystalline  $\text{V}_2\text{O}_5$  [31]. Furthermore, Baddour-Hadjean *et al.* utilized *ex situ* Raman spectroscopy to investigate thin films of  $\text{Li}_x\text{V}_2\text{O}_5$  ( $0 \leq x \leq 1.8$ ) [17], and Zhang and Frech studied the transformation of  $\gamma\text{-LiV}_2\text{O}_5$  into  $\gamma'\text{-V}_2\text{O}_5$  and  $\zeta\text{-Li}_2\text{V}_2\text{O}_5$  with *in situ* Raman spectroscopy [4].

*In situ* Raman spectra (between  $650\text{--}80\text{ cm}^{-1}$ ) of the modified  $\text{Li//V}_2\text{O}_5$  coin cells are collected at various points along the first cycle and presented in Fig. 5-3. The Raman spectrum of the  $\text{V}_2\text{O}_5$  cathode prior to discharging agrees very well with the previous spectroscopic investigations (labeled OCV on Fig. 5-3). The spectrum has an excellent signal-to-noise ratio and is dominated by an intense band at  $146\text{ cm}^{-1}$ . This vibrational

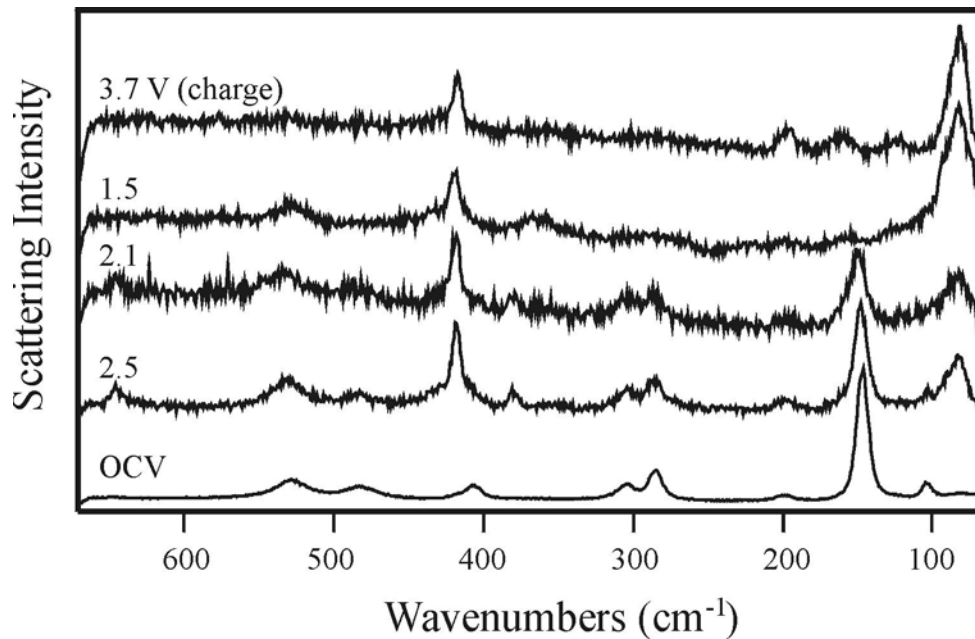


**Figure 5-3:** *In situ* Raman scattering spectra recorded during the first cycle of a  $\text{Li//V}_2\text{O}_5$  cell.



mode has been assigned to the  $B_{2g}$  irreducible representation of the  $D_{2h}$  point group and corresponds to pseudo-rotational motions of  $V_2O_5$  units within a unit cell [31]. Internal vibrations of the  $V_2O_5$  units have also been identified with Raman spectroscopy. These modes primarily consist of O–V–O or V–O–V bending motions and V–O stretching vibrations. For instance, Abello *et al.* assigned the band at  $526\text{ cm}^{-1}$  to V–O stretching motions, while the  $406\text{ cm}^{-1}$  band is attributed to a V–O–V bending vibration [31].

Discharging the cells to 2.5 V produces a compound that is essentially  $\epsilon\text{-LiV}_2\text{O}_5$ . At this potential, the signal-to-noise ratio decreases dramatically and new bands appear at  $645$ ,  $380$ , and  $82\text{ cm}^{-1}$ . Furthermore, the weak shoulder at  $416\text{ cm}^{-1}$  in the Raman spectrum of pure  $V_2O_5$  significantly increases in intensity and becomes a dominant feature at  $418\text{ cm}^{-1}$ . Further discharging to 2.1 V (approximately  $\gamma\text{-Li}_2\text{V}_2\text{O}_5$ ) produces subtle changes for a few of the bands. For example, the frequency of the  $146\text{ cm}^{-1}$  band in the uncharged cathode increases to  $149\text{ cm}^{-1}$  and its relative intensity slightly decreases. At 1.5 V, many of the bands characteristic of the 2.1 V sample have vanished (e.g., the  $644$ ,  $303$ ,  $286$ , and  $149\text{ cm}^{-1}$  bands), and only very weak bands at  $124$ ,  $156$ , and  $199\text{ cm}^{-1}$  may be resolved. The lack of strong Raman bands throughout most of the spectrum is probably due to structural disorganization accompanying the insertion of the third  $\text{Li}^+$  ion to form  $\omega\text{-Li}_3\text{V}_2\text{O}_5$ . The intense bands at  $419$  and  $82\text{ cm}^{-1}$  are probably bending and lattice modes of the disordered  $V_2O_5$  units, respectively, for this phase. As expected, charging the cells to 3.7 V does not recover the Raman spectrum of pure  $V_2O_5$ . Instead, the 3.7 V spectrum is characterized by a strong band at  $80\text{ cm}^{-1}$  and four bands at  $123$ ,  $166$ ,  $196$ , and  $417\text{ cm}^{-1}$ . The  $529\text{ cm}^{-1}$  band of the 1.5 V sample is not observed in fully charged cathodes. The spectral changes observed in Fig. 5-3 agree with the *ex situ*

spectroscopic measurements of Baddour-Hadjean *et al.* [17] and McGraw *et al.*[18]; thus, demonstrating the feasibility of using the modified coin cells to perform *in situ* Raman spectroelectrochemical experiments.

### 5.2.3 Lithium Insertion into Phosphate-Based Cathodes

Unfortunately, the compounds investigated in this dissertation could not be studied with *in situ* Raman spectroscopy. This is primarily because the scattering intensities of the compounds are too small. For example, LiFePO<sub>4</sub> must be coated with graphite in order to increase the specific capacity of the material to practical levels. However, the carbon surface layer significantly reduces the scattering intensity of the cathode material (see Fig. 2-20 in Section 2.3.4), making detailed spectroscopic experiments very difficult. The Raman intensities of the Li<sub>3</sub>V<sub>2</sub>(PO<sub>4</sub>)<sub>3</sub> materials are too low to warrant an *in situ* Raman spectroscopic study. Conversely, Raman spectra can be recorded during lithium insertion into LiTi<sub>2</sub>(PO<sub>4</sub>)<sub>3</sub> but the spectral changes are very small. The infrared spectra provide more information about the local structural rearrangements that occur as the lithium concentration is increased in the titanium-containing material compared to the Raman spectra.

## 5.3 *In Situ* Transmission FTIR Spectroelectrochemistry

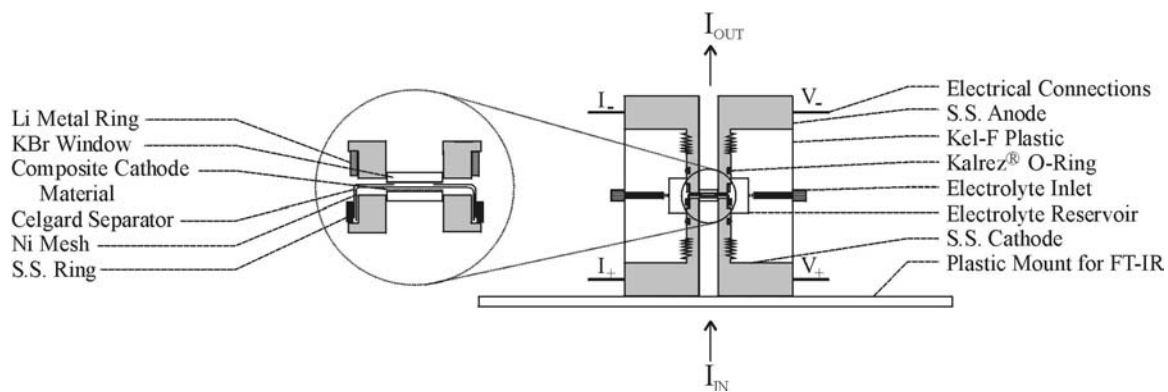
### 5.3.1 *In Situ* Transmission FTIR Spectroelectrochemical Cell

5.3.1.1 Cathode Preparation – High quality LiFePO<sub>4</sub> is obtained from Kerr-McGee Chemical, LLC. This material is reacted with an excess of Br<sub>2</sub> in acetonitrile to

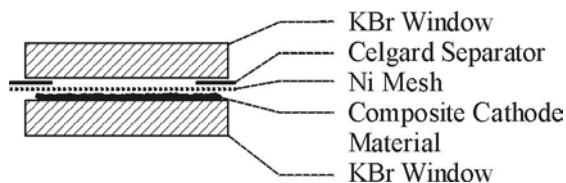
synthesize FePO<sub>4</sub>. Composite cathodes consist of 70wt% FePO<sub>4</sub>, 25wt% KS-6 graphite (Tim Cal, Inc.), and 5wt% PVDF (Aldrich). A slurry is formed by adding 2-methylpyrrolidinone to the above mixture.

5.3.1.2 Spectroelectrochemical Cell – The primary difficulty in designing an *in situ* transmission FTIR spectroelectrochemical cell is maintaining electrochemical performance while maximizing spectroscopic throughput. It is crucial that the path length through the cell be as small as possible with a minimum number of cell components placed in the infrared beam. One problem in designing an *in situ* transmission FTIR cell is that the material required to physically separate the two electrodes (either microporous polyethylene-polypropylene or a polymer electrolyte) strongly absorbs infrared radiation at the frequencies of interest. In this work, which is concerned with cathode processes, the anode is removed from the path of the infrared beam. Thus, a separator does not have to completely cover the cathode material if a nonaqueous liquid electrolyte is used. This allows the infrared beam to sample only the cathode and electrolyte.

A diagram of the *in situ* FTIR spectroelectrochemical cell used in this experiment is presented in Scheme 5-2. The cylindrical cell consists of four parts: a plastic base to mount the cell inside the FTIR spectrometer, two stainless steel electrode assemblies, and a plastic mount to hold the electrode assemblies together. The plastic mount is also modified to contain a reservoir of electrolyte solution. The interior of the spectroelectrochemical cell is magnified on the left side of Scheme 5-2. The cell is further magnified in Scheme 5-3 to illustrate the path of the infrared beam through the



**Scheme 5-2:** A diagram of the *in situ* transmission FTIR spectroelectrochemical cell (not drawn to scale).  $I_{IN}$  and  $I_{OUT}$  refer to the intensity of the infrared beam before and after passing through the cell, respectively.



**Scheme 5-3:** A drawing of the KBr windows in the *in situ* transmission FTIR spectroelectrochemical cell (not drawn to scale).

cathode. Both electrodes contain 13 mm × 2 mm KBr windows mounted to the electrode assemblies with an epoxy resin. On one electrode, a small amount of cathode slurry is painted onto the surface of the KBr window. Evaporation of the solvent leaves a thin layer of composite cathode deposited on the window. It is extremely important that the cathode layer is not too thick; otherwise, the transmittance of the cell will be too low to detect any spectral features of the electrode material. A piece of very thin Ni MicroMesh is placed over the cathode to provide electrical conduction, and a ring of Celgard 2700 separator (22.2 mm OD, 9.22 mm ID) is placed over the Ni mesh to prevent electrical

shorts with the other electrode assembly. The inside diameter of the separator ring is large enough that it does not interact with the infrared beam. The Ni mesh and separator are firmly held in place with a stainless steel ring as shown in Scheme 5-2. The anode consists of a thin ring of metallic lithium pressed onto the exterior wall of the anode assembly nearest to the KBr window (see Scheme 5-2). The entire cell is then assembled and flooded with an electrolyte (1 M LiPF<sub>6</sub> dissolved in a 1:1 mixture of ethylene carbonate and diethyl carbonate (EC-DEC)).

5.3.1.3 Electrochemical and Spectroscopic Experiments – Transmission FTIR spectra are measured with a Bruker IFS 66v (Globar source, KBr beamsplitter, DTGS detector). The experimental data consist of 64 averaged scans collected under flowing dry air.

Electrochemical experiments are performed with a Maccor battery cycler (model #4304). The cells are potentiostatically discharged at 0.5 mV/sec to 2.0 V and then held at that potential. The electrochemical performance of chemically synthesized FePO<sub>4</sub> is also evaluated in “normal” electrochemical cells. Size 2430 coin cells are constructed with the above cathodes, a lithium metal anode (Aldrich), two pieces of Celgard 2700 separator, a Whatman GF glass microfiber separator, and the electrolyte solution. The coin cells are cycled under the same conditions as the *in situ* cells.

### 5.3.2 Lithium Insertion in Orthorhombic FePO<sub>4</sub>

The electrochemical performance of the *in situ* transmission FTIR spectroelectrochemical cell is evaluated with Li|1M LiPF<sub>6</sub> EC-DEC|FePO<sub>4</sub> half-cells. The resulting data are presented in Fig. 5-4. Discharging the cell produces a broad peak

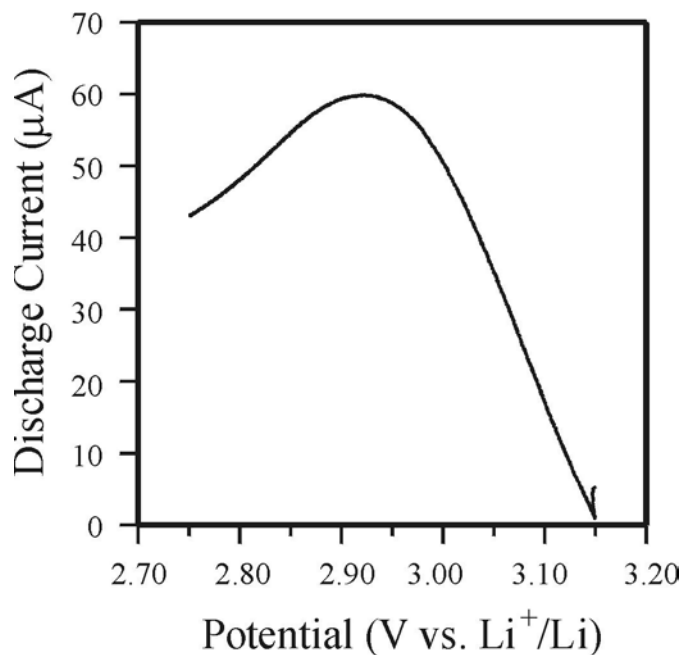


**Figure 5-4:** First discharge of FePO<sub>4</sub> in the *in situ* transmission FTIR spectroelectrochemical cell.

centered at 2.92 V vs. Li<sup>+</sup>/Li in the cyclic voltammogram. This corresponds to the reduction of Fe<sup>3+</sup> to Fe<sup>2+</sup> in the cathode material. Interestingly, the insertion of Li<sup>+</sup> into FePO<sub>4</sub> occurs at somewhat lower potentials than are typically reported for Li<sub>x</sub>FePO<sub>4</sub> cathodes (i.e., 2.92 V compared to 3.5 V) [32]. To further address this issue, the electrochemical performance of chemically prepared FePO<sub>4</sub> is investigated in standard coin cell assemblies (Fig. 5-5). These cells also exhibit a lower voltage on the first discharge; however, the charging process occurs at 3.64 V, which is much closer to the reported values. On the subsequent discharge the maximum current intensity occurs at 3.23 V. This suggests that the voltage discrepancy between the Fe<sup>2+</sup>/Fe<sup>3+</sup> redox couple in the *in situ* spectroelectrochemical cell and the literature value is probably due to the chemical preparation of FePO<sub>4</sub> and is not an inherent problem in the design of the cell.

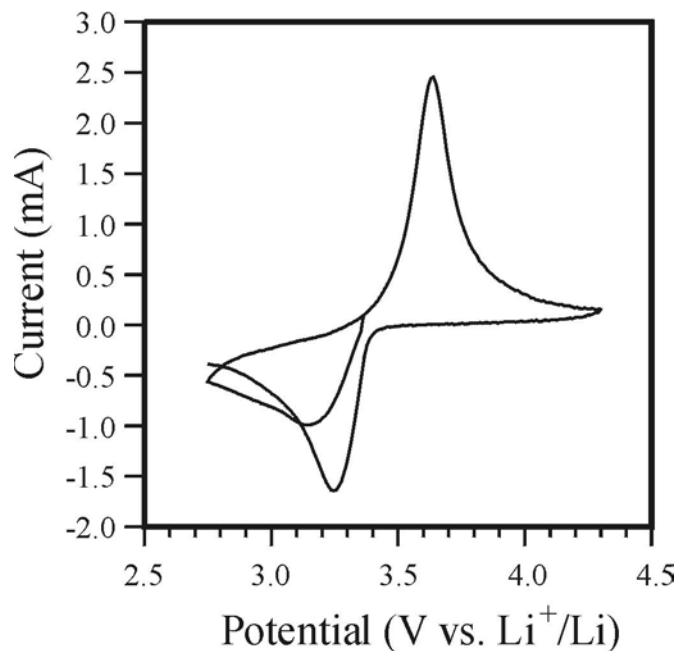


**Figure 5-5:** Electrochemical cycling of FePO<sub>4</sub> inside a coin cell. The negative currents correspond to the discharging step, whereas positive currents refer to the charging step.

Modifying the *in situ* transmission cell to include a reference electrode would also increase confidence in the measured reduction potentials.

Charging the Li//FePO<sub>4</sub> half-cells leads to an accumulation of lithium metal at the edge of the KBr window on the anode assembly. Further charging causes the lithium metal to gradually encroach over the KBr window and eventually reach the inside edge of the separator. At this point, the *in situ* cell internally shorts. Replacing the lithium metal with an intercalation anode (e.g., graphite fibers, Sn-alloys, or Li<sub>4</sub>Ti<sub>5</sub>O<sub>12</sub> spinel) could alleviate this issue, but this avenue of research has not been explored in this preliminary report.

Infrared transmission spectra recorded during the electrochemical insertion of Li<sup>+</sup> into FePO<sub>4</sub> are shown in Fig. 5-6. Although the intramolecular PO<sub>4</sub><sup>3-</sup> stretching modes

of  $\text{FePO}_4$  ( $\nu_1$  and  $\nu_3$ ) could not be observed because the solvent molecules used in the electrolyte solution strongly absorb infrared radiation at the same frequencies (900 to  $1400\text{ cm}^{-1}$ ), good infrared spectra can be recorded between  $800$  and  $450\text{ cm}^{-1}$ .

Antisymmetric  $\text{PO}_4^{3-}$  bending vibrations ( $\nu_4$ ) of  $\text{FePO}_4$  are identified at  $657\text{ cm}^{-1}$  prior to discharging (denoted with dashed lines in Fig. 5-6), and several bands due to the electrolyte solution are also observed in the spectra. For example, the bands at  $717$  and

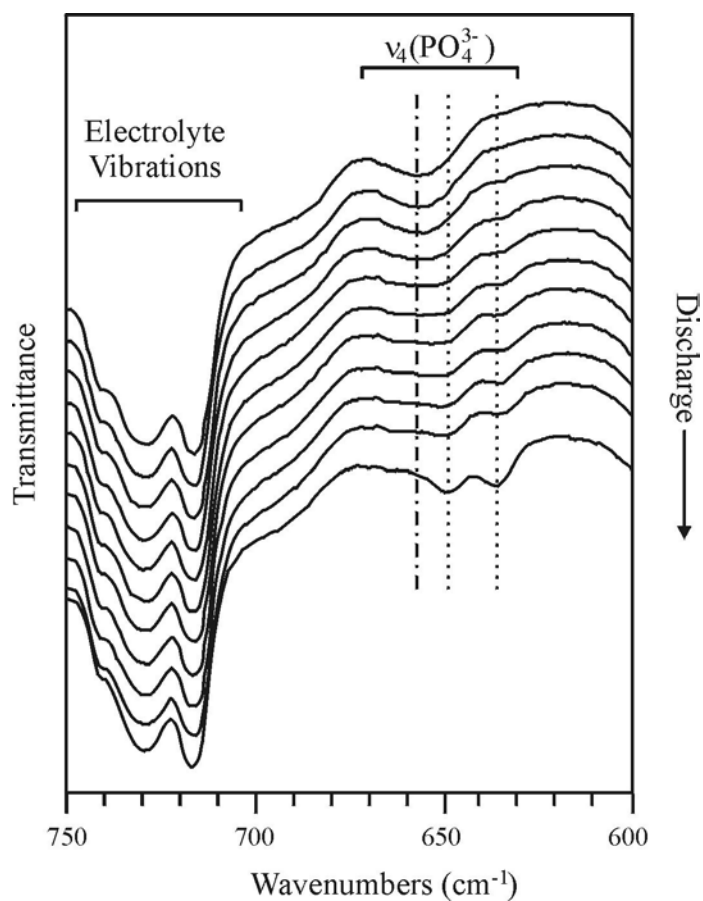


**Figure 5-6:** *In situ* transmission FTIR spectra recorded during the first discharge of  $\text{FePO}_4$ . The  $\text{FePO}_4$  bands are marked with alternating dashes and dots ( $- \cdot -$ ), while the  $\text{LiFePO}_4$  vibrations are denoted with dotted lines ( $\cdot \cdot \cdot$ ).



526  $\text{cm}^{-1}$  may be assigned to ring bending and O-C-O bending vibrations of ethylene carbonate [33]. A high frequency shoulder on the 730  $\text{cm}^{-1}$  band occurs near 741  $\text{cm}^{-1}$ . This band is assigned to the totally symmetric stretching vibration of ion-paired  $\text{PF}_6^-$  anions. Normally, this mode is Raman active and infrared inactive; nevertheless,  $\text{Li}^+$  coordination to  $\text{PF}_6^-$  breaks the octahedral symmetry of the anion, causing the mode to become simultaneously IR and Raman active. Experimental data to support this assignment is provided in Chapter 6.

During lithium insertion, the spectroscopic data reveal changes in the  $\nu_4$  bands as  $\text{Li}^+$  ions are inserted into the cathode material. For instance, the 657  $\text{cm}^{-1}$  band gradually decreases in intensity at the expense of the 648 and 635  $\text{cm}^{-1}$  bands. Moreover, the

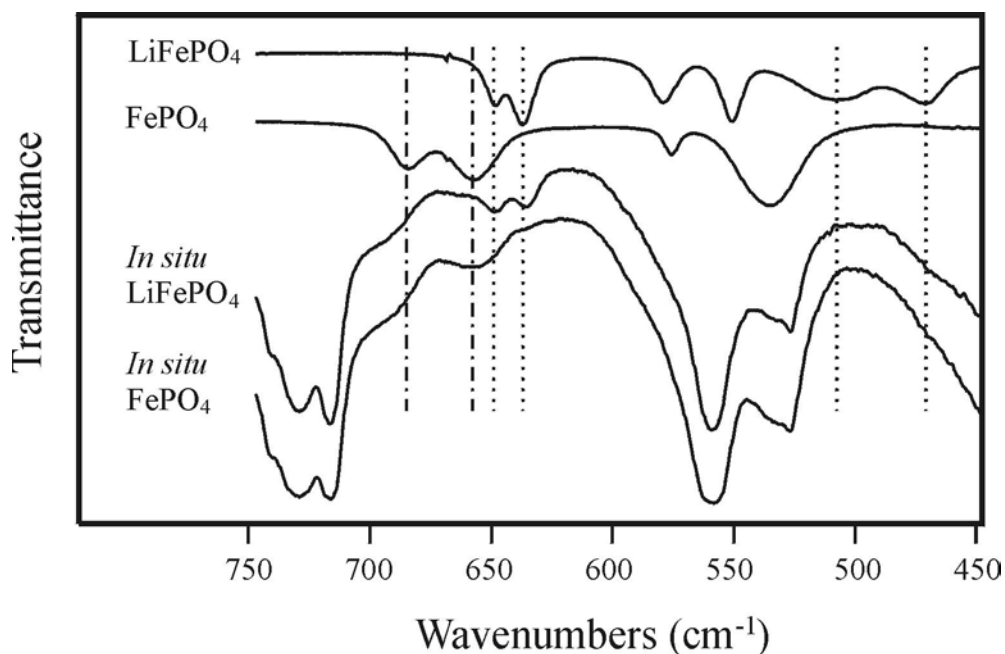


**Figure 5-7:** Infrared transmission spectra of  $\text{FePO}_4$  and  $\text{LiFePO}_4$ . The  $\text{FePO}_4$  bands are marked with alternating dashes and dots ( $-\cdot-$ ), while the  $\text{LiFePO}_4$  vibrations are denoted with dotted lines ( $\cdot\cdot\cdot$ ).

electrolyte bands remain unchanged throughout the entire discharge step, indicating that the concentration of  $\text{Li}^+\cdots\text{PF}_6^-$  ion pairs and the conformation of the solvent molecules are not significantly affected by the discharging process. Fig. 5-7 compares *in situ* infrared spectra of  $\text{FePO}_4$  and a spectrum of the fully discharged sample to chemically prepared  $\text{FePO}_4$  and  $\text{LiFePO}_4$ . As expected, the frequencies of the  $\nu_4$  modes for electrochemically prepared  $\text{LiFePO}_4$  (648 and  $635\text{ cm}^{-1}$ ) are consistent with of chemically synthesized  $\text{LiFePO}_4$  (cf. Fig. 5-7 to the data in Section 2.3.1 and Ref. [34]). In the fully discharged material, a small degree of spectral intensity detected near  $500\text{ cm}^{-1}$  may correspond to  $\text{Li}^+$  ion cage modes of  $\text{LiFePO}_4$  ( $506$  and  $470\text{ cm}^{-1}$ ) [34]. In these modes,  $\text{Li}^+$  ions vibrate in a potential energy environment determined by their nearest neighbor oxygen atoms. However, identification of the  $\text{Li}^+$  ion cage modes with the *in situ* spectroelectrochemical cell is tenuous and an unambiguous assignment cannot be made.

The spectral changes illustrated in Figs. 5-6 and 5-7 coupled with the electrochemical data of Fig. 5-4 clearly demonstrate the ability to follow lithium insertion into  $\text{FePO}_4$  with *in situ* transmission FTIR spectroelectrochemistry. The technique could become valuable for investigating advanced electrode materials, especially materials with polyatomic anions such as  $\text{PO}_4^{3-}$  or  $\text{SO}_4^{2-}$ , as a function of lithium content and should be used to complement other *in situ* spectroscopic methods.

## 5.4 Conclusions

In this chapter, a modification to industrially available coin cells is described to facilitate routine *in situ* Raman spectroelectrochemical measurements of rechargeable

lithium batteries. This would enable researchers to easily construct *in situ* Raman spectroelectrochemical cells alongside cells used for normal electrochemical evaluations. To test this strategy, *in situ* Raman spectroelectrochemical data are collected from Li//V<sub>2</sub>O<sub>5</sub> cells. There is good agreement between the Raman spectra collected from the modified coin cells and the previous spectroscopic analyses of the various Li<sub>x</sub>V<sub>2</sub>O<sub>5</sub> phases. The electrochemical cycling performance of the *in situ* cells is also very similar to the modified coin cells. This illustrates the ability to collect good spectroscopic and electrochemical data from these cells. Care should be taken to perform these experiments under a controlled atmosphere. Otherwise, water may diffuse through the seal between the optical window and the cell casing. This would contaminate the *in situ* cells and affect the electrochemical and/or spectroscopic results. Unfortunately, it is not possible to collect *in situ* Raman spectroelectrochemical measurements of the phosphate-based materials explored in this dissertation. This is primarily due to intrinsic properties of the compounds rather than an inherent problem with the spectroelectrochemical cell design.

The general strategy of modifying coin cells for *in situ* spectroscopic analysis could be expanded to include other spectroscopic techniques. The cells described in this paper could be directly used for *in situ* optical microscopy and potentially *in situ* reflection UV-Vis spectroscopy. Likewise, it may be possible to collect *in situ* reflection FTIR spectra of practical electrode materials from similarly modified coin cells if an appropriate optical window is used. However, at this time these possibilities have not been explored.

A new *in situ* transmission infrared spectroelectrochemical cell is used to monitor the electrochemical insertion of lithium into phospho-olivine FePO<sub>4</sub>. Bands belonging to the electrolyte and the cathode material are identified in the infrared spectra of complete

Li//FePO<sub>4</sub> *in situ* cells. For example, the totally symmetric stretching vibration of ion-paired PF<sub>6</sub><sup>-</sup> anions is detected at 741 cm<sup>-1</sup>. The antisymmetric PO<sub>4</sub><sup>3-</sup> bending vibrations (ν<sub>4</sub>) are used to follow Li<sup>+</sup> insertion as FePO<sub>4</sub> is discharged. The spectral changes are consistent with the formation of LiFePO<sub>4</sub>, thereby demonstrating the ability to collect *in situ* transmission FTIR spectra of electrode materials in functioning lithium batteries.

## 5.5 References

- [1] A. Manthiram, in *Lithium Batteries: Science and Technology*, G.-A. Nazri and G. Pistoia, Eds., Kluwer Academic Publishers: Boston, (2004) 3-4.
- [2] E. Cazzanelli, G. Marriotto, S. Passerini and F. Decker, *Solid State Ionics*, **70-71**, (1994) 412-416.
- [3] T. Itoh, H. Sato, T. Nishina, T. Matue and I. Uchida, *J. Power Sources*, **68**, (1997) 333-337.
- [4] X. Zhang and R. Frech, *J. Electrochem. Soc.*, **145**, (1998) 847-851.
- [5] W. Huang and R. Frech, *J. Power Sources*, **81-82**, (1999) 616-620.
- [6] D. E. Irish, Z. Deng and M. Odziemkowski, *J. Power Sources*, **54**, (1995) 28-33.
- [7] W. Huang and R. Frech, *J. Electrochem. Soc.*, **145**, (1998) 765-770.
- [8] J.-C. Panitz, F. Joho and P. Novak, *Appl. Spectrosc.*, **53**, (1999) 1188-1199.
- [9] D. A. Totir and D. A. Scherson, *Electrochem. Solid-State Lett.*, **3**, (2000) 263-265.
- [10] J.-C. Panitz, P. Novák and O. Haas, *Appl. Spectrosc.*, **55**, (2001) 1131-1137.
- [11] Y. Luo, W.-B. Cai and D. A. Scherson, *J. Electrochem. Soc.*, **149**, (2002) A1100-A1105.
- [12] Y. Luo, W.-B. Cai and D. A. Scherson, *Electrochem. Solid-State Lett.*, **4**, (2001) A101-A104.
- [13] Y. Luo, W.-B. Cai, X.-K. Xing and D. A. Scherson, *Electrochem. Solid-State Lett.*, **7**, (2004) E1-E5.

- [14] I. Rey, J. C. Lassègues, P. Baudry and H. Majastre, *Electrochim. Acta*, **43**, (1998) 1539-1544.
- [15] D. Aurbach, *Nonaqueous Electrochemistry*, Marcel Dekker: New York (1999).
- [16] D. Aurbach and A. Zaban, in *Nonaqueous Electrochemistry*, D. Aurbach, Ed., Marcel Dekker, Inc.: New York, (1999) 119-122.
- [17] R. Baddour-Hadjean, V. Golabkan, J. P. Pereira-Ramos, A. Mantoux and D. Lincot, *J. Raman Spectrosc.*, **33**, (2002) 631-638.
- [18] J. M. McGraw, J. D. Perkins, J.-G. Zhang, P. Liu, P. A. Parilla, J. Turner, D. L. Schulz, C. J. Curtis and D. S. Ginley, *Solid State Ionics*, **113-115**, (1998) 407-413.
- [19] W.-B. Cai, Q. Shi, M. F. Mansuetto and D. A. Scherson, *Electrochem. Solid-State Lett.*, **3**, (2000) 319-320.
- [20] S. Migge, G. Sandmann, D. Rahner, H. Dietz and W. Plieth, *J. Solid State Electrochem.*, **9**, (2005) 132-137.
- [21] H. G. Bachmann, F. R. Ahmed and W. H. Barnes, *Z. Krist.*, **115**, (1961) 110-131.
- [22] D. Gourier, A. Tranchant, N. Baffier and R. Messina, *Electrochim. Acta*, **37**, (1992) 2755-2764.
- [23] M. Broussely, J. Labat, J. M. Bodet and J. M. Cocciantelli, *Power Sources*, **13**, (1991) 429-436.
- [24] K. West, B. Zachau-Christiansen, T. Jacobsen and S. Skaarup, *Solid State Ionics*, **776**, (1995) 15-21.
- [25] C. Delmas, H. Cognac-Auradou, J. M. Cocciantelli, M. Ménétrier and J. P. Doumerc, *Solid State Ionics*, **69**, (1994) 257-264.
- [26] J. M. Cocciantelli, M. Ménétrier, C. Delmas, J. P. Doumerc, M. Pouchard, M. Broussely and J. Labat, *Solid State Ionics*, **78**, (1995) 143-150.
- [27] J. M. Cocciantelli, J. P. Doumerc, M. Pouchard, M. Broussely and J. Labat, *J. Power Sources*, **34**, (1991) 103-111.
- [28] C. Delmas, S. Brèthes and M. Ménétrier, *J. Power Sources*, **34**, (1991) 113-118.
- [29] J. M. Cocciantelli, M. Ménétrier, C. Delmas, J. P. Doumerc, M. Pouchard and P. Hagenmuller, *Solid State Ionics*, **50**, (1992) 99-105.
- [30] J. M. Cocciantelli, P. Gravereau, J. Doumerc, M. Pouchard and P. Hagenmuller, *J. Solid State Chem.*, **93**, (1991) 497-502.

- [31] L. Abello, E. Husson, Y. Repelin and G. Lucazeau, *Spectrochim. Acta*, **39A**, (1983) 641-651.
- [32] A. K. Padhi, K. S. Nanjundaswamy and J. B. Goodenough, *J. Electrochem. Soc.*, **144**, (1997) 1188-1194.
- [33] B. Fortunato, P. Mirone and G. Fini, *Spectrochim. Acta*, **27A**, (1971) 1917-1927.
- [34] M. T. Paques-Ledent and P. Tarte, *Spectrochim. Acta*, **30A**, (1974) 673-689.

## Chapter 6: IONIC ASSOCIATION OF LiPF<sub>6</sub> IN NON-AQUEOUS ELECTROLYTES

*Christopher M. Burba and Roger Frech, J. Phys. Chem. B., 109 (2005) 15161-15164\**

---

### 6.1 Introduction

Lithium hexafluorophosphate dissolved in aprotic solvents has become a standard electrolyte for secondary Li<sup>+</sup> ion batteries [1]. A major focus of the research on these electrolyte systems has been devoted to optimizing the conductivity of mixed solvent solutions for practical battery applications [2-9]. The literature covering this field of research is vast, and it is not in the interest of this chapter to provide a comprehensive literature review of the subject. Ionic association in electrolytes can affect the conductivity of a solution by producing low mobility aggregates or reducing the number of charge carriers in solution through the formation of neutral ion pairs [10]. Therefore, it is important to understand on a molecular level how LiPF<sub>6</sub> behaves in nonaqueous solvents.

Vibrational spectroscopic techniques are extremely useful for probing ionic associations in many electrolytes [11-18]. Early work focused on solutions of LiClO<sub>4</sub> [12,19] or LiCF<sub>3</sub>SO<sub>3</sub> [13,15] and utilized frequency shifts of nondegenerate modes in the Raman spectrum. Later work also examined frequency shifts of nondegenerate modes in the infrared spectrum [20,21]. Several researchers have demonstrated that LiXF<sub>6</sub> salts (X = P, As, or Sb) form ion pairs in aprotic solvents by investigating the infrared-active modes of the XF<sub>6</sub><sup>-</sup> anion [22-26]. Most of these studies have focused on the ν<sub>3</sub>(F<sub>1u</sub>) and

\*Reproduced with permission from Christopher M. Burba and Roger Frech, *J. Phys. Chem. B.*, **109** (2005) 15161-15164. Copyright 2005 American Chemical Society.

$\nu_4(F_{1u})$  vibrations. The symmetry labels designate the point group irreducible representations of  $\nu_3$  and  $\nu_4$  in the isolated anion. Ion-ion interactions perturb the octahedral symmetry of the  $XF_6^-$  ion and break the 3-fold degeneracy of  $\nu_3$  and  $\nu_4$ , producing multiple bands in the spectral regions containing these vibrations.

During the *in situ* transmission FT-IR spectroscopic measurements of the Li | 1 M LiPF<sub>6</sub> EC-DEC | FePO<sub>4</sub> cells (Sec. 5-3, especially Fig. 5-7), bands were observed in the spectral region where the  $\nu_1$  mode is expected (approximately 740 cm<sup>-1</sup>). According to theory, the  $\nu_1$  mode of isolated PF<sub>6</sub><sup>-</sup> anions is only Raman active. However, the working hypothesis of this chapter is that ion-ion interactions between Li<sup>+</sup> and PF<sub>6</sub><sup>-</sup> result in  $\nu_1$  being simultaneously Raman and IR active, and hence observable in an infrared transmission measurement. The modification of symmetry-based selection rules through ion-ion interactions offer an alternative spectroscopic method for examining fundamental questions of ionic association in electrolyte solutions. It is known that ionic association decreases with increasing solution dielectric constant [18,27]. Therefore, to test this hypothesis, infrared spectra are measured in a series of solutions whose solvents have dielectric constants that span a range of values.

## 6.2 Experimental Methods

Lithium hexafluorophosphate was dissolved in the following solvents (dielectric constants in parentheses): diethyl carbonate (2.8), dimethyl carbonate (3.1), ethyl acetate (6.0), 2-methoxyethyl ether [diglyme] (7.3), 2-pentanone (13.48), 2-hexanone (15.45), acetone (20.7), dimethyl sulfoxide (46.7), and propylene carbonate (64.4). All of the



solvents were stored in an Ar glove box ( $\text{H}_2\text{O} < 1$  ppm,  $\text{O}_2 < 100$  ppm) over 4Å molecular sieves. These solvents were chosen because they do not have spectral features in the region of interest ( $\sim 740$   $\text{cm}^{-1}$ ) and they cover a wide range of dielectric constants. In general, solutions were prepared by dissolving the appropriate amount of  $\text{LiPF}_6$  to make a 20:1 (solvent: $\text{LiPF}_6$ ) mole ratio solution. Some lower concentration solutions were also prepared to investigate ion-solvent interactions. All of the solutions were made under an argon atmosphere, and each sample was stirred for at least one hour to ensure sample homogeneity. Details concerning the instrumental procedures may be found in App. A.

## 6.3 Results and Discussion

### 6.3.1 Ion–Ion Interactions

Isolated  $\text{PF}_6^-$  anions have three Raman-active modes ( $A_{1g} + E_g + F_{2g}$ ), two IR-active modes ( $2F_{1u}$ ), and one mode that is neither IR- nor Raman-active ( $F_{2u}$ ). The coordination of  $\text{Li}^+$  cations to the  $\text{PF}_6^-$  anions reduces the symmetry of the  $\text{PF}_6^-$  molecule from  $O_h$  to  $C_{nv}$  ( $n = 2-4$ ). The exact symmetry of the ion pair will depend on the coordination geometry (see Fig. 6-1). For example, in a bidentate configuration, the  $\text{Li}^+$  ion interacts with two adjacent fluorine atoms of the  $\text{PF}_6^-$  molecule and the symmetry of the  $\text{Li}^+ \cdots \text{PF}_6^-$  species would be  $C_{2v}$ . The three possible coordination geometries of the  $\text{Li}^+ \cdots \text{PF}_6^-$  ion pair all destroy the center of symmetry of the  $\text{PF}_6^-$  anion and change the symmetry of the  $\nu_1$  mode from  $A_{1g}$  to  $A_1$ . Consequently,  $\nu_1(A_1)$  for ion-paired  $\text{PF}_6^-$

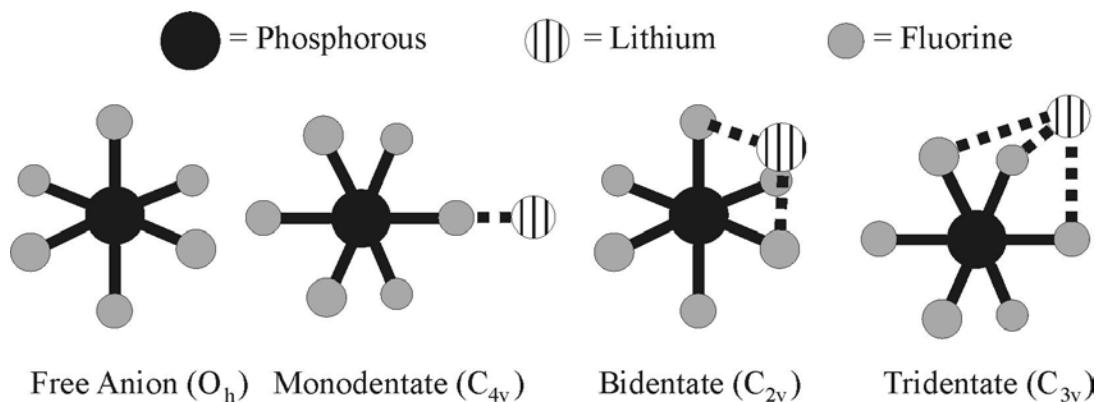


**Figure 6-1:** Possible coordination environments of the  $\text{Li}^+ \cdots \text{PF}_6^-$  ion pairs. The point group symmetry is given in parentheses.

anions will be simultaneously Raman and IR active. Throughout the remainder of this chapter,  $\nu_1(A_1)$  will refer to the  $\nu_1$  mode of ion-paired  $\text{PF}_6^-$  anions while  $\nu_1(A_{1g})$  denotes the  $\nu_1$  vibration of “spectroscopically free”  $\text{PF}_6^-$  anions.

Fig. 6-2 contains infrared spectra of  $\text{LiPF}_6$  dissolved in a series of solvents (20:1 mole ratio). As pointed out by Perelygin *et al.* [22], the  $\nu_4$  band at  $558 \text{ cm}^{-1}$  is only marginally affected by salt concentration and solvent type; therefore, all of the spectra are scaled with respect to this band. In Fig. 6-2, the band centered at  $741 \text{ cm}^{-1}$  gradually decreases in intensity as the dielectric constant of the solvent increases. The frequency of this band is nearly identical to the  $\nu_1(A_{1g})$  mode in Raman spectra of solid  $\text{KPF}_6$  ( $751 \text{ cm}^{-1}$ ) [28] and aqueous solutions of  $\text{NH}_4\text{PF}_6$  ( $741 \text{ cm}^{-1}$ ) [29]. Accordingly, the observation of this band in the infrared spectra of  $\text{LiPF}_6$  solutions is attributed to  $\nu_1$  and is postulated to result from a breakdown in selection rules for  $\text{PF}_6^-$  anions that participate in  $\text{Li}^+ \cdots \text{PF}_6^-$  ion pairs.

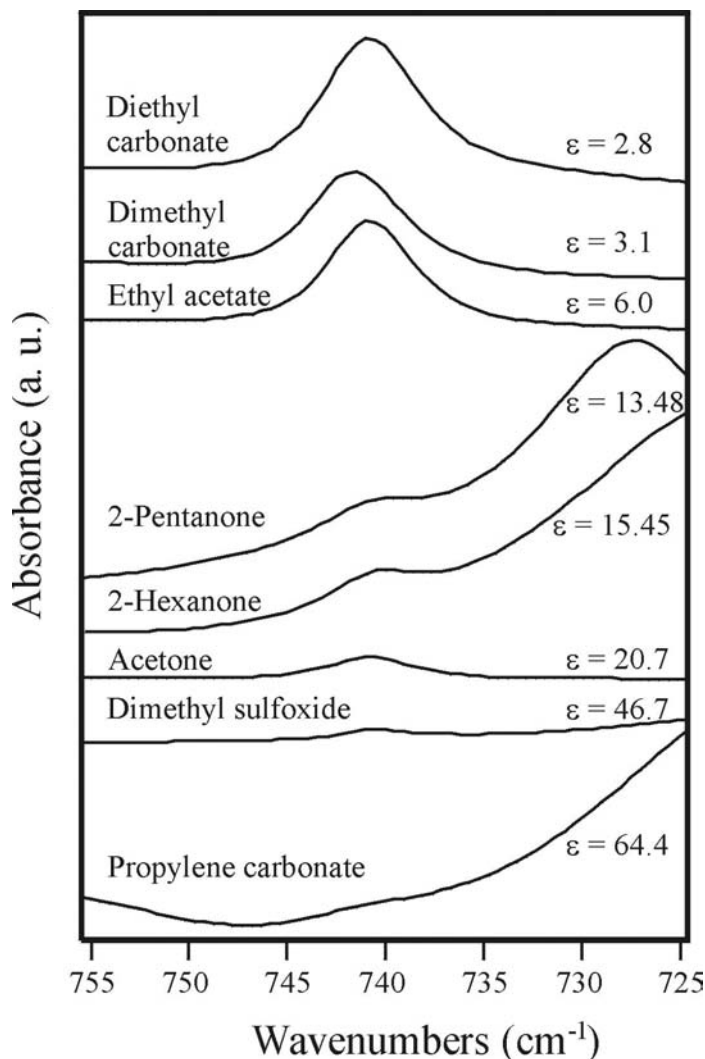


**Figure 6-2:** Infrared absorption spectra of  $\text{LiPF}_6$  dissolved in a series of aprotic solvents (20:1 composition).

In high dielectric solvents such as dimethyl sulfoxide and propylene carbonate, the  $\nu_1$  band essentially vanishes. It is useful to think of solvent-cation interactions in terms of the polarizability of the solvent molecules rather than the macroscopic dielectric constant of the solvent because the number of ion pairs in solution depends on the polarizability of the solvent molecules. Highly polarizable molecules can solvate the  $\text{Li}^+$  ions and hinder  $\text{Li}^+ \cdots \text{PF}_6^-$  ion pair formation more effectively than molecules that are not

very polarizable. The dielectric constant of a solvent is related to the molecular polarizability through the Clausius–Mossotti relationship [30]. Therefore, more ion pairs are able to form in low dielectric solvents than in high dielectric solvents, and the intensity of the  $\nu_1(A_1)$  band in the infrared spectrum increases. In high dielectric solutions, it is more likely that a  $\text{Li}^+$  ion is surrounded by a cloud of solvent molecules and counterions rather than forming contact ion pairs.

### 6.3.2 Ion–Solvent Interactions

Lithium ion-solvent coordination is also expected to influence ionic association in these systems [18]. Indeed, it has been demonstrated that  $\text{Li}^+$  ions can interact strongly with the carbonyl groups of solvents such as dimethyl carbonate and diethyl carbonate. Aroca *et al.* [25] showed that adding  $\text{LiPF}_6$  to either diethyl carbonate or dimethyl carbonate significantly affects the carbonyl stretching frequency. Moreover,  $\text{LiAsF}_6$  salts have been shown to strongly affect the conformational equilibrium of dimethyl carbonate [24]. The effect of lithium-solvent interactions on  $\nu_1$  was explored for two different solutions:  $\text{LiPF}_6$  dissolved in ethyl acetate ( $\epsilon = 6.0$ ) and  $\text{LiPF}_6$  in diglyme ( $\epsilon = 7.3$ ). The solvents were chosen because they have similar dielectric constants and are important components in practical electrolytes for  $\text{Li}^+$  ion batteries [1,31]. In addition, diglyme is a useful spectroscopic model for poly(ethylene oxide)-based polymer electrolytes [32].

Crystal structures for  $\text{P(EO)}_6\text{LiXF}_6$  [33,34] and  $(\text{diglyme})_2\text{LiXF}_6$  [35,36] ( $\text{X} = \text{P}, \text{As}, \text{or Sb}$ ) have been reported in the literature. In these systems, the ether oxygen atoms of the solvent molecules fully coordinate the  $\text{Li}^+$  ions, leaving “free”  $\text{XF}_6^-$  anions. For example, in the  $(\text{diglyme})_2\text{LiSbF}_6$  crystals,  $\text{Li}^+$  cations are completely wrapped by two

diglyme molecules, which produces a six-fold coordination environment for the  $\text{Li}^+$  ions. Grondin *et al.* [36] used vibrational spectroscopy to identify “free”  $\text{PF}_6^-$  ions in  $(\text{diglyme})_2\text{LiPF}_6$  crystals. Furthermore, Seneviratne *et al.* [35] demonstrated that diglyme: $\text{LiSbF}_6$  solutions contain mostly “free”  $\text{SbF}_6^-$  anions. By way of comparison, the  $\text{Li}^+$  ion coordination environment in diglyme: $\text{LiPF}_6$  solutions would be expected to be similar to the  $(\text{diglyme})_2\text{LiPF}_6$  crystals and the diglyme: $\text{LiSbF}_6$  solutions; hence, diglyme: $\text{LiPF}_6$  solutions should contain predominantly “free”  $\text{PF}_6^-$  anions.

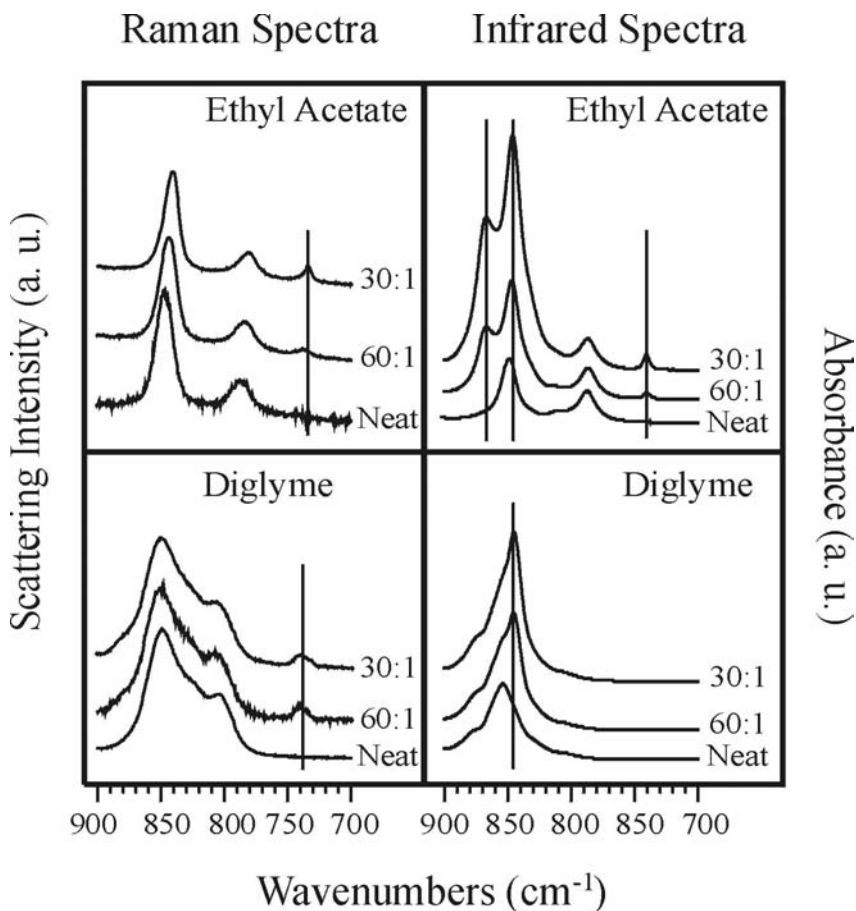


**Figure 6-3:** Raman scattering and infrared absorption spectra of diglyme: $\text{LiPF}_6$  and ethyl acetate: $\text{LiPF}_6$  solutions. The dotted lines (•••) denote  $\nu_1$  vibrations and the lines with alternating dashes and dots (•—•) mark  $\nu_3$  vibrations.

Fig. 6-3 compares Raman and infrared spectra of the ethyl acetate:LiPF<sub>6</sub> and diglyme:LiPF<sub>6</sub> solutions at several different concentrations. The Raman spectra of both systems show a gradual increase in  $\nu_1$  scattering intensity (741 cm<sup>-1</sup>) as the LiPF<sub>6</sub> concentration is increased. The relative Raman scattering intensity of the  $\nu_1$  mode in these solutions agrees with previously published results for LiPF<sub>6</sub> solutions at similar concentrations [25]. Inspection of the 741 cm<sup>-1</sup> band in the infrared spectra indicates that ion pairing is much more prevalent in ethyl acetate:LiPF<sub>6</sub> solutions than in diglyme:LiPF<sub>6</sub> solutions. In fact, the diglyme:LiPF<sub>6</sub> solutions essentially lack any IR-activity for  $\nu_1(A_1)$  over this concentration range. Fig. 6-4 further illustrates the unique nature of the diglyme:LiPF<sub>6</sub> solutions. Here, an infrared spectrum of a 20:1 diglyme:LiPF<sub>6</sub> solution is compared to ethyl acetate:LiPF<sub>6</sub> and acetone:LiPF<sub>6</sub> solutions at the same concentration. The IR-intensity of the  $\nu_1(A_1)$  band is much less in the diglyme:LiPF<sub>6</sub> solution than the other two solutions even though diglyme has a relatively low dielectric constant.

The degenerate  $\nu_3$  mode is also sensitive to the presence of Li<sup>+</sup>⋯PF<sub>6</sub><sup>-</sup> ion pairs in solution [22-25], and strong  $\nu_3$  bands appear in the infrared spectra of both systems between 800 and 900 cm<sup>-1</sup> (Fig. 6-3). The Raman bands above 775 cm<sup>-1</sup> are due to the solvent molecules. Although solvent bands overlap the PF<sub>6</sub><sup>-</sup> vibrations in the infrared spectrum, it is clear that two bands appear at 845 and 867 cm<sup>-1</sup> in the ethyl acetate-based solutions, yet only one band emerges at 845 cm<sup>-1</sup> in the diglyme-based solutions. Aroca *et al.* [25] and Pereygin *et al.* [22] both assigned the 845 cm<sup>-1</sup> band to “free” PF<sub>6</sub><sup>-</sup> anions and the 867 cm<sup>-1</sup> band to Li<sup>+</sup>⋯PF<sub>6</sub><sup>-</sup> ion pairs. Therefore, the spectroscopic data suggest that the diglyme:LiPF<sub>6</sub> solutions contain predominantly “free” anions rather than

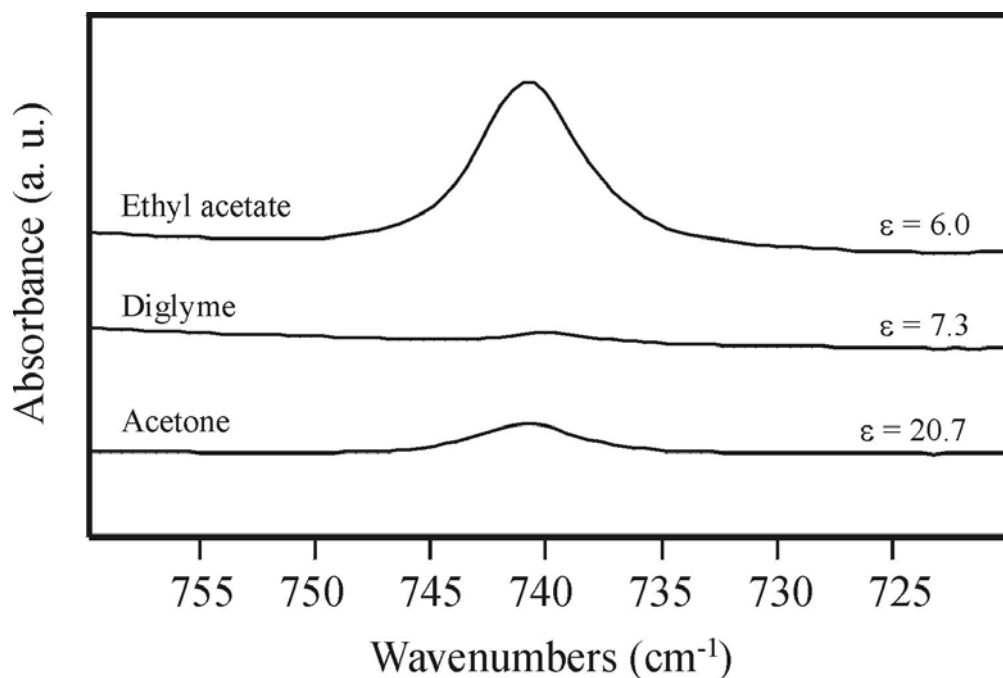


**Figure 6-4:** Infrared absorption spectra comparing diglyme: $\text{LiPF}_6$  solutions to ethyl acetate:  $\text{LiPF}_6$  and acetone: $\text{LiPF}_6$  solutions. The composition is 20:1 for all of three electrolytes.

$\text{Li}^+ \cdots \text{PF}_6^-$  ion pairs because diglyme molecules are able to completely coordinate  $\text{Li}^+$  ions in a very stable configuration. This type of interaction is analogous to  $\text{Li}^+$  complexation by crown ethers. Molecular dynamics simulations of  $\text{LiPF}_6$  dissolved in crown ethers show very little ionic association [37]. In these types of solvents, ion pairing is unfavorable even though the dielectric constant of the solvent is low enough to allow ionic association. Low dielectric, linear carbonate-based solvent molecules such as ethyl acetate are unable to solvate the  $\text{Li}^+$  ions as efficiently as diglyme or crown ethers. Consequently, higher concentrations of  $\text{Li}^+ \cdots \text{PF}_6^-$  ion pairs may form in those solutions.

## 6.4 Conclusions

Cation-anion interactions (presumably ion pairs) of the  $\text{PF}_6^-$  anion in solutions have been spectroscopically observed via an unusual mechanism involving the nondegenerate  $\nu_1$  mode. In the isolated anion, this mode can be observed only in the Raman spectrum due to the presence of a center of symmetry. In  $\text{LiPF}_6$  solutions, the interaction of  $\text{Li}^+$  with  $\text{PF}_6^-$  destroys the octahedral symmetry of the anion and results in  $\nu_1$  becoming simultaneously IR and Raman active. Ionic association in these solutions is strongly affected by the dielectric constant of the solvent. In high dielectric solvents, the solvent molecules can interact strongly with  $\text{Li}^+$  cations, and only a small fraction of the  $\text{PF}_6^-$  anions can penetrate the  $\text{Li}^+$  solvation shell to form ion pairs. Cation-solvent interactions also influence ionic association in  $\text{LiPF}_6$ -based electrolytes. The IR-intensity of  $\nu_1(\text{A}_1)$  is smaller in diglyme: $\text{LiPF}_6$  solutions than in ethyl acetate: $\text{LiPF}_6$  solutions even though the solvents have comparable dielectric constants. It is believed that two diglyme molecules wrap  $\text{Li}^+$  cations in a six-fold coordination environment, which severely hinders the ability of the  $\text{PF}_6^-$  anions to coordinate with the  $\text{Li}^+$  cations. Although the IR-intensity of the  $\nu_1(\text{A}_1)$  band is proportional to the number of  $\text{Li}^+\cdots\text{PF}_6^-$  ion pairs present in solution, this avenue of quantifying the ion pairs was not pursued.

## 6.5 References

- [1] K. Xu, *Chem. Rev.*, **104**, (2004) 4303.



- [2] Y. Matsuda, M. Morita and F. Tachihara, *Bull. Chem. Soc. Jpn.*, **59**, (1986) 1967.
- [3] Y. Matsuda and M. Morita, *J. Power Sources*, **20**, (1987) 273.
- [4] J. T. Dudley, D. P. Wilkinson, G. Thomas, R. LeVae, S. Woo, H. Blom, C. Horvath, M. W. Juzkow and B. Denis, *J. Power Sources*, **35**, (1990) 59.
- [5] S.-I. Tobishima, K. Hayashi, K.-I. Saito and J.-I. Yamaki, *Electrochim. Acta*, **40**, (1995) 537.
- [6] M. S. Ding, K. Xu, S. S. Zhang, K. Amine, G. L. Henriksen and T. R. Jow, *J. Electrochem. Soc.*, **148**, (2001) A1196.
- [7] M. S. Ding and T. R. Jow, *J. Electrochem. Soc.*, **150**, (2003) A620.
- [8] L. F. Xiao, Y. L. Cao, X. P. Ai and H. X. Yang, *Electrochim. Acta*, **49**, (2004) 4857.
- [9] G. Y. Gu, R. Laura and K. M. Abraham, *Electrochem. Solid-State Lett.*, **2**, (1999) 486-489.
- [10] M. Nicolas and R. Reich, *J. Phys. Chem.*, **83**, (1979) 749.
- [11] R. Dupon, B. L. Papke, M. A. Ratner, D. H. Whitmore and D. F. Shriver, *J. Am. Chem. Soc.*, **104**, (1982) 6247.
- [12] S. Schantz, L. M. Torell and J. R. Stevens, *J. Appl. Phys.*, **64**, (1988) 2038.
- [13] S. Schantz, J. Sandahl, L. Börjesson, L. M. Torell and J. R. Stevens, *Solid State Ionics*, **28-30**, (1988) 1047.
- [14] M. Kakihana, S. Schantz, L. M. Torell and J. R. Stevens, *Solid State Ionics*, **40-41**, (1990) 641.
- [15] S. Schantz, L. M. Torell and J. R. Stevens, *J. Chem. Phys.*, **94**, (1991) 6862.
- [16] G. Petersen, P. Jacobsson and L. M. Torell, *Electrochim. Acta*, **37**, (1992) 1495.
- [17] R. Frech, J. Manning and B. Black, *Polymer*, **30**, (1989) 1785.
- [18] J. R. Stevens and P. Jacobsson, *Can. J. Chem.*, **69**, (1991) 1980.
- [19] S. Schantz and L. M. Torell, *Solid State Ionics*, **60**, (1993) 47.

- [20] W. Huang, R. Frech, P. Johansson and J. Lindgren, *Electrochim. Acta*, **40**, (1995) 2147.
- [21] S. Chintapalli, C. Quinton, R. Frech and C. A. Vincent, *Macromolecules*, **30**, (1997) 7472.
- [22] I. S. Pereygin, M. A. Klimchuk, L. V. Rabchuk and L. V. Chaukina, *Russ. J. Phys. Chem.*, **68**, (1994) 44-47.
- [23] M. Nazri, G. A. Nazri and R. Aroca, *Mater. Res. Soc. Symp. Proc. Vol.*, **548**, (1999) 389-393.
- [24] L. Doucey, M. Revault, A. Lautié, A. Chaussé and R. Messina, *Electrochim. Acta*, **44**, (1999) 2371-2377.
- [25] R. Aroca, M. Nazri, G. A. Nazri, A. J. Camargo and M. Trisc, *J. Solution Chem.*, **29**, (2000) 1047-1060.
- [26] S. E. Popov, A. E. Nikiforov, O. V. Bushkova and V. M. Zhukovsky, *J. Phys. Chem. A*, **108**, (2004) 10280.
- [27] C. A. Kraus and R. M. Fuoss, *J. Am. Chem. Soc.*, **55**, (1933) 21.
- [28] G. M. Begun and A. C. Rutenberg, *Inorg. Chem.*, **6**, (1967) 2212-2216.
- [29] L. A. Woodward and L. E. Anderson, *J. Inorg. Nucl. Chem.*, **3**, (1956) 326.
- [30] D. J. Griffiths, *Introduction to Electrodynamics*, 2<sup>nd</sup> ed., Prentice Hall: Englewood Cliffs (1989).
- [31] S. Tobishima, H. Morimoto, M. Aoki, Y. Saito, T. Inose, T. Fukumoto and T. Kuryu, *Electrochim. Acta*, **49**, (2004) 979.
- [32] C. P. Rhodes and R. Frech, *Macromolecules*, **34**, (2001) 2660.
- [33] Z. Gadjourova, D. M. Marero, K. H. Andersen, Y. G. Andreev and P. G. Bruce, *Chem. Mater.*, **13**, (2001) 1282-1285.
- [34] R. Frech, V. Seneviratne, Z. Gadjourova and P. Bruce, *J. Phys. Chem. B*, **107**, (2003) 11255.

- [35] V. Seneviratne, R. Frech, J. E. Furneaux and M. Khan, *J. Phys. Chem. B*, **108**, (2004) 8124.
- [36] J. Grondin, L. Ducasse, J.-L. Bruneel, L. Servant and J.-C. Lasségues, *Solid State Ionics*, **166**, (2004) 441-452.
- [37] K. Tasaki, *J. Electrochem. Soc.*, **149**, (2002) A418-A425.

## Chapter 7: CONCLUDING REMARKS

---

Some of the major results and conclusions of this study are the following:

- Confirmed lithium intercalation mechanisms for a variety of phosphate-based electrode materials using vibrational spectroscopy,
- Assigned lithium ion cage modes in the infrared spectra of orthorhombic  $\text{LiMPO}_4$  ( $M = \text{Fe, Mn, Co, Ni}$ ), monoclinic  $\text{Li}_3\text{V}_2(\text{PO}_4)_3$ , and rhombohedral  $\text{Li}_3\text{M}_2(\text{PO}_4)_3$  ( $M = \text{V, Ti}$ ) cathodes,
- Discovered the formation of a carbonate-based solid electrolyte interphase layer on  $\text{LiSn}_2(\text{PO}_4)_3$  and  $\text{Sn}_3(\text{PO}_4)_2$  anodes,
- Qualitatively measured unreacted metallic tin in fully discharged  $\text{LiSn}_2(\text{PO}_4)_3$  and  $\text{Sn}_3(\text{PO}_4)_2$  with differential scanning calorimetry
- Applied wavelength dispersive spectrometry and the imaging capabilities of an electron microprobe to several electrode materials,
- Developed and tested modified coin cells for *in situ* Raman spectro-electrochemistry,
- Extended the field of *in situ* infrared spectroelectrochemistry to include transmission experiments, and tested the new technique on orthorhombic  $\text{Li}_x\text{FePO}_4$  cathodes,
- Applied symmetry-based arguments to understand ionic association in  $\text{LiPF}_6$ -based electrolytes

These experiments further our understanding of the fundamental reactions that occur inside lithium batteries. The spectroscopic studies demonstrate the usefulness of

vibrational spectroscopy for gaining insight into the charge compensation reactions associated with cycling phosphate-based electrodes. For instance, key features of the vibrational spectrum of  $\text{LiFePO}_4$  could be determined by comparing the spectra of  $\text{LiMPO}_4$  ( $M = \text{Fe, Mn, Ni, and Co}$ ) and  $\text{NaFePO}_4$ . These bands are then observed to be highly sensitive to the electrode's states of charge. Irreversible reactions are also investigated in this dissertation. In particular, a carbonate-based solid electrolyte interphase (SEI) layer is detected on the surface of discharged  $\text{LiSn}_2(\text{PO}_4)_3$  and  $\text{Sn}_3(\text{PO}_4)_2$  anodes with infrared spectroscopy. Furthermore, it is determined that this layer forms over a narrow voltage range. SEI layers are known to strongly influence the cyclability of lithium batteries; therefore, the qualitative identification of the components forming the SEI layer and how it forms is critical information in understanding the electrochemical cycling performance of these materials.

Wavelength dispersive spectrometry is used to estimate the composition of the electrode materials, and the imaging capabilities of the electron microprobe provide information about the particle sizes and morphologies of the samples. These techniques are not commonly used in the lithium battery community. The composition and morphological information ascertained from the electron microprobe could be used to complement other techniques such as transmission electron microscopy (TEM) or scanning electron microscopy (SEM).

A major aspect of this dissertation is the development of new *in situ* electrochemical cells for Raman and infrared spectroscopy. For most laboratories, *in situ* vibrational spectroelectrochemistry is largely hampered by construction costs of the spectroelectrochemical cells. A cheaper *in situ* Raman cell based on modified coin cells

is described and tested with  $V_2O_5$  cathodes. The cycling performance of the modified cells mimics the “normal” cell when cycled under an inert atmosphere, and good Raman spectra could be measured at various states of discharge. The field of *in situ* infrared spectroscopy is also extended to include transmission experiments. The new *in situ* transmission infrared spectroelectrochemical cell is tested with  $FePO_4$  cathodes. Spectroscopic changes in the  $Li_xFePO_4$  can be easily identified as the cell is discharged. Bands belonging to the supporting electrolyte solution are identified in the spectra. These new cell designs provide alternative techniques for investigating lithium intercalation in advanced electrode materials and can be used to study a broad range of materials in addition to the ones discussed here.

## **Appendix A: EXPERIMENTAL METHODS**

---

### **A.1 Powder X-Ray Diffraction**

Powder X-ray diffraction experiments are performed on a Scintag X'Tra XRD system with Cu K $\alpha$  radiation (45 kV, 40 mA). The diffractometer is configured in Bragg-Brentano geometry. Diffractograms are typically recorded at a rate of 0.50°/sec.

### **A.2 Elemental Analysis**

Samples are characterized using a Cameca SX50 electron probe microanalyzer. The materials are mounted in low-viscosity epoxy, ground flat with SiC-impregnated lapping films under H<sub>2</sub>O to a 5  $\mu$ m grit size, and polished using 3, 1, and 0.25  $\mu$ m diamond grits suspended in water. Particle sizes are characterized using backscattered electron imaging and energy-dispersive x-ray analysis. Most of the compositional analysis is performed by wavelength-dispersive spectrometry (20 kV, 10 nA, and 20  $\mu$ m defocused spot). Unfortunately, the epoxy used in the sample preparation prevents an accurate measurement of the oxygen content for the sample, so a complete elemental analysis is not possible. Lithium content is determined by inductively coupled plasma-optical emission spectroscopy.

### **A.3 Particle Size and Surface Area Measurements**

Particle size analyses are performed with a Microtrac-x100. The surface areas for

the samples are measured with the Brunauer-Emmett-Teller [1] method from nitrogen adsorption isotherms.

#### **A.4 Impedance Spectroscopy**

An HP 41292A LF Impedance Analyzer is used to record impedance data (5 Hz to 10 MHz, 0.025 V). Cathodes are composed of 97 wt% active material and 3 wt% Teflon to remove any ambiguity in resolving the graphite's contribution to the electronic conductivity. Discharge rates are lowered to compensate for the lack of graphite.

#### **A.5 Infrared Spectroscopy**

Infrared absorption spectra are measured at  $1\text{ cm}^{-1}$  resolution with a Bruker IFS 66v spectrometer. All spectra are recorded with a DTGS detector and consist of 64 averaged scans. Mylar and KBr beamsplitters are used for far- and mid-IR spectroscopy, respectively. Solid samples are prepared using KBr and CsI pellet techniques, and the spectra are collected under vacuum. Solutions are sandwiched between two 25 mm diameter KBr windows and measured under a dry air purge.

#### **A.6 Raman Spectroscopy**

Raman scattering experiments are conducted on a Jobin Yvon ISA T64000



spectrometer in the triple subtractive mode. The spectrometer is equipped with a CCD detector and a television monitor. A 532 nm laser (Spectra-Physics Millennia Vs) is focused onto the surface of the powders through either the 50× or 80× objective lens of an Olympus microscope. All spectra are recorded in a 180° backscattering configuration. Solid samples are susceptible to thermal damage from the laser; hence, the laser power is set to approximately 10 mW at the laser head. The television is used to monitor the particle surfaces before and after data collection, and spectra are rejected if the sample underwent thermal damage during data acquisition. The duration and number of accumulations averaged together is varied for each material to increase the signal-to-noise ratio. Spectra of the LiPF<sub>6</sub> solutions are collected in a 90° scattering geometry with the laser power set to 80 mW. These samples are contained in glass vials, and each spectrum is an average of ten accumulations (2 min/accumulation).

### **A.7 Differential Scanning Calorimetry**

Samples for DSC are hermetically sealed in 40 µl aluminum crucibles. Thermal scans are recorded on a Mettler-Toledo DSC820 between 100°C and 300°C with a 5°C/min rate.

### **A.8 Reference**

- [1] S. Brunauer, P. H. Emmett and E. Teller, *J. Am. Chem. Soc.*, **60**, (1938) 309-319.